CO_2 SELECTIVE CERAMIC MEMBRANE FOR WATER-GAS-SHIFT REACTION WITH CONCOMITANT RECOVERY OF CO_2

Final Report
For the period September 1, 2000 to March 31, 2005

Paul K. T. Liu
Project Director

July 15, 2005

PREPARED FOR THE UNITED STATES
DEPARTMENT OF ENERGY
Under Cooperative Agreement
No. DE-FC26-00NT40922

By
MEDIA AND PROCESS TECHNOLOGY, INC.
1155 William Pitt Way
Pittsburgh, PA 15238
and
UNIVERSITY OF SOUTHERN CALIFORNIA
Department of Chemical Engineering
Los Angeles, CA 90089-1211

Disclaimer

Abstract

A high temperature membrane reactor (MR) has been developed to enhance the water-gas-shift (WGS) reaction efficiency with concomitant CO_2 removal for sequestration. This improved WGS-MR with CO_2 recovery capability is ideally suitable for integration into the Integrated Gasification Combined-Cycle (IGCC) power generation system. Two different CO_2-affinity materials were selected in this study. The Mg-Al-CO_3-layered double hydroxide (LDH) was investigated as an adsorbent or a membrane for CO_2 separation. The adsorption isotherm and intraparticle diffusivity for the LDH-based adsorbent were experimentally determined, and suitable for low temperature shift (LTS) of WGS. The LDH-based membranes were synthesized using our commercial ceramic membranes as substrate. These experimental membranes were characterized comprehensively in terms of their morphology, and CO_2 permeance and selectivity to demonstrate the technical feasibility. In parallel, an alternative material-base membrane, carbonaceous membrane developed by us, was characterized, which also demonstrated enhanced CO_2 selectivity at the LTS-WGS condition. With optimization on membrane defect reduction, these two types of membrane could be used commercially as CO_2-affinity membranes for the proposed application. Based upon the unique CO_2 affinity of the LDHs at the LTS/WGS environment, we developed an innovative membrane reactor, Hybrid Adsorption and Membrane Reactor (HAMR), to achieve ~100% CO conversion, produce a high purity hydrogen product and deliver a concentrated CO_2 stream for disposal. A mathematical model was developed to simulate this unique one-step process. Finally a bench-top reactor was employed to generate experimental data, which were consistent with the prediction from the HAMR mathematical model. In summary, the project objective, enhancing WGS efficiency for hydrogen production with concomitant CO_2 removal for sequestration, has been theoretically and experimentally demonstrated via the developed one-step reactor, HAMR. Future development on reactor scale up and field testing is recommended.

Executive Summary

A hybrid adsorption-membrane reactor (HAMR) process has been developed to enhance the water-gas-shift (WGS) reaction efficiency with concomitant CO_2 removal for sequestration. This improved WGS with CO_2 recovery capability is ideally suitable for integration into the Integrated Gasification Combined-Cycle (IGCC) power generation system. One adsorbent and two membranes were investigated in this project for their use for the proposed process. A bench-scale HAMR process was performed to demonstrate the process feasibility. Further, its performance was consistent with the prediction from the mathematical model developed in this project. In summary, the project objective, enhancing WGS efficiency for hydrogen production with concomitant CO_2 removal for sequestration, has been theoretically and experimentally demonstrated via the developed one-step reactor, HAMR. Future development on reactor scale-up and field-testing is recommended.

Two different CO_2-affinity inorganic materials were selected in this study. One of them, the Mg-Al-CO_3-layered double hydroxide (LDH), was investigated as an adsorbent or a membrane for CO_2 separation. Several *in-situ* techniques were applied in this study to investigate the thermal evolution behavior of the Mg-Al-CO_3 LDH material as a function of temperature and atmosphere. In the temperature range of 180 to 280°C, significant water and some CO_2 released while the layer structure of LDH remained. In the temperature range of 280 - 405°C, degradation of the LDH structure began. Further, in a cyclic experimental study simulating the LTS condition, about 1.3wt% CO_2 released in the 1st cycle. After 9th cycle, the reversible CO_2 affinity reached a steady state. About 1/3 of the original capacity was determined to be reversible. In summary, the CO_2 release at >190°C was experimentally verified to be reversible, an essential feature for preparing a commercially viable adsorbent or membrane.

The LDH adsorbent developed in this study demonstrated a sufficient adsorption capacity and intraparticle diffusivity at 180 to 250°C, suitable for low temperature shift (LTS) of WGS. Diffusivity constants and adsorption isotherms for carbon dioxide in Mg-Al-CO_3 LDH at 200 - 250°C were determined by the gravimetric method. Diffusivity constants determined by experiments and those obtained by molecular dynamic simulations are in good qualitative agreement. The experimental adsorption isotherms for CO_2 in LDH were studied with the Langmuir isotherm equation as well as various empirical adsorption isotherm equations. It was observed that the heterogeneity of the material and the interaction between CO_2 and LDH increased with temperature. Also it was found that the experimental data were nonlinearly fitted best with the Toth equation based on χ^2 values. Further, it was observed that the amount of CO_2 uptake and the (BET) surface area increased as the particle size decreased. When the uptake amount was normalized with the BET surface area, the uptake amount was fairly constant for all the range of particle sizes. The adsorption isotherm data with different particle sizes of LDH were studied with Langmuir isotherm and Langmuir-Freundlich equation. It was observed that the values of b_{CO_2} and n (constants used in the isotherms) were relatively constant for the whole range of particle sizes. The uptake and isotherm parameters and their best-fitted equation were used for simulating the CO_2 removal via LDH adsorbents in the HAMR reactor.

The technical feasibility of forming a CO_2-affintiy membrane with the LDH material has been demonstrated successfully. The two synthesis techniques and one post-treatment technique

were investigated in this project. Combining the observations from permeance, pore size distribution, EDAX and SEM, we concluded that the LDH crystals were deposited within the pore size of the starting membranes with the pore sizes of 40Å, 500 Å, and 0.2µm. This LDH-based membrane via in-situ crystallization was then post-treated by the CVD/I technique to minimize defects. The CO_2 permeance enhancement was exhibited in the membrane thus formed. For instance, the CO_2 permeance of 0.26 $m^3/m^2/hr/bar$ at 300°C was observed for one of the membranes after the post treatment by chemical vapor deposition/infiltration (CVD/I) technique. Further, our analysis indicated that >50% of the CO_2 permeance was likely attributed to the enhancement by the LDH materials. The balance was contributed by defects remaining in the membrane. The ideal selectivity for CO_2/N_2 ~1.6 at 100 to 300°C was obtained for the LDH membrane prepared via in-situ crystallization and the CVD/I post treatment. In comparison with the ideal selectivity through Knudsen diffusion of 0.8, the selectivity obtained here was about double of what delivered by the Knudsen diffusion. Evidently, the enhanced selectivity was not sufficient to be commercially viable. Optimization study was necessary to reduce the defect to a minimum via the membrane synthesis; thus, minimal post treatment is required to achieve the CO_2 enhancement without sacrificing permeance significantly. The other membrane synthesis technique, the slip casting technology developed here successfully developed a hydrotalcite membrane with the residual pore size of <40Å while maintaining most original permeance, i.e., 30 to 40 $m^3/m^2/hr/bar$, which could be an ideal starting material for the post treatment with CVD/I. No post treatment study was performed for this type of the LDH membrane due to the time constraint. Additional work with the focus on minimization of defects is recommended to upgrade the CO_2 selectivity and permeance for future commercial use.

In parallel, an alternative membrane, carbonaceous membrane developed by us, was characterized, which also demonstrated enhanced CO_2 selectivity at the LTS-WGS condition. This CO_2 affinity membranes demonstrated a higher selectivity for CO_2/N_2, i.e., 4 to 10, up to 220°C, which was much beyond the Knudsen selectivity. Surface affinity of the membrane toward the CO_2 was identified as the dominating mechanism at this operating temperature range. Selectivity at this level is comparable or higher than the selectivity of CO_2/N_2 reported in the literature at the proposed reaction temperature. Additional study including characterization of this type of membrane in a mixture environment is recommended for future development.

Based upon the unique CO_2 affinity of these materials at the LTS/WGS environment, we investigated a novel reactor system, termed the HAMR, for hydrogen production through water gas shift reaction with concomitant CO_2 removal for sequestration. The HAMR combined the reaction and membrane separation steps with adsorption on the membrane feed or permeate side. A mathematical model was developed to simulate this unique one-step process. The reactor characteristics were investigated for a range of temperature, pressure, and other experimental conditions relevant to the aforementioned applications and compared with the behavior of the traditional packed-bed reactor, the conventional membrane reactor (MR) and an adsorptive reactor (AR). The HAMR outperformed all of the other more conventional reactor systems. It exhibited enhanced CO conversion, hydrogen yield, and product purity. The disadvantage of the HAMR system was, similar to that for the ARs, in that they required regeneration of the spent adsorbent, for continuous operation. The HAMR might require a

dual reactor system, where one of the reactors is in operation while the other reactor is being regenerated. Our preliminary experimental results were consistent with the prediction with the mathematical model prediction. HAMR, offers potential to achieve ~100% CO conversion, produces a high purity hydrogen product and delivers a concentrated CO_2 stream for disposal. According to our preliminary economic analysis, about 10% reduction in hydrogen production cost could be achieved under the selected operating condition. More importantly, significant capital cost reduction potential can be realized as a result o the process intensification by the proposed HAMR system. In summary, the project objective, enhancing WGS efficiency for hydrogen production with concomitant CO_2 removal for sequestration, has been theoretically and experimentally demonstrated via the developed one-step reactor, HAMR. Future development on reactor scale-up and field-testing is recommended.

Table of Contents

Chapter **Page**

List of Figures

Figure **Page**

List of Figures (continued)

List of Figures (continued)

List of Figures (continued)

List of Tables

List of Tables (continued)

Chapter 1

Hydrogen Production with Concomitant CO_2 Removal for Sequestration - Introductory Remarks

Since substantial (1/4-1/3) anthropogenic emissions of carbon to the atmosphere result from power generation [1,4], control of CO_2 emission from this particular source is considered one of the most efficient strategies to achieve the national goal of greenhouse gas management. This centralized, instead of dispersed, CO_2 source will provide an attractive opportunity to implement a cost-effective treatment solution. However, the conventional end-of-the-pipe treatment approach, i.e., capture of CO_2 after combustion with air, is not considered economical because the gas volume increases tremendously (~ 3 times) after combustion. According to the literature, this approach costs ~$40/ton of carbon (for a 500 MW fossil fuel-fired power plant, [1]), not including the additional cost for transportation and disposal of CO_2. To develop a cost acceptable solution for CO_2 sequestration, a new direction has been suggested [1] which requires a combination of the following:

- increased base power plant efficiencies,
- reduced capture process energy needs, and
- integration of the capture process with the power plant.

Under this direction we proposed the development of a high temperature CO_2-selective membrane as a reactor (MR), which can enhance the water-gas-shift (WGS) reaction efficiency while recovering CO_2 simultaneously for disposal.

The MR can offer significant advantages to the WGS reaction, mainly (i) reduced capital cost because the high conversion can be achieved in a single stage, (ii) reduced operating cost because steam usage can be reduced, and (iii) reduced CO_2 sequestration cost because CO_2 can be separated from the MR simultaneously. A comprehensive analysis performed by the European Consortium [3] estimated that the net efficiency of the IGCC process with integrated WGS-MR is 42.8% (based upon lower heating value, LHV) with CO_2 recovery (80% based on coal input). This figure is compared with 40.5% (LHV) for an IGCC with conventional CO_2 removal. Therefore, CO_2 separation with significant improvement in power generation efficiency can potentially be delivered by the implementation of the WGS-MR.

The specific affinity to CO_2 of our proposed MR is accommodated by the two unique membrane materials selected in this study. More importantly, they present several unique advantages in membrane synthesis over other existing or emerging materials. This improved WGS-MR w/ CO_2 recovery capability is ideally suitable for integration into the Integrated Gasification Combined-Cycle (IGCC) power generation system. Thus, the high purity hydrogen (high pressure and CO_2 -free) produced from the IGCC can be used either as a product for power generation via a turbine or a fuel cell, or as a reactant for fuel and chemical production.

To achieve this project objective, we proposed the development of MR process to enhance the WGS conversion with concomitant separation of CO_2. Two synthesis concepts on the CO_2-selective ceramic membrane have been pursued under this project: (i) imbedding the Al-Mg-CO_3 layered double hydroxides (LDH) material with CO_2 transport channels, and (ii) depositing carbonaceous material with surface affinity to CO_2 membrane, into the porous structure of the Al_2O_3 ceramic membrane available from us. In this project, we performed synthesis and characterization of these base materials and further evaluated their technical feasibility for the formation of CO_2 affinity membranes. Then, an innovative hybrid reactor process concept was developed and evaluated for its hydrogen production with the concomitant CO_2 removal. Finally a bench-scale WGS reactor study was conducted to experimentally demonstrate the proposed MR concept and its benefit to CO_2 recovery. This project report summarizes rationals, experimental approach, results and discussion, and conclusions for each individual technology element involved in this unique process.

Literature Cited

1. Herzog, H., E. Drake, E. Adams, CO2 Capture, Reuse, and Storage Technologies for Mitigating Global Climate Change, Final Report, DOE Order No. DE-AF22-96PC01257 January 1997.
2. US DOE, Program Solicitation No. DE-PS26-99FT40613, Sep. 8, 1999.
3 Bracht, M., Alderliesten, PT., Kloster, R., Pruschker, R., Haupt, G., Xue, E., Ross, JR., Koukou, M.K., Papayannakos, N., Energy Conservation and Management, 38, 8159 (1997).
4. US DOE, Working Paper on Carbon Sequestration Science and Technology, February 1999

Chapter 2

Thermal Evaluation Study of Mg-Al-CO_3 Layered Double Hydroxides

2.1 Introduction

To develop an CO_2-affinity adsorbent or membrane for our proposed water gas shift reaction at ~200 to 400°C, knowledge on the thermal evolution behavior of this material and its corresponding surface and structure change are essential. In this chapter, the thermal evolution behavior of one of the two selected materials, the Mg-Al-CO_3 LDH is presented using various *in-situ* techniques, including DRIFTS, TG/DTA, TG/MB-MS, and HTXRD. DRIFTS is a sensitive and powerful technique that was utilized in this study to monitor *in-situ* the changes of functional groups of the Mg-Al-CO_3 LDH as a function of temperature and other experimental conditions. *In-situ* TG/DTA techniques were used to monitor the weight and energetic changes of the Mg-Al-CO_3 LDH as a function of temperature. Combining DRIFTS with TG/TDA provides quantitative insight into functional group changes at various temperatures. In addition *in-situ* TG/MB-MS techniques were used to monitor gaseous products generated during their thermal evolution as a function of temperature and other conditions. Combining DRIFTS with TG/MB-MS provides additional quantitative insight into functional group changes at various conditions. Finally, *in-situ* HTXRD was employed to detect the structural changes of Mg-Al-CO_3 LDH as a function of temperature. The results obtained from these *in-situ* techniques allow us to comprehensively characterize the surface and structure change as a function of temperature and eventually develop a model for the thermal evolution behavior of the Mg-Al-CO_3 LDH material, which is essential to design intelligently a CO_2-affinity membrane.

2.2 Experimental

The LDH sample was provided by the Media and Process Technology, Inc., of Pittsburgh, PA. Its composition is $Mg_{0.71}Al_{0.29}(OH)_2(CO_3)_{0.15}{\cdot}0.46(H_2O)$ (hereinafter referred to as LDH1), as determined by ICP and TGA. Experimental methods performed in this chapter are briefly described below:

- DRIFTS spectra were recorded *in-situ* using a Genesis II (Mattson, FT-IR) instrument equipped with a DRIFTS COLLECTOR™ II chamber (SpectraTech, Inc.) capable of operating under high temperatures (up to 900 ^oC) and pressures (up to 1500 psi). The chamber windows are made of ZnSe to withstand these conditions, and to allow for better infrared transmission. A controller is used to control the chamber temperature utilizing a ceramic heater and a thermocouple in intimate contact with the sample. With this chamber, the temperature and the sample environment can be easily controlled. The experimental operating conditions were a DRIFTS scan-range from 4000 cm^{-1} to 500 cm^{-1}, scan numbers 16, and a scan resolution of 2 cm^{-1}. The spectra were calibrated for background with KBr. To obtain a strong signal intensity and better resolution for quantitative measurements, the sample was first ground to 2-10 μm, diluted with KBr to

5~10% wt., placed in the sample cup and leveled with a spatula. Experiments were carried out in an inert gas atmosphere. The temperature was raised at a rate of 0.5 ^{o}C/s, and spectra were recorded at different temperatures about 20 ^{o}C apart.

- For the thermal evolution of LDH's study, the thermogravimetric (TG) curve was recorded on a Pyris 1 TGA HT instrument (PE Company) by heating the sample from 50 to 600 ^{o}C in an Ar atmosphere, at a rate of 5 ^{o}C/min, and an Ar flow rate of 20 ml/min. Differential thermal analysis (DTA) was performed with a DTA 7 instrument (PE Company) at the same conditions as TG. For *in-situ* TG/MB-MS techniques, the thermogravimetric (TG) curve was recorded on a Cahn TGA 121 instrument, and TG/MB-MS instrument that is custom-made, using a MKS UTI 100C Precision Gas Analyzer.

- HTXRD experiments were carried out in the temperature range 30 - 650^{o}C under vacuum (10^{-2} Torr) using a Siemens D-5000 X-ray diffractometer equipped with a Buhler high-temperature chamber HDK 1.4. The chamber is made of stainless steel with Be-windows for X-ray transmission and Ta thermal shields acting as the isothermal block. The sample and its surroundings were heated by Pd heaters at a rate of 0.5 ^{o}C/s; the spectra were recorded at different temperatures, typically 20 ^{o}C apart. The sample was equilibrated at any given temperature for 30 min. The Cu K_α line was used for the X-ray source with a monochromator positioned in front of the detector. Scans were performed over a 2θ range from 5^{o} to 75^{o}.

2.3 Results and Discussion

The thermal evolution pattern obtained with the use of the above instrumentations is discussed below:

Spectra Assignment…Figure 2.1 compares the DRIFTS and FT-IR spectra of the LDH1 at room temperature in Ar. It shows that all key bands in the DRIFTS spectra for the LDH1 are in the same position as those in the FT-IR spectra. The intensities of the DRIFTS signals are sufficiently strong to clearly identify all the important functional groups. In accordance with prior FT-IR studies[1,2], the DRIFTS bands were assigned to the following groups:

(1) The DRIFTS signal at ~3470 cm^{-1} is due to the OH^- group vibration in the Mg-Al-CO_3 LDH sample;
(2) the DRIFTS signal at ~3070 cm^{-1} is due to hydrogen bonding between water and the carbonate species in the interlayer space of the Mg-Al-CO_3 LDH sample;
(3) the DRIFTS signal at ~1620 cm^{-1} is due to the H_2O bending vibration of interlayer water in the Mg-Al-CO_3 LDH sample and;
(4) The DRIFTS signals at ν_3=1370cm^{-1}, ν_2=940cm^{-1}, and ν_4=680cm^{-1} at room temperature are due to the CO_3^{2-} group vibration bands in the Mg-Al-CO_3 LDH sample; the CO_3^{2-} group in the hydrotalcite behaves more like it would in a water solution, in which the vibration bands of CO_3^{2-} are observed at ν_3=1415cm^{-1}, ν_2=880cm^{-1}, and ν_4=680cm^{-1}. No ν_1 mode vibration at ~1080cm^{-1}, and no

splitting of the ν_3 band are observed. The splitting of the ν_3 band and the ν_1 mode vibration band are usually generated from the symmetry degradation, which results from the interaction between CO_3^{2-} and Mg^{2+}. This means that CO_3^{2-} in the Mg-Al-CO_3 LDH sample at room temperature has a very weak, if any, direct interaction with positive ions, such as Mg^{2+} and Al^{3+}.

Thermal Evolution based upon DRIFTS…Based on the above band assignments, one can use the *in-situ* DRIFTS technique to characterize the LDH structural evolution process, especially the changes of the functional groups of the Mg-Al-CO_3 LDH sample as a function of temperature. The *in-situ* DRIFTS results are shown in Figure 2.2, for which the LDH1 was treated in Ar. In these experiments, starting from room temperature, the sample temperature was increased at a rate of 0.5 ^oC/s. Every 20 ^oC or so the temperature increase was on-hold, and the DRIFTS spectra would be recorded after keeping the sample isothermal for a period of ~2 min. The testing was continued until the temperature of the sample had reached 580 ^oC. From Figure 2.2 one can draw the following conclusions:

(1) The intensities of the interlayer water bands at 3070 cm^{-1} and 1620 cm^{-1} gradually decrease with increasing temperature, and disappear around 190^oC. This means that increasing amounts of interlayer water in the LDH1 are removed with increasing temperature. In the presence of Ar beyond 190 ^oC the water that remains in the sample is below the detection limit of the DRIFTS instrument.
(2) The intensity of the OH^- vibration band at 3470cm^{-1} begins to decrease at 190 ^oC, and completely disappears at 440 ^oC. This suggests that in the presence of Ar dehydroxylation of LDH1 begins at 190 ^oC; by the time the temperature reaches 440 ^oC the concentration of the remaining OH^- groups is below the detection limit of the DRIFTS instrument.
(3) The band at 1370 cm^{-1} for the CO_3^{2-} ν_3 vibration begins to decrease in size as the temperature increases, and also shifts to ~ 1350 cm^{-1}. Gradually a band at 1530 cm^{-1} begins to form at temperatures higher than 170 ^oC. The band size at the lower wave number (~1350 cm^{-1}) decreases as the temperature increases (and so are the peaks at 940 and 680 cm^{-1}). This is to be expected as the amount of interlayer water decreases and, as a result, the CO_3^{2-} group begins to interact more strongly with the backbone of the hydrotalcite itself. For comparison purposes, Figure 2.3 shows the DRIFTS spectrum of $MgCO_3$. The behavior of the two bands at 1499 and 1425 cm^{-1} qualitatively mirrors that of the bands at 1530 and 1350 cm^{-1}. On the other hand, the state of CO_3^{2-} in the hydrotalcite is distinctly different from that in $MgCO_3$. Note that bands corresponding to the ν_3 vibration of CO_3^{2-} in $MgCO_3$ are at different positions, namely 1499cm^{-1} and 1425cm^{-1}. In Figure 2.3, one observes the ν_1 vibration band of CO_3^{2-} in $MgCO_3$. This band is not present in Figure 2.2. At higher temperatures all peaks corresponding to CO_3^{2-} species in Mg-Al-CO_3 LDH disappear. This is consistent with the MS data (see the discussion below), which show that by that temperature all CO_3^{2-} has left the hydrotalcite structure as CO_2.

Figure 2.4 summarizes the *in-situ* DRIFTS results of Figure 2.2, indicating the fraction of each particular species that was removed at a given temperature. The calculations based on the peak area of the corresponding species recorded at different temperatures. The 3470 cm^{-1} band represents the OH^- group, and the 3070 cm^{-1} and 1620 cm^{-1} bands represent the interlayer water. For CO_3^{2-}, since the DRIFTS band at 1370cm^{-1} at lower temperatures was split into two DRIFTS bands, i.e., 1530cm^{-1} and 1350cm^{-1}, in the quantitative analysis, the fraction removed was calculated only at temperatures higher than 180 °C using the 1530cm^{-1} and 1350cm^{-1} band to represent CO_3^{2-}. 100% removal in Figure 2.4 corresponds to the point when the particular band is no longer detectable by DRIFTS. It can be seen in Figure 2.4 that the interlayer water starts to disappear at 70 °C, with the band no longer detectable at 190 °C. For the OH^- groups, there is a noticeable difference in the slope of the removal rate between the temperature ranges 190 - 250°C and 250 – 440 °C, suggesting, perhaps, that in these two temperature ranges the OH^- group finds itself in two different environments in the Mg-Al-CO_3 LDH sample. Figure 2.4 also indicates that most of the CO_3^{2-} was removed in the temperature range 390 - 580°C. These results were also confirmed by *in-situ* MS and TG/MS experiments. Figure 2.5, for example, shows the results of *in-situ* MS analysis. It indicates that H_2O is continuously removed from the Mg-Al-CO_3 LDH1 sample until 420 °C, which is consistent with the results of DRIFTS, shown in Figure 2.4. *In-situ* DRIFTS is a powerful technique to monitor the changes of the functional groups in Mg-Al-CO_3 LDH sample as the temperature changes.

Thermal Evolution based upon TG/DTA/MS…*In-situ* TG/MS and TG/DTA, as previously noted, provide complimentary technical information. Figure 2.6 shows, for example, the results of *in-situ* TG/MS analysis. It indicates that a relatively small amount of CO_2 (~11.5%) from the LDH1 was detected in the temperature range of 190 – 390 °C, and most of the CO_2 (~88.5%) from the Mg-Al-CO_3 LDH was detected in the temperature range of 390 – 580 °C. These results are consistent with the results of DRIFTS, shown in Figure 2.4. Figure 2.7 shows the corresponding results of the TG/DTA analysis of the Mg-Al-CO_3 LDH1 sample as a function of temperatures in an inert gas atmosphere.

In-situ DRIFTS with TG/MS for 70 – 190°C…Combining the *in-situ* DRIFTS results with the TG/MS observations, one can draw quantitative conclusions concerning the behavior of the various functional groups. One can conclude, for example, that in Figure 2.6 the first weight loss, ~13.5% by weight, in the temperature range of 70 - 190 °C should be mostly due to the interlayer water in the Mg-Al-CO_3 LDH, together with relatively smaller amounts of CO_2 and H_2O resulting from the desorption of the OH^- group. The theoretical weight fraction of the interlayer water in Mg-Al-CO_3 LDH1 with the reported composition of $Mg_{0.71}Al_{0.29}(OH)_2(CO_3)_{0.15}.0.46H_2O$ is calculated to be 10.84 % by weight. The difference (2.66 % by weight) between the experimental value (13.5 % by weight) and the theoretical value (10.84 % by weight) should be attributed to the contribution of CO_2 and H_2O from the OH^- group, because there are, indeed, small amounts of CO_2 and H_2O from the OH^- group that were removed in the temperature range of 70°C to 190°C, as shown in Figures 2.4 and 2.6. The DTA results (Figure 2.7) show no distinct peaks in the temperature range of 70 - 190°C, which is consistent with

the conclusion that the removal of interlayer water, which is physically adsorbed in the nano-slits between the layers of Mg-Al-CO_3 LDH, is predominantly responsible for the sample weight loss in this region.

In-situ DRIFTS with TG/MS for 190-400°C…The second distinct weight loss region of 22.17 wt.% (Figure 2.7) is in the temperature range ~190 - ~400 ^oC. It is accompanied by the evolution of H_2O and CO_2 species (see Figures 2.4 and 2.6), and various heat flows (Figure 2.7). The first small heat flow shoulder peak (endothermic) is centered at ~205^oC, and seems to be coincident with the change of the 1370 cm^{-1} peak in Figure 2.2. The mass spectrometric data indicate the evolution of CO_2 and some H_2O in this region. From ~190 to ~220 ^oC the weight change is ~ 0.2 %, of which 0.08 % corresponds to CO_2 and 0.12 % to H_2O. The small heat flows are indicative that the OH^- and CO_3^{2-} that are exchanged in this region may be physically bound in the LDH sample. Between ~220 and ~ 400 ^oC, there is a 21.97 % weight change; there are also two characteristic endothermic flows in this region, one centered at ~255 ^oC and the other at ~340 ^oC. The DTA data seem to be consistent with the DRIFTS data, which indicate potentially two types of OH^- groups that are removed in the same approximate region of temperatures. In order to clarify the properties of these two types of OH^- groups, TG/DTA experiments with pure $Al(OH)_3$ and pure $Mg(OH)_2$ samples were also performed; the results are shown in Figures 2.8 and 2.9. Figure 2.8 indicates that the OH^- group associated with Al^{3+} is lost in the temperature range ~190 - ~ 300 ^oC, and two heat flow peaks (endothermic) are observed in the same region. Figure 2.9 shows that the OH^- group associated with Mg^{2+} is removed in the temperature range 300 – 405 ^oC; only one heat flow peak (endothermic) is observed at this case. Comparing Figure 2.7 with Figures 2.8 and 2.9, one observes that the thermal behavior of Mg-Al-CO_3 LDH1 in Figure 2.7 is a composite of the thermal behavior of $Al(OH)_3$ and $Mg(OH)_2$. The weight loss in the temperature range 190 - 300 ^oC is ~8.93 %. Of this 0.19 % corresponds to CO_2 and 8.74 % to the removal of H_2O, which likely results from Al-(OH)-Mg OH^- groups. Between 300 ^oC and 405 ^oC the weight loss is ~13.24 %. Of this 0.72 % corresponds to CO_2 and 12.52 % to the removal of H_2O, which for this case, more likely, results from Mg-(OH)-Mg OH^- groups. Assuming that Al^{3+} associates only with OH^- groups, the total weight change one would expect due to the evolution of H_2O from OH^- is 10.37 %. This compares favorably with the 8.74 % change due to water measured in the region of 190 – 300 ^oC. The weight change one would expect due to the evolution of H_2O from the OH^- groups associated with Mg^{2+} is 13.20 %. The experimental value in the region 300 – 405 ^oC is 12.52 %, which compares favorably with the calculated value.

In-situ DRIFTS with TG/MS for 405 -580°C…The total weight loss from 405 to 580 ^oC is 7.33 %, which can be attributed to the removal CO_2 from CO_3^{2-} in the Mg-Al-CO_3 LDH, because almost no water was detected in this temperature range by *in-situ* MS. This brings the total weight loss due to CO_2 to 8.32 %, as compared with the calculated value of 7.15%.

Proposed Model for Structure Change…Based on the results of *in-situ* DRIFTS coupled with the *in-situ* TG/DTA and TG/MS studies, a model is proposed for the evolution of the structure of the Mg-Al-CO_3 LDH sample under an inert atmosphere (Figure 2.10). In

Figure 2.10 five distinct stages were identified during the thermal evolution of this particular Mg-Al-CO_3 LDH sample. The original Mg-Al-CO_3 LDH sample is referred to as Stage A; Stage B develops from Stage A by the removal of the loosely held interlayer water in the temperature range 70 - 190 ^oC; Stage C evolves from Stage B by the removal of OH^- groups, likely bonded in a bridge Al-(OH)-Mg configuration, in the temperature range 190 - 300 ^oC; Stage D was achieved from Stage C by the removal of OH^- groups, likely bonded mostly with Mg^{2+} (Mg-(OH)-Mg) in the temperature range 300 - 405 ^oC; Stage E is obtained by the decarbonation of Stage D in the temperature range 405 - 580 ^oC.

HTXRD…It is also interesting to investigate how the changes in the number and type of functional groups with temperature manifest themselves in changes in the crystal structure of the Mg-Al-CO_3 LDH1 sample. In order to study this, *in-situ* HTXRD has been utilized. Figure 2.11 shows the HTXRD patterns of the Mg-Al-CO_3 LDH treated at different temperatures. There are five temperature regions that can be identified based on the HTXRD patterns, i.e., (1) 30 ^oC = T = 140 ^oC, (2) 140 ^oC = T = 180 ^oC, (3) 180 ^oC = T = 280 ^oC, (4) 280 ^oC = T = 360 ^oC, and (5) 360 ^oC = T = 650 ^oC.

For the first temperature region 30 - 140 ^oC, all the HTXRD patterns are attributed to the hydrotalcite-like structure, as reported by Kanezaki[3]. The intensities of HTXRD lines are strong, and stay almost unchanged with increasing temperature, meaning that the LDH structure is well preserved in this temperature region. More detailed analysis of HTXRD data has shown that the basal spacing of

Table 2.1 The changes in the basal spacing of Mg-Al-CO_3 LDH with temperature calculated from the HTXRD patterns.

T,^oC	30	50	70	100	120	140		160		180	
2θ	11.60	11.60	11.60	11.69	11.69	11.79	13.4	12.06	13.4	12.06	13.4
d, Å	7.63	7.63	7.63	7.56	7.56	7.50	6.59	7.33	6.59	7.33	6.59

Table 2.2 The changes in the basal spacing of Mg-Al-CO_3 LDH with temperature calculated from the HTXRD patterns.

T, ^oC	200	220	240	260	280	300	320	340	360
2?	13.5	13.6	13.8	13.9	13.9	14.0	14.0	14.0	14.0
d, Å	6.54	6.50	6.40	6.36	6.36	6.31	6.31	6.31	6.31

LDH has decreased from 7.63 Å to 7.5 Å, as the temperature increased from 30 to 140 ^{o}C (Table 2.1).

In the second temperature region 140 – 180 ^{o}C, the strong X-ray diffraction line at 11.6 starts shifting towards ~12^{o}, and a new line appears around 13.4^{o}, which intensifies with increasing temperature. This X-ray diffraction line was indexed as 001 by Kanezaki[3]. Based on the X-ray diffraction spectrum one can identify two different co-existing crystal phases of Mg-Al-CO_3 LDH: Phase I with a basal spacing ranging from 7.5 Å to 7.3Å, and Phase II with basal spacing of ~ 6.6Å. The basal spacing of Phase I is approximately equal to the sum of the thickness of one layer of Mg-Al-CO_3 LDH (4.8 Å) and the interlayer distance of Mg-Al-CO_3 LDH (~3.0 Å), as reported, for example, by Cavini, Trifiro, & Vaccari[4]. By assuming the same thickness of one layer of Mg-Al-CO_3 LDH (4.8 Å) for both phases the interlayer distance of Phase II of Mg-Al-CO_3 LDH is calculated to be 1.79 Å, a decrease from the 2.83 Å interlayer distance of Phase I. The decrease of the interlayer distance can be attributed to the shrinkage of the layers of Mg-Al-CO_3 LDH due to the removal of interlayer H_2O, since only interlayer H_2O was removed (DRIFTS and TG/DTA results) in the temperature range 70 - 190^{o}C.

In the third temperature region 180 - 280^{o}C, the X-ray diffraction line at ~12^{o} gradually disappears, and the line at ~13.4^{o} becomes stronger and simultaneously shifts towards 13.9^{o}. This means that, in this region, Phase I transforms to Phase II. With increasing temperature, the basal spacing of Phase II decreases from 6.59 Å to 6.36 Å. Simultaneously, the other X-ray diffraction lines of hydrotalcite begin to weaken in this temperature region, but the hydrotalcite structure stays intact though the interlayer spacing has decreased. This is consistent with the DRIFTS and TG/TDA data, which indicate removal of Al-(OH)-Mg OH^- groups, while the OH^-/CO_3^{2-} groups likely bonded with Mg^{2+} still remain intact; the LDH, thus, retains the brucite-like structure, as shown in Figure 2.10 (Stage C). The decrease of the basal spacing is attributed to the decrease in the thickness of the Mg-Al-CO_3 LDH layer due to the removal of Al-(OH)-Mg OH^- groups.

In the fourth temperature region 280 - 360 ^{o}C, the intensity of the diffraction line at ~14^{o} decreases, the line disappearing when the temperature exceeds 360 ^{o}C. This means that the layered structure of Mg-Al-CO_3 LDH falls apart above 360 ^{o}C, consistent with the observation that the OH^-/CO_3^{2-} groups (likely bonded with Mg^{2+}) begin to leave at 280 ^{o}C and are completely removed at 405 ^{o}C (Stage D), as shown in Figure 2.10. Removing these groups results in a collapse of the brucite-like layers and the Mg-Al-CO_3 LDH layered structure.

For the fifth temperature region 360 - 650^{o}C, the HTXRD results for temperatures higher than 360 ^{o}C are not shown in Figure 2.11, because all these patterns are similar to those shown for 360 ^{o}C. No HTXRD peaks are observed in this temperature region. At this stage (Figure 2.10) a solid solution of MgO and Al_2O_3 is obtained by decarbonation of the Stage D compound in the temperature range 410 - 580^{o}C.

2.4 Conclusions

In-situ DRIFTS, DTA, TG/MS and HTXRD techniques were applied in this study to investigate the thermal evolution behavior of the Mg-Al-CO_3 LDH as a function of temperature and atmosphere. Based on the results obtained from the individual and combined techniques, key conclusions may be drawn as follows:

(1) In the temperature range of 70 - 190^{o}C, loosely held interlayer water is lost, and there are two different co-existing crystal phases of Mg-Al-CO_3 LDH present, i.e., Phase I with a basal spacing ranging from 7.5 Å to 7.3Å, and Phase II with basal spacing of ~ 6.6Å. The LDH structure remains intact.

(2) In the temperature range of 190 - 280^{o}C, the OH^- group bonded with Al^{3+} begins to disappear at 190 ^{o}C, and is completely lost at 280^{o}C. In this temperature region, Phase I is transformed into Phase II. In addition a small amount of CO_2 releases.

(3) In the temperature range 280 - 405^{o}C, the OH^- group bonded with Mg^{2+} begins to disappear at 280^{o}C and is completely lost at 405^{o}C. Degradation of the LDH structure is observed in this region. Again a small amount of CO_2 releases.

(4) Finally, in the temperature range 405 - 580^{o}C, CO_3^{2-} loss begins and is completed at 580^{o}C. In this temperature range the material becomes a metastable mixed solid oxide solution.

Based upon the CO_2 loss vs temperature profile, a real opportunity exists in utilizing the LDH materials as a CO_2 affinity material at temperature >190°C. The LDH maintains its double layer structure up to 280°C. Beyond this temperature, the degradation of the LDH structure was observed under the inert atmosphere studied here. However, the LDH structure can be restored when the exposed atmosphere is appropriate. The CO_2 release at >190°C will be further verified with regard to its reversibility in Chapter 3, an essential feature for being used as a commercially viable adsorbent or membrane.

Literature Cited

1. Hibino, T.; Yamashita, Y.; Kosuge, K.; Tsunashima, A. Decarbonation behavior of Mg-Al-CO_3 hydrotalcite-like compounds during heat treatment. *Clays and Clay Min.*, **1995**, *43(4)*, 427.
2. Perez-Ramirez, J.; Mul, G.; Kapteijn, F.; Moulijn, J. A. (2000). Comments on "Infrared emission spectroscopic study of the thermal transformation of Mg-, Ni-, and Co-hydrotalcite catalysts" [*Appl. Catal A:General*, **1999,** *18*, 61]. *Appl. Catal, A: General*, **2000**, *204*, 256.
3. Kanezaki, E. Thermal behavior of the hydrotalcite-like layered structure of Mg and Al-layered double hydroxides with interlayer carbonate by means of *in-situ* powder HTXRD and DTA/TG. *Sol. State Ion.*, **1998**, *106(3-4)*, 279.
4. Cavini, F.; Trifiro, E.; Vaccari, A. Hydrotalcite-type anionic clays – preparation, properties and applications. *Cat. Today*, **1991**, *11*, 173.

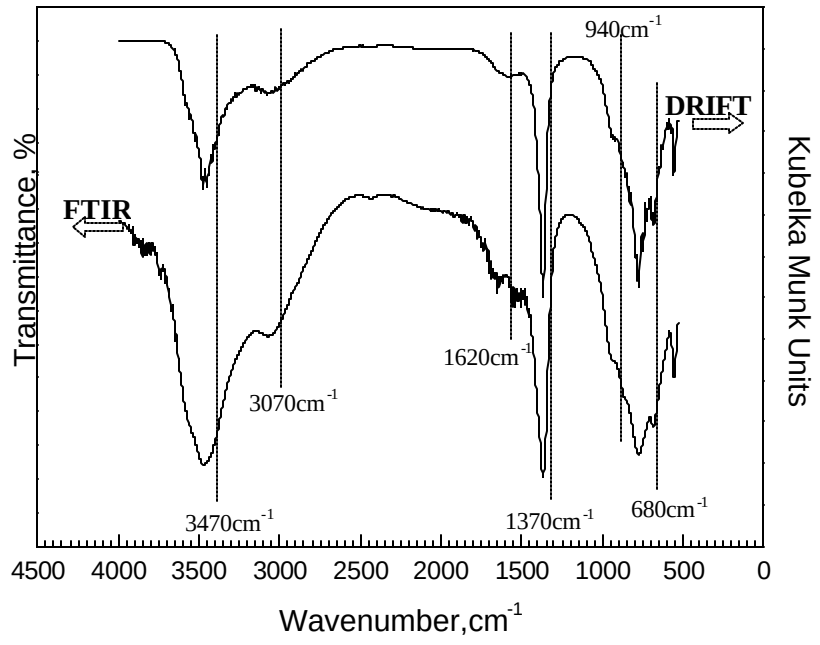

Figure 2.1 Comparison between the DRIFTS and FTIR results of Mg-Al-CO_3 LDH.

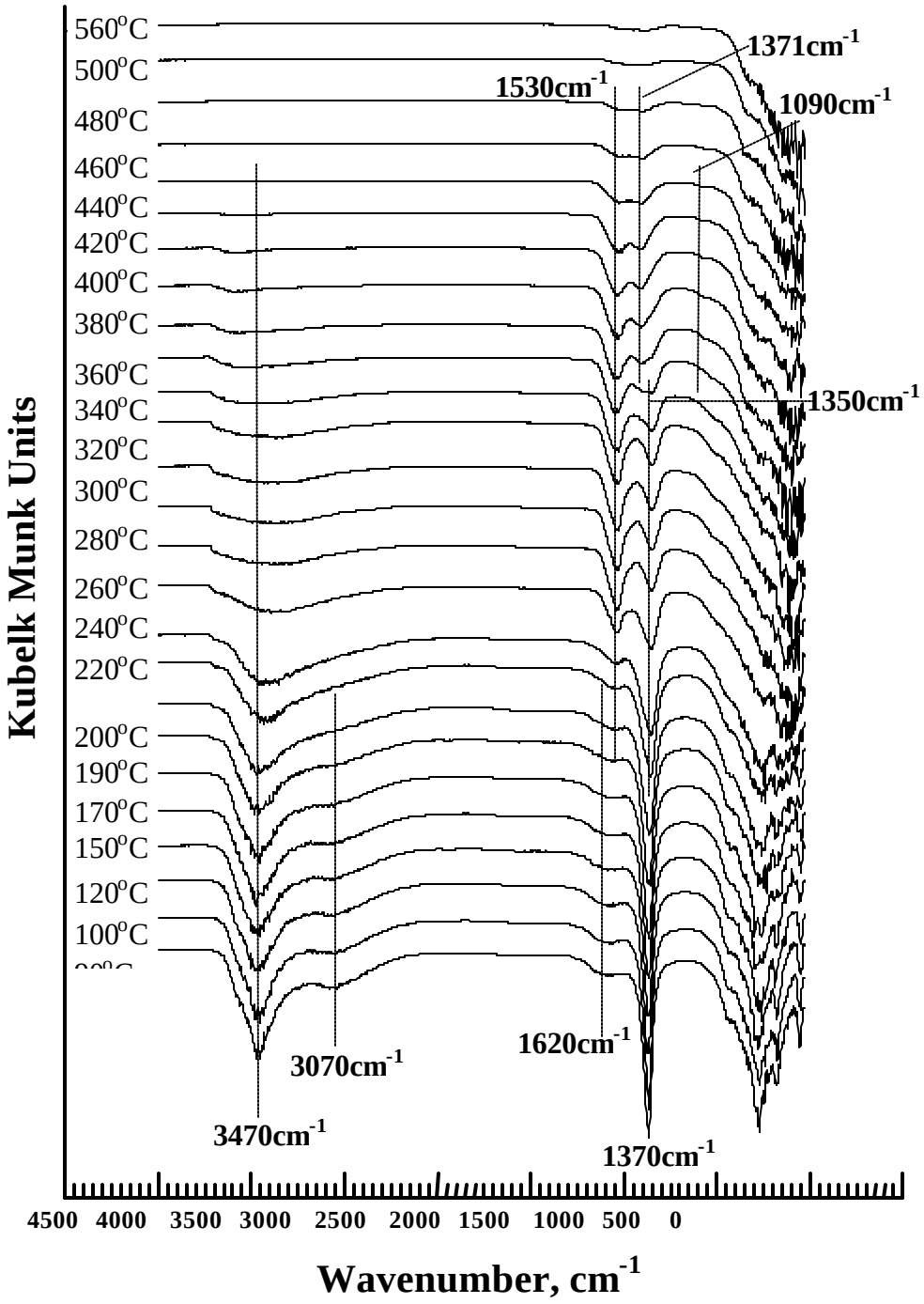

Figure 2.2 *In-situ* DRIFTS of Mg-Al-CO_3 LDH as a function of temperature.

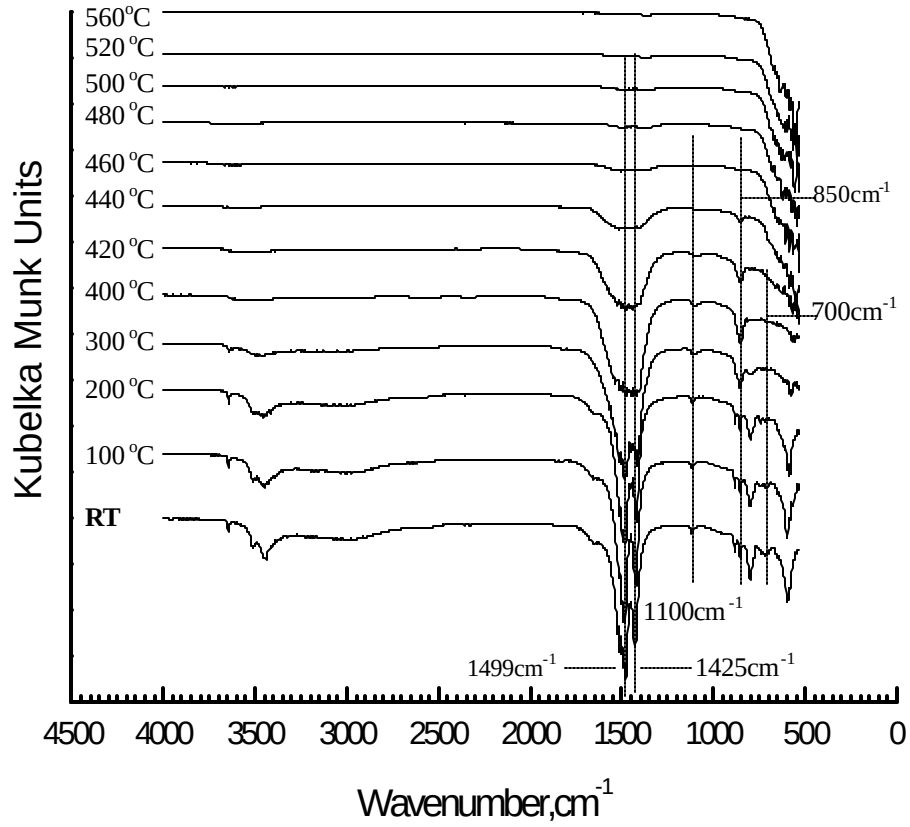

Figure 2.3 *In-situ* DRIFTS of $MgCO_3$ as a function of temperature.

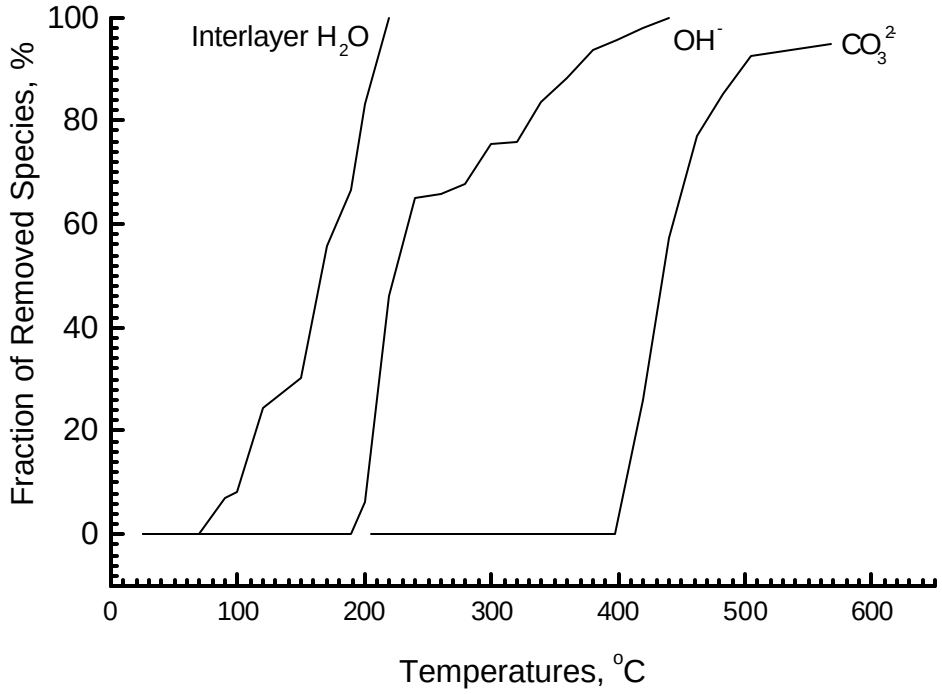

Figure 2.4 Fraction of species removed from Mg-Al-CO_3 LDH as a function of temperature.

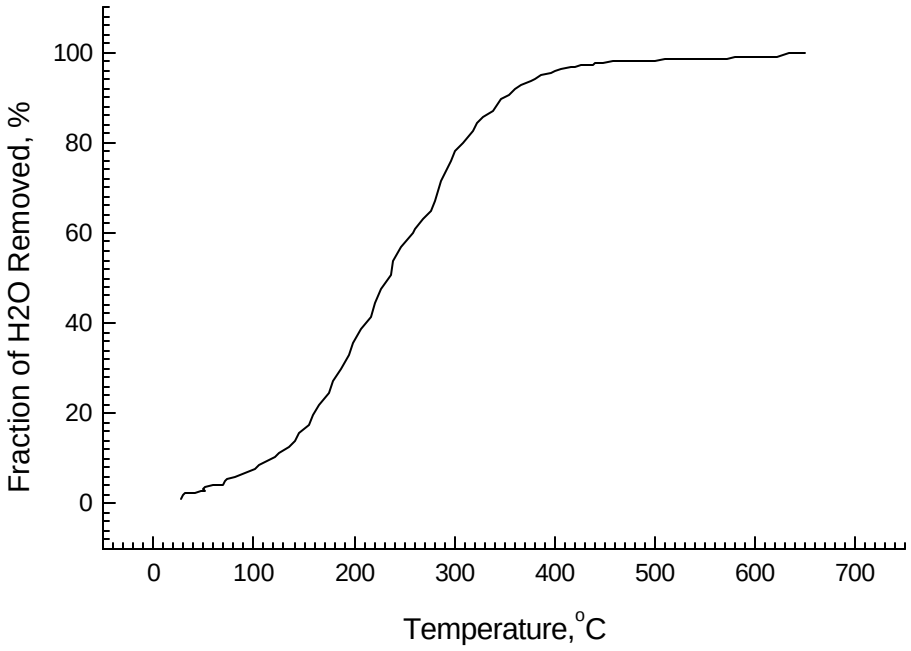

Figure 2.5 *In-situ* MS of Mg-Al-CO_3 LDH as a function of temperature.

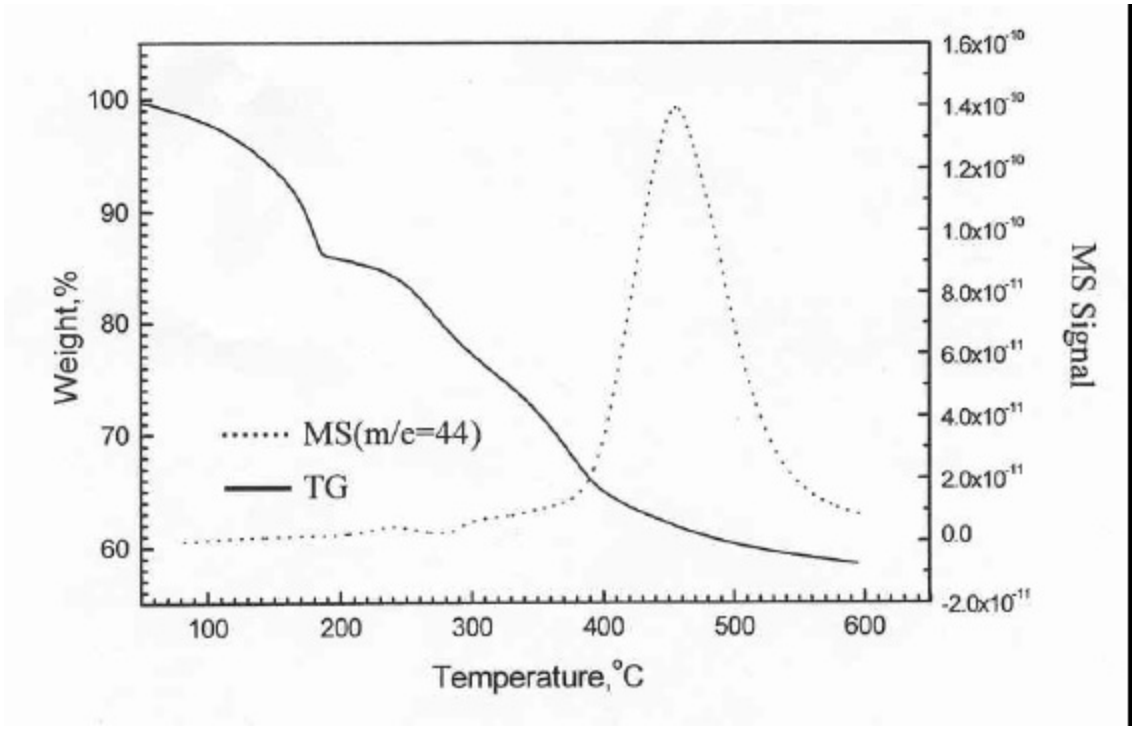

Figure 2.6 *In-situ* TG/MS of Mg-Al-CO_3 LDH as a function of temperature.

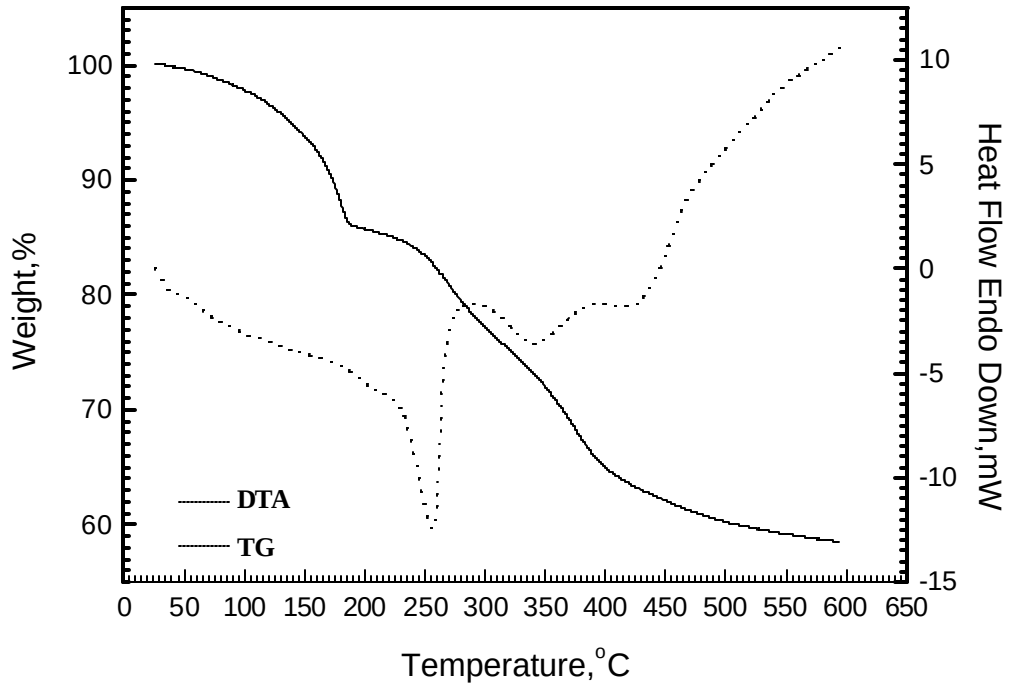

Figure 2.7 *In-situ* TG/DTA of Mg-Al-CO_3 LDH as a function of temperature.

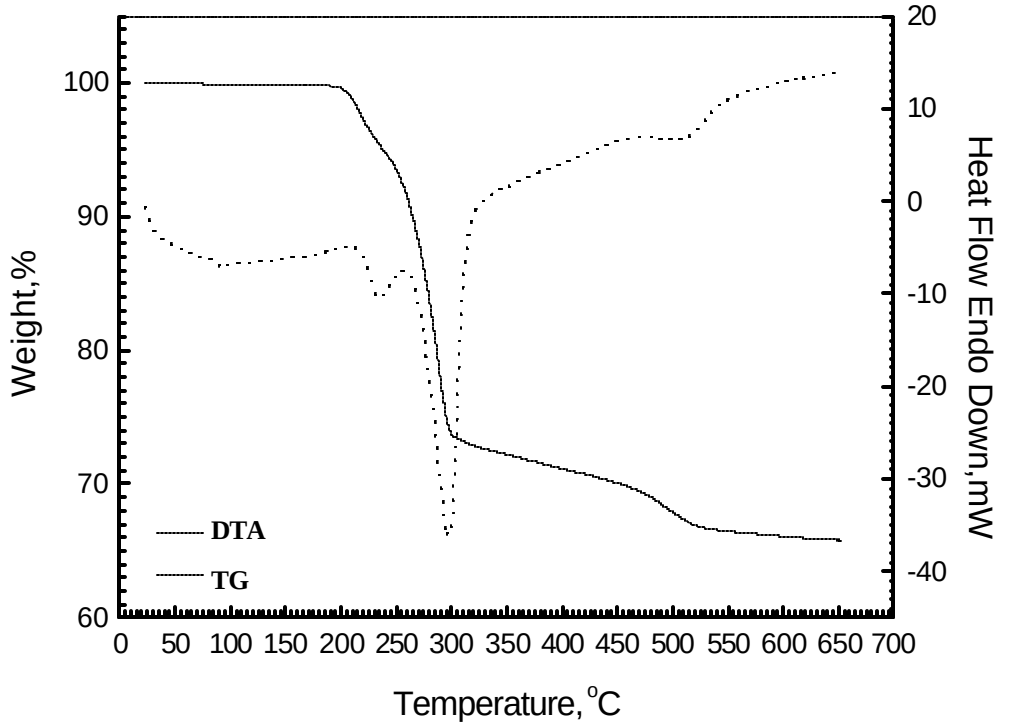

Figure 2.8 *In-situ* TG/DTA of $Al(OH)_3$ as a function of temperature.

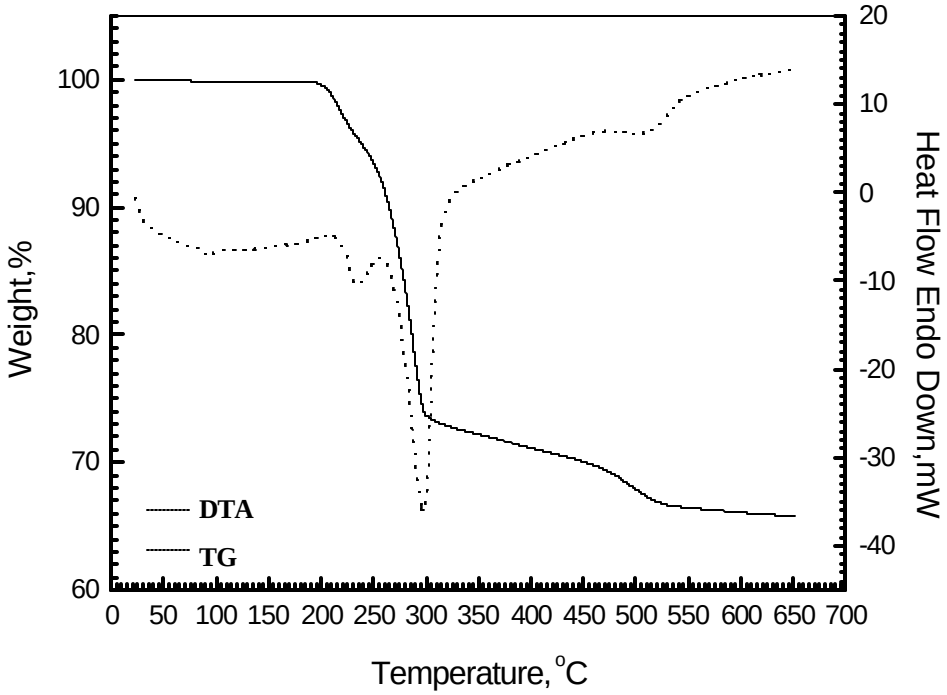

Figure 2.9 *In-situ* TG/DTA of $Mg(OH)_2$ as a function of temperature.

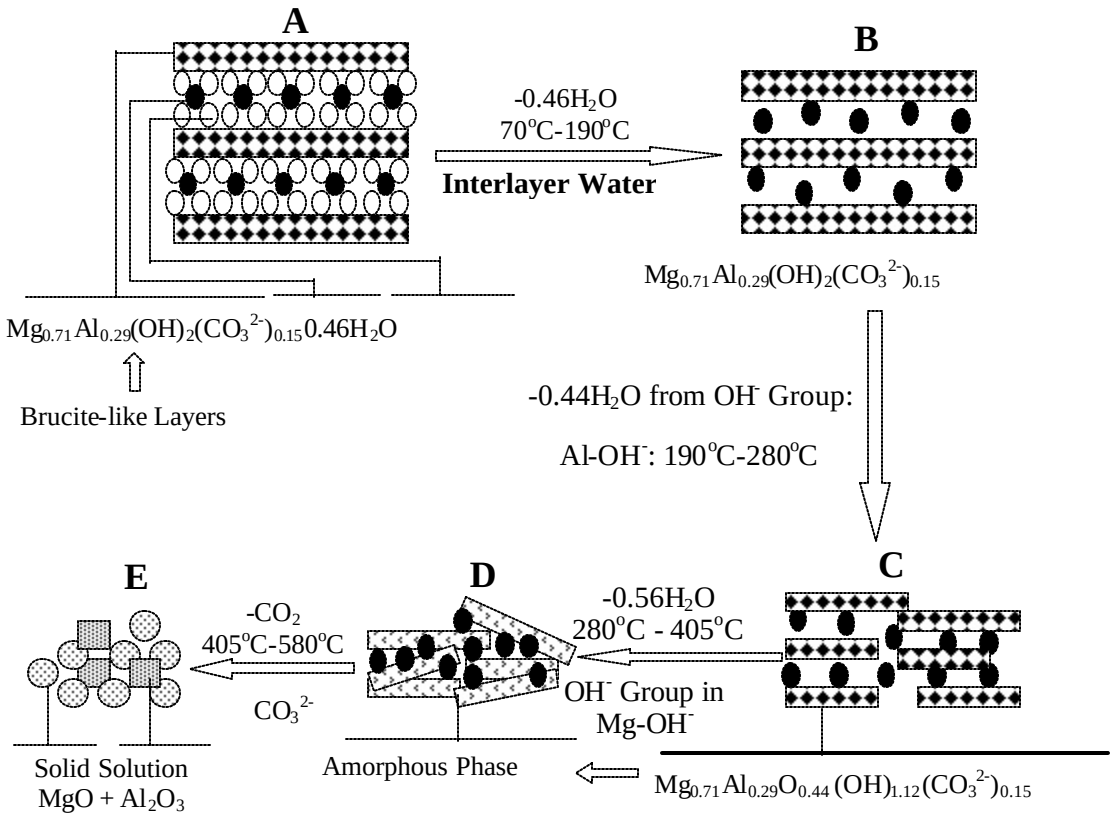

Figure 2.10 The thermal evolution of Mg-Al-CO_3 LDH as a function of temperature.

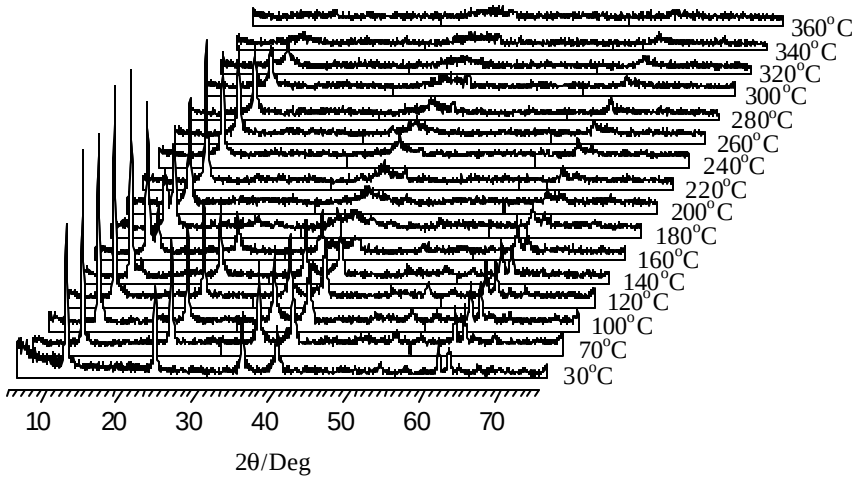

Figure 2.11 *In-situ* HTXRD of Mg-Al-CO_3 LDH as a function of temperature.

Chapter 3

CO_2 Affinity of Mg-Al-CO_3 LDHs and its Reversibility

3.1 Introduction

Thermal evolution pattern of the Mg-Al-CO_3 LDH material is discussed in the previous chapter. A notable feature of the Mg-Al-CO_3-LDH is its significant amount of CO_2 release at a higher temperature, indicating its CO_2 affinity. This chapter focuses on the study of the reversibility of the CO_2 affinity under both inert and reactive atmospheres. The reversibility of the CO_2 affinity under a reasonable industrial operating condition (i.e., in terms of temperature, pressure and atmosphere) is an essential property required for the formation of a commercially viable CO_2 adsorbent and membrane based upon the proposed LDH material.

3.2 Experimental

Material Characterization… The two LDH samples used in this chapter were represented by $Mg_{0.71}Al_{0.29}(OH)_2(CO_3)_{0.15}\cdot 0.46(H_2O)$ (LDH1; the same LDH sample utilized in previous chapter), and $Mg_{0.645}Al_{0.355}(OH)_2(CO_3)_{0.178}\cdot 0.105(H_2O)$ (hereinafter referred to as LDH2) based upon the analysis by ICP and TGA. These samples were characterized with the instrumentation described below:

- DRIFTS (Diffused Reflectance Infrared Founier Transform Spectroscopy) spectra vs temperature, pressure, and various atmospheres were recorded *in situ* using a Genesis II (Mattson, FT-IR) instrument equipped with a DRIFTS COLLECTOR™ II chamber (SpectraTech, Inc.) capable of operating under high temperatures (up to 900 ^oC) and pressures (up to 1500 psi). The experimental operating conditions were a DRIFTS scan-range from 4000 cm^{-1} to 500 cm^{-1}, scan numbers 16, and a scan resolution of 2 cm^{-1}.
- TGA curve was recorded with a Cahn TGA 121 instrument to determine the weight loss vs temperature. The MB-MS instrument is custom-made, using a MKS UTI 100C Precision Gas Analyzer.
- Surface analysis performed in this chapter includes SEM, TEM, and XRD. SEM images were taken with Cambridge Stereoscan 360, and TEM images were taken with Philips EM420 instrument. XRD figures were generated with Rigaku X-ray diffractometer.

The results obtained from the above analysis were used in this chapter to decipher the CO_2 reversibility of the Mg-Al-CO_3 LDHs and the operating condition required to achieve the reversibility.

Operating Condition for Adsorption/Desorption…We investigated, therefore, the ability of the LDH materials to reversibly adsorb CO_2 under a broad range of experimental

conditions. For each series of experiments, 100-120 mg of a fresh LDH sample was utilized. During the adsorption part of the cycle, 30 sccm of CO_2 was bubbled through a beaker containing distilled water (the CO_2 stream's RH being ~ 70%) and the sample was exposed to this humidified CO_2 stream for varying periods of time. Subsequently to adsorption, the flow of CO_2 was shut-down and the desorption part of the cycle was initiated. To find optimal experimental conditions for sorption studies, the effect of varying the duration of adsorption was investigated. And it was observed that increasing the time of adsorption from 1 to 2 hr increased the total amount adsorbed by about 5%, but a subsequent increase from 2 hr to 3 hr had no additional significant effect. Therefore, for the remainder of the study, an adsorption step time of 3 hr was utilized. Also two different methods to carry out the desorption step were investigated. In the first method, upon termination of the CO_2 flow, the sample was exposed to flowing UHP dry Ar at a rate of 30 sccm. Typically, after 30 min the weight change of the sample ceased. Subsequently, Ar was flowed to continue for a total desorption period of 1 hr. In the second method, the chamber was evacuated for a period of 1 hr at a pressure below 40 mTorr. Evacuation was shown to be a more effective means for carrying out the desorption step (~ a 10% increase in weight gain upon subsequent readsorption), and was adopted for the remainder of the study.

Reversibility via Pressure Swing... For each experiment, at any given temperature, a fresh LDH2 sample (100-120 mg) was used. The temperature was increased from room temperature at a rate of 5°C/min in an Are atmosphere (flow rate of 30 scum) to the preset point (e.g., 200°C, 250 °o, etc.), and kept at this temperature until the sample weight became constant, typically for 20~30 min. Subsequently, the cyclic sorption/adsorption experiments were initiated via the pressure swing. Multiple adsorption/adsorption cycles were then carried out at two selected temperatures, 150 and 250°C. Upon reaching the desired temperature, the feed was switched to humidified carbon dioxide (20 scums, 70% RH) and kept there for 3 hr. Then the sample was evacuated for 1 hr, switched back to humidified carbon dioxide for 3 hr, and so on. Upon completion of the 14 cycles at 150°C, the LDH1 sample was heated in UHP dry Are (20 scum; 5°C/min) until its temperature reached 250°C; the feed was then switched to humidified CO_2 (20 scum, 70% RH), and kept there for 3 hr. Then, the sample was evacuated for 1 hr, switched back on to humidified CO_2 for 3 hr, and so on.

Reversibility Study via Temperature Swing…After the cyclic sorption/adsorption experiments with the LDH samples were completed, a number of experiments were initiated in which the weight-gain/loss of the sample was monitored as its temperature was cycled from room temperature to a preset temperature, and back down to room temperature. The same LDH1 sample was used in all of temperature cycling experiments reported in this section. In the first experiment, the sample was heated in flowing Are (20 scum) with a heating rate of 3°C/min from room temperature to a temperature of 150°C; subsequently the flowing Ar feed was substituted with a humidified CO_2 feed (20 scum) and was cooled down to room temperature with a 3°C/min cooling rate. Upon reaching room temperature, the sample was kept at this temperature for an additional 2 hr. The weight-loss/gain data are shown in Figure 3.12. The total weight-loss for the LDH1 sample was ~5.5% at 150°C; upon cooling in the humidified CO_2 atmosphere, the sample

recovered 98.4% of its original weight. The gaseous components evolved during the heating step were monitored by mass spectrometry (Figure 3.13); only water was detected during the experiment.

Upon termination of the experiment at 150°C, the humidified CO_2 atmosphere was switched back to flowing UHP dry argon, and the temperature was slowly (3°C/min) increased to 200°C. Upon reaching this temperature, the same experimental protocol was followed. The weight-loss curve leveled-off after 240 min. The sample was then cooled to determine the percentage of weight recovered (Figure 3.12). The gases evolved during the heating part of the cycle were also monitored (Figure 3.14). Water was detected throughout the whole temperature range, and trace amounts of carbon dioxide were detected from 195°C ~ 200°C. Most of the weight loss was observed below 150°C; only ~0.2 % of the weight-loss was observed between 180 °o and 200 °o.

Upon completion of the experiment at 200°C, the humidified CO_2 atmosphere was switched back to dry argon, and the temperature was slowly (1°C/min) increased to 250°C (in the 250°C and higher temperature cycling experiments, the cooling/heating rates were changed from 3°C/min to 1°C/min). Upon reaching this temperature, the flowing Ar feed was substituted with a humidified CO_2 feed (20 scum), and the sample was cooled down to room temperature with a 1°C/min cooling rate. Also the sample was allowed to equilibrate at room temperature for as long as necessary for the weight-gain curve to level-off.

Reversibility Study at Increased Pressure…To further study the sorption reversibility behavior of the LDH at the water gas shift (WGS) membrane reactor environment, similar experiments were carried out using a moderate-pressure adsorption flow system. The experimental system was equipped with mass flow controllers and a flow control valve at the exit to maintain the system pressure constant under flow conditions. Two types of experiments were performed. In the first series of experiments the flow system was first pressurized with flowing dry argon (50 scum) to 50 psig , then the temperature was increased to 250 °C, using a 5 °C /min heating rate (it took ~ 45 min), and the system was kept at 250 °C for 1 hr as a adsorption step. When the adsorption step was over, the system was cooled down to 150°C (cooling rate 5°C/min, ~ 20 min) in flowing dry argon (50 scums). Subsequently, the inlet gas was changed to dry CO_2 (50 scum) from argon, while keeping the same pressure of 50 psig for 3 hr as an adsorption step. During the adsorption step, the outlet flow rate was monitored by a digital flow meter (while the reactor pressure was maintained constant at 50 psig), and, from the flow rate change, the amount of adsorption was calculated. Table 3.3 shows the weight gain during the sorption step for the first 3 sorption/adsorption cycles with the LDH2 sample.

In the second series of experiments the LDH2 sample (~ 14 g) was first heated to a preset temperature in Ar gas (50 scum). Each cycle involved first evacuating the sample for 1 hr as a desorption step. After the evacuation step, the flow system was then again pressurized to 50 psig in flowing Ar. When the outlet flow rate was stabilized in flowing Ar at 50 psig, the inlet gas was then changed to either dry or humidified CO_2 (50 sccm) for 3 hr while maintaining the same pressure of 50 psig. Upon completing the first

adsorption/desorption cycle the procedure was repeated for a number of additional cycles, and for a number of temperatures.

3.3 Results and Discussion

Characterization with TGA and XRD…The weight losses for the two LDHs were studied by TG-MS, and the results were shown to be consistent with the ICP results, as indicated in Table 3.1. The LDH2 sample has a higher Al/Mg ratio (the value of x being near the higher end of the typical LDH range), and contains less interlayer water. XRD characterization of these two LDH samples indicates that the materials have the typical LDH XRD spectra as shown in Figure 3.1[1-3], but the XRD spectrum of LDH2 is noisier than that ofLDH1, and not as strong as the spectrum of LDH1 (compare Figure 3.1a with Fig 3.1b). The TGA spectra for the two LDHs generated with a scan rate of 5^oC/min, and the corresponding *in-situ* MS signals of CO_2 are shown in Figure 3.3a. The cumulative amounts of H_2O evolved are shown in Figure 3.3b. Though differences in the TGA and mass evolution spectra exist, the thermal evolution profiles of the two LDH's are about similar, only the ranges of temperatures for each peak are slightly different. Hibino *et* al[4] also observed differences in the TGA spectra of Mg-Al-CO_3-LDH with a different Al:Mg ratios, but even between LDH with the same Al:Mg ratio and different crystallite sizes[4]. For the LDH2, the loosely-held interlayer water is lost in the temperature range of 80 - 190^oC, the OH^- group begins to disappear at 190^oC and is completely lost around 520^oC. While some CO_3^{2-} loss is observed at lower temperatures, its substantial loss begins at 450 ^oC, and is completed at 720 ^oC. The fractions in terms of the total of H_2O and CO_2 evolved in different temperature ranges for both LDH1 and LDH2 are shown in Table 3.2. In summary, based upon the results of the thermal analysis and the XRD patterns, the two HT samples show typical hydrotalcite behaviors.

Table 3.1 Weight-loss from the TG/MB-MS studies, and calculated weight-loss based on the ICP data for the samples. (a) LDH1; and (b) LDH2.

(a)

Weight-Loss	H_2O	OH^- from Al	OH^- from Mg	CO_2 from CO_3^{2-}	Total Weight-Loss %
ICP Value	10.8%	10.4%	13.2%	7.2%	41.6%
Experimental from TG/MS	12.93%	8.93%	12.65%	7.72%	42.23%

(b)

Weight-Loss	H_2O	OH^- from Al	OH^- from Mg	CO_2 from CO_3^{2-}	Total Weight-Loss %

ICP Value	2%	11.0%	16.1%	10.9%	40%
Experimental from TG/MS	2%	12.08%	15.94%	11.06%	41.08%

Effect of Heating Rate and Atmosphere on Thermal Evolution Pattern…Up to 250 ^{o} C, heating rates up to 10C/min show no effect on the TGA curves; most likely the thermal evaluation behaviors are within the equilibrium, not the kinetic, control. However, >250°C, some of the heating rates effects are apparent and likely the thermal evaluation behavior is within the kinetic control. Similar observations were previously made by Costantino and Pinnavaia[5], and most recently by Rhee and Kang[6]. To investigate the effect of heating rate further, the weight-loss characteristics of the LDH2 sample have been studied for 4 different heating rates, namely, 1, 3, 5 and 10^{o}C/min, and in three different atmospheres. The weight-loss results in an inert Ar atmosphere and the corresponding MS signals of CO_2 are shown in Figure 3.4a. For the results in Figure 3.4, a fresh LDH2 sample ~110-120 mg was used in every experiment, and dry inert Ar (ultra high purity grade) was utilized as a purge gas at a flow rate of 20 sccm. For heating rates below 5 ^{o}C/min the weight-loss curves and the MS signals coincide, indicating that the structural changes (loss of interlayer water, hydroxyl, and CO_3^{2-} losses) occur rapidly enough, so that the LDH structure equilibrates within the time frame allotted by the changing temperature. However, the results with the 10 ^{o}C/min heating rate show kinetic effect in comparison with the lower heating rate results. Similar observations were also made in the presence of dry and humid CO_2 atmospheres, with the results showing absence of kinetic effects for heating rates below 5 ^{o}C/min.

Table 3.2 The fractions of H_2O and CO_2 (as % of the total sample weight) that are evolved in different temperature ranges for both LDH1 and LDH2.

	LDH1			LDH2		
	Weight-Loss, %	H_2O	CO_2	Weight-Loss, %	H_2O	CO_2
RT~100^{o}C	2.61	2.61	-	0.59	0.59	-
100~200^{o}C	11.39	11.31	0.08	1.48	1.46	0.02
200~300^{o}C	8.03	7.94	0.09	7.41	7.33	0.08
300~400^{o}C	12.64	11.95	0.69	8.31	8.04	0.27
400~500^{o}C	4.8	0.7	4.1	10.42	9.91	0.51
500~600^{o}C	2.76	-	2.76	11.38	2.69	8.69
600~750^{o}C	-	-	-	1.49	-	1.49
Total	42.23	34.51	7.72	41.08	30.02	11.06

The effect of varying the heating rate on weight-loss for the LDH2 sample was also studied in the presence of a reactive atmosphere. For the experiments in Figure 3.4b, in addition to the weight-loss of the LDH2 sample in the presence of inert Ar, we also show

the weight-loss curve for the case in which dry CO_2, instead of Ar, was utilized as a purge gas atmosphere at a flow rate of 20 mL/min and a heating rate of 5°C/min. The weight-loss results in the presence of a humidified CO_2 atmosphere are also shown in the same figure. Measurements of the water concentration of the gas exiting the beaker indicate that the relative humidity (RH) of the CO_2 stream was ~ 70%. The results in Figure 3.3b indicate little effect of the gaseous atmosphere on the weight-loss curve in the first region of temperatures associated with the evolution of interlayer water. Differences exist, however, in the other regions. In the region where mostly CO_2 evolves, DRIFTS indicates that all hydroxyls in the LDH structure have already disappeared, the weight-loss curves for the humidified and dry CO_2 atmospheres coincide, but are still different from the weight-loss curve under inert conditions; the presence of CO_2 in the purge atmosphere appears to slow-down somewhat the rate of CO_2 evolution. The dry and humidified CO_2 weight-loss curves are different in the region associated with hydroxyl evolution, particularly in the range of temperatures associated with loss of hydroxyls in an Mg-(OH)-Mg configuration. Previously, Ding and Alpay[7], who studied CO_2 adsorption on a K-promoted commercial Mg-Al hydrotalcite at 400 °C, noted a small (~ 10%) beneficial effect of the presence of water on CO_2 adsorption. They also noted, however, that the actual partial water pressure did not really matter, with even traces of water vapor being capable of providing the same beneficial effect. Ding and Alpay[7] attributed this beneficial effect to the ability of water vapor to either maintain the hydroxyl concentration on the surface or to prevent the sites from poisoning through carbonate or coke deposition. In summary, heating rate of 5°C/min or less shows no kinetic effect, which was adopted in the later study. In addition, the presence of CO_2 in the desorption atmosphere appears slow down the desorption process as expected.

CO_2 Reversibility via Pressure Swing…The ability of the LDH to reversibly adsorb CO_2 and H_2O is of significance in the use of these materials as adsorbents and membranes. In the former case, the ability to reversibly adsorb CO_2 is critical from the standpoint of being able to regenerate the adsorbent via pressure swing; in the latter case the presence of a relatively mobile CO_2 phase within the LDH structure is beneficial to the permeation of CO_2 through the membrane as a pressure driven process. The adsorption/desorption behavior of the LDH2 at selected temperatures ranging from 150 to 350°C was performed. Figure 3.5a shows the total weight gain (as percent fraction of the original weight of the LDH sample) during the adsorption part of the cycle. Figure 3.5b shows the corresponding total weight-loss during the desorption part of the cycle. Figure 3.5c presents the weight change of individual components, H_2O and CO_2, during the desorption part of the cycle.

Three distinct regions can be distinguished in Figure 3.5c. The first region is for temperatures below 190°C, in which the LDH2 sample reversibly adsorbed only water and slight amounts of CO_2. The cyclic adsorption/desorption results indicate that the exchange of interlayer water is a fairly reversible process. In the second temperature range, from 190°C to 280°C, water from the hydroxyl groups that are bonded with Al cations releases. In addition, some CO_2 is also emitted in this region. After the initial sorption/desorption cycle, however, only CO_2 appears to be reversibly adsorbed in this

region, with very little H_2O emitted; the sample weight change can be fully attributed to the reversibly adsorbed CO_2.

In the temperature range of 280 – 440 ^oC, the previous studies indicate that the OH^- group bonded with Mg^{2+} begins to disappear at 280^{o}C, and is completely lost at 440 ^oC (for the LDH2 the upper temperature extends higher – see Table 3.2). Degradation of the hydrotalcite structure is also observed in the same region. Again, after the initiation of the sorption/desorption cycle, however, only CO_2 appears to be reversibly adsorbed in this region, with very little H_2O emitted. Hence, the sample weight change can be mostly attributed to the reversibly adsorbed CO_2. As can be seen in Fig 3.5c, the amount of CO_2 that is reversibly adsorbed in this region decreases as the temperature increases, consistent with the observations that the crystallinity of the hydrotalcite material also decreases, and its structure begins to fall apart in this region.

To further validate the cyclic sorption/desorption behavior, *in situ* cyclic flow sorption/desorption experiments using the DRIFTS system were carried out, following the same experimental protocol as with TG/MB-MS experiments described above. Figure 3.5 presents the DRIFTS spectra with temperature as a parameter. Figure 3.6b shows the peak area representing the CO_3^{2-}, ν_3, vibration during the cyclic adsorption/ desorption experiments[1]. Figure 3.6c shows the peak area representing 3470 cm^{-1} band corresponding to the OH^- vibration, and the combined peak areas for the interlayer water peaks (3070 cm^{-1} and 1620 cm^{-1})[1]. In Figure 3.6b and 3.6c it was observed that at 150^{o}C only the combined peak area representing the interlayer water changed in a reversible manner. No substantial changes are observed through the adsorption/ desorption cycles in the peak areas reflecting the CO_3^{2-},ν_3, vibration or the 3470 cm^{-1} band corresponding to the OH^- vibration. According to the above observations, the hydrotalcite exchanges reversibly the interlayer water at temperature <150°C. At a higher temperature, i.e., >150°C, after the initial adsorption/desorption cycle, the hydrotalcite exchanges reversibly only CO_2. These observations are consistent with the TG-MS experiments and the observations of previous chapter.

Multiple cyclic adsorption/desorption experiments were also performed. Figure 3.7 shows the weight change and the residual weight (both as percent fraction of the original sample weight) observed for a total of 14 cycles. Figure 3.8 shows the corresponding MS signals during the heating and evacuation part of the cycle. The system reaches a steady-state reversible behavior after the 11th cycle, with the corresponding weight change being 0.23%.

Figure 3.9 shows the weight change observed for a total of 14 cycles for the LDH1 sample at 250 ^oC. The sample reaches a steady state behavior after the 9th cycle, with the corresponding reversible weight change being 0.31%. Figure 3.10 shows the corresponding MS signals during the heating and evacuation parts of the cycle. Figure 3.11 describes a long-term cycling experiment using 113 mg of LDH2 at 250 ^oC, following the same other experimental conditions as with the experiments involving the LDH1 sample. The sample reaches a steady state behavior after the 14th cycle, with the corresponding reversible weight change being 0.32%. In summary, ~0.3% reversible and

steady CO_2 capacity was observed, implying the permeation of CO_2 with LDH-based membrane via the CO_2 pressure drop can be accomplished.

CO2 Reversibility via Temperature Swing… In addition to pressure swing, temperature swing was also considered by us as a means to demonstrate the reversibility although temperature swing was rarely practiced. Upon cooling from 250 to 25°C, 99.2% of original weight of the sample was recovered as shown in Figure 3.15. The components evolved during the heating part of the cycle were also monitored (Figure 3.16). Water was detected throughout the whole temperature range, similar to the previous experiments, and smaller amounts of carbon dioxide were detected in the range from 195 - 250°C. The experiment was repeated with the temperature raised (1°C/min) to 300°C, cooled down in humidified CO_2 to room temperature. As shown in Figure 3.15, it took a much longer time than in the previous experiments for the sample to re-gain the weight, which leveled off at 96% of original weight. The composition of outlet gas showed water evolution through the whole range of temperatures; carbon dioxide was again detected between 195 and 300°C. The experimental results with the temperature raised to 350°C are also shown in Figure 3.15. Once more, it took a much longer time for the sample to recover its weight, which leveled off at 93.8% of its original weight; water was evolved through the whole region of temperatures and carbon dioxide was detected between 195 and 350°C. The CO_2 reversibility was demonstrated via the temperature swing from 150 – 350°C to room temperature, consistent with the results from pressure swing with temperature as a parameter.

Study of Reversibility at Increased Pressure…The reversibility property was further studied here under a moderate pressure, i.e., 50 psig, in reference to the use of these materials for the low temperature water gas shift (WGS) reaction. Similar experiments were carried out using a moderate-pressure adsorption flow system.

Table 3.3 Weight-gain during the sorption step for the moderate-pressure flow experiments using dry CO_2.

	Weight-gain during the adsorption step (wt. %)
1st Cycle	2.621
2nd Cycle	2.542
3rd Cycle	2.476

Table 3.4 Weight-gain during the adsorption step for the moderate pressure flow experiments at various temperatures using dry CO_2.

	150°C	200°C	250°C
1st Cycle	2.02	1.84	1.72
2nd Cycle	1.97	1.79	1.69
3rd Cycle	1.87	1.71	1.68
4th Cycle	1.84	1.69	1.66

Table 3.5 Weight-gain during the sorption step for the moderate pressure flow experiments at various temperatures using humidified CO_2.

200 °C	Weight gain at adsorption step (wt. %)
1st Cycle	1.85
2nd Cycle	1.79
3rd Cycle	1.73
4th Cycle	1.71

The cyclic adsorption/desorption results for the various temperatures for dry CO_2 are summarized in Table 3.4, while those for humidified CO_2 for one temperature are shown in Table 3.5 (a fresh LDH2 sample was utilized for each set experiments at every new temperature). For the experiments in Table 3.5, the CO_2 stream contains 2% mol of water, which corresponds approximately to 70% RH at the temperature and pressure of the experiment. Again, at 150°C, the weight loss during the desorption part was attributed to the release of water with trace CO_2. Opposite to the run at 150°C, the runs at 200 and 250°C released primarily CO_2. Comparing between the run in humidified CO_2 (Table 3.5) and dry CO_2, little difference was observed in the weight change, which was consistent with the observation under atmospheric conditions. In summary, the CO_2 reversibility under moderate pressure conditions is in agreement with the TG/MB-MS and DRIFTS data under atmospheric conditions. The effect of water appears insignificant for the temperature and pressure range we studied.

3.4 Conclusions

The thermal evolution of CO_2 under atmospheric and moderate pressure conditions is in agreement with the LDH structural model suggested in the previous chapter. The LDHs are shown capable of CO_2 exchanging reversibly for a broad region of conditions. These experimental observations qualify the LDH as base material for the formation of CO_2 permselective membranes and CO_2-affinity adsorbents for high temperature membrane reactor applications as proposed in this project. The ability to reversibly adsorb CO_2 is critical from the standpoint of being able to regenerate the adsorbents. The presence of a relatively mobile CO_2 phase within the LDH structure is important in determining the

permeation rate through the membrane. The CO_2 capacity and its transport rate as an adsorbent, as well as the permeability and selectivity as a membrane, were experimentally determined which are presented in Chapter 4&6

Literature Cited

1. Kanezaki, E. Effect of atomic ratio Mg/Al in layers of Mg and Al layered double hydroxide on thermal stability of hydrotalcite-like layered structure by means of *in-situ* high temperature powder X-ray diffraction. *Mater. Res. Bull.,* 1998, *33(5),* 773.
2. Kanezaki, E. Thermal behavior of the hydrotalcite-like layered structure of Mg and Al-layered double hydroxides with interlayer carbonate by means of *in-situ* powder HTXRD and DTA/TG. *Solid State Ionics,* 1998, *106(3-4),* 279.
3. Cavini, F.; Trifiro, E.; Vaccari, A. Hydrotalcite-type anionic clays – preparation, properties and applications. *Catal. Today,* 1991, *11,* 173.
4. Hibino, T.; Yamashita, Y.; Kosuge, K.; Tsunashima, A. Decarbonation behavior of Mg-Al-CO_3 hydrotalcite-like compounds during heat treatment. *Clays and Clay Minerals,* 1995, *43(4),* 427.
5. Constantino, V. R. L.; Pinnavaia, T. J. Basic properties of $Mg_{1-X}(2+)Al_X(3+)$ layered double hydroxides intercalated by carbonate, hydroxide, chloride, and sulfate anions, *Inorg. Chem.,* 1995, *34*, 883.
6. Rhee, S. W.; Kang M. J. Kinetics on dehydration reaction during thermal treatment of Al-CO3-LDHs, *Kor. J. Chem. Eng.,* 2002, *19*, 653.
7. Ding, Y.; Alpay, E. Equilibria and kinetics of CO_2 adsorption on hydrotalcite adsorbent. *Chem. Eng. Sci.,* 2000, *55,* 3461.

(a)

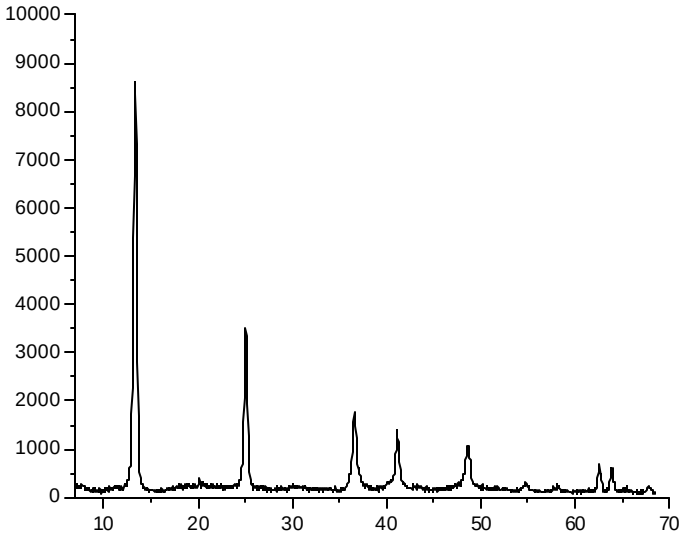

(b)

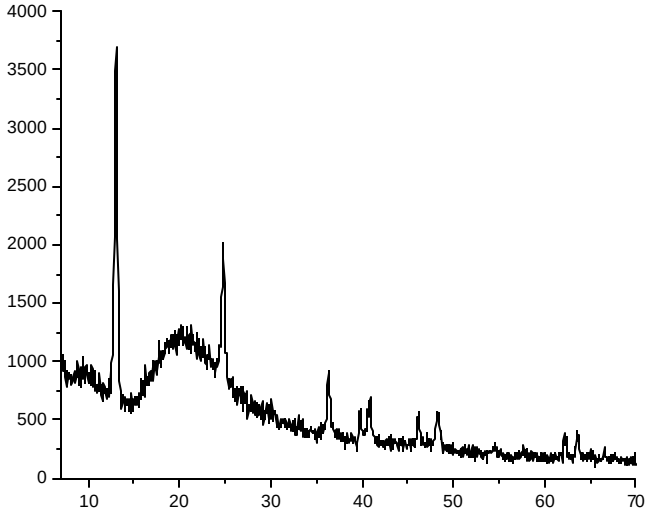

Figure 3.1 The XRD spectra of the LDH samples (a) LDH1 sample; (b) LDH2 sample.

(a)

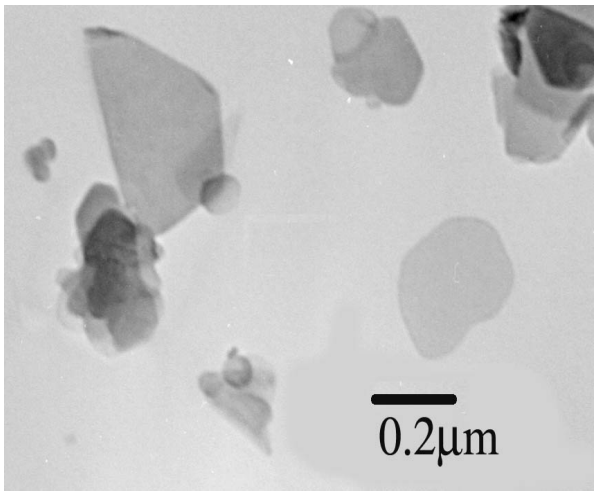

(b)

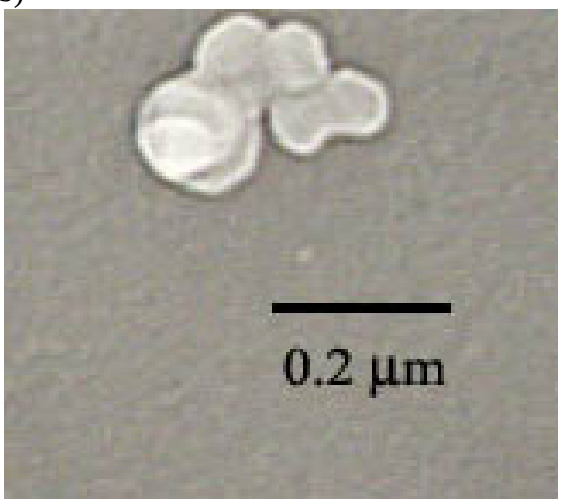

Figure 3.2 (a) TEM picture of LDH1; (b) TEM picture of LDH2.

(a)

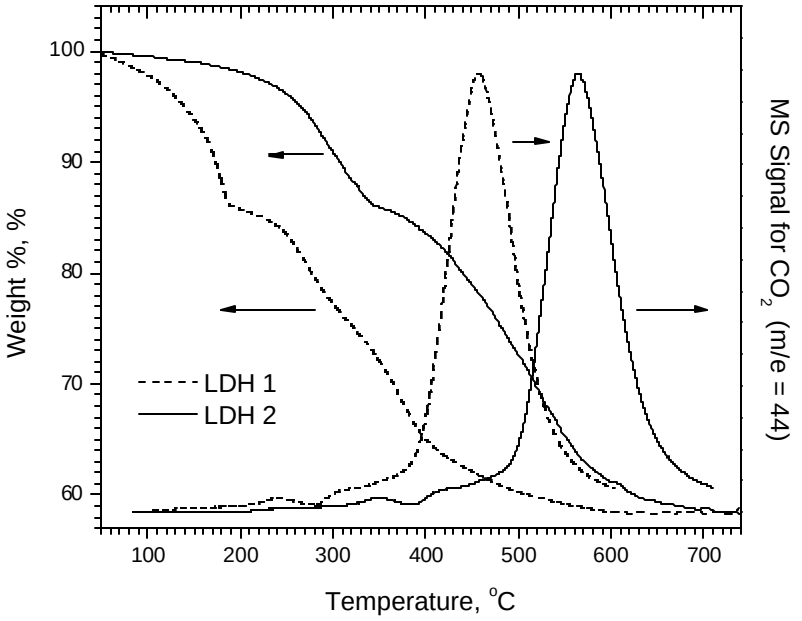

(b)

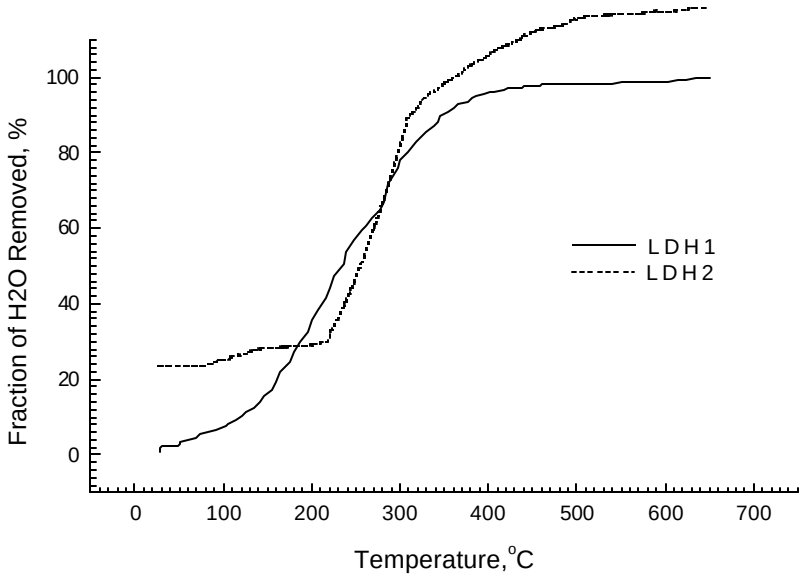

Figure 3.3 The TGA spectra and CO_2 MS signal for the two LDH samples generated with a scan rate of 5°C/min; (b) cumulative amount of H_2O evolved.

(a)

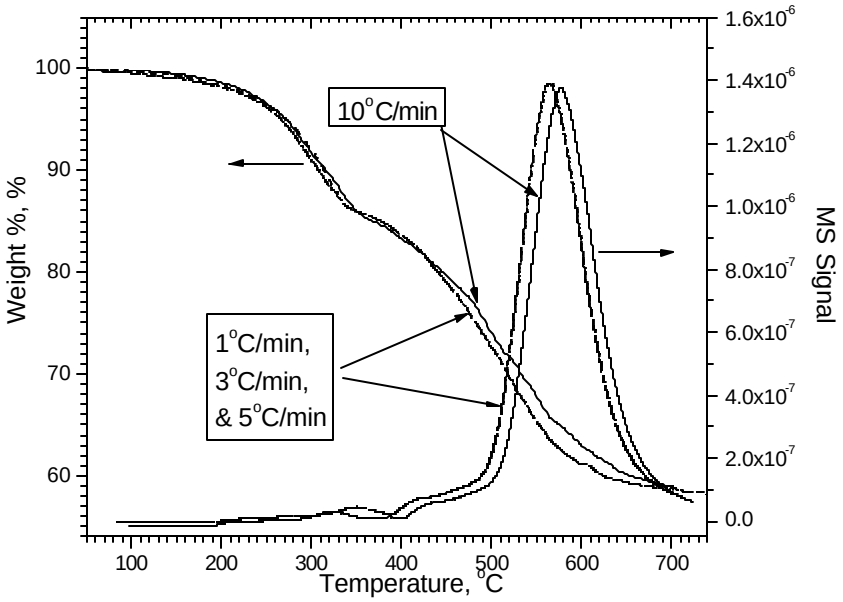

(b)

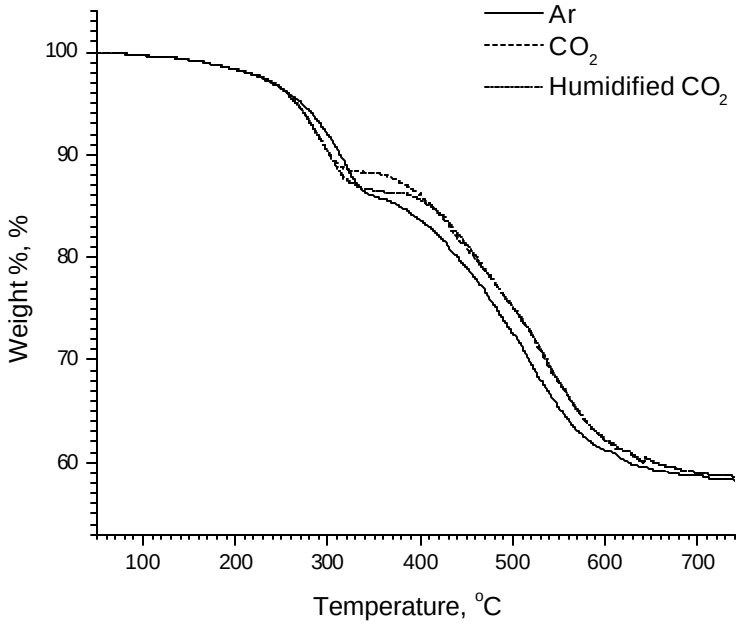

Figure 3.4 The effect of varying (a) the heating rate; and (b) of using different purging gases on the weight-loss for the LDH2 sample.

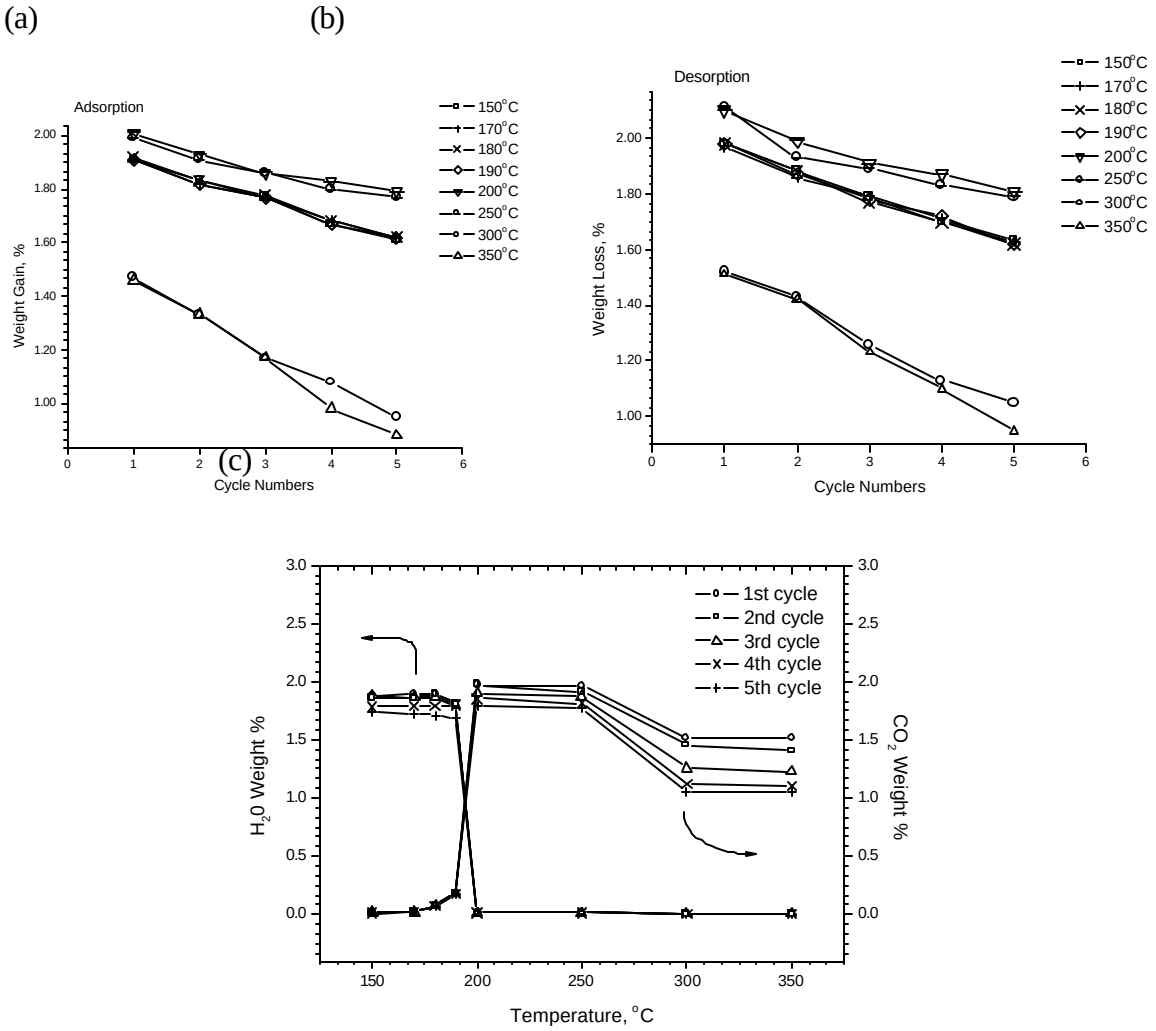

Figure 3.5 Weight-gain or loss. (a) weight-gain during adsorption for various temperatures as a function of the cycle number; (b) weight-loss during desorption for various temperatures as a function of the cycle number; (c) weight-change due to loss of water or CO_2 during desorption as a function of temperature.

(a)

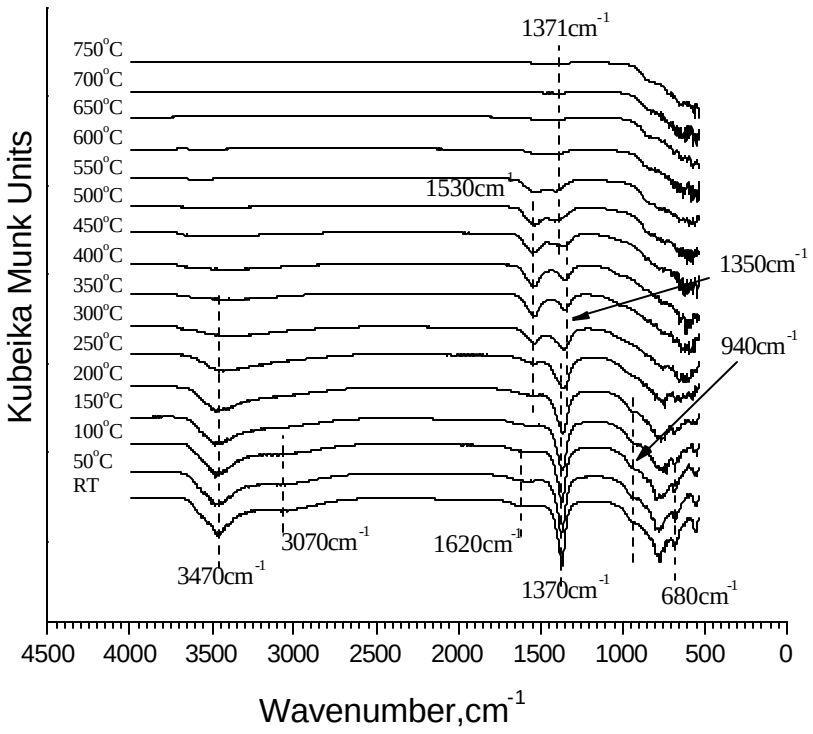

(b)

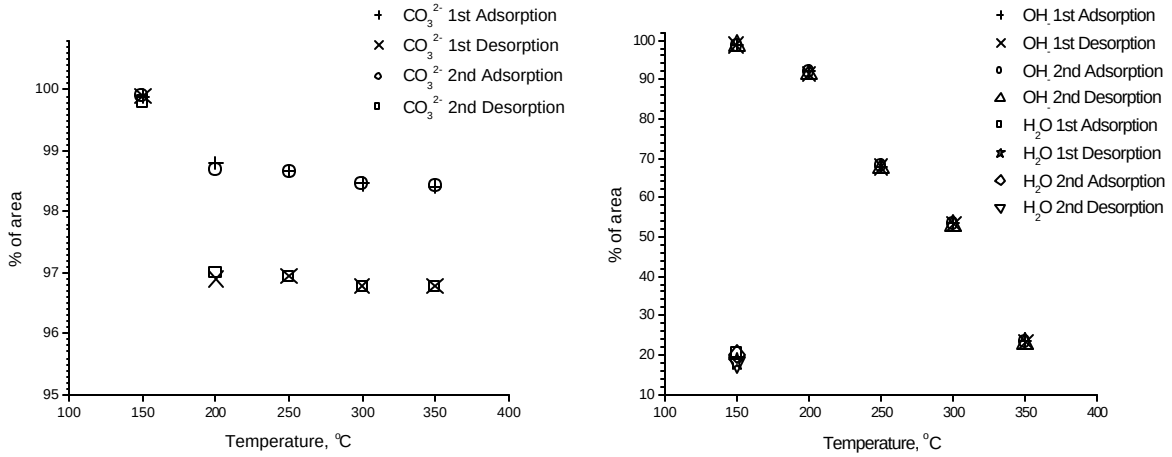

Figure 3.6 (a) *In-situ* DRIFTS of LDH2 as a function of temperature; (b) change in the CO_3^{2-} integrated peak area (left), and change in the OH^- and H_2O integrated peak areas as a per cent fraction of the original peak area (right) during the sorption/desorption cycles.

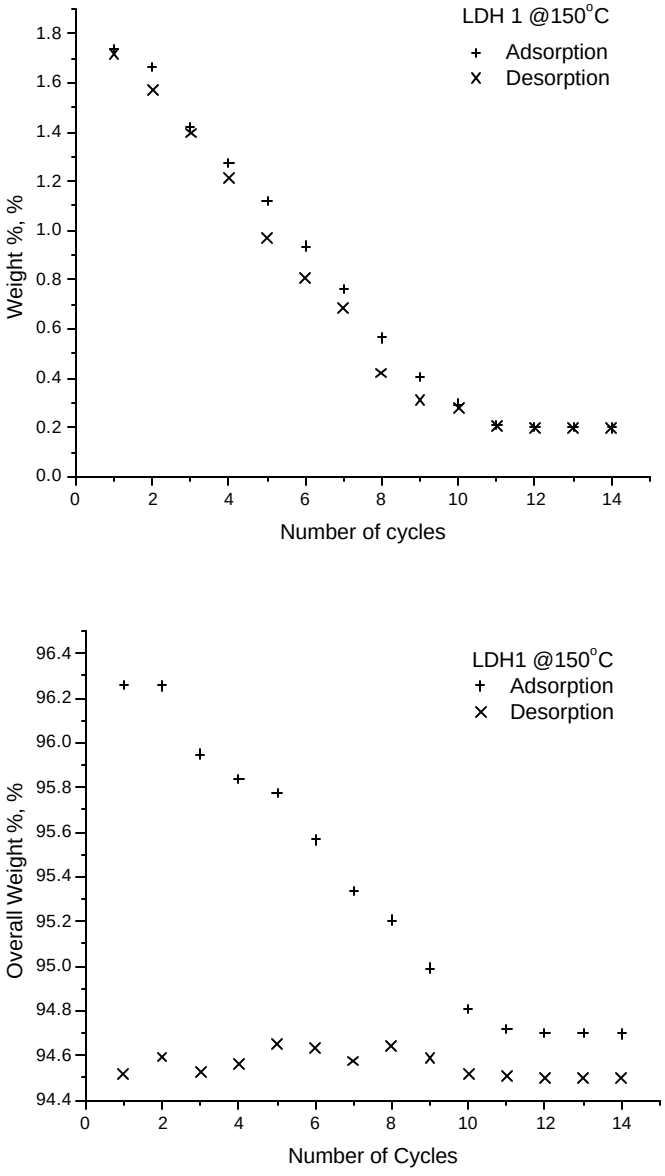

Figure 3.7 Weight-gain or loss (top) and total sample weight (bottom) during the sorption/desorption cycles.

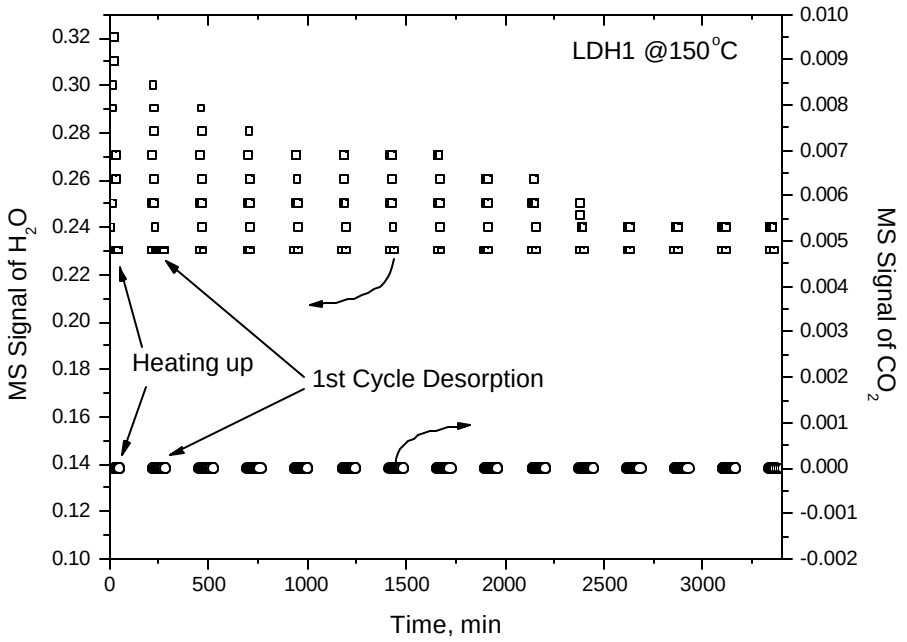

Figure 3.8 H_2O and CO_2 MS signals during the heating, and the desorption part of the cycles as a function of time.

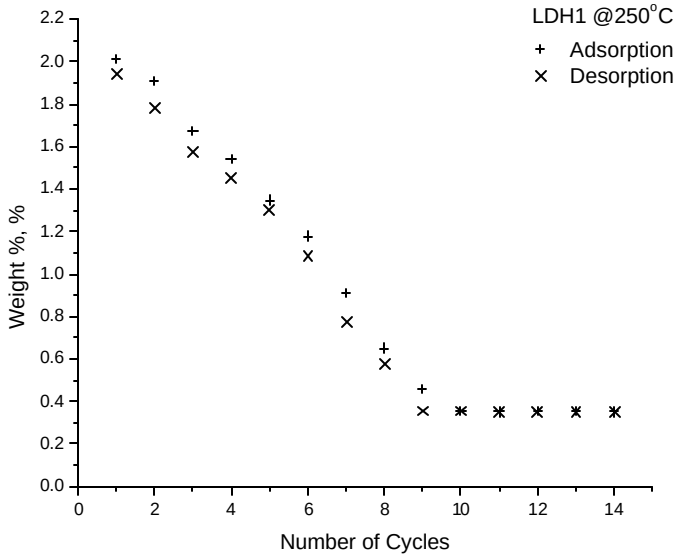

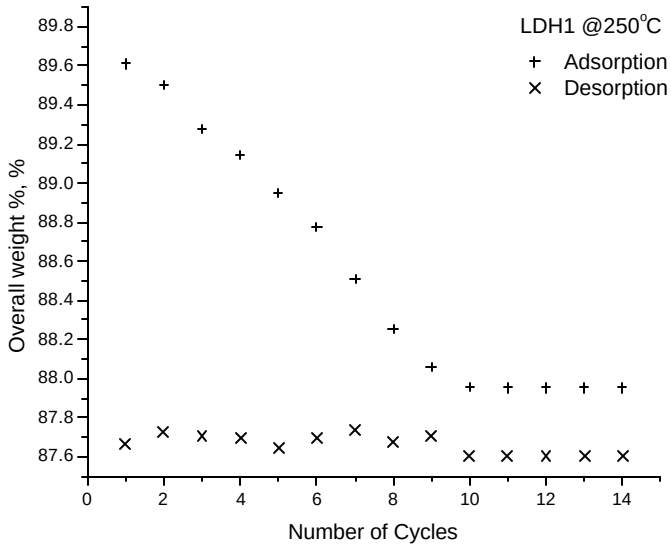

Figure 3.9 Weight-gain or loss (top) and total sample weight (bottom) during the sorption/desorption cycles.

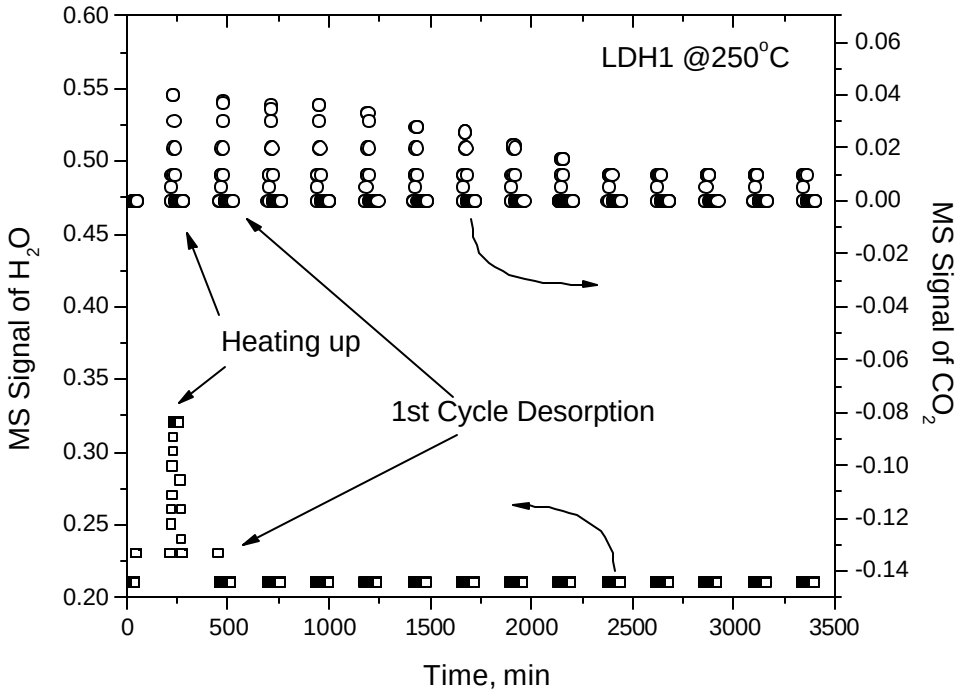

Figure 3.10 H_2O and CO_2 MS signals during the heating, and the desorption parts of the cycle as a function of time.

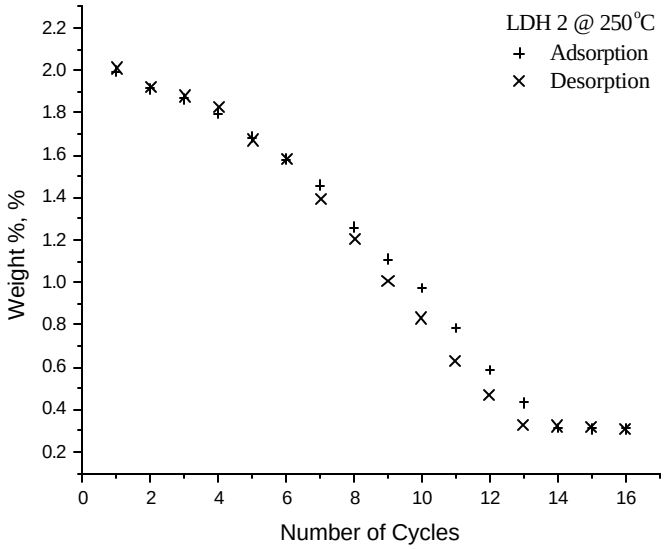

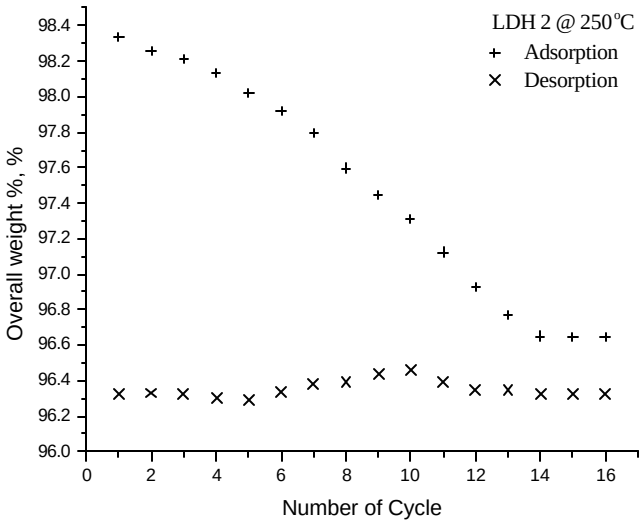

Figure 3.11 Weight-gain or loss (top) and total sample weight (bottom) during the sorption/desorption cycles.

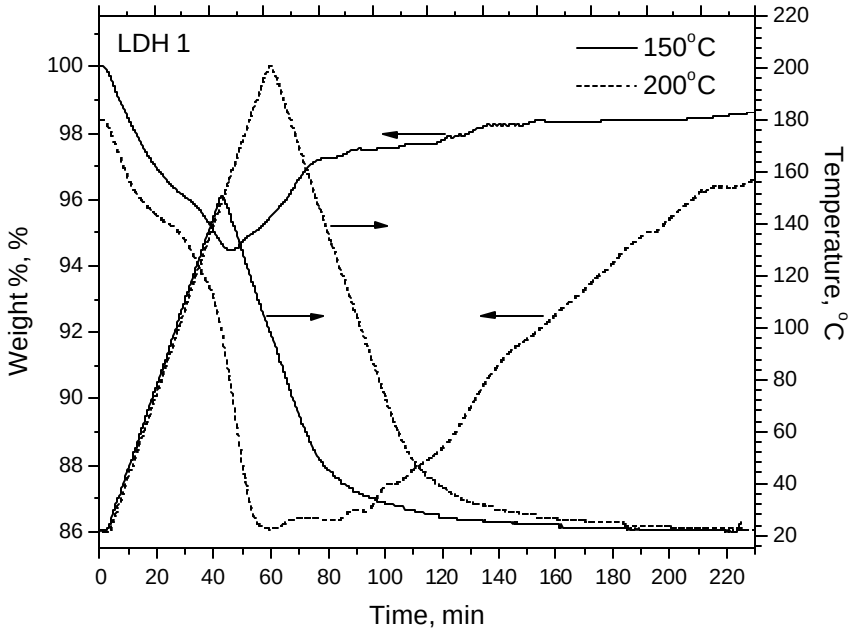

Figure 3.12 Weight-loss/gain during the temperature cycling experiments. Solid lines are the experiments from room temperature to 150°C; Dotted lines are experiments from room temperature to 200°C.

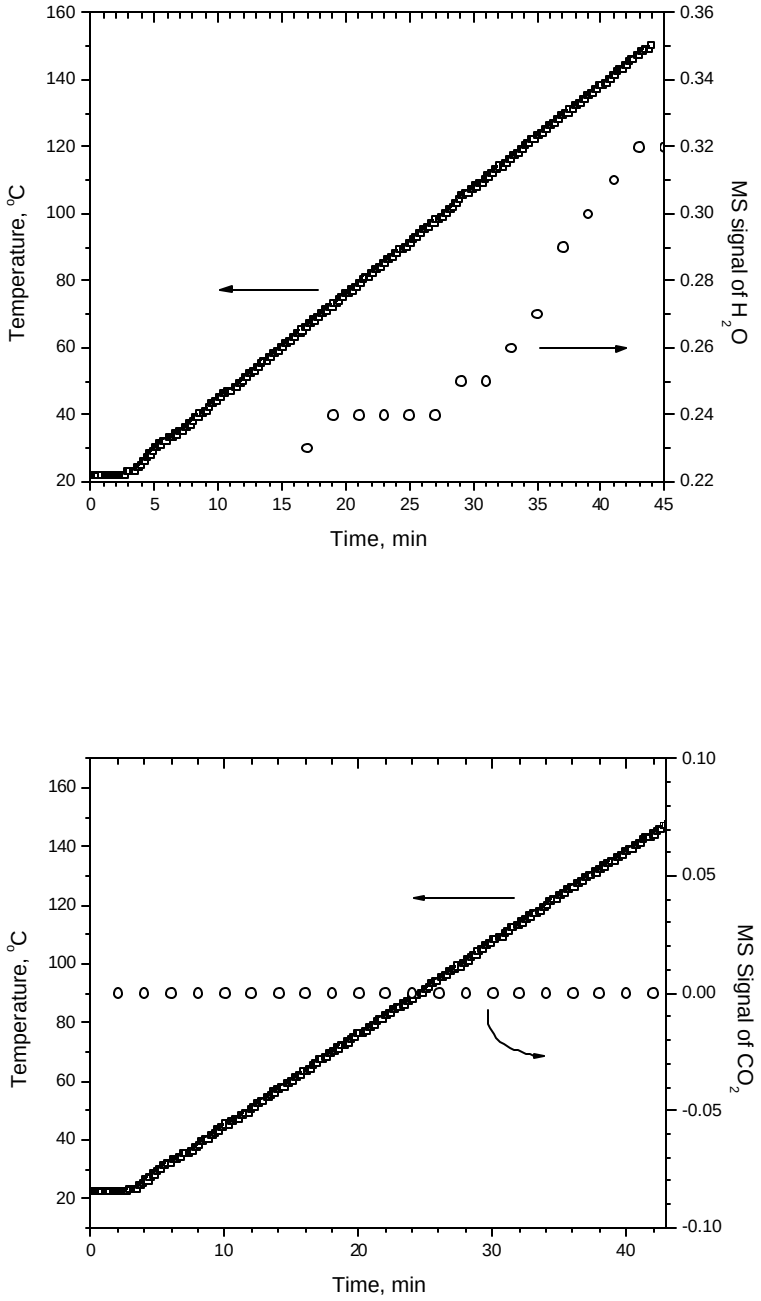

Figure 3.13 MS signals for H_2O (top) and CO_2 (bottom) during the temperature cycling experiment from room temperature to 150°C.

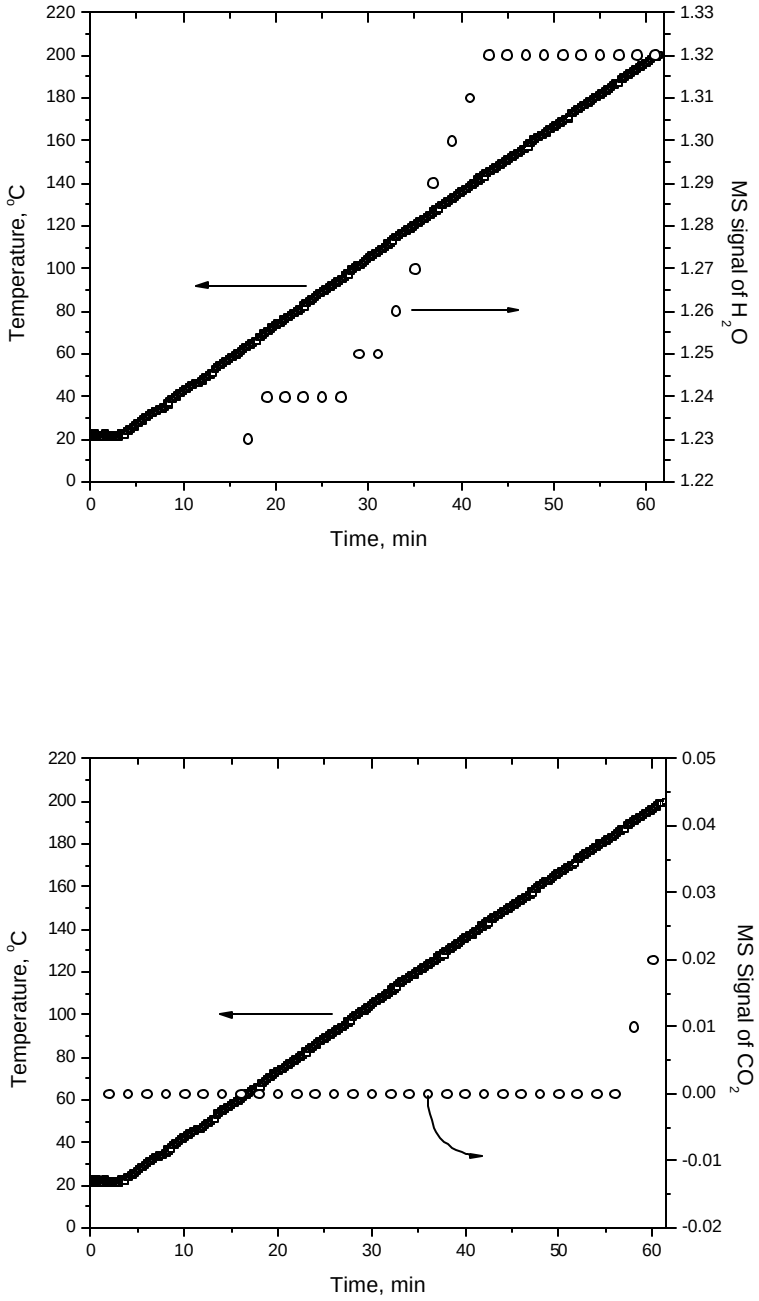

Figure 3.14 MS signals for H_2O (top) and CO_2 (bottom) during the temperature cycling experiment from room temperature to 200°C.

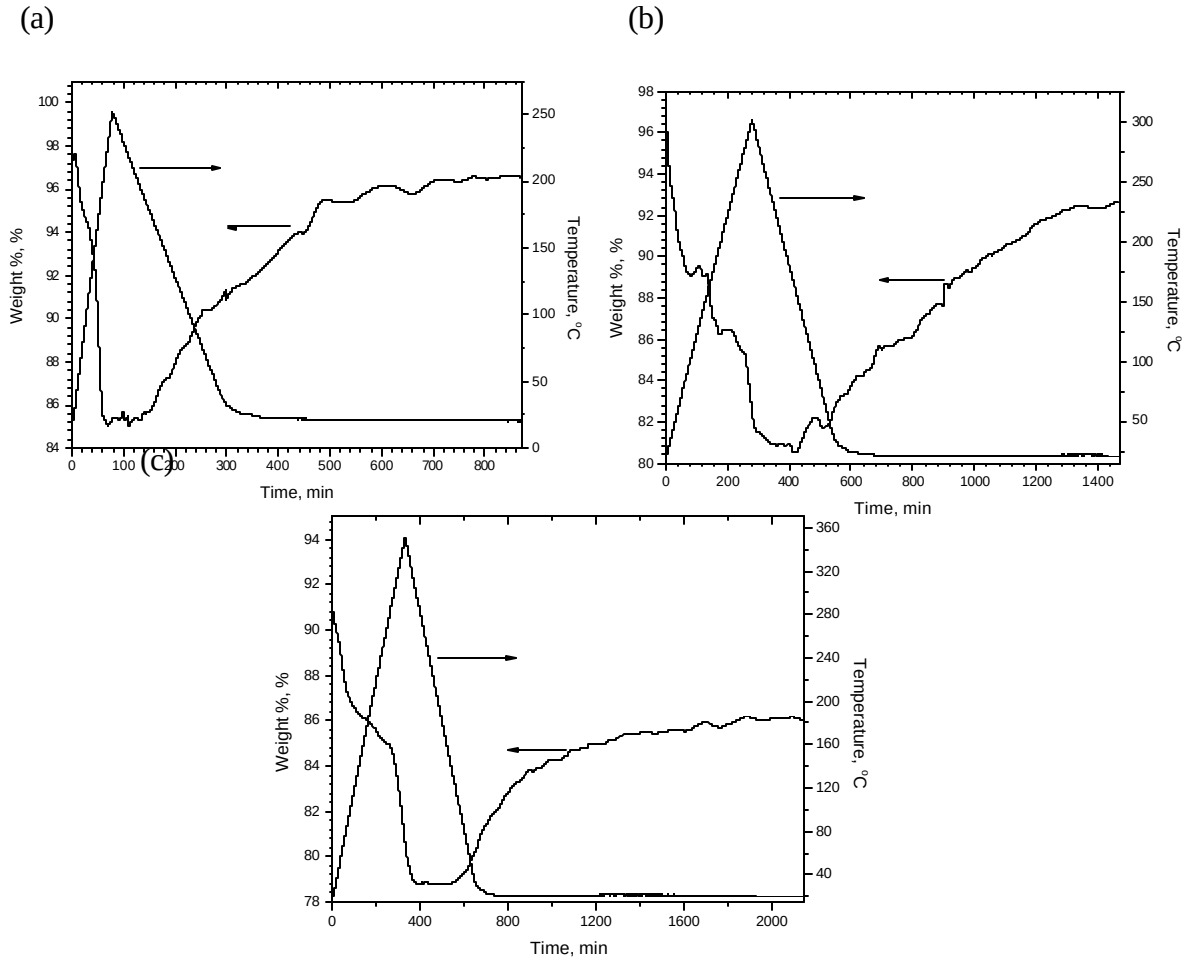

Figure 3.15 Weight-loss/gain during the temperature cycling experiments (a) from room temperature to 250°C; (b) from room temperature to 300°C; (c) from room temperature to 350°C.

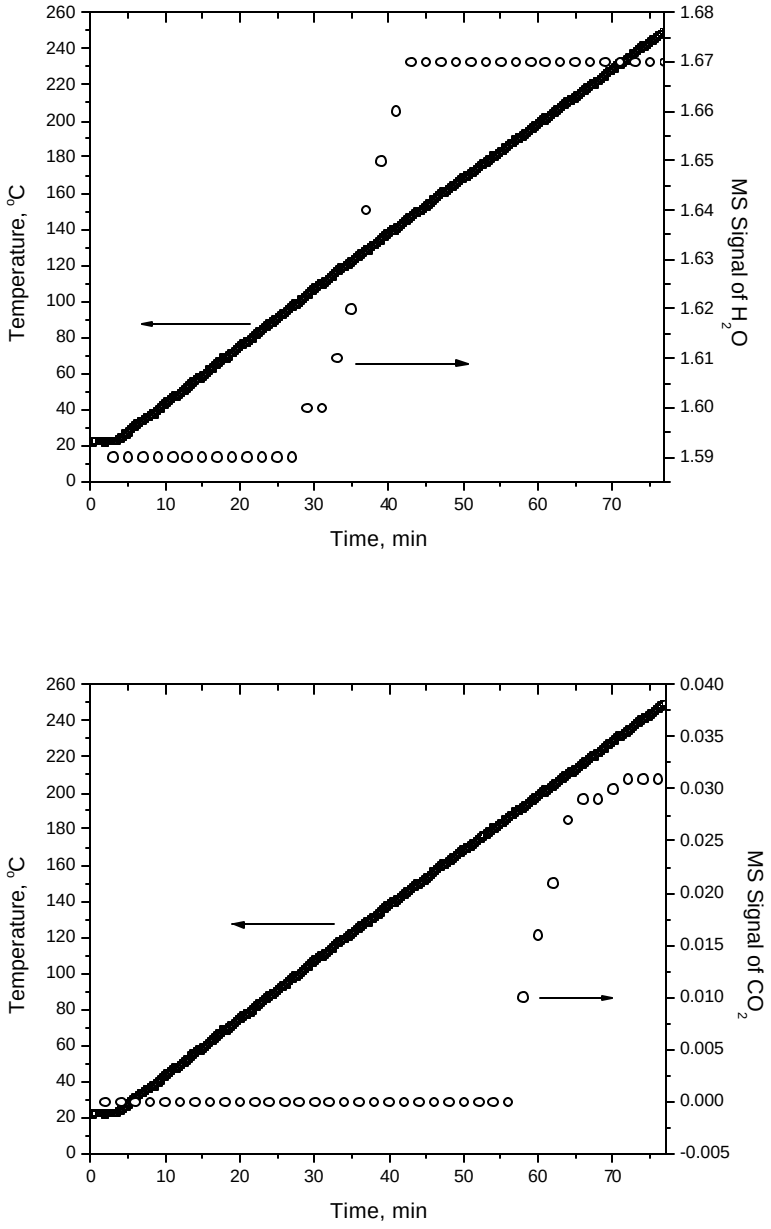

Figure 3.16 MS signals for H_2O (top) and CO_2 (bottom) during the temperature cycling experiment from room temperature to 250°C.

Chapter 4

Synthesis and Characterization of CO_2 Affinity Membrane with LDH Material

4.1 Introduction

Based upon its CO_2 reversibility presented in Chapter 3, the LDH material could form an ideal CO_2 semipermeable membrane (see conceptual schematic in Figure 4.1) if a thin and defect free LDH film can be deposited on porous substrate. This chapter focuses on the synthesis aspect of the LDH membrane undertaken in this project. Two different methods were attempted for the preparation of the LDH membrane. They are (i) in-situ crystallization, and (ii) slip casting. In addition, chemical vapor deposition/infiltration (CVD/I) was also investigated for back patching the synthesized LDH membranes. Our experience on each method is summarized in this chapter along with the results, discussions and recommendations for future study.

4.2 Hydrotalcite Membrane Formation via In-situ Crystallization

Our previous study suggested the possibility that hydrotalcite crystals in the neighborhood of 0.2μm or greater are immediately formed when the two precursor reagents (i.e., Na_2CO_3 and $AlCl_3/MgCl_2$) are combined together. The conventional approach (such as methods developed for the zeolitic membrane) involving the deposition of pre-formed crystals as seeds for crystal growth within the porous structure of the membrane becomes unnecessary. It is feasible to form a single crystal of hydrotalcite within the membrane porous structure if the two reagents can be combined together within the porous structure of substrate. This rationale represents a major advantage for membrane synthesis, which can eliminate many tedious steps in the crystal formation as in the zeolitic membrane development. A two-phase contactor using the membrane as an interphase appears to be an ideal device for us to achieve in-situ crystal formation within the porous structure of the membrane. To demonstrate feasibility, a batch type two phase contactor was used to simplify the equipment design, acquisition and set-up.

4.2.1 Experimental

- *Approch*…To deposit hydrotalcite into the porous structure of the ceramic substrate as described in Figure 4.2, we proposed the interphase contact approach. It was hoped that the precipitate could be deposited within the porous structure to form constriction with hydrotalcite crystals. Detailed procedures are described below:

    a. In the beginning, we filled the tube side of a membrane (plugged at one end *a prior* with one of the reactants, $AlCl_3/MgCl_2$), thereby completely wetting the pores of the substrate with the reactant. Then, the tube was dipped into a batch of

well-mixed Na_2CO_3 solution. This approach was designed to embed hydrotalcite crystals in the pores of the support near the outer tubular surface because the two solutions in contact at the membrane surface are stagnant and do not intermix rapidly.

b. Three porous ceramic membranes with 40Å, 500Å and 0.2μm pore sizes (available commercially from Media and Process Technology Inc.) were selected as candidate substrates for this study. Each tubular membrane was 10" long, 5.5mm OD and 3.5mm ID; one end was plugged with epoxy to hold the $AlCl_3/MgCl_2$ solution.

c. The tube was left in the batch solution for 0.5 to 1 hour to assure complete crystal formation. Then the tube was withdrawn and thoroughly rinsed with water and then dried. As part of the feasibility study, this crystal formation step was repeated up to 4 times to study the degree of crystal embedding/coverage. Thus 4 samples were generated for each pore size.

d. The experimental condition we selected was pH=10 to form the precipitate in-situ. Then, the impregnated membrane was autoclaved at 150ºC for 4 hours to insure the transformation of the precipitate into hydrotalcite crystals. Although our results indicated the formation of crystals even without autoclaving, we performed autoclaving for the time being to eliminate the uncertainty associated with this parameter. Several trials were performed for the preparation of the membranes via impregnation. Between each impregnation, the membrane is subject to autoclaving, water rinsing, and drying.

- *Characterization*…The permeance of the membrane after impregnation was used as an index for the degree of pore plugging of the starting membrane. Generally the above procedure was repeated for 2 to 4 times to reduce the nitrogen permeance of the membrane to <1-3 $m^3/m^2/hr/bar$ for post treatment by CVD to plug the residual opening/defects. In this section, three membranes were selected representing the starting membrane after 1st, 2nd and 4th layer of the in-situ crystallization step. These membranes were characterized by (i) He and N_2 permeance at room temperature, (ii) pore size distribution with a flow-weighted pore condensation porometer, and (iii) SEM.

4.2.2 Results and Discussions

- Evidently the hydrotalcite crystal was formed within the porous structure of the a-Al_2O_3 substrate with 0.05 and 0.2μm pore size based upon (i) the significant reduction in permeance of He and N_2 as shown in Table 4.1, (ii) the increase in the selectivity of He/N_2 (Table 4.1), (iii) the reduction in the pore size and/or pore volume (see Figure 4.4), and (iv) XRD spectrum of the hydrotalcite membrane (see Figure 4.15). As expected, the pore size reduction for the 0.05μm membrane was substantial after the 4th deposition. The increase in selectivity and reduction in

permeance are supportive of the pore size reduction by the in-situ formation of the hydrotalcite crystal.

- SEM photomicrographs of the inner and outer tubular surface of the 0.2µm membrane after in-situ crystal formation are presented in Figure 4.5. No plugging of the inner surface of the membrane was observed. The pore plugging was clearly shown in the outer tubular surface under both low (top, Figure 4.5) and high magnification (bottom, Figure 4.5). EDX mapping shown in Figure 4.6 confirms the formation of the presence of hydrotalcite crystals.

- The penetration of the crystal is believed to be very limited, since the microporous structure of the cross section of the membrane did not exhibit any deposition even near the outer tubular surface (see Figure 4.5). On the other hand, crystal spill-over to the top of the outer tubular surface is believed to be minimal because the surface topography of the substrate still visible as indicated by the absence of Mg in these areas (see Figure 4.7). Thus, the morphological evidence indicates that the proposed synthesis protocol delivers an ultrathin hydrotalcite patch within the pores very near the surface of the substrate with little or no excess crystal formation on the surface via the proposed synthesis protocol.

- Again, a similar result was obtained with the 500Å substrate shown in Figure 4.8. The pore size reduction in this case was reduced dramatically by the crystals (see Figure 4.4) because of the large reduction in gas permeability of the membrane shown in Table 4.1.

- Repeated additional depositions of the hydrotalcite crystals further reduced the permeance and pore size (see Table 4.7). It is believed that the additional depositions resulted in further infiltration of the residual pore openings remained due to incomplete or non-uniform coverage from previous depositions. However, the majority of the crystals were embedded in the substrate during the 1^{st} deposition cycle based upon the dramatic permeance reduction after the first cycle.

- It appears that hydrotalcite does not cover the substrate completely based upon the SEM pictures of the top surface as shown in Figures 4.9 to 4.12 corresponding to the 1^{st}, 2^{nd}, and 4^{th} impregnation. Evidently the permeance levels off after the 4^{th} impregnation, more importantly, 85% permeance was reduced. However, the selectivity after the 4^{th} impregnation remains low, around Knudsen separation, indicating that defects exist. Further the SEM photograph after the 4^{th} impregnation (shown in Figures 4.11 & 4.12) is consistent with our speculation that defects remain. It appears that the defect shown in Figures 4.11 & 4.12 is resulted from the incomplete coverage left from the in-situ impregnation. The defect in the dimension of about 0.2 micron is not covered by the precipitate, most likely resulted from the lack of the reagents filled into this gap (for example an air pocket), during impregnation, and then no precipitate would form within the gap. The other possibility is that the membrane layer cracked after drying.

- Due to larger defects present in the membranes deposited on the 0.2 and 0.05 µm substrate, we then attempted to deposit hydrotalcite on the 40Å substrate. Figure 4.13 presents the SEM and EDAX profiles of the hydrotalcite membrane thus deposited. Permeances vs no. of layer deposition presented in Table 4.2 and Figure 4.3 indicate that >~90% permeance flux reduction was achieved after the 3rd layer of deposition. The selectivity of He/N_2 was enhanced to near or slightly above Knudsen selectivity, indicating that the deposition may have covered defects and possibly reduced the pore size of the starting membrane. The pore size distribution of the membrane after 4th deposition was compared with that of the starting membrane as shown in Figure 4.14. It appears that nearly all the pore size available from the substrate was covered with hydrotalcite. However, based upon its resultant selectivity in the neighborhood of Knudsen selectivity, defects remain dominant although the defect sizes are much smaller in this case.

Table 4.1: Permeance and Selectivity of the 500Å and 0.2µm Pore Size Ceramic Substrates Following In-situ Deposition/Crystal Growth of Hydrotalcite within the Pores. Based Upon the SEM Analysis, Crystal Growth is Concentrated at the Surface of the Membrane.

Pore Size of Substrate [µm]	Times of Deposition [-]	Permeance [$m^3/m^2/hr/bar$] @ 25°C		Ideal Selectivity [-]	Remarks
		Helium	Nitrogen		
0.05	0	81.2	41.5	1.96	control
0.05	1	2.04	0.913	2.24	
0.05	2	-	-	-	
0.05	3	5.22	2.35	2.22	
0.2	0	113	66.3	1.70	control
0.2	1	18.8	11.2	1.68	
0.2	2	-	-	-	
0.2	3	15.0	6.52	2.30	

Table 4.2 Permeance of Hydrotalcite Membranes prepared via 1st, 2nd and 3rd In-Situ Crystalization Step using 40Å Al_2O_3 Membranes as Starting Membranes

Sample ID	No. of Crystalization	Permeance (m3/m2/hr/bar) He	N2	Selectivity (He/N2)	
40A, typical		~60	~30	~2	
HT-IA-60-6	1st	23.34	8.93	2.61	
HT-IA-40-4	1st	28.57	11.47	2.49	
	2nd	13.98	6.19	2.26	
HT-IA-40-5	1st	16.93	6.67	2.54	
	2nd	8.75	3.19	2.74	
	3rd	8.47	3.24	2.61	?????
Knudsen, theoretical				2.65	

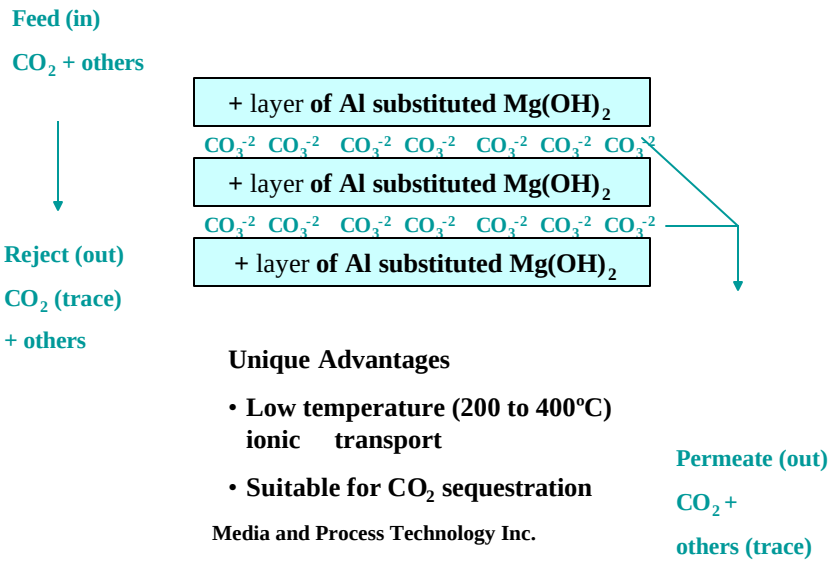

Figure 4.1 Affinity Ceramic Membrane with 2-D Transport Channel for CO_2

STEP	PURPOSE
1. Interphase contact of reactants	Formation of precipitates as precursors
2. Aging via autoclaving	Enhancing crystal stability and crystallinity
3. Rinsing	Removing impurities

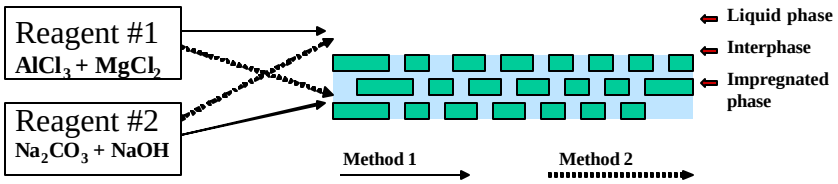

Figure 4.2 Hydrotalcite Membrane Synthesis via Impregnation

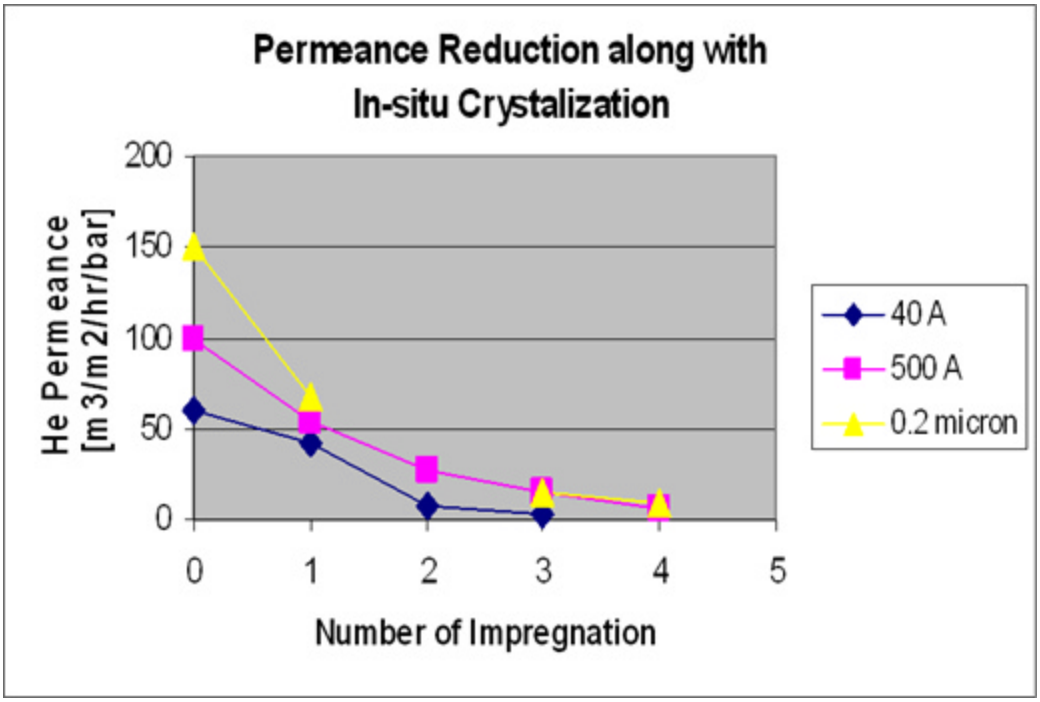

Figure 4.3 Permeance reduction along with number of in-situ crystallization for substrates with pore sizes of 40Å, 500Å and 0.2 µm

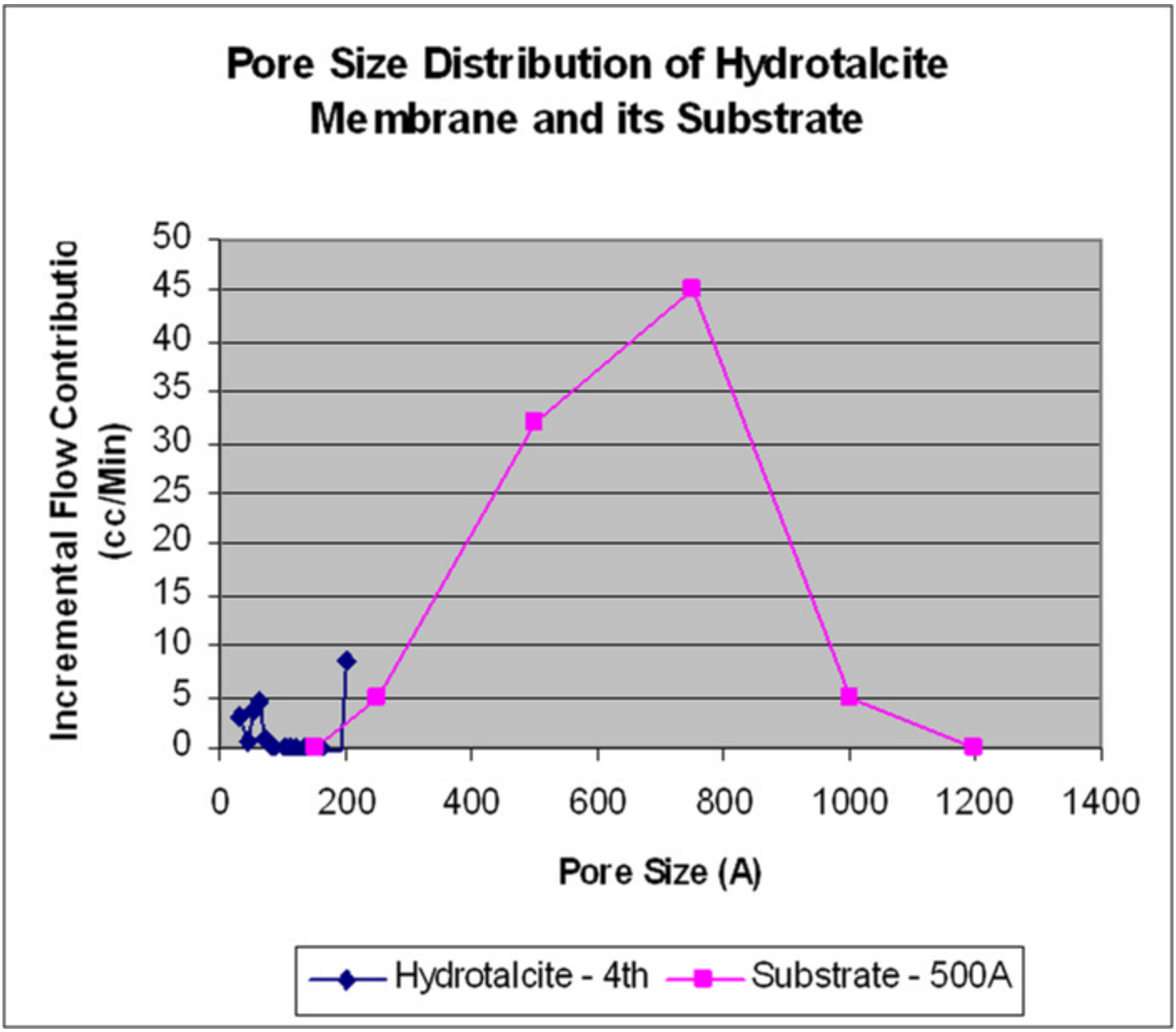

Figure 4.4 Pore size distribution of hydrotalcite membrane and its substrate with 500Å pore size.

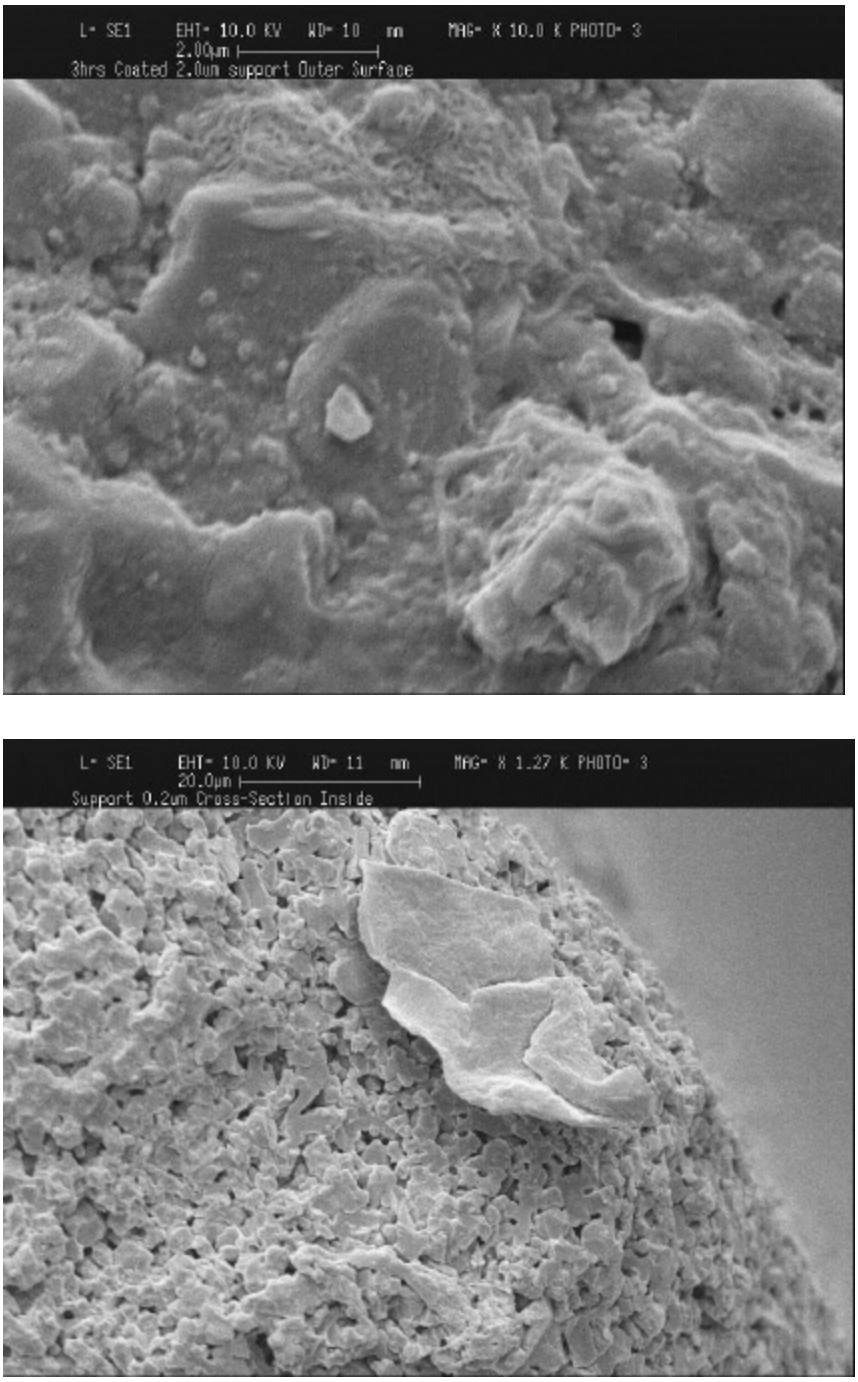

Figure 4.5 SEM Photomicrograph of the outer tubular surface (top) and cross section (bottom) of the 0.2µm substrate. Pore plugging by the hydrotalcite is evident under this higher magnification on the outer surface but not in the cross section.

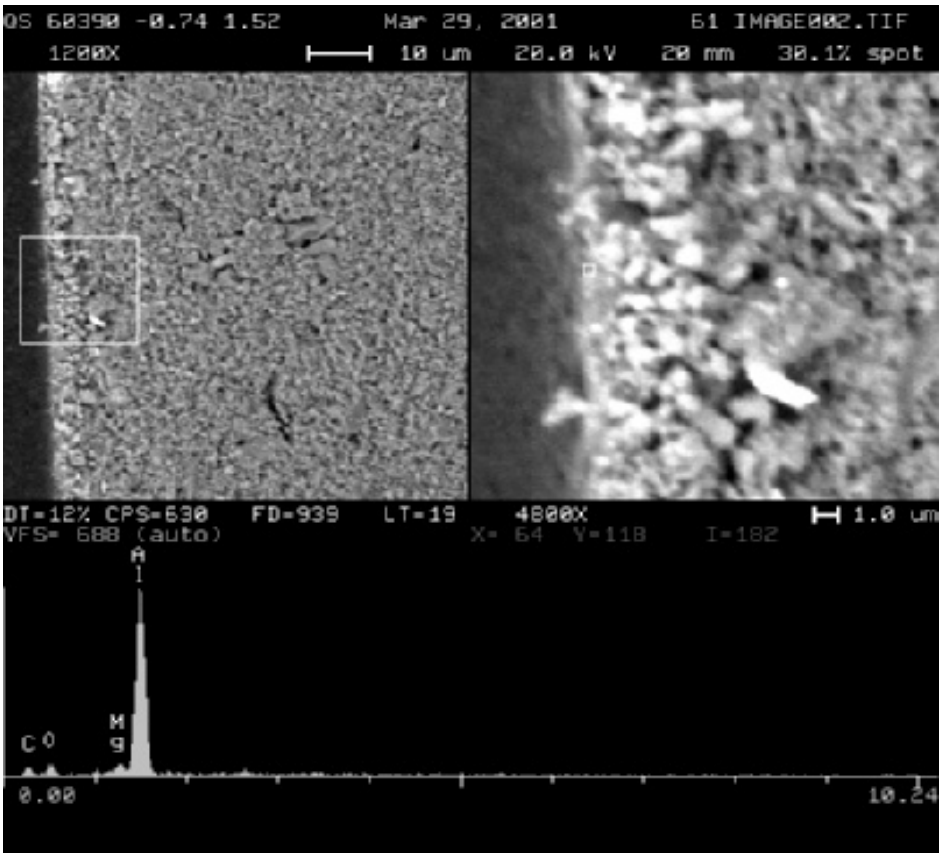

Figure 4.6 SEM photomicrograph and EDX of the outer surface of the 500Å substrate after in-situ crystallization of hydrotalcite. The presence of Mg confirms the formation of hydrotalcite on the outer tubular surface.

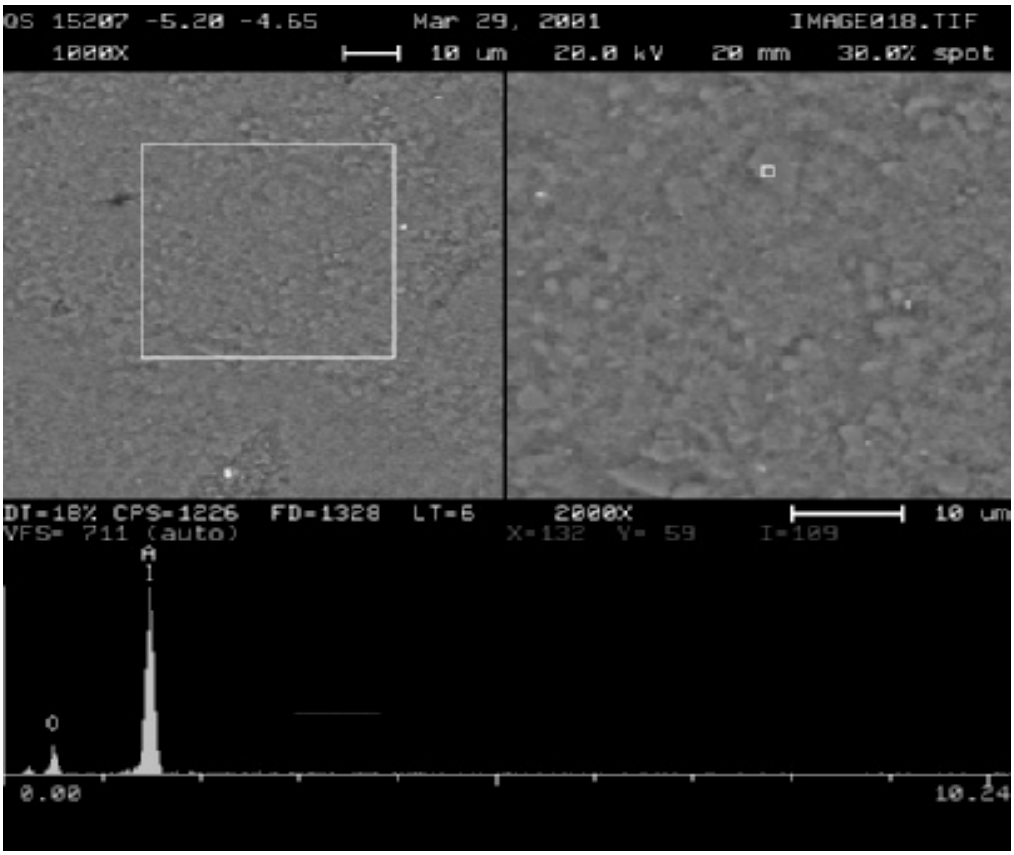

Figure 4.7 SEM Photomicrograph and EDX focused on one of the substrate particle. No Mg was detected. Combining the result from Figure 4.6 verifies that in-situ crystallization takes place within the porous structure of substrate, not on the top of the substrate.

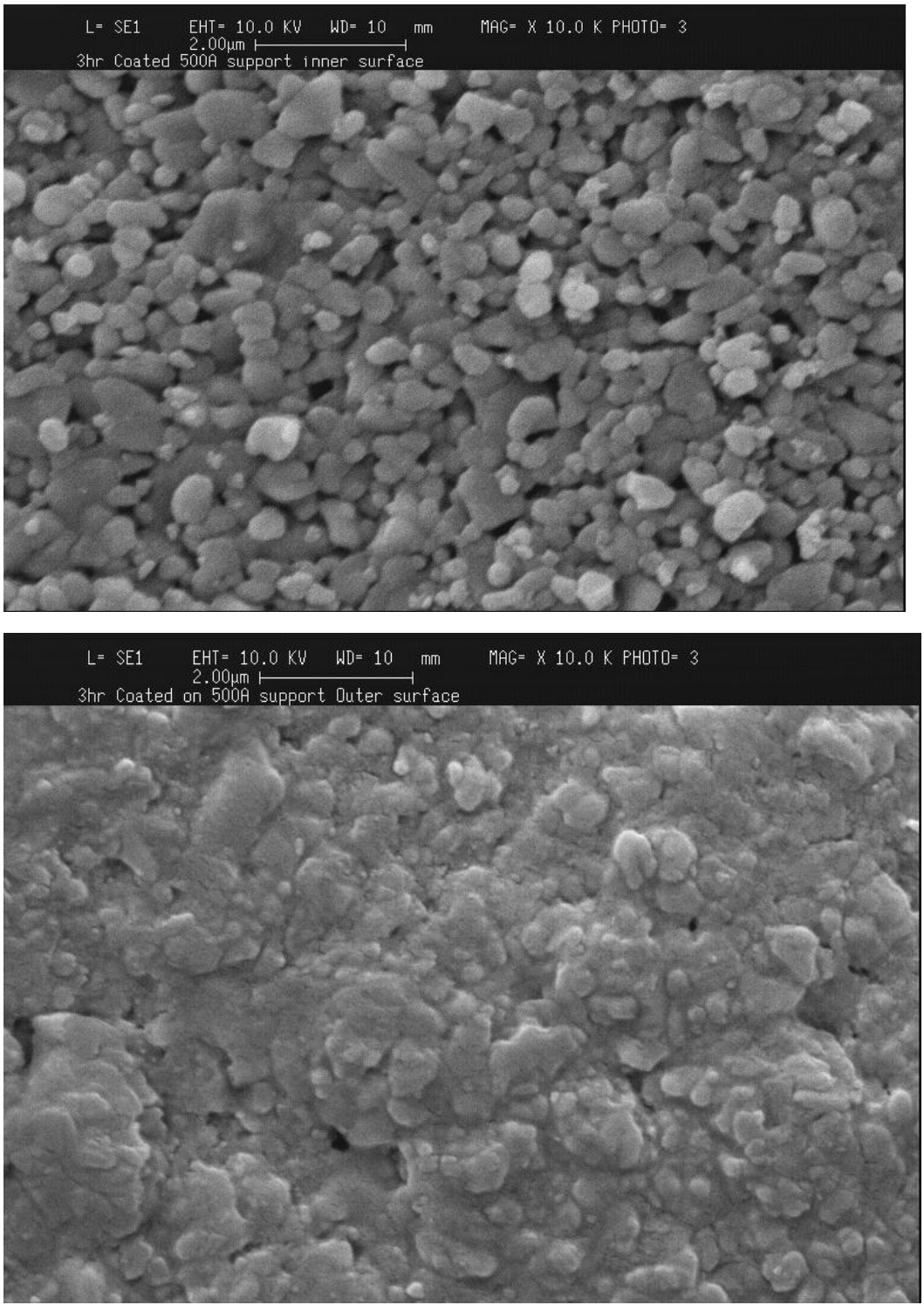

Figure 4.8 SEM Photomicrograph of 500Å substrate after in-situ crystallization of hydrotalcite: Inner tubular surface (top), and outer tubular surface (bottom). Pore plugging by hydrotalcite on the outer tubular surface is evident.

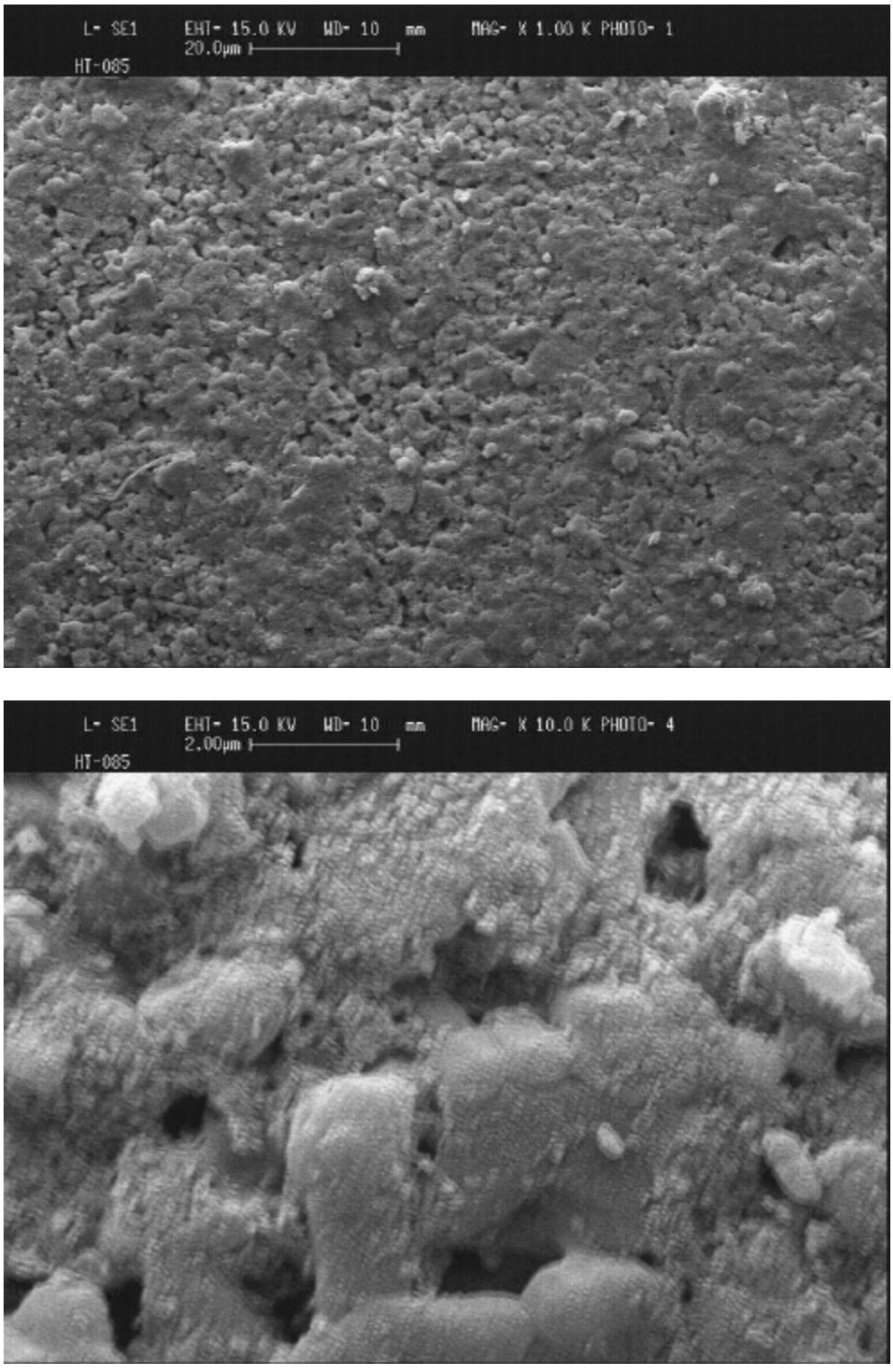

Figure 4.9 SEM photomicrograph for hydrotalcite membrane prepared Via impregnation: 1st deposition (Top: 1K mag, Bottom: 10K mag)

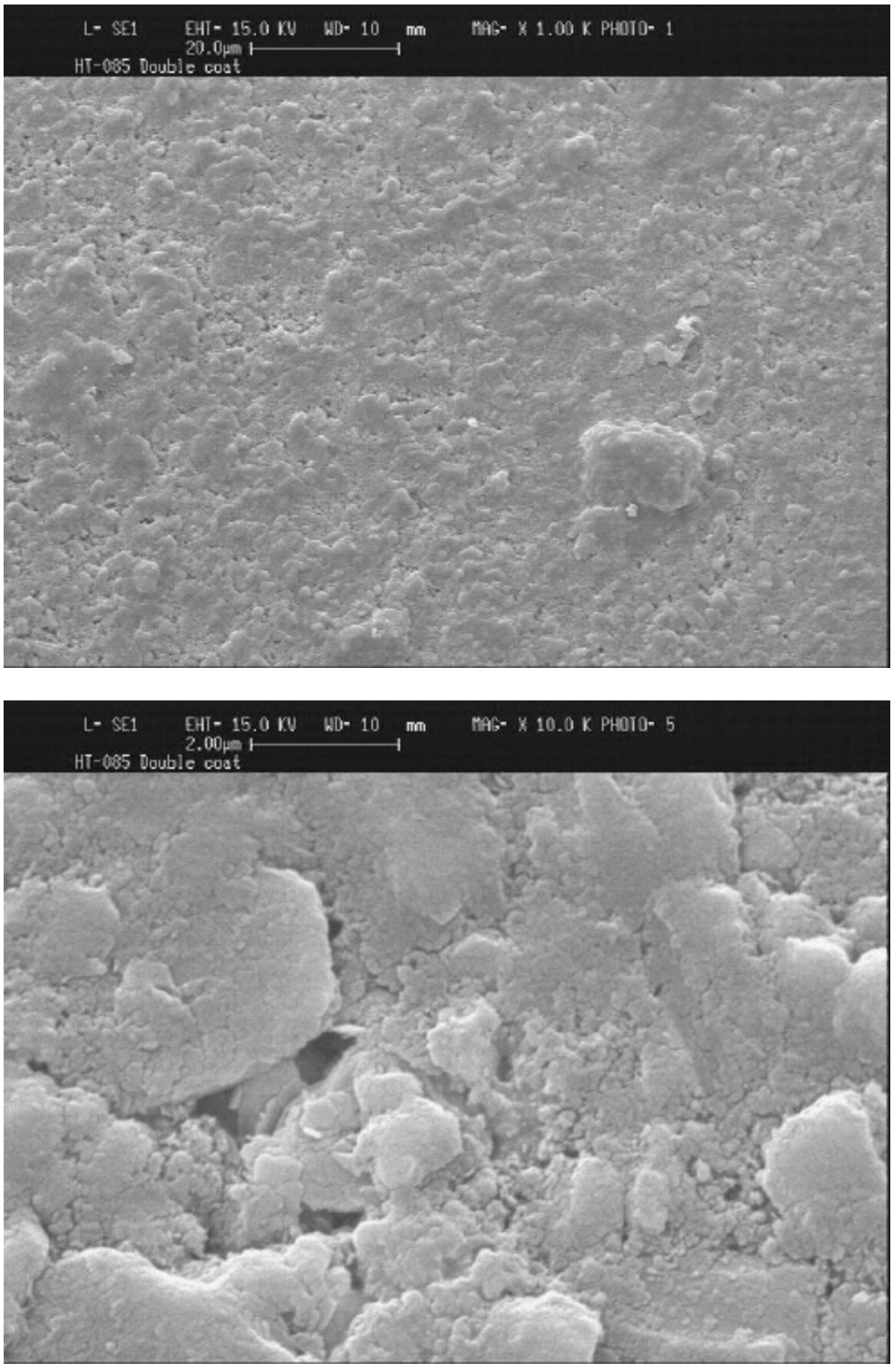

Figure 4.10 SEM photomicrograph of hydrotalcite membrane prepared via impregnation: 2nd deposition (Top: 1K mag, bottom: 10K mag)

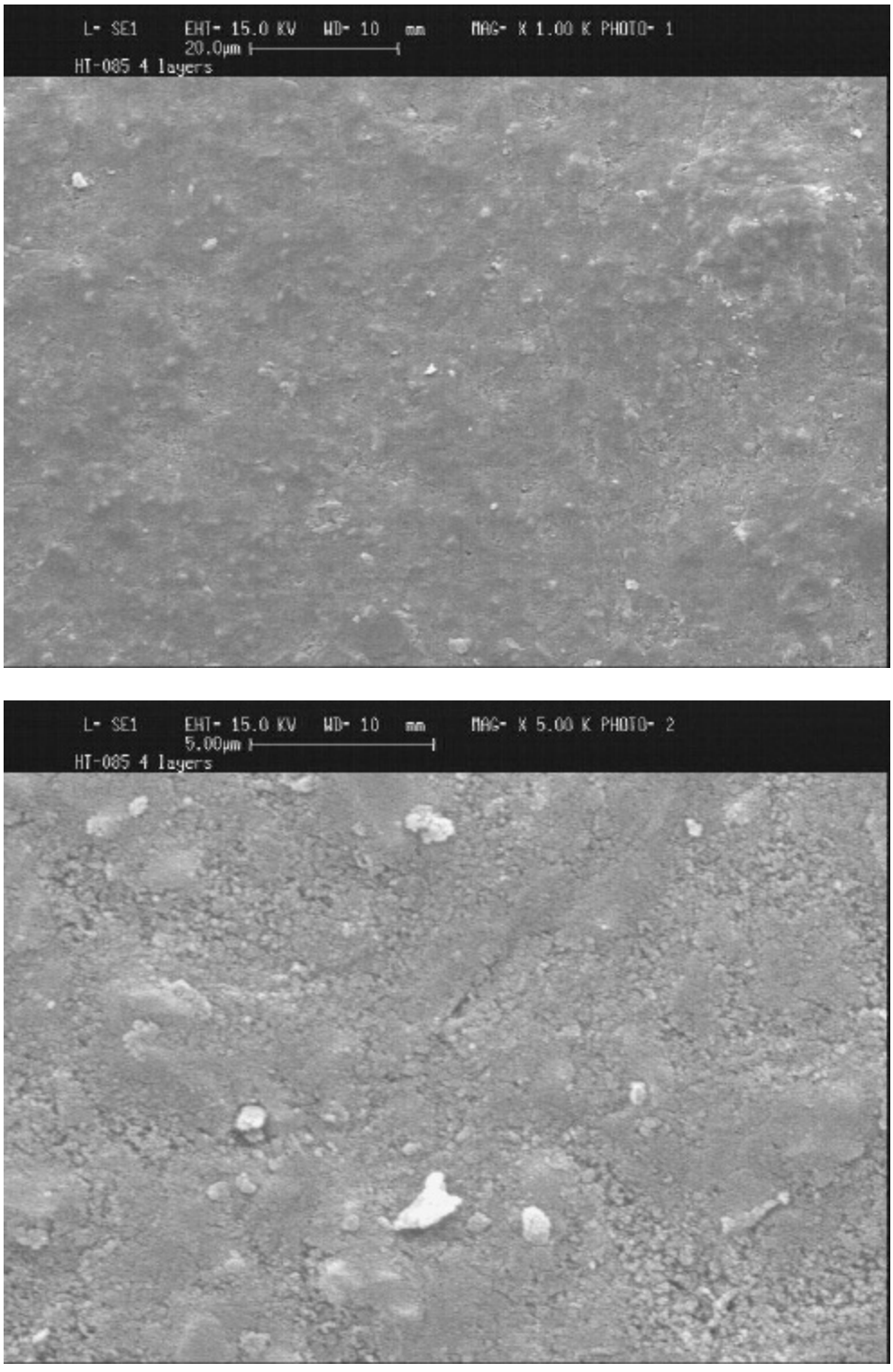

Figure 4.11 SEM photomicrograph of hydrotalcite membranes prepared from impregnation (4 times). Magnification: 1K top, 5K bottom.

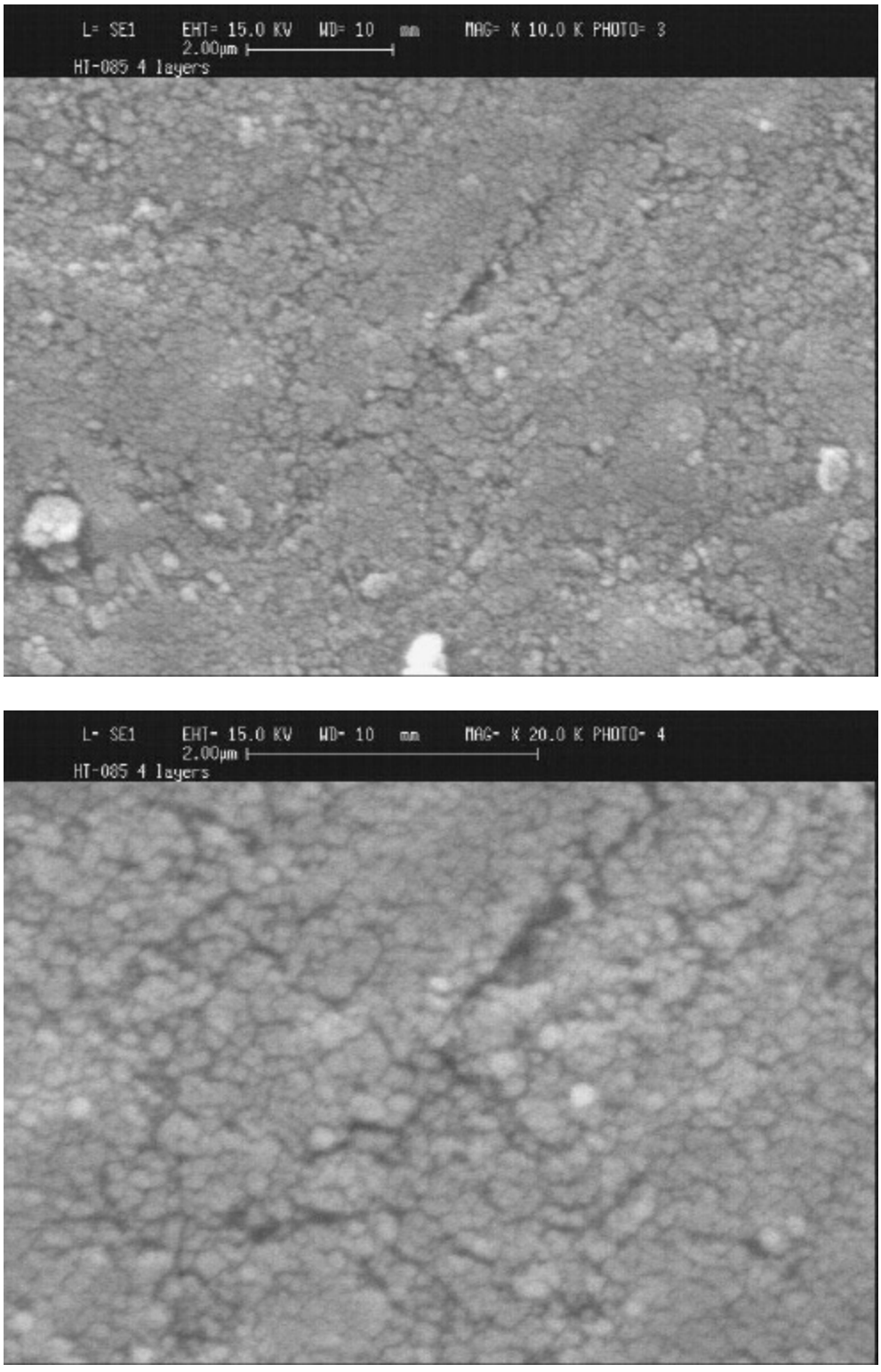

Figure 4.12 SEM photomicrograph of hydrotalcite membranes prepared from in-situ crystalization (4 times) on the 0.2µm Al_2O_3 membrane. Magnification: 10K top, 20K bottom.

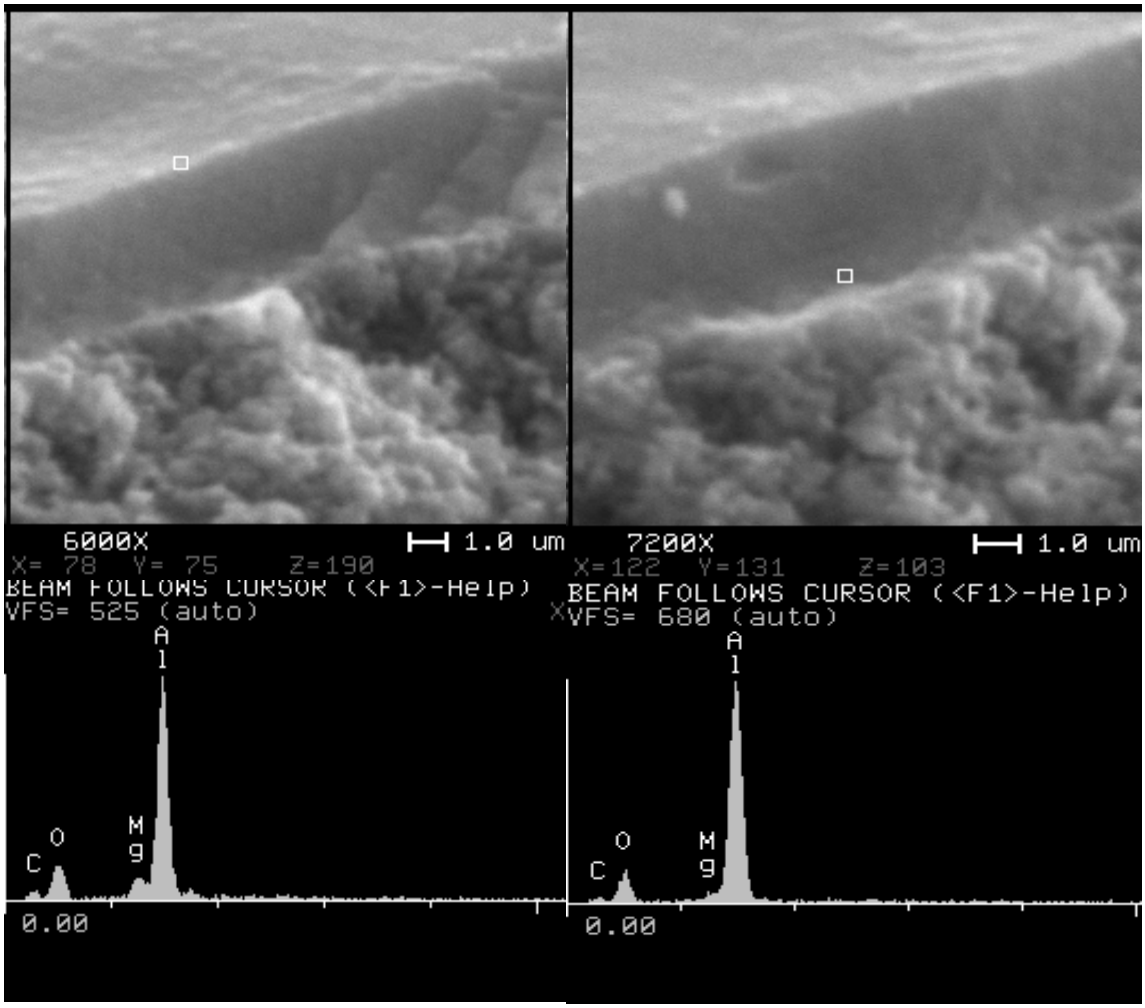

Figure 4.13 SEM and EDX profiles of hydrotalcite membrane deposited on the 40Å substrate.

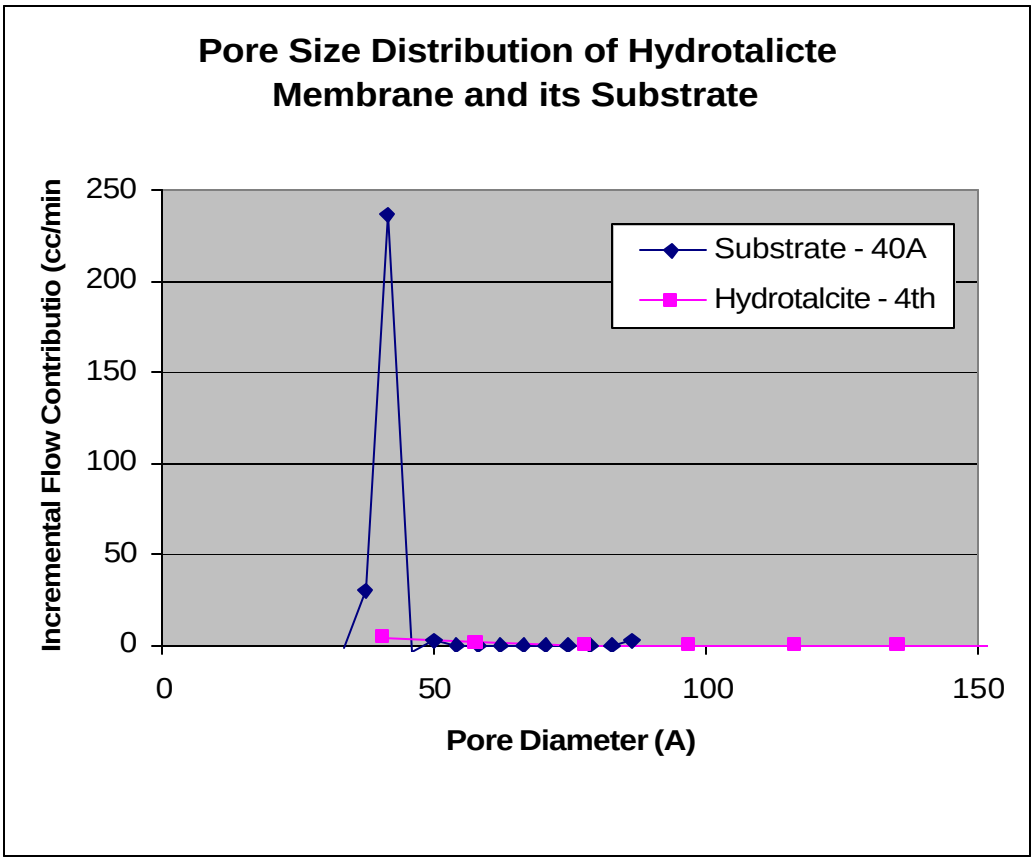

Figure 4.14 Pore size reduction of the ceramic membrane with 40Å pore size after deposition of hydrotalcite via in-situ crystallization.

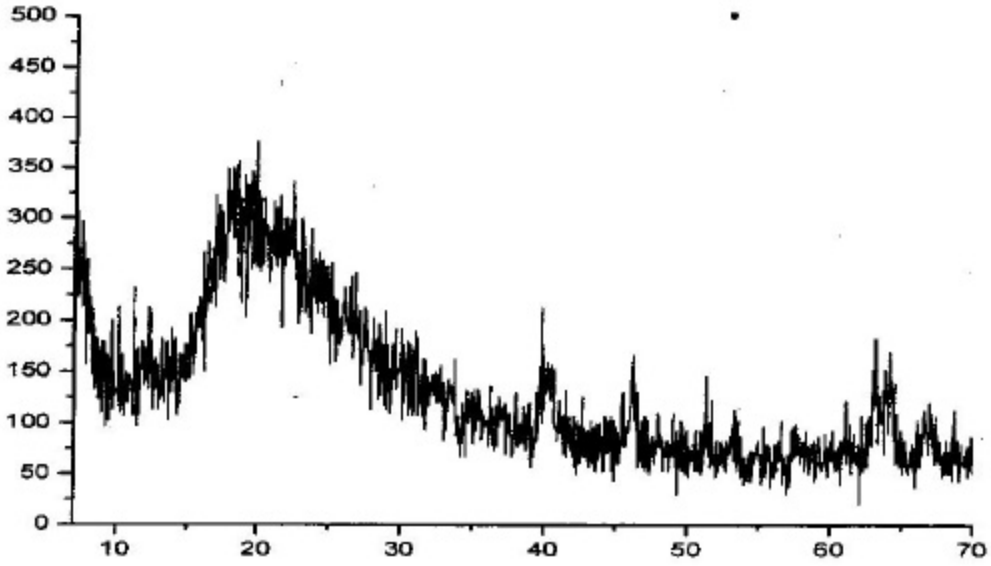

Figure 4.15 XRD of hydrotalcite membrane synthesized via in-situ crystallization.

4.3 Hydrotalcite Membrane Synthesis via Slip Casting

As illustrated in Figure 4.16, slip casting of the hydrotalcite thin film is not different from the slip casting of existing mesoporous $A1_2O_3$ membranes (with pore size in the range of 40Å to <0.2µm). The critical parameters for this approach include the preparation of the slip with (i) a proper particle size, and (ii) appropriate rheology. Thus, a defect free thin film can be deposited on the surface of the membrane without defects after thermal annealing. Our goal here is to deposit a thin film of hydrotalcite with ~100Å pore size; then CVD/I technique can be applied to seal the opening in this range.

4.3.1 Experimental

- *Particle Size of Slip*…Hydrotalcite precipitates were prepared from the precursor chemicals, which was then compared with the particle size of our commercial mesoporous membranes (0.2µm or less in pore size). The hydrotalcite particles comparable with the particles size of the Al_2O_3 membranes was selected for the preparation of the slip.

- *Rheology of Slip*…The formula for the preparation of the mesoporous Al_2O_3 membrane was modified for our purpose here.

4.3.2 Results and Discussions

- *Particle Size of Hydrotalcite Slip*…According to our experience with Al_2O_3, the particle size required to form this range of pore size is in the neighborhood of 500 to 800Å as shown in Figure 4.17. Particles from the hydrotalcite gel are in fact smaller than this range and appear very uniform in size as shown in Figure 4.17. Based upon this observation, we believe that the hydrotalcite gel we prepared satisfies the first requirement in terms of the particle size.

- *Rheology of Hydrotalcite Slip*…As far as the rheology of the slip is concerned, we found that, without the modification of the viscosity of the sol, the layer quality was very poor. Our first attempt is to adapt the gel formula we use to prepare the Al_2O_3 thin film for our purpose. The result from this attempt appears very promising. The membranes with the 1, 2, and 3- layer casting have been prepared and well characterized. Each membrane was calcined at 400ºC before the characterization. Figures 4.18 & 4.19 show the membrane with one layer casting. The hydrotalcite evidently covered most opening of the substrate. However, some uncovered defects were observed. Figures 4.20 & 4.21 show the membranes with the two-layer casting. The quality was improved significantly. It is clear that the particles formed by the gel are very uniformly and evenly deposited on the surface of the substrate. Figures 4.22 & 4.23 show the membrane with the 3-layer deposition. It appears that the layer quality is not improved; in fact, it shows some missing spots possibly due to its thickness. The

permeance was measured for the 1, 2 and 3 layer membrane, which are presented in Table 4.3. About 50% permeance reduction was achieved with the 1-layer casting. The permeance after the 1st layer was not reduced noticeably, consistent with the observation from the SEM. Figure 4.24 shows the membrane prepared with two layers. However, this sample was calcined between the layers. Some micro crack was observed and its layer quality was not improved. Thus, we conclude from this study that the two-layer casting appears sufficient to prepare a uniform membrane. As shown in Table 4.3, the hydrotalcite membrane prepared with the 2-layer casting appears comparable to the existing 100Å membrane based upon the permeance.

- *Characterization of the Green Layer*…As indicated above, the green layer formed with the improved formula appeared defect free according to SEM examination. We also conducted initial flow analysis using helium flow saturated with water at room temperature. According to our previous experience, no initial flow can be detected for an Al_2O_3 membrane with 100Å commercially available from us. The initial flow measurements from the two samples are presented in Table 4.4. It is believed that the green layer after drying at 80°C is nearly defect free as indicated by the very low initial flow for both 94-7-1/2 and 94-7-1. Drying at 200°C increases the initial flow slightly, i.e., from 1.6 to 6.4%; however, this increased level of initial flow is considered within the tolerance of the micro porous membrane. Calcination at 300°C apparently significantly increased the initial flow, i.e.. ~87%, indicative of the layer collapse. Hydrotalcite began to release its interlayer water approaching 200°C according to TGA. Thus, the layer shrank during the calcinations; however, when the layer exposed to the initial flow testing, the layer re-expanded, causing major defects throughout the layer.

Table 4.3 Characterization of Green Layer of Hydrotalcite Deposited via Slip Casting

Sample ID	Calcination Temperature ©	Initial Flow (%)	Selectivity (He/N_2)
94-7-1/2-1	80	3.6	1.98
94-7-1/2-2	80	1.6	1.76
	200	6.4	1.83
94-7-1-1	80	1.5	1.89
	200	0.97	1.82
	300	87[1]	1.91
94-7-1-2	80	2.0	1.78

Table 4.4 Permeance of Membranes prepared via Slip Casting

Sample ID	He Permeance [$m^3/m^2/hr/bar$]	N2 Permeance [$m^3/m^2/hr/bar$]	Selectivity
HT 94-02 -1 layer	69.85	33.54	2.08
HT 94-02 -2 layer	65.54	33.74	1.90
HT 94-02 -3 layer	64.81	35.41	1.83
Control M & P 100Å	87	40	2.18

- Composition of slip, particularly binder/HT ratio.
- Particle size to form porous thin film suitable for CVD backpatching

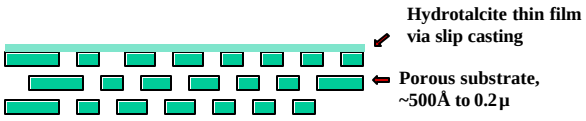

Figure 4.16 Concept on hydrotalcite membrane synthesis via slip casting.

[1] The initial flow went through a minimum, i.e., <1%, and then increased to this level throughout the measurement.

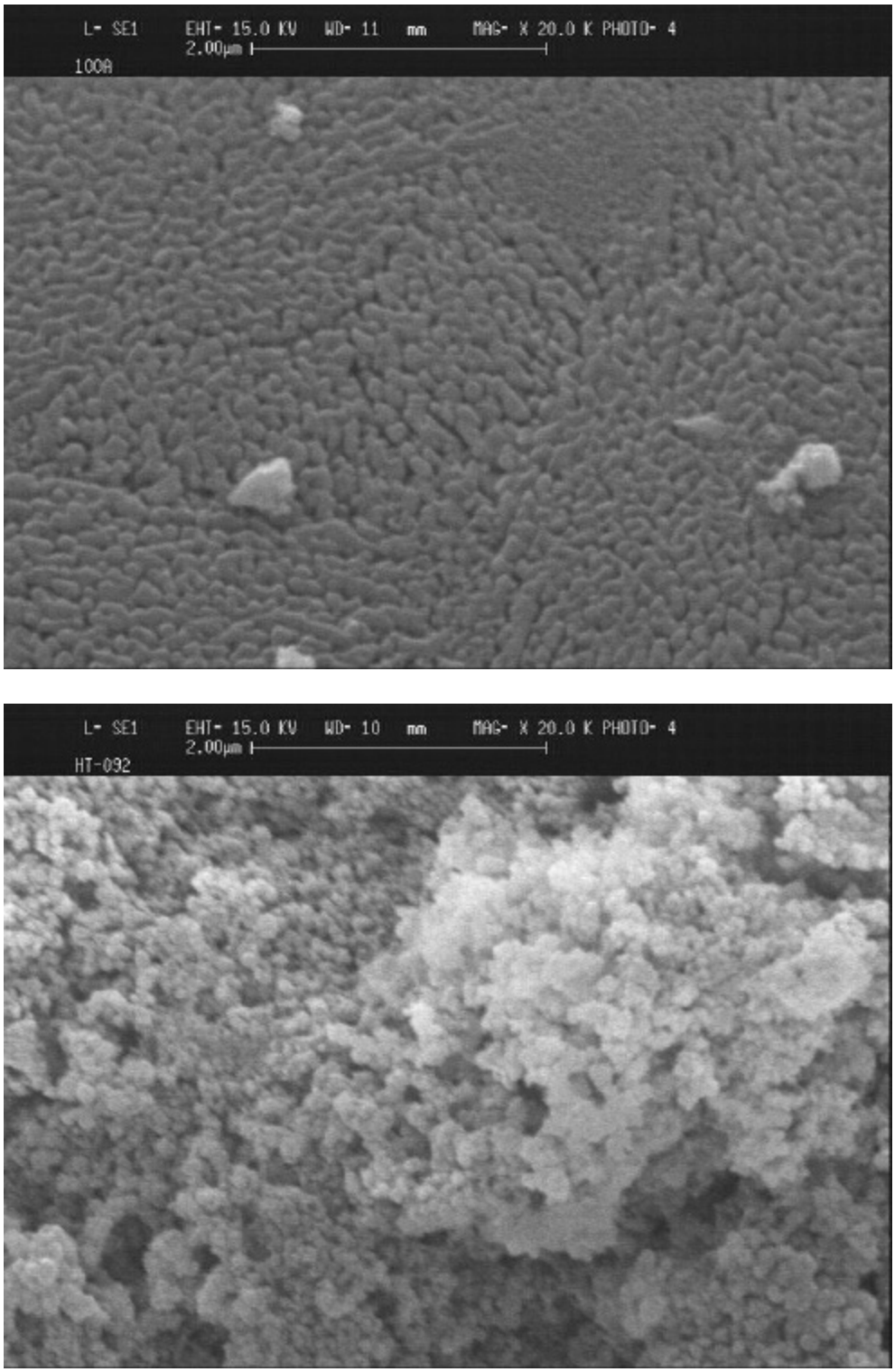

Figure 4.17 Particle size comparison between M&P's commercial ceramic membrane with 100Å pore size (top) vs hydrotalcite gel prepared by us (bottom).

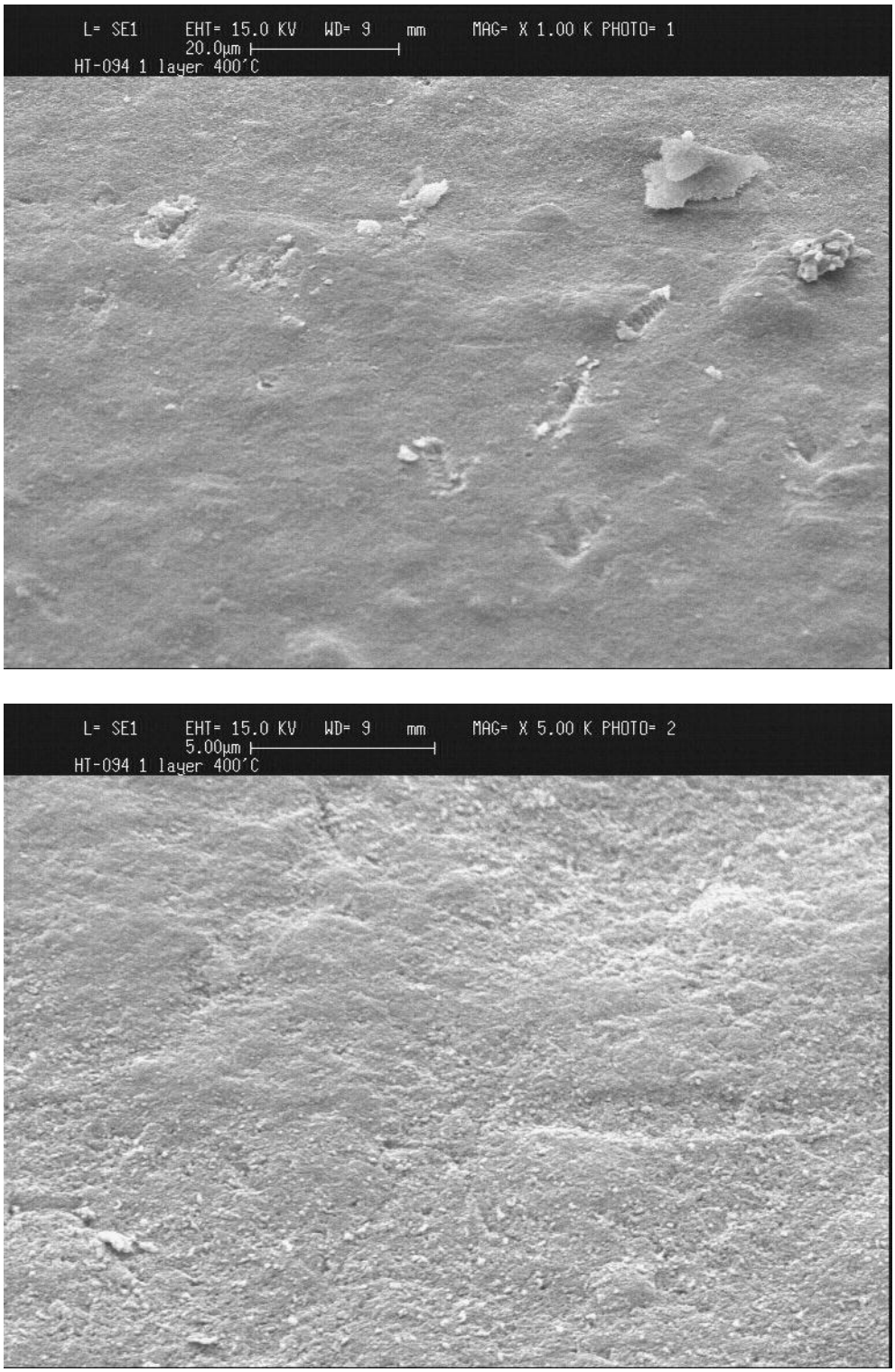

Figure 4.18 SEM photomicrograph of hydrotalcite membrane prepared from Slip casting: one layer casting and then calcined at 400ºC (Top: 1 K mag, Bottom: 5K)

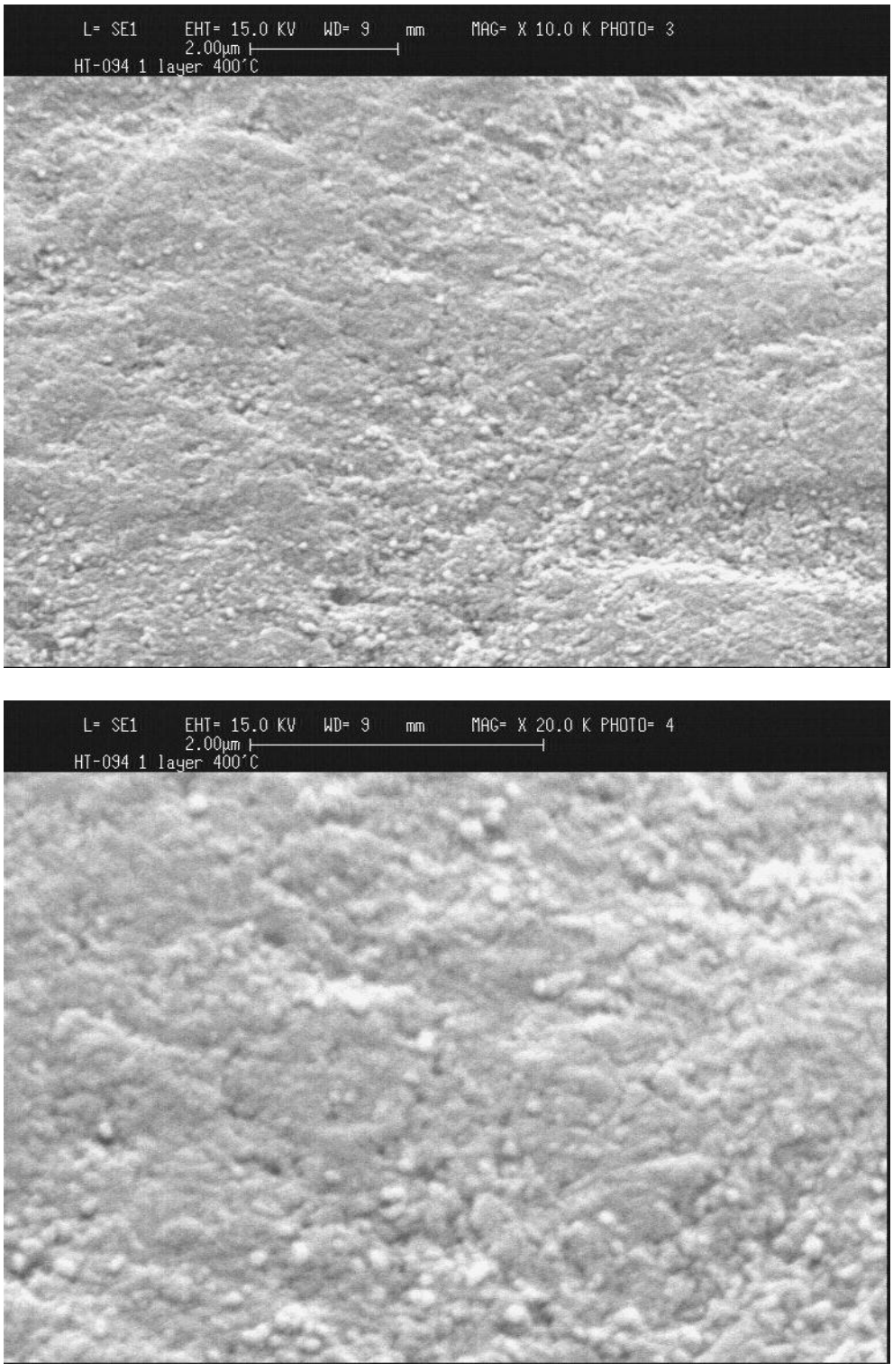

Figure 4.19 SEM photomicrograph of hydrotalcite membrane prepared from slip casting: one layer casting and then calcined at 400ºC (Top: 10 K mag, Bottom: 20K)

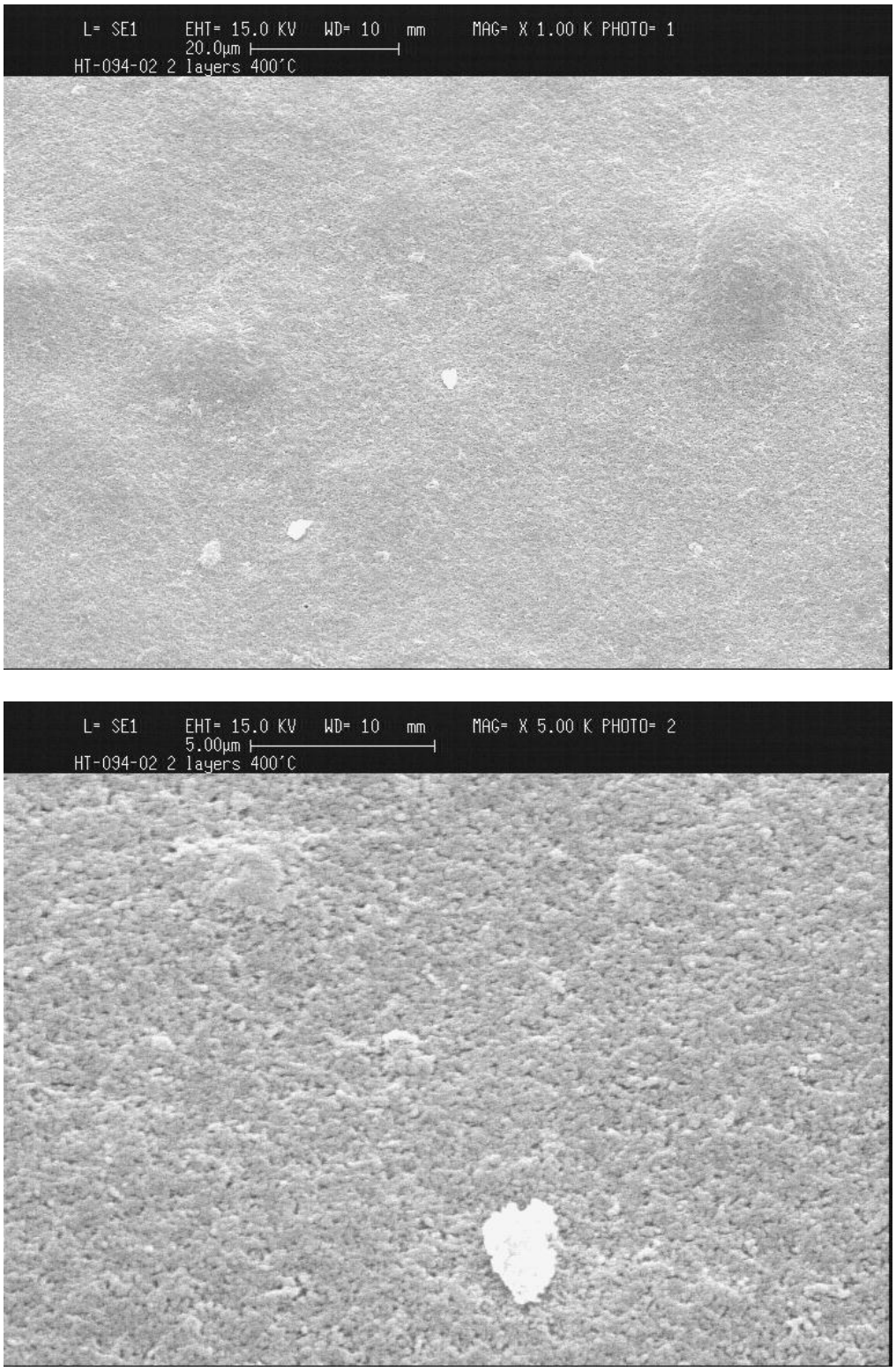

Figure 4.20 SEM photomicrograph of hydrotalcite membrane prepared from slip casting: two-layer casting and then calcined at 400ºC (Top: 1 K mag, Bottom: 5K mag)

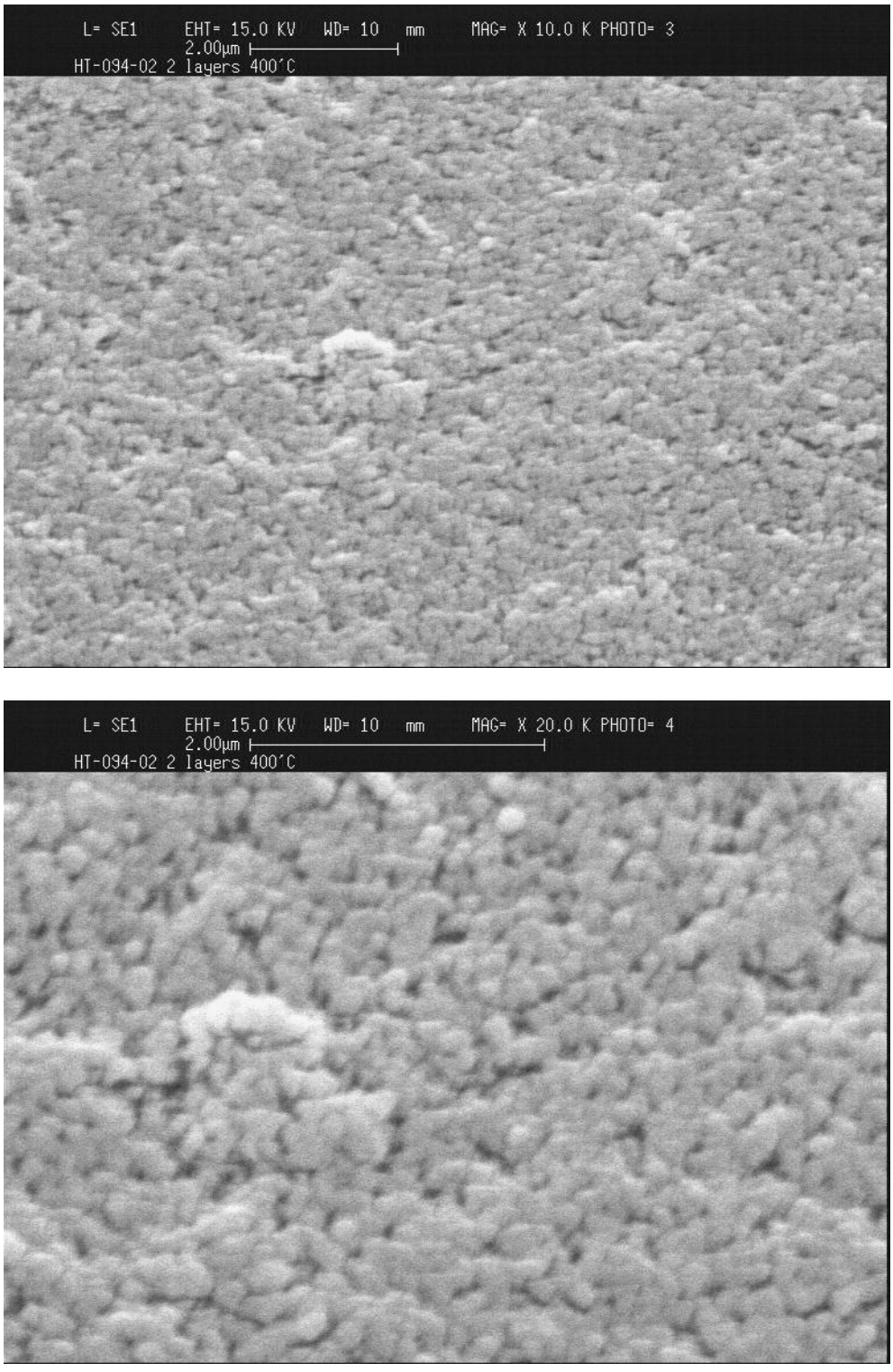

Figure 4.21 SEM photomicrograph of hydrotalcite membrane prepared from slip casting: two-layer casting and then calcined at 400ºC (Top: 10 K mag, Bottom: 20K mag)

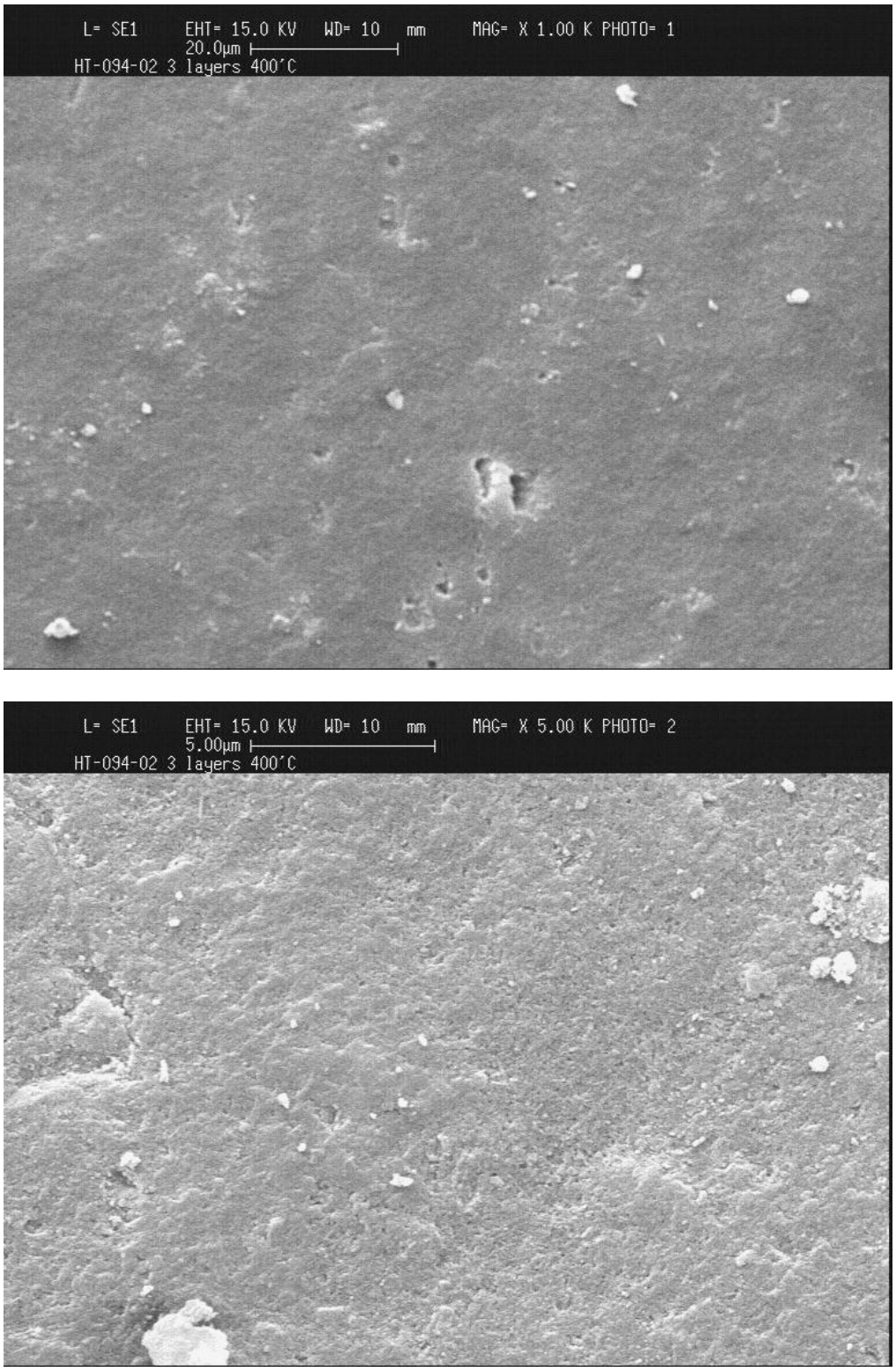

Figure 4.22 SEM photomicrograph of hydrotalcite membrane prepared from slip casting: three-layer casting and then calcined at 400ºC (Top: 1 K mag, Bottom: 5K mag)

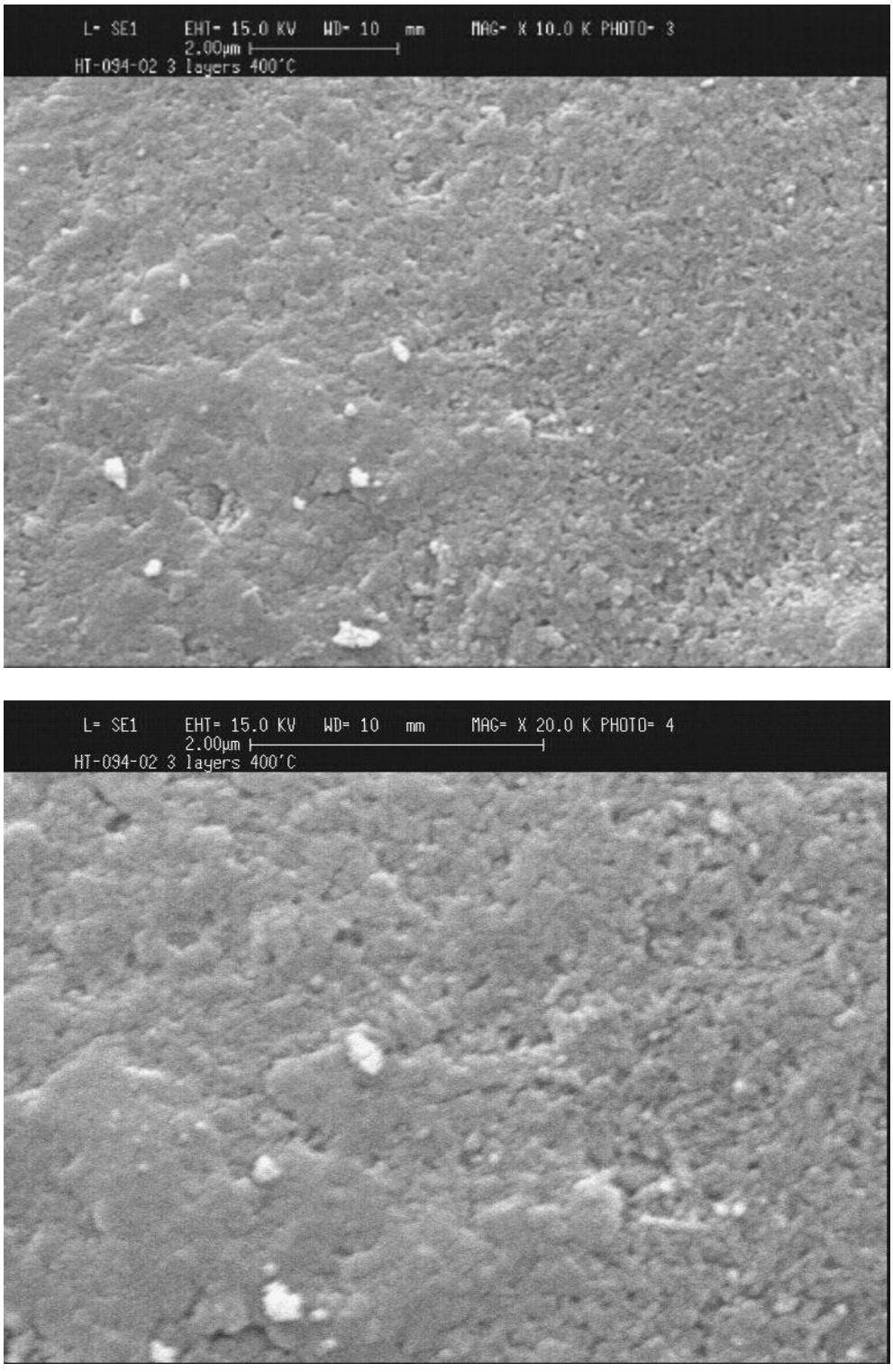

Figure 4.23 SEM photomicrograph of hydrotalcite membrane prepared from slip casting: three layer casting and then calcined at 400ºC (Top: 10 K mag, Bottom: 20K mag)

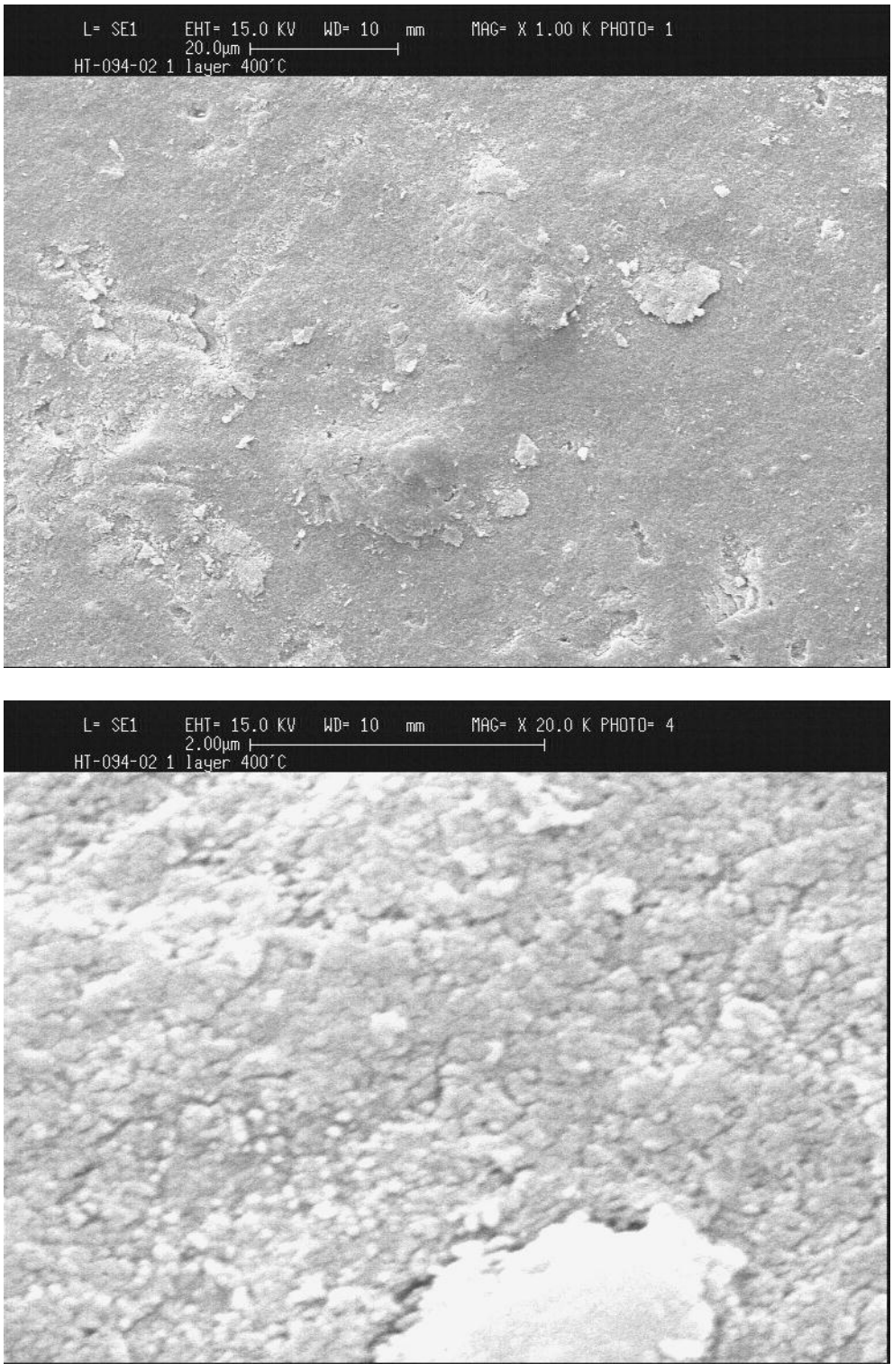

Figure 4.24 SEM photomicrograph of hydrotalcite membrane prepared from slip casting: one layer casting, calcined at 400ºC, another layer casting and calcined at 400ºC. (Top: 1 K mag, Bottom: 20K)

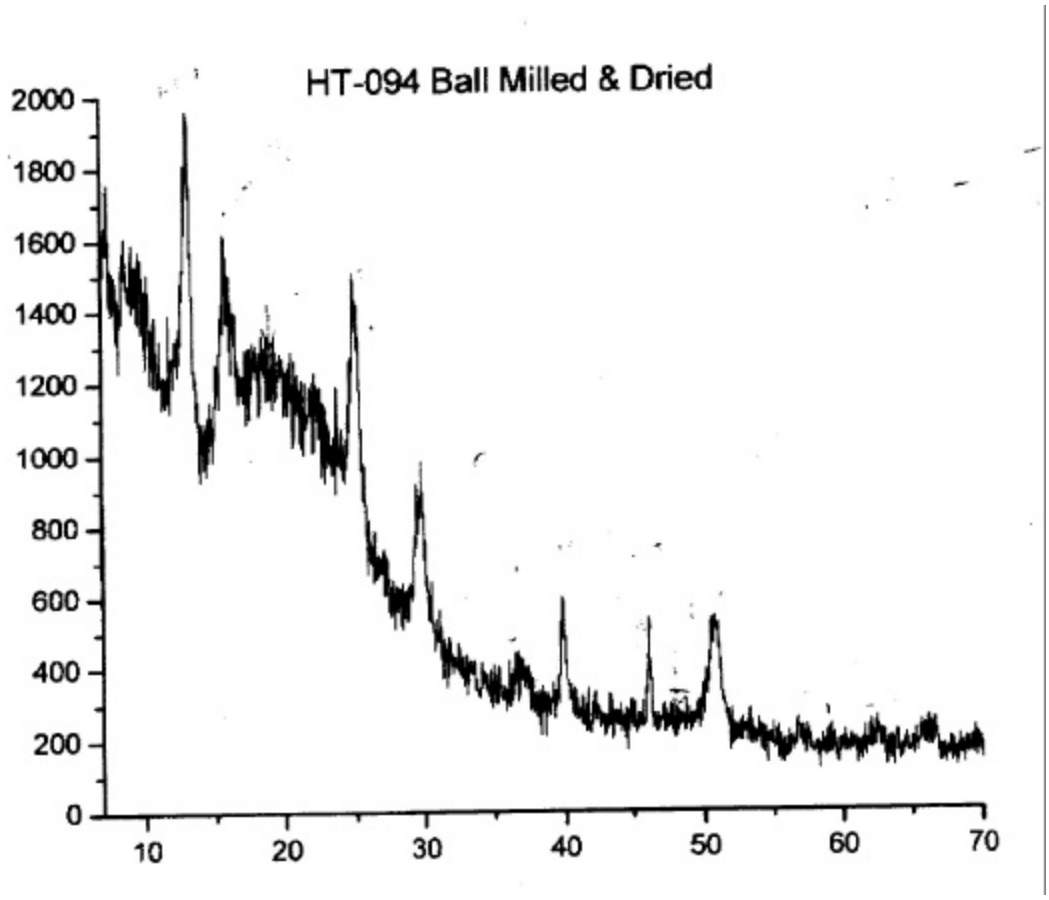

Figure 4.25 XRD of the starting materials used to prepare HT-094-7-1/2 and HT-094-7-1)

4.4 Post Treatment via Chemical Vapor Deposition

To avoid non-selective transport through voids between crystals and the base substrate, a chemical vapor deposition/infiltration (CVD/I) technique was proposed. The method has been developed and used by us in the development of our hydrogen selective membranes (SiO_2 and SiC based) [1,2]. Our past experience indicates that a thin (~1 micron) silicon-based film can be deposited on top of the 40Å membrane using tetraethylorthosilicate (TEOS) as a precursor at the temperature of 300ºC. To avoid the potential plugging of the hydrotacite opening, the deposition temperature was lowered to 200ºC based upon the TGA study of the hydrotacite material. CO_2 intercalated within hydrotalcite begin to release at the temperature of ~180ºC. It is hoped that TEOS precursor can selectively plug the residual opening at this temperature range. After the deposition, the membrane can be calcined at >200ºC to open the channel for reversible transport of CO_2. Certainly, calcination of the deposited silica layer at the temperature higher than the deposition temperature may introduce additional undesirable pore opening, which is not specific to CO_2. We do not take this factor into consideration at this moment.

4.4.1 Estimation of CO_2 Enhancement by Hydrotalcite Membrane after CVD/I

4.4.1.1 *Experimental*

- To prove the technical feasibility during this project effort, M&P's existing CVD/I technique was employed without modifications in the precursor selection and deposition condition. The precursor used is tetraethylothosilicate(TEOS), the deposition condition is 300°C. At this temperature, the TGA data obtained previously shows that part of the CO_2 transport channels are opened. However, the TEOS precursor molecule is too large to penetrate these openings in the range of 3 to 6Å. In the feasibility tests, the CVI process was stopped when the reduction in He/O_2 carrier gas permeance was negligible with time.

- Permeances of single components, including He, N_2 and CO_2, were measured at 300, 400 and 500°C to determine whether the membrane showed any affinity to CO_2. In our TEOS CVD/I based hydrogen (and helium) selective membranes, the permeance of N_2 (and CO_2) strictly results from Knudsen flow through defects in the SiO_2 infiltrated layer. Hence, a CO_2 permeance above that expected from Knudsen flow through the defects (which can be estimated from the N_2 permeance) must result from selective transport of CO_2 through the hydrotalcite crystals in the membrane.

- Enhancement of the CO_2 transport by the hydrotalcite material peaks between 300 and 400°C according to the TGA study of this hydrotalcite material. The enhancement diminishes to negligible levels as the temperature is increased much beyond 400°C, since the hydrotalcite material begins to undergo phase change to a mixed oxide at these temperatures.

4.4.1.2 *Results and Discussions*

- The CVD/I technique was demonstrated to reduce the residual pore openings of the membrane that remained following the in-situ crystallization. Table 4.6 shows that the permeance of a hydrotalcite membrane was reduced from 1.36 to 0.37 $m^3/m^2/hr/bar$ at 300°C, indicating that the selected CVD/I condition was sufficient to plug the residual pore openings following in-situ hydrotalcite crystallization.

- SEM/EDX analysis of a 500Å substrate following CVD/I shows that the silicon oxide deposition does not increase the layer thickness of the substrate membrane as evidenced by the grain structure of the top surface of the substrate shown in Figure 4.27. On the other hand, the EDX analysis shows that significant silicon deposition occurs in the first several microns inside the outer surface of the substrate. Thus, it is believed that the CVD/I technique employed here satisfies our performance requirement, specifically, penetration and plugging of the pore openings without indiscriminant deposition of an overlayer on the top of the existing substrate.

- At 300°C, the CO_2 permeance doubled as a result of the enhancement by the hydrotalcite embedded in the pores as shown in Table 4.6. The total CO_2 permeance was 0.26 $m^3/m^2/hr/bar$. It is estimated that the contribution to the CO_2 permeance from defects in the membrane is 0.14 $m^3/m^2/hr/bar$ based upon the measured nitrogen permeance and the Knudsen selectivity. Thus, 0.12 $m^3/m^2/hr/bar$ is the contribution to the CO_2 permeance due to transport of CO_2 through the CO_2 channels in the hydrotalcite crystals.

- The enhancement at 400°C is reduced to 0.02 $m^3/m^2/hr/bar$ using a similar analysis as above. The enhancement is expected to be reduced under this experimental condition, since the low partial pressure of CO_2 does not promote adsorption of the CO_2 molecule at this temperature level. In addition, most of the hydroxyl groups available for forming CO_2 via the carbonate ion may be lost so that the injection of water is also likely to be necessary to promote CO_2 permeance enhancement.

4.4.2 Post-Treatment via Chemical Vapor Deposition

4.4.2.1 *Experimental*

Two hydrotalcite membranes were CVD/Ied under this section. The first one, HT-IA-40-01 (TEOS-04) was deposited for about ~10 hours at 200ºC. A hydrotalcite membrane, HT-IA-45-01**,** prepared according to the protocol described in Sec. 4.2 (its XRD characterization shown in Figure 4.25) was CVD/I post treated. The permeances of the starting membranes at room temperature are listed below:

Sample ID	No. of In-situ Crystallization	He Permeance ($m^3/m^2/hr/bar$)	N_2 Permeance ($m^3/m^2/hr/bar$)	Selectivity (He/N_2)
HT-IA-45-01	1	10.75	4.52	2.38
HT-IA-45-01	2	2.47	0.94	2.64

The membrane selectivity of He/N_2 after the 2nd in-situ crystallization is about Knudsen selectivity, indicating the membrane likely has minimal defects and is suitable as a starting membrane for CVD/I post treatment.

4.4.2.2 *Results/Discussion*

The permeances (at room temperature) before and after deposition are listed below:

Treatment	He Permeance ($m^3/m^2/hr/bar$)	N_2 Permeance $m^3/m^2/br/bar$)	Selectivity, ideal (He/N_2)
Before CVD	9.65	3.51	2.75
After CVD	0.1380	0.024	6

The permeances of nitrogen and helium were reduced to a very low level during this extended CVD/I. The selectivity improvement was resulted from the creation of the nanopore by the deposited silica known for it permeability to He and H_2.

Since the membrane was CVD/Ied at 200ºC and then its permenance was measured at >250ºC, two factors have to be taken into consideration in data interpretation:

- Membranes treated at the temperature (i.e., 250 and 300ºC) higher than the CVD/Ied temperature (200ºC) could undergo densification of the CVD/I film, resulting in the decrease in He permeance according to our past experience.
- According to the TGA study, most free water releases at temperature <180ºC. Thus, CO_2 permeation after CVD/I takes place in the absence of water. However, if the membrane was stored in the atmosphere subsequently, the permeation could take place in the presence of water adsorbed during the storage.

The helium permeance does not follow Knudsen diffusion as expected. However, it is very obvious that CO_2 permeance is enhanced to higher than Knudsen diffusion as shown in the table. More importantly, the membrane permeance at 300ºC follows Knudsen diffusion in terms of N_2/CO_2 ratio, while the enhancement increases when the temperature decreases from 300 to 250ºC and then decreases when the temperature further decreases to 100ºC. The maximum CO_2 enhancement in the range of 200 to 300ºC is consistent with the TGA study. The unique enhancement at the temperature of 200 to 300ºC is indicative of the affinity of CO_2 by hydrotalcite. The enhancement at the low temperature could be contributed by the surface interaction of CO_2 with the metal oxide of the deposited silicon-based material. A similar study with another membrane is presented in Table 4.8, showing a similar trend. More study is required to differentiate the contribution by surface interaction vs intercalated CO_2.

To double-check this result on enhancement, this membrane was re-measured after storage for several days. The measurement started from room temperature and then went up to 300ºC. The result is presented in the same table. In general the trend of the CO_2 enhancement at the temperature 200 to 300°C is reproducible. In this case, however, the helium permeance follows Knudsen diffusion; most likely that the membrane densified as a result of moisture during storage, losing its microporosity for helium permeance. Nitrogen permeance follows Knudsen diffusion except at the low temperature of 100ºC, which results from the interaction of CO_2 and metal oxide surface to form carbonate bonds in the presence of water.

To further determine the effectiveness of CVD/I, this membrane was CVD/Ied at 300ºC for many hours, to determine the CO_2 permeance under the condition that most defects were plugged. The result is presented in Table 4.9. Evidently the permeances of all gases diminished dramatically. The helium permeance increases significantly due to the formation of micropores at this CVD/I temperature. Again, the CO_2 enhancement was evidently in the temperature range of 200ºC.

4.4.3 Effect of CVD/I Time on CO_2 Enhancement

4.4.3.1 Experimental

This membrane was CVDed for up to 40 hours at 200ºC. Its permeance was periodically checked during the deposition. Thus, we can determine the degree of CO_2 enhancement vs N_2 permeance decrease. A hydrotalcite membrane (HT-IA-47-3) was selected for this study as shown in Figure 4.26. Its residual permeance after in-situ crystallization is presented in Table 4.10. Its helium permeance increases along with the temperature, likely resulted from the release of water from the membrane during heating.

4.4.3.2 *Results and Discussion*

Table 4.11 and Figure 4.27 show the He, N_2, and CO_2 permeances as a function of the CVD/I time. The CO_2 permeance becomes higher than nitrogen permeance after 35 hours of CVD/I at 200ºC with this membrane. When the CVD/I was stopped at 40 hours, the N_2/CO_2 is ~0.8, which is much lower than the Knudsen selectivity of 1.25 at 200ºC. The permeance of this membrane was then characterized as a function of temperature from 60 to 250ºC as shown in Table 4.12. It was found that both nitrogen and CO_2 permeances increase inversely with the temperature, which is different from the membrane prepared in the previous section. We believe that in addition to CO_2 enhancement by hydrotalcite, it is possible that some surface diffusion may contribute the enhancement at the low temperature.

4.5 Conclusions

The LDH-based permselective membrane via the in-situ crystallization technique was successfully developed in this chapter. The performance of this membrane was well characterized. Key conclusions can be drawn from this study as follows:

- Combining the observations from permeance, pore size distribution, EDAX and SEM, we concluded that the hydrotalcite crystals were deposited within the pore size of the starting membranes with the pore sizes of 40Å, 500 Å, and 0.2μm. >90% gas permeance was reduced and the pore size was reduced dramatically, capable of delivering Knudsen selectivity or better. This LDH-based membrane via in-situ crystallization is suitable for post-treatment by the CVD/I technique.

- The permeance reduction and the observations under SEM both offer clear evidence that the post treatment by CVD with the protocol we developed is effective in reducing the residual permeance to a minimum. For instance, the CO_2 permeance of 0.26 $m^3/m^2/hr/bar$ at 300°C was observed for one of the membranes after the post treatment by CVD/I technique. Further, our analysis indicates that >50% of the CO_2 permeance is likely attributed to the enhancement by the LDH materials. The balance is contributed by defects remaining in the membrane.

- The ideal selectivity for CO_2/N_2 ~1.6 at 100 to 300°C was obtained for the hydrotalcite membrane prepared via in-situ crystallization and the CVD/I post treatment. In comparison with the ideal selectivity through Knudsen diffusion of 0.8, the selectivity obtained here is about double of what delivered by the Knudsen diffusion. Evidently, the enhanced selectivity is not sufficient to be commercially viable. An optimization study is necessary to reduce the defect to a minimum via the membrane synthesis; thus, minimal post treatment is required to achieve the CO_2 enhancement without sacrificing permeance significantly.

- The slip casting technology developed here successfully developed a hydrotalcite membrane with the residual pore size of <40Å while remaining most of original permeance intact, i.e., 30 to 40 $m^3/m^2/hr/bar$, which could be an ideal starting material for the post treatment with CVD/I. No post treatment study is performed for this type of the LDH membrane due to the time constraint.

In summary, the CO_2 enhancement via the LDH material was demonstrated in several experimental membranes prepared in this chapter. The two synthesis techniques and one post-treatment technique developed here successfully demonstrated the technical feasibility of the formation of the LDH-based membrane. Additional work with the focus on minimization of defects is recommended to upgrade the CO_2 selectivity and permeance for future commercial use.

Table 4.5 Chemical Vapor Infiltration as a Backpatch for Hydrotalcite Membranes

Samples	Temperature [°C]	Helium Permeance [$m^3/m^2/hr/bar$]	Nitrogen Permeance [$m^3/m^2/hr/bar$]	Experimental He/N_2 Selectivity	Theoretical He/N_2 Selectivity
Before CVD	300	1.36	0.59	2.32	2.65
After CVD	300	0.37	0.16	2.23	2.65

Table 4.6 Chemical Vapor Infiltration as a Backpatch for the Hydrotalcite Membrane. The Improvement in CO_2 Permeance due to Active Transport is shown at various. The CO_2 Permeance in the Defects is Determined Using the Nitrogen Permeance and the Knudsen Selectivity. Permeance is in $m^3/m^2/hr/bar$.

	Temp [°C]	Pres [psi]	He Perm	N_2 Perm	CO_2 Perm	CO_2 Permeance due to Defects	***CO_2 Permeance due to Enhanced Transport***
Before CVD	300		1.36	0.59	-	-	-
After CVD	300		0.37	0.16	-	-	-
Post-CVD	300	15	0.36	0.17	0.26	0.14	***0.13***
Post-CVD	400	15	0.46	0.19	0.17	0.15	***0.02***
Post-CVD	500	15	0.84	0.36	0.29	0.29	***0.00***

Table 4.7 Permeance of Hydrotalcite Membranes prepared via 1st, 2nd and 3rd In-Situ Crystalization Step using 40Å Al_2O_3 Membranes as Starting Membranes				
		Permeance (m3/m2/hr/bar)		
Sample ID	No. of Crystalization	He	N2	Selectivity
40Å, typical		~60	~30	~2
HT-IA-60-6	1st	23.34	8.93	2.61
HT-IA-40-4	1st	28.57	11.47	2.49
	2nd	13.98	6.19	2.26
HT-IA-40-5	1st	16.93	6.67	2.54
	2nd	8.75	3.19	2.74
	3rd	8.47	3.24	2.61
Knudsen, theoretical				2.65

Table 4.8 Permeance vs Temperature of Hydrotalcite Membrane after CVD: TEOS-6 (HT-45-01)							
Temperature	Permeance (m3/m2/hr/bar)			Selectivity, ideal			
	He	N2	CO2	He/N2	He/CO2	N2/CO2	CO2 Knudsen
21	0.507	0.211	0.224				
100	0.686	0.285	0.262	2.41	2.62	1.09	
200	0.713	0.279	0.273	2.56	2.61	1.02	
250	0.708	0.265	0.276	2.67	2.57	0.96	
300	0.82	0.309	0.254	2.65	3.23	1.22	
Theoretical, Knudsen Diffusion				2.65	3.32	1.25	

The membrane was CVDed at 200°C on 7/21 for 4 hrs. Then its performance was measured up to 300°C

Temperature	Permeance (m^3/m^2/hr/bar)			Effect of Temperature, (lower T/higher T)			
	He	N2	CO2	Theoretical	He	N2	CO2
301	0.82	0.309	0.254				
250	0.708	0.265	0.276	1.048	0.863	0.858	1.087
200	0.713	0.279	0.273	1.052	1.007	1.053	0.989
110	0.686	0.285	0.262	1.051	0.962	1.022	0.960
Theoretical, Knudsen Diffusion							

7/24/2003 (repeated the measurement of the above sample, water may have adsorbed during storage)

Temperature	Permeance (m^3/m^2/hr/bar)			Selectivity, ideal			
	He	N2	CO2	Theoretical	He	N2	CO2 Knudsen
110	0.898	0.377	0.382	2.38	2.35	0.99	
201	0.834	0.324	0.31	2.57	2.69	1.05	
250	0.799	0.311	0.328	2.57	2.44	0.95	
301	0.7911	0.286		2.77			
Theoretical, Knudsen Diffusion				2.65	3.32	1.25	

Temperature	Permeance (m^3/m^2/hr/bar)			Effect of Temperature, (lower T/higher T)			
	He	N2	CO2	Theoretical	He	N2	CO2 Knudsen
301	0.7911	0.286					
250	0.799	0.311	0.328	1.048	1.010	1.087	
200	0.834	0.324	0.31	1.052	1.044	1.042	0.945
110	0.898	0.377	0.382	1.065	1.077	1.164	1.232

Table 4.9	Permeance vs Temperature of Hydrotalcite Membrane after Extended CVD at 300°C: TEOS-6 (HT-45-01)						
7/28/2003	Permeance ($m^3/m^2/hr/bar$)			Selectivity, ideal			
Temperature	He	N2	CO2	He/N2	He/CO2	N2/CO2	CO2 Knudsen
106	0.0384	0.00186	0.00178	20.65	21.57	1.04	
200	0.0582	0.00117	0.0016	49.74	36.38	0.73	
Theoretical, Knudsen Diffusion				2.65	3.32	1.25	

	Permeance ($m^3/m^2/hr/bar$)			Effect of Temperature, (lower T/higher T)			
Temperature	He	N2	CO2	Theoretical	He	N2	CO2 Knudsen
200	0.0582	0.00117	0.0016	1.052			
106	0.0384	0.00186	0.00178	1.056	0.660	1.590	1.113

Table 4.10 Permeance vs Temperature of Hydrotalcite Membrane before CVD: TEOS-10 (HT)-47-3

TEOS-HT-10 (HT-47-3)

As received					2.65 (theoretical)	3.32 (theoretical)	1.25 (theoretical)
Temp ©	He ($m^3/m^2/hr/bar$)	N_2 ($m^3/m^2/hr/bar$)	CO_2 ($m^3/m^2/hr/bar$)	He/N_2	He/CO_2	N_2/CO_2	
25	2.98	1.53		1.95			
200	3.18	1.61	1.29	1.98	2.47	1.25	

Table 4.11 Permeances vs CVD Time of Hydrotalcite Membrane TEOS-HT-10 (HT-IA**-47-3)A**

8/18/2003							CO2	at 200C CVD	Cumulative		
Temp	He	N2	CO2	He/N2	He/CO2	N2/CO2	Knudsen	(hr)	CVD(hr)		
200	3.18	1.61	1.29	1.98	2.47	1.25		0	0		
200	2.67	1.08	0.897	2.47	2.98	1.20		3.2	3.2		
200	1.74	0.692	0.598	2.51	2.91	1.16		11	14.2		
200	1.14	0.417	0.385	2.73	2.96	1.08		9.3	23.5		
201	0.69	0.278	0.265	2.48	2.60	1.05		6.6	30.1		
200	0.45	0.144	0.143	3.13	3.15	1.01		5.3	35.4		
250	0.505	0.189	0.162	2.67	3.12	1.17		0	36		35.4 actual
200	0.596	0.185	0.219	3.22	2.72	0.84		0	36.5	cool down overnight	36
250	0.556	0.142	0.167	3.92	3.33	0.85		3.7	40.2	before reheating to 200C	
200	0.586	0.155	0.193	3.78	3.04	0.80		0	40.5		40.2

Table 4.12 Permeance vs Temperature of Hydrotalcite Membrane after CVD: TEOS-10 (HT-47-3)
8/27/2003

	Permeance (m3/m2/hr/bar)			Selectivity, ideal			
Temperature ©	**He**	**N2**	**CO2**	**He/N2**	**He/CO2**	**N2/CO2**	**CO2 Knudsen**
250	0.556	0.142	0.169	3.92	3.29	0.84	
200	0.5855	0.155	0.193	3.78	3.03	0.80	
150	0.578	0.156	0.2195	3.71	2.63	0.71	
100	0.566	0.166	0.255	3.41	2.22	0.65	
60	0.548	0.181	0.288	3.03	1.90	0.63	
Theoretical, Knudsen Diffusion				2.65	3.32	1.25	

	Permeance (m3/m2/hr/bar)			Effect of Temperature, (lower T/higher T)			
Temperature ©	**He**	**N2**	**CO2**	**Theoretical**	**He**	**N2**	**CO2**
250	0.556	0.142	0.169				
200	0.5855	0.155	0.193	1.052	1.053	1.092	1.142
150	0.578	0.156	0.2195	1.056	0.987	1.006	1.137
100	0.566	0.166	0.255	1.065	0.979	1.064	1.162
60	0.548	0.181	0.288	1.058	0.968	1.090	1.129

Note: Theoretical ratio is based upon Knudsen diffusion

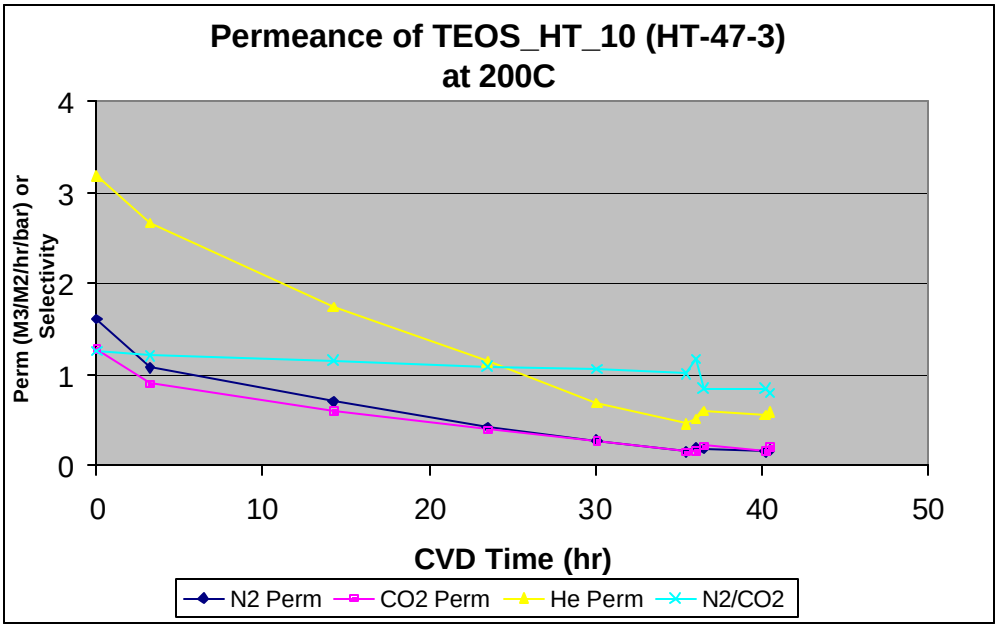

Figure 4.26 Permeance of TEOS HT 10(HT-47-3) at 200C

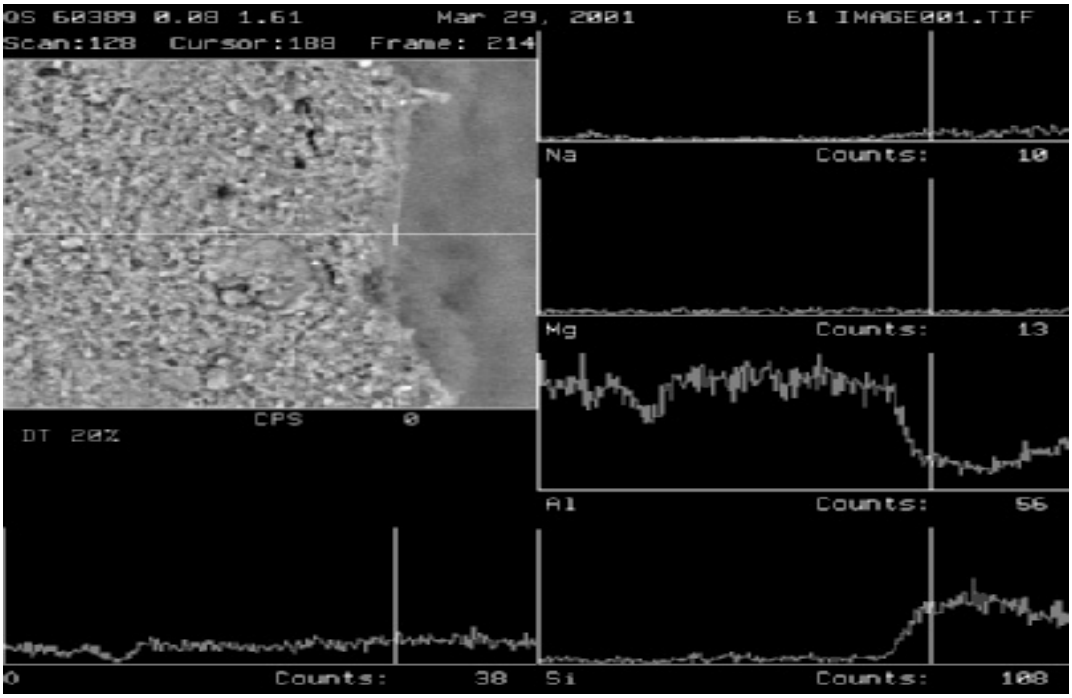

[——— Cross section ———————] [———— Cross Section ————] [—Inner—]
of 500 Å substrate of 500 Å substrate Tubular Surface

Figure 4.27 SEM Photomicrograph and EDX of the substrate after CVI. No visible layer deposition was observed from SEM. Significant SiC precursor of CVD was observed on the inner tubular surface with very limited penetration into the substrate. The results indicate the CVD/I infiltrates into the porous structure of the substrate to form an ultra-thin effective membrane.

Literature Cited

1. Wu., J.C.S., Sabol, H.K., Smith, OW., Flowers, D.F., Liu, P.K.T., J. Membrane Science,96, 275 (1994).
2. Liu, P.K.T., and Wu, J.C.S., U.S. Patent 5.415.891, May 16(1995).
3. Corning Ceramic Bulletin on Pyroceram.

Chapter 5

Development of CO_2-Affinity Membranes with Carbonaceous

5.1 Introduction/Literature Study

Two different types of CO_2-affinity membranes were explored throughout this project for the purpose of hydrogen production with concomitant CO_2 removal via water gas shift reaction. One (Type I) as discussed in Chapter 4 is based upon the LDH material which has demonstrated a unique affinity to CO_2 at a high temperature in the presence of steam. The other one (Type II), the carbonaceous microporous membrane, which exhibits surface affinity to CO_2, is discussed in this chapter. These two materials offer commercially viable separation media for implementing the membrane reactor concept (MR) for WGS reaction. In this chapter, the representative performance of the Type II membranes we prepared and characterized is presented.

A literature search was performed to review the literature available for CO_2/N_2 or CO_2/CH_4 separation at a high temperature, i.e., >100°C as an indication of the CO_2 affinity for the proposed application environment. Moon etc. [2] reported the selectivity of CO_2/N_2 of ~12 at 100°C, and then declined to ~10 at 168°C in a mixture separation environment using the membrane of methyltriethoxysilane templating silica/a-alumina composite membrane. Another study [1] using polybenzimidazole membrane exhibited the selectivity of ~50 for CO_2/CH_4 at ~300°C. Its selectivity is lower at a lower temperature. However, its permeance of CO_2 is extremely low, e.g., ~0.002 to 0.003 $m^3/m^2/hr/bar$. There are several zeolitic and other membranes published for CO_2/CH_4 separations at a lower temperature range [3,4]. In summary, there are few literature studies known to us showing membranes with CO_2 affinity at a high temperature.

In this chapter, the CO_2 permeance and selectivity of the proposed Type II membrane experimentally determined at the LTS/WGS reaction temperature, i.e., 200-250°C are presented.

5.2 Experimental

Using our commercial ceramic membranes as starting substrates, numerous CO_2-affinity carbonaceous thin film has been deposited on the inside of the tubular membrane for the proposed CO_2 sequestration application with the concomitant hydrogen production. Experimental activities involved in this type of membranes are highlighted below:

1. A series of Type II membranes (10”L) have been prepared using our commercial ceramic membranes as substrate. They are first deposited with selected polymeric precursors and then calcined at a selected temperature to form the desired pore size and surface properties. The single component gas permeation study was performed to

measure their permeances of CO_2, N_2 and others at 25, 120, 180 and sometimes 220°C.

2. The protocol developed for 10" L was employed for the preparation of the 30"L membrane to evaluate its scale up possibility. The 30"L membranes were characterized for its CO_2 and N_2 permeances at a similar temperature range.
3. One of the 10"L membranes was deposited an additional membrane layer to evaluate the potential improvement in selectivity via pore size reduction. The additional layer was prepared and characterized following a similar protocol as above.

5.3 Results and Discussion

- SEM photomicrograph was taken for the CMS membrane prepared in this chapter as shown in Figure 5.1. A very thin CMS layer was deposited on our commercial nanoporous ceramic membrane. The membrane surface appears smooth and defect free although the actual pore size is much smaller than the resolution achievable by SEM.

- Table 5.1 summarizes all the membranes prepared and characterized for this project. Their single component permeances (including He, H_2, N_2, and CO_2, and CH_4) at 23 to 220°C were presented. Then ideal selectivities were calculated. CO_2 permeance vs selectivity (over N_2) at 120°C for all the 10"L membranes is presented in Figure 5.2. In general, the overall trend for permeance vs selectivity follows the familiar inverse relationship. When the CO_2 permeance is $> 3 m^3/m^2/hr/bar$, the selectivity for CO_2/N_2 ranges from 2 to 4. On the other hand, when the CO_2 permeance is <0.5 $m^3/m^2/hr/bar$, the selectivity between 6 and 12 is obtained. In comparison with the Knudsen selectivity of 0.798, our selectivities obtained here are definitely enhanced to much beyond the Knudsen selectivity.

- Majority of the membrane tubes were prepared with a lab scale substrate, i.e., 10"L as presented in Table 5.1. Four 30" long tubes were prepared following the same protocol as the 10"L tubes. The permeance and selectivity obtained from the 30" L are in line with the trend established by the 10" tubes. Thus, the scale-up from the lab scale (10"L) to the full scale of 30"L appears acceptable.

- The permeances and selectivities at 180 to 220°C were presented in Figure 5.3. This temperature range is the usual temperature range for the LTS-WGS as we proposed. Since the data points at these temperatures were much fewer than those of the 120°C shown in Figure 5.2, the permeance vs selectivity trend was not well defined. However, the permeance and selectivity fell within the range of 0.5 to 2.5 $m^3/m^2/hr/bar$ and 4 to 8, respectively. In comparison with the data obtained at a lower temperature, i.e., 120°C, the selectivity at the higher temperature is somewhat lower than that at the lower temperature.

- Figures 5.4a to 5.4c show the effect of temperature on the CO_2 permeance from 120 to 180°C. It appears that CO_2 permeance decreases along with the temperature increase. For Figure 5.4a and 5.4b, about 50% reduction of the CO_2 permeance was

observed along with the temperature increase in this range. The CO_2 permeance reduction ratio for Figure 5.4c, however, is <<50%. The helium permeance decreases in Figure 5.4b while increases in Figure 5.4c, so is the trend for the hydrogen permeance. It is possible that the majority of the pore size in Figure 5.4a and 5.4b are larger than those in Figure 5.4c; thus, the helium and hydrogen permeances are somewhat influenced by the Knudsen diffusion in Figure 5.4b, while the helium and hydrogen permeances are dominated by activated diffusion in Figure 5.4c. Since the CO_2 permeance reduction vs temperature in Figure 5.4a and 5.4b is much more sever than the theoretical prediction based upon the Knudsen diffusion (i.e., 7%), it is concluded that the permeance for CO_2 is at least partially contributed by another mechanism, surface diffusion. When the pore size is small enough as shown in Figure 5.4c, the surface diffusion contribution decreases and the molecular sieving effect becomes emerged. Even with the pore size decreases in Figure 5.4c, no improvement in CO_2 selectivity was observed. Thus, it is believed that the separation mechanism for this type of material is contributed by both surface diffusion and molecular sieving. At the temperature range interested to us, both mechanisms are likely involved.

- Table 5.2 presents the permeance and selectivity for the membrane with an additional layer of deposition and calcination for the purpose of narrowing the pore size. The result indicated no improvement in selectivity although the permeance was reduced dramatically, from 1.88 to 0.035 $m^3/m^2/hr/bar$. This is consistent with the mechanisms proposed above. The pore size reduction theoretically could improve the selectivity although the difference in the kinetic diameters of CO_2 vs N_2 is very smaller. On the other hand, when the pore size becomes small, the surface diffusion contribution is diminished. Thus, the permeance is reduced dramatically while no clear sign of selectivity improvement is observed.

5.4 Conclusions

The Type II CO_2 affinity membranes prepared in this project demonstrated significant selectivity for CO_2/N_2, i.e., 4 to 10, up to 220°C, which was much beyond the Knudsen selectivity. Surface affinity of the membrane toward CO_2 was identified as the dominating mechanism at this operating temperature range. Selectivity at this level is comparable or higher than the selectivity of CO_2/N_2 reported in the literature at the proposed temperature reaction. Pore size reduction was attempted without any success in boosting the CO_2 affinity. Additional study including characterization of this type of membrane in a mixture environment is recommended for future development.

Literature Cited

1. Pesiri, d. R., B. Jorgensen, and R. C. Dye, "Thermal optimization of polybenzimidazole meniscus membranes for the separation f hydrogen, methane, and carbon dioxide", *J. Memb. Sci., 218*, 11(2003)
2. Moon, J. H., Y. Park, M. Kim, s. Hyun, and C. Lee, "Permeation and separation of a carbon dioxide/nitrogen mixture in a methyltrietoxysilane templating silica/alumina composite membrane", *J. Memb. Sco., 250*, 195(2005)
3. Houston, K. s., d. H. Weinkauf, f. F. Stewart, "Characterization of gas transport in selected rubbery amorphous polyphosphazene membranes", *J. Memb. Sci*., 186, 249(2001)
4. Li, s., G. Alvarado, R. d. Noble, J. L. Falconer, "Effects of impurities on CO_2/CH_4 separations through SAO-34 membranes", *J. Memb. Sci.*, 251, 59(2005).

Table 5.1 Summary of Type II CO_2 Affinity Membranes and their Performance Characterization

Sample ID	Temp [c]	Press [psi]	Permeance [$m^3/m^2/hr/bar$] He	H_2	N_2	CO_2	CH_4	Ideal Selectivity He/N_2	H_2/N_2	CO_2/N_2	N_2/CH_4
10" CO2 Affinity Membraens											
NN-01-2	**23**	30	2.051	3.846	0.748	4.011		2.7	5.1	5.4	
	120	30	1.765	4.198	0.330	2.239		5.3	12.7	6.8	
NN-02&03	**120**	20	1.231	2.816	0.080	0.846		15.3	35.1	10.6	
	180	20	1.483	3.039	0.097	0.633		15.2	31.2	6.5	
NN-06-03	**180**	20	1.203	2.753	0.140	0.730	0.098	8.6	19.6	5.2	1.4
	120	20		2.939	0.155	1.216			19.0	7.8	
NN-10-03	**120**	20	0.541	1.373	0.081	0.432	0.059	6.7	16.9	5.3	1.4
	180	20	0.585	1.227	0.064	0.254		9.1	19.1	4.0	1.4
NN-14	**120**	30	2.804	5.529	0.998	3.152		2.8	5.5	3.2	
NN-15	**120**	20	1.171	1.866	0.083	0.595	0.089	14.2	22.6	7.2	0.9
NN-47	**120**	20	3.429	7.344	0.276	1.880	0.157	12.4	26.6	6.8	1.8
NN-66	**120**	20	2.420	6.362	0.188	1.578	0.092	12.9	33.9	8.4	2.0
NN-71	**120**	20	0.707	1.804	0.037	0.418		19.2	48.9	11.3	
NN-80	**120**	20	2.868	7.464	0.494	3.585	0.523	5.8	15.1	7.3	0.9
	180	20	3.215	7.285	0.470	2.315	0.458	6.8	15.5	4.9	1.0
	120	30	2.010	4.646	0.185	1.655	0.169	10.9	25.2	9.0	1.1
NN-81	**120**	20	2.642	6.129	0.289	2.048		9.1	21.2	7.1	
NN-82	**120**	20	1.654	4.349	0.234	1.726	0.112	7.1	18.6	7.4	2.1
NN-94	**120**	20	1.819	4.250	0.335	2.110	0.355	5.4	12.7	6.3	0.9
	120	20	1.545	3.462	0.191	1.288	0.173	8.1	18.1	6.7	1.1
30" Length CO2 Affinity Membranes											
NN-27	**120**	20	1.370	3.106	0.445	2.229		3.1	7.0	5.0	
NN-29	**120**	20	1.643	4.650	0.304	1.994	0.200	5.4	15.3	6.6	1.5
	220	20	2.015	4.544	0.299	1.222	0.215	6.7	15.2	4.1	1.4
NN-30	**120**	20	0.990	2.956	0.176	1.360		5.6	16.8	7.7	
	220	20	0.879	2.082	0.103	0.821		8.5	20.1	7.9	
NN-49	**120**	20	2.136		0.632	3.354		3.4		5.3	

Figure 5.1 Synthesis of Carbonaceous CO_2- Affinity Membrane

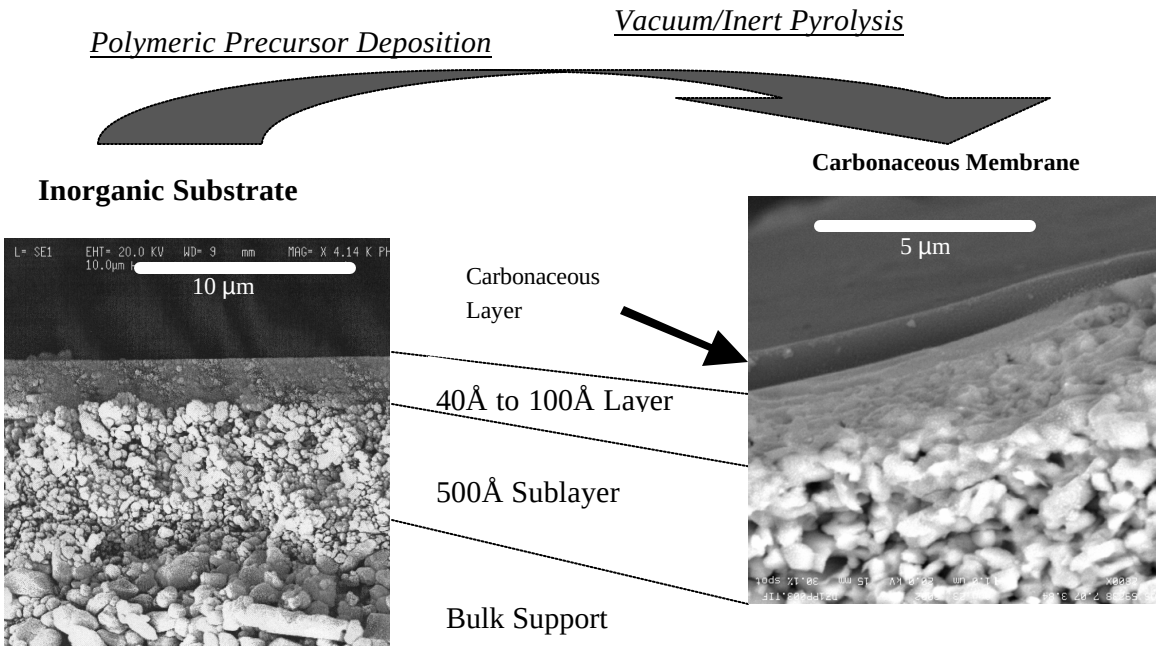

Figure 5.2

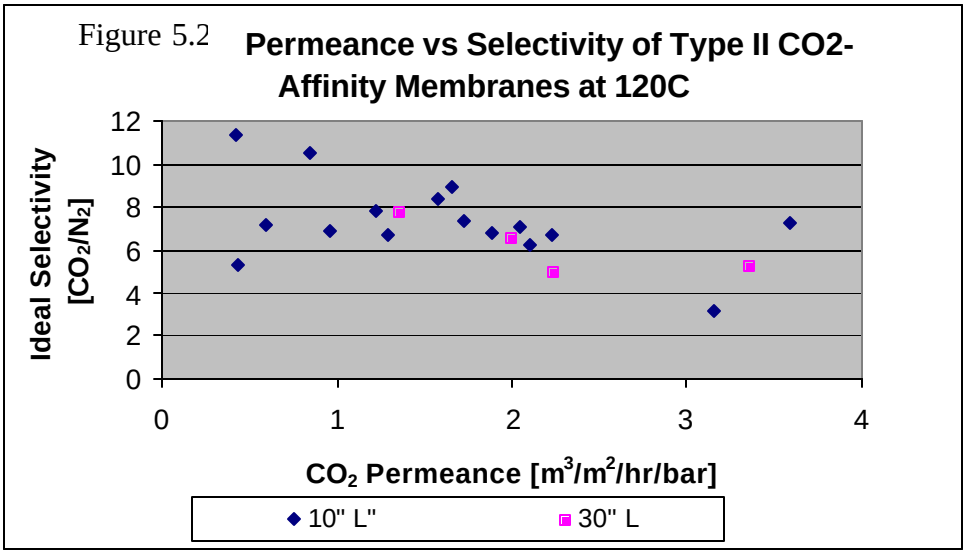

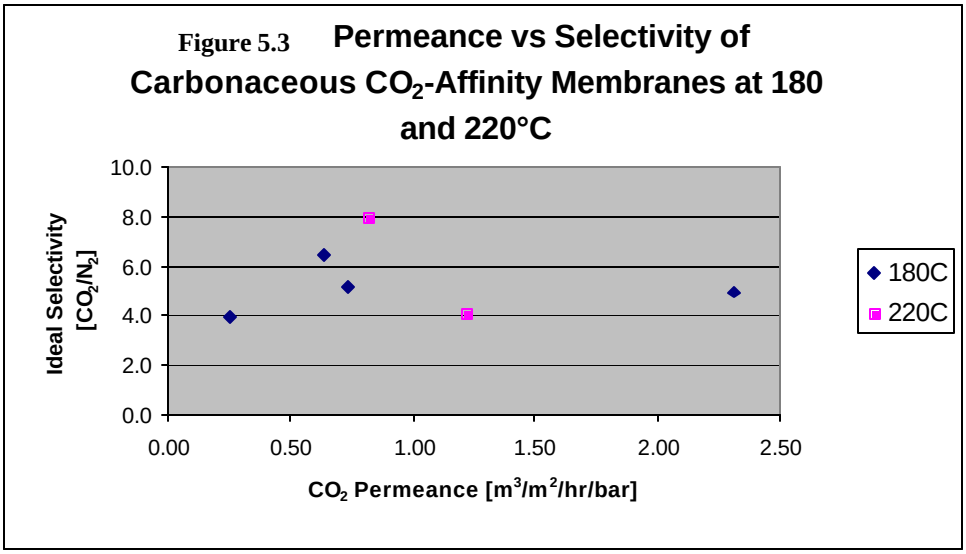
Figure 5.3 Permeance vs Selectivity of Carbonaceous CO_2-Affinity Membranes at 180 and 220°C
Ideal Selectivity [CO_2/N_2]
10.0
8.0
6.0
4.0
2.0
0.0
0.00
0.50
1.00
1.50
2.00
2.50
CO_2 Permeance [$m^3/m^2/hr/bar$]
180C
220C

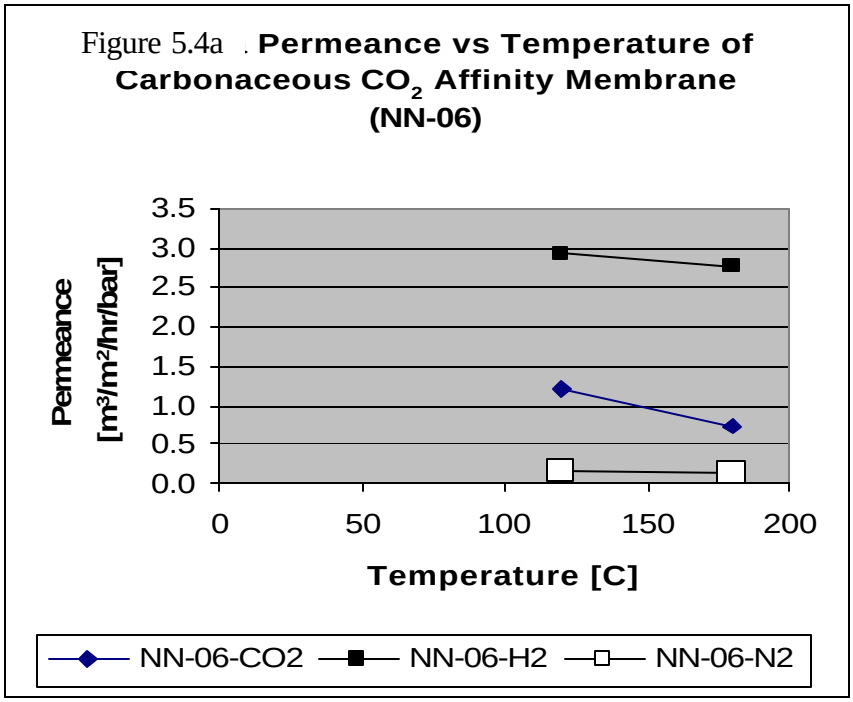
Figure 5.4a . Permeance vs Temperature of Carbonaceous CO_2 Affinity Membrane (NN-06)
Permeance [$m^3/m^2/hr/bar$]
3.5
3.0
2.5
2.0
1.5
1.0
0.5
0.0
0
50
100
150
200
Temperature [C]
NN-06-CO2
NN-06-H2
NN-06-N2

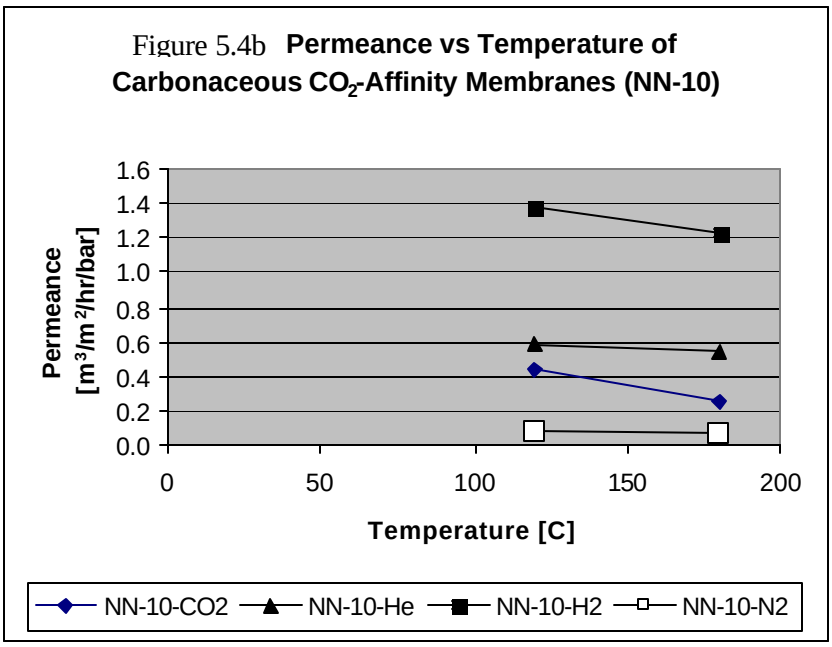

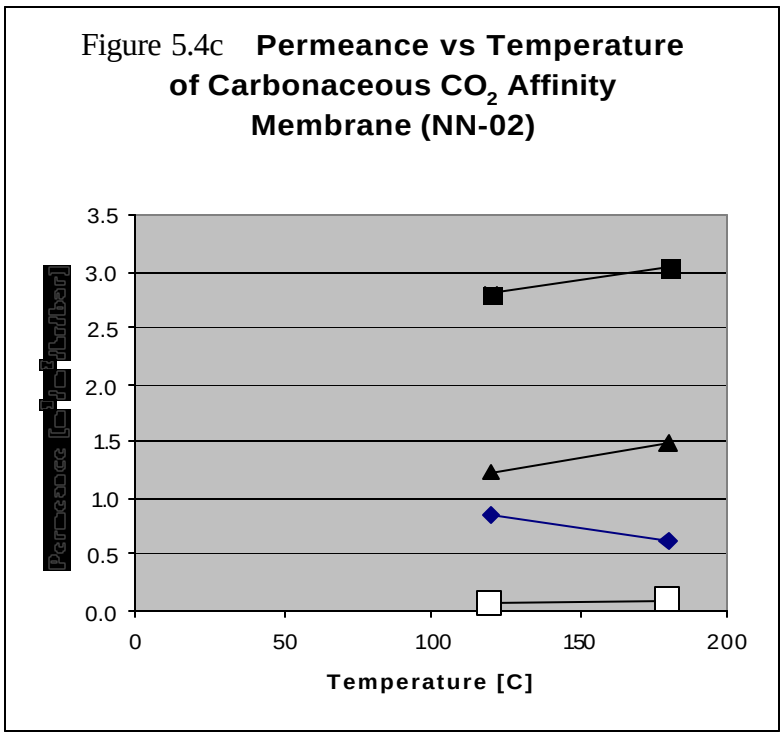

Table 5.2 Effect of Additional Layer Deposition on Performance of Type II CO_2Affinity Membrane

Sample ID	Notes	Temp [c]	Press [psi]	Permeance [$m^3/m^2/hr/bar$] He	H_2	N_2	CO_2	CH_4	He/N_2	H_2/N_2	CO_2/N_2	N_2/CH_4
NN-47		**120**	20	3.429	7.344	0.276	1.880	0.157	12.4	26.6	6.8	1.8
	additonal deposition and firing	**120**	20	0.665	0.965	0.044	0.035	0.044	15.2	22.0	0.8	1.0

Chapter 6

Diffusivity and Adsorption Isotherms of Carbon Dioxide in Mg-Al-CO_3 LDH at Elevated Temperatures

6.1 Introduction/Literature Review

In addition to its use as a membrane, the LDH material is an ideal CO_2 adsorbent for CO_2 sequestration application. The CO_2 diffusivity and adsorption capacity of the LDH material allow us to gauge its value as an adsorbent. The transport characteristics and adsorption isotherms of carbon dioxide on Mg-Al-CO_3 LDH were investigated using CO_2 uptake data measured gravimetrically in the temperature range of 200~250 ^oC, targeting the low temperature shift of water gas shift reaction. The gravimetric method for uptake rate measurements is simple and straightforward. Several research groups reported the value of CO_2 diffusivity data measured by this method at ambient temperature, as shown in Table 6.1. For the transport properties reported here, the transient CO_2 uptake data were measured gravimetrically at each elevated temperature, and then the diffusion coefficient was estimated by fitting acquired experimental data to the solution of the relevant diffusion equation. In addition to providing the experimental results, the obtained diffusivities are compared with molecular dynamic simulation results from a parallel research project. Adsorption isotherm data were also acquired by the gravimetric method, and the experimental data were fitted with the Langmuir equation and various empirical adsorption isotherm equations.

Table 6.1 Diffusivity data (D/r^2) for CO_2 measured by the gravimetric method.

Adsorbent	D/r^2, s^{-1}	Temperature, K	References
Coconut derived CMS	7×10^{-2}	273	6
Bergbau Forschung CMS	5×10^{-6}	298	7
Zr-pillared clay	8×10^{-2}	298	8
Own zeolite crystals (7.3-34 μm)	4.7×10^{-5}	500	9
LDH2 (r ~ 100 μm)	3.6×10^{-4}	473	This work

LDH2 ($r \sim 100$ µm)	8.9×10^{-4}	498	This work
LDH2 ($r \sim 100$ µm)	1.3×10^{-3}	523	This work

During the course of diffusivity and adsorption isotherm experiments, it was found that the equilibrium uptake amount of CO_2 by Mg-Al-CO_3 used in this study was dependent upon the particle size. When LDH2 was utilized for CO_2 uptake without fractionating the LDH2 particles by size, the overall equilibrium uptake amount was ~2 wt%. However, when the sieved LDH2 of the average radius of 100µm particles was used, the overall uptake of CO_2 was ~1.1 wt%. Since the only difference between above experiments was particle size of LDH2 selected, it seems that particle size of LDH affects the transport and sorption properties. The LDH particle size effect on the CO_2 adsorption capacity has not been reported in the published literature so far, but several research groups have reported about particle size effect on their adsorption experiments. For example, Badruzzaman *et al*. observed that there was a nonlinear relationship between surface diffusivity and particle radius for arsenate adsorption onto granular ferric hydroxide[2]. And, unlike the observation of Badruzzaman *et al*., Grande *et al*. reported that the adsorption capacity of propane and propylene was independent of the crystal size in their research with synthesized 4A zeolites[3].

6.2 Experimental

- Sample Preparation and Measurements for LDH2…One of Mg-Al-CO_3 LDH samples was provided by Media and Process Technology, Inc., of Pittsburgh, PA. The composition of the sample was $Mg_{0.645}Al_{0.355}(OH)_2(CO_3)_{0.178} \cdot 0.105(H_2O)$ as determined by ICP and TGA, and this was the LDH2 sample previously studied in Chapter 3 for sorption reversibility. Prior to the diffusivity and adsorption isotherm experiments the LDH2 sample was sieved, and only particles radii within the range 90~105 µm were retained. For CO_2 uptake measurement, 100-120 mg of a freshly sieved LDH2 sample was utilized for each diffusivity and isotherm experiments. UHP dry CO_2 and UHP dry argon gas mixtures were prepared with Brooks 5850E mass flow controllers and sorption data were recorded by a Cahn TGA 121 instrument. The LDH sample was spread out at room temperature, as thinly as possible, on a bowl-shape quartz container in order to minimize external mass transfer resistance. The sample was then heated to a preset temperature in UHP dry argon (at a flow rate of 30 mL/min) with a heating rate of 5°C/min. Ar was utilized as a purge gas in order to minimize the buoyancy force effect when the purge gas was switched to dry CO_2. The temperature of experiments was selected between 200 and 250°C since (i) the interlayer water of LDH can be removed without significant transformation of LDH structure in this range as outlined in Chapter 2, and, (ii) based on the results of preliminary experiments at temperatures less than 190 °C, there was no significant uptake of CO_2 in LDH2. When the temperature reached the preset point, the sorption system was kept at the same temperature for 70 min to stabilize the TGA

microbalance. Only after the microbalance showed less than 10μg change, the purge gas was then switched to carbon dioxide with the flow rate of 30 ml/min. However, for the adsorption isotherm experiments, the purge gas was switched to an argon and CO_2 gas mixture with preset compositions instead of pure CO_2.

- Sample Preparation and Measurements for LDH3… The other LDH sample (LDH3) was synthesized by the typical co-precipitation reaction from aqueous solution[4-5] to investigate the particle size effect, and its chemical composition was $Mg_{0.743}Al_{0.257}(OH)_2(CO_3)_{0.129}{\cdot}0.098(H_2O)$ as determined by ICP-MS and TGA. LDH3 was fractionated to 6 different particle sizes using Fisher Scientific U.S. Standard test sieves, for which mesh sieve designations were 325, 230, 200, 170, 120, 80, and 70 (corresponding nominal sieve opening is 43, 63, 75, 90, 125, 180, and 212 μm respectively). For each sieved LDH3 sample with a given particle size, diffusivity and adsorption isotherm experiments for CO_2 were conducted at 200°C with the same manner as described for LDH2 previously. The surface area of each sieved LDH3 was determined by a Micrometrics ASAP 2010 BET instrument based upon the BET method at liquid nitrogen temperature; the micropore volume of LDH3 was also determined by the same instrument using the Horvath-Kawazoe method.

6.3 Results and Discussion

- Mathematical Model for Diffusity Measurement… To estimate the diffusion constant of CO_2 in LDH2, Crank's model for diffusion into a spherical particle was used[10]. According to this model, the governing equation for the concentration C of a species diffusing into a homogeneous spherical particle of radius r is given as:

$$\frac{\partial C}{\partial t} = D\left(\frac{\partial^2 C}{\partial r^2} + \frac{2}{r}\frac{\partial C}{\partial r}\right) \quad (1)$$

where D is the diffusivity constant.
From the solution of Eqn. (1), the uptake M_t at time t is given by:

$$\frac{M_t}{M_\infty} = 1 - \frac{6}{p^2}\sum_{n=1}^{\infty}\frac{1}{n^2}\exp\left(-n^2 \cdot p^2 \cdot \frac{D}{r^2}\cdot t\right) \quad (2)$$

where $M_¥$ is the uptake at large times (equilibrium).
For small times ($M_t/M_¥ < 0.25$) Eqn. (2) is approximated as:

$$\frac{M_t}{M_\infty} = \frac{6D^{1/2}t^{1/2}}{p^{1/2}r} \quad (3)$$

Therefore, if Eqn. (3) applies, the plot of $M_t/M_¥$ versus $t^{1/2}$ should give a linear relationship, with a slope of $6D^{1/2}/p^{1/2}r$. However, as shown in Figure 6.1a, Figure 6.2a, and Figure 6.3a, the results do not match linear plots. The short-time nonlinear behavior implies the existence of a crystalline structure in LDH2 particles. Actually, it was also reported by Ruthven that the linearity of $M_t/M_¥$ against $t^{1/2}$ is destroyed for some crystalline materials, but the reasons were not provided[11].

Since nonlinear behavior in the short time region was not observed, the long time region was selected for the diffusivity constant calculations. For long times (M_t/M_∞ > 0.5) the higher-order terms in Eqn. (2) become negligible so that the expression simplifies to:

$$\frac{M_t}{M_\infty} = 1 - \frac{6}{p^2}\exp(-p^2 D \cdot t / r^2) \qquad (4)$$

Therefore, a plot of $\ln(1 - M_t/M_\infty)$ versus t is linear with a slope of $-p^2D/r^2$ and intercept of $\ln(6/p^2)$. In this region, fairly good linearity is observed with the experimental data at all three temperatures as shown in Figures 4.1b, 4.2b, and 4.3b.

Table 6.2 Diffusivity constants measured by experiment and calculated by molecular dynamic simulation.

Temperature, ^oC	by molecular dynamic simulation, cm^2/s	by experiment, cm^2/s
200	3.23×10^{-7}	3.61×10^{-8}
225	4.84×10^{-7}	8.90×10^{-8}
250	5.78×10^{-7}	1.33×10^{-7}

Table 6.3 Langmuir adsorption parameters of CO_2 in LDH2.

Temperature, ^oC	m_{CO_2}, mmol/g sample	b_{CO_2}, bar^{-1}
200	0.27904	15.6125
225	0.26136	17.8243
250	0.24189	22.1608

- Diffusivities Determination…The diffusion constants for CO_2 in LDH were estimated from the slopes of the plots at long times at each elevated temperature, and the results were summarized in Table 6.2. According to Ruthven, the linearity in the long time region implies that the distribution of the crystal size of LDH is not significantly wide[11]. As a parallel study, diffusion coefficients were also calculated by molecular dynamic simulations at each temperature[12]; it can be observed that the resulting values from molecular dynamic simulation are in good qualitative agreement with experiments, as shown in Table 6.2. The temperature dependence of diffusivity constant for CO_2 is shown in Figure 6.4, and the activation energy of diffusion was calculated as 52.86 kJ/mol (12.64 kcal/mol) by the Arrehnius equation.

- Adsorption Isotherms…To analyze the adsorption isotherm data, firstly the experimental data were fitted with the Langmuir equation. The Langmuir theory is based on a kinetic principle, by which the rate of adsorption is equal to the rate of desorption from the surface [16]. The Langmuir model for CO_2 adsorption isotherm can be written as

$$q_{CO_2} = \frac{m_{CO_2} b_{CO_2} P_{CO_2}}{1 + b_{CO_2} P_{CO_2}}$$

where q_{CO_2} is the equilibrium concentration of adsorbed CO_2, m_{CO_2} is the Langmuir model constant for CO_2, b_{CO_2} is the Langmuir model constant for CO_2, and P_{CO_2} is partial pressure of gas phase CO_2. The experimental data and the fitted curves are shown in Figure 6.5, and the values of parameters in Langmuir model are summarized in Table 6.3. The Langmuir constant b_{CO_2} is also called the affinity constant since it represents how strong the molecule is adsorbed onto an adsorbent surface. And the temperature dependence of b_{CO_2} can be written as

$$b_{CO_2} = b_\infty \exp(Q / R_g T)$$

where Q is the heat of adsorption ($-DH_{ad}$) and is same as the activation energy for desorption, and R_g is ideal gas constant (8.314 J/mole·K). The heat of adsorption (Q) of LDH2 was estimated as -2.8739 kJ/mol from the slope of a linear plot of $\ln b_{CO_2}$ versus $1/T$, of which the negative value means that the process is endothermic.

Normally, the affinity constant decreases with the temperature increase since the heat of adsorption is usually positive, which adsorption is an exothermic process. For the adsorption to occur the free energy must decrease and the entropy change is also negative since the degree of freedom decreases. Therefore, the enthalpy change must be negative, and it means the heat is released from the adsorption process. However, it was observed that the value of b_{CO_2} increased with temperature, and consequently the calculated value of the heat of adsorption is negative. It implies that the adsorption isotherm with LDH2 is chemisorption rather than physisorption, and to understand the adsorption isotherm of LDH2 better, the acquired data need to be analyzed with different models as well.

One of the earliest empirical equations used to describe isotherm is the Freundlich equation [17]. The equation for CO_2 adsorption may be the following form:

$$q_{CO_2} = KP^{1/n}$$

where q_{CO_2} is the concentration of the adsorbed CO_2, K and n is the parameter of the Freundlich equation. The parameter K and n are generally temperature-dependent. To find the parameters of the Freundlich equation, the data are usually plotted in $\log_{10}(q_{CO_2})$ versus $\log_{10}(P)$, which yields a straight line with a slope of $(1/n)$ and as intercept of $\log_{10}(K)$.

$$\log_{10}(q_{CO_2}) = \log_{10}(K) + \frac{1}{n}\log_{10}(P)$$

Since the Freundlich equation does not have a Henry law behavior in the low pressure, and since it does not have a finite limit in high pressure, the Freundlich equation is only valid in a narrow range of adsorption data. The selection of data is also arbitrary, and here the first five data points were chosen at each temperature. The calculated parameter values of Freundlich equation were summarized in Table 6.4, and the experimental data with linear fitting were shown in Figure 6.6. From the fitting data shown in Figure 6.6, it was observed that the parameter *K* decreases with temperature, but the parameter *n* increases. Since the temperature dependence of parameters of *K* and *n* is complex, and also since it may be incorrect outside of the range of validity, the trend of parameter *K* and *n* of the Freundlich equation have to be regarded as specific case. For example, Rudzinski and Everett also reported that the 1/*n* value is proportional to temperature with the system of CO adsorption on charcoal, but it was taken as a specific trend rather than general one [18].

Table 6.4 Values of parameters of the Freundlich equation for CO_2 adsorption in LDH2.

Temperature, ^oC	*K*	*n*
200	0.5573	1.8842
225	0.4990	2.0544
250	0.4084	2.5003

Table 6.5 The Langmuir-Freundlich equation parameters for CO_2 in LDH2.

Temperature, ^oC	m_{CO_2}, mmol/g sample	b_{CO_2}, bar^{-1}	*n*
200	0.25677	16.8464	0.69837
225	0.24339	18.6860	0.72111
250	0.23116	22.3253	0.79789

Similar to the Langmuir equation (but with additional parameter *n*) with a finite limit at sufficiently high pressures, Sips proposed the Langmuir-Freundlich equation[19] written as:

$$q_{CO_2} = m_{CO_2} \frac{(b_{CO_2} P)^{1/n}}{1+(b_{CO_2} P)^{1/n}}$$

When the parameter of *n* is unity, the equation becomes the Langmuir model, which is applicable for ideal surfaces. Therefore, the parameter *n* is usually regarded as the parameter characterizing the system heterogeneity. The larger is the parameter of *n*,

the higher is the degree of heterogeneity, but the source of heterogeneity is not provided with this parameter. The heterogeneity could be caused by the solid structural properties, the solid energetic properties, the sorbate properties, or the combination of these. The experimental data and fitted curves with the Langmuir-Freundlich equation are shown in Figure 6.7. And the values of the parameters in the Langmuir-Freundlich model are summarized in Table 6.5. From Table 6.5, it is observed that the value of parameter n increases with temperature, and hence the system becomes apparently more heterogeneous as temperature increases.

The temperature dependence of b_{CO_2} and exponent n may take the following form [17]:

$$b_{CO_2} = b_\infty \exp(Q / R_g T) = b_0 \exp[\frac{Q}{R_g T_0}(\frac{T_0}{T} - 1)]$$

$$\frac{1}{n} = \frac{1}{n_0} + a\,(1 - \frac{T_0}{T})$$

where b_∞ is the adsorption affinity constant at infinite temperature, b_0 is the adsorption affinity at reference temperature T_0, n_0 is the parameter n at the same temperature and α is a constant parameter. In the Langmuir equation Q is the heat of adsorption and is not changed by the surface loading. However, in the Langmuir-Freundlich equation, the parameter Q is only a measure of the adsorption heat. Only when the fractional loading is equal to one half, Q is equal to the isosteric heat. Therefore, the parameter Q in Langmuir-Freundlich equation means the isosteric heat at the fractional loading of 0.5.

Though Langmuir-Freundlich equation provides some sense of the system heterogeneity, it does not possess the correct Henry law behavior. The Freundlich equation is not valid at high and low end of the pressure range. To satisfy the both end limits, Toth proposed the empirical adsorption isotherm equation, and the Toth equation describes well the system with sub-monolayer coverage [20, 21]. The Toth equation for the CO_2 adsorption may be written as:

$$q_{CO_2} = m_{CO_2} \frac{bP}{[1 + (bP)^t]^{1/t}}$$

where t is a parameter, which t and b are specific for adsorbate-adsorbent pairs. When t is equal to 1, the Toth isotherm equation reduces to the Langmuir equation. Therefore, like the Langmuir-Freundlich equation, the parameter t can be regarded as the measure of the system heterogeneity. The experimental data and fitted curves are shown in Figure 6.8, and the values of the parameters in the Toth model are summarized in Table 6.6. It is observed that the values of the parameter t are greater than unity, which indicates a strong degree of heterogeneity of the system.

Table 6.6 The Toth equation parameters for CO_2 in LDH2.

Temperature, ^oC	m_{CO_2}, mmol/g sample	b_{CO_2}, bar^{-1}	t
200	0.25218	10.19558	1.80226
225	0.24019	11.86695	1.64989
250	0.22934	15.97911	1.38246

Table 6.7 The exponential equation parameters for CO_2 in LDH2.

Temperature, ^oC	q_{CO_2}, mmol/g	b, bar^{-1}
200	0.2455	11.9684
225	0.2318	13.2177
250	0.2175	15.8356

Although it is not widely used as other empirical equations, the exponential equation is also a useful empirical equation. The exponential equation for the CO_2 adsorption isotherm can be written as

$$q_{CO_2} = q_S(1 - e^{-bt})$$

$$b = b_\infty \exp(Q / R_g T)$$

where q_{CO_2} is equilibrium concentration of adsorbed CO_2, q_S is saturation concentration, and b_∞ is the affinity at infinite temperature. At low pressure the exponential equation reduces to Henry's law, and at high pressure the equation reaches the saturation limit. The experimental data and nonlinear fitting curves are shown in Figure 6.9, and the values of parameters in the exponential model are summarized in Table 6.7. It is observed that q_{CO_2} is decreased as temperature increases, but *b* is increased as temperature increases like previous models.

For the empirical equations described, so far, the adsorption mechanism is assumed to be surface layering (formation of successive layers). However, for microporous solids, another important adsorption mechanism is pore filling, which was originally developed by Dubinin [22-25]. Also, according to the suggestion of Bering *et al.* [27, 28], the adsorption in pores less than 15Å should follow the pore filling mechanism rather than surface coverage. For the description of adsorption isotherm in microporous solids with pore filling mechanism, a widely used semi-empirical equation is the Dubinin-Radushkevich (DR) equation, which may be written as:

$$C = C_s \exp\left[-\frac{1}{E^2}(R_g T \ln\frac{P}{P_0})^2\right]$$

where C is the amount adsorbed, C_s is maximum adsorption capacity, E is characteristic energy, R_g is ideal gas constant. The increase of characteristic energy means the adsorption is stronger since the solid has stronger energy of interaction with adsorbate. To find the values of characteristic energy E, the adsorption data of different temperatures were plotted as the logarithm of the fractional loading versus the square of logarithm of reduced pressure. From the slopes of the linear fit, the values of E were calculated. The experimental data and linear fit are shown in Figure 6.10, and the summary of results is shown in Table 6.8. It is observed that the characteristic energy increased as the temperature increased, and, therefore, it implies that the interaction between LDH and CO_2 also increases as temperature increases.

Table 6.8 The characteristic energies for CO_2 in LDH2 with DR equation.

Temperature, ^oC	E, kJ/mol
200	12.350
225	13.677
250	15.782

Table 6.9 The uptake amount and BET surface area of LDH3 particles.

Particle radius [μm]	Uptake [mmol/g]	BET surface area [m^2/g]	Normalized uptake [mmol/m^2]
26.5	0.64545	36.2732	0.01779
34.5	0.57727	32.9144	0.01754
43.75	0.53500	30.8792	0.01733
53.75	0.49318	30.0916	0.01639
76.25	0.45227	25.4140	0.01780
98.75	0.43636	21.8627	0.01996

- Effect of Particle Size…It was observed that at the temperature of 200°C the uptake amount of CO_2 in LDH3 decreases as the particle radius increases (Figure 6.11), and it may be explained with surface area of LDH3 particles as shown in Table 6.9. According to Table 6.9, it is evident that the surface area of LDH3 particle decreases when the particle radius increases. And, when the uptake amount was normalized with corresponding surface area, it is found that the uptake amount is fairly constant all over the range of particle size.

Table 6.10 The Langmuir adsorption parameters of CO_2 in LDH3 at 200°C with different particle size.

Particle radius, μm	m_{CO_2}, mmol/g sample	b_{CO_2}, bar^{-1}
26.5	0.75129	10.5694
34.5	0.65995	11.6985
43.75	0.56710	10.6203
53.75	0.52253	11.0997
76.25	0.51523	13.2044
98.75	0.43705	13.6583

The experimental data and the fitted curves with the Langmuir equation are shown in Figure 6.12, and the values of parameters are summarized in Table 6.10. According to Table 6.10 and Figure 6.12(b), it is evident that Langmuir parameter b_{CO_2} is relatively constant over the range of particle sizes. The b_{CO_2} value obtained here is close to the one obtained from Langmuir equation with LDH2 at 200°C in Table 6.5. The experimental data were also studied with Langmuir-Freundlich equation since

Table 6.11 The Langmuir-Freundlich equation parameters of CO_2 in LDH3 at 200°C with different particle size.

Particle radius, μm	m_{CO_2}, mmol/g sample	b_{CO_2}, bar^{-1}	n
26.5	0.68824	12.33558	0.76988
34.5	0.6578	11.77357	0.79127
43.75	0.53429	11.85758	0.74523
53.75	0.48755	12.55263	0.71473
76.25	0.47115	12.96453	0.72593
98.75	0.41754	13.05532	0.74152

Langmuir-Freundlich equation provides more information and since the experimental data were better fitted with this equation than others. The nonlinear fitting curves are shown in Figure 6.15, and the values of parameters are summarized in Table 6.11. It was observed that the parameter values of b_{CO_2} and n are not changing significantly,

and hence it implies that the interaction between CO_2 and LDH3 does not change significantly with particle size, and that the heterogeneity of system is not changing, either.

6.4 Conclusions

Based upon the rate and equilibrium capacity measurement for the LDH materials, key conclusions are drawn here:

- Diffusivity constants and adsorption isotherms for carbon dioxide in Mg-Al-CO_3 LDH2 at 200 - 250°C were determined by the gravimetric method. Diffusivity constants determined by experiments and those obtained by molecular dynamic simulations are in good qualitative agreement.

- The experimental adsorption isotherms for CO_2 in LDH2 have been studied with the Langmuir isotherm equation and various empirical adsorption isotherm equations. It was observed that the heterogeneity of the material and the interaction between CO_2 and LDH2 increases with temperature. Also it was found that the experimental data were nonlinearly fitted best with the Toth equation based on χ^2 values.

- For the study of particle size effect on CO_2 uptake and adsorption isotherm experiments, it was observed that the amount of CO_2 uptake, and the BET surface area increased as the particle size decreased. When the uptake amount was normalized with BET surface area, it was found that the uptake amount was fairly constant for all the ranges of particle sizes. The adsorption isotherm data with different particle sizes of LDH3 were studied with Langmuir isotherm and Langmuir-Freundlich equation. It was observed that the values of b_{CO_2} and n were relatively constant for the whole range of particle sizes.

The parameters and the best fitted equation obtained in this chapter were used for simulating the CO_2 removal via an LDH adsorbents in an innovative membrane reactor as presented in Chapter 7.

Literature Cited

1. Callaghan, P. T. *Principles of NMR Microscopy*, Clarendon Press, Oxford, 1991.
2. Badruzzaman, M; Westerhoff, P; Knappe, D. R. U. Intraparticle diffusion and adsorption of arsenate onto granular ferric hydroxide., *Water Research*, **2004**, *38*, 4002-4012.
3. Grande, C. A.; Basaldella, E.; Rodrigues, A. E. Crystal size effect in vacuum pressure-swing adsorption for propane/propylene separation., *Ind. Eng. Chem. Res.*, **2004**, *43*, 7557-7565.
4. Miyata, S. The syntheses of hydrotalcite-like compounds and their structures and physico-chemical properties I. The systems magnesium(2+)-aluminum(3+)-

nitrate(1-), -chloride(1-) and -perchlorate(1-), nickel(2+)-aluminum(3+)-chloride(1-), and zinc(2+)-aluminum(3+)-chloride(1-). *Clays and Clay Minerals*, **1975**, *23*, 369.
5. Prinetto, F.; Ghiotti, G.; Graffin, P.; Tichit, D. Synthesis and characterization of sol-gel Mg/Al and Ni/Al layered double hydroxides and comparison with co-precipitated samples. *Microporous and Mesoporous Materials*, **2000**, *39*, 229-247.
6. Chagger, H. K.; Ndaji, F. E.; Sykes, M. L.; Thomas, K. M. Kinetics of adsorption and diffusional characteristics of carbon molecular sieves, *Carbon*, **1995**, *33*, 1405.
7. Kapoor, A.; Yang, T. Kinetic separation of methane-carbon dioxide mixture by adsorption on molecular sieve carbon, *Chem. Eng. Sci.*, **1989**, *44*, 1723.
8. Yang, R. T.; Baksh, M. S. A. Pillared clays as a new class of sorbents for gas separation, *AIChE J.*, **1991**, *37*, 679.
9. Yucel, H.; Ruthven, D. M. Diffusion of Carbon dioxide in 4A and 5A zeolite crystals, *J. Colloid Interface Sci*., **1980**, *74*, 186.
10. Crank, J. *The Mathematics of Diffusion*, 2nd Edition, Clarendon Press, Oxford, 1975.
11. Ruthven, D. M., in *Adsorption, Science and Technology (Edited by Rodriguez, A. E.)*, Kluwer Academic Publishers, Netherlands, 87-114, 1989.
12. Kim, N.; Kim, Y.; Tsotsis, T. T.; Sahimi, M., Molecular modeling of the thermal evolution of the structure of Mg-Al-CO_3 layered double hydroxide., presented at AIChE's Annual Meeting, November 16-21, San Francisco, CA, 2003.
13. Kärger, J.; Pfeifer, H.; Heink, W. Principles and application of self-diffusion measurement by nuclear magnetic resonance, *Adv. Mag. Res*. **1988**, *12*, 1.
14. Abragam, A. Principles of Nuclear Magnetism, Oxford University Press, New York, 1961.
15. Stejskal, E. O.; Tanner, J. E. Spin diffusion measurement: spin echoes in the presence of a time-dependent field gradient. *J. Chem. Phys*. **1965**, *42(1)*, 288.
16. Langmuir, I. The adsorption of gases on plane surface of glass, mica, and platinum, *J. Ame. Chem. Soc.*, **1918**, *40*, 1361.
17. Freundlich, H. Kinetics and energetics of gas separation, *Trans. Farad. Soc.*, **1932**, *28*, 195.
18. Rudzinski, W.; Everett, D. H., *Adsorption of Gases on Heterogeneous Surfaces*, Academic Press, San Diego, 1992.
19. Sips, R. Structure of catalyst surface, *J. Chem. Phy.*, **1948**, *16*, 490.
20. Do, D. D. *Adsorption Analysis: Equilibria and Kinetics*, Series on Chemical Engineering Vol. 2, Imperial College Press, London, 1988.
21. Toth, J. Uniform interpretation of gas/solid adsorption, *Adv. Colloid Interface Sci*., **1995**, *55*, 1.
22. Toth, J. *Adsorption. Theory, Modeling, and Analysis*, Dekker, New York, 2002.
23. Dubinin, M. M., Porous structure and adsorption properties of active carbon, *Chemistry and Physics of Carbon*, **1966**, *2*, 51.
24. Dubinin, M. M., Adsorption in micropores, *J. Colloid Interface Sci*., **1967**, *23*, 487.

25. Dubinin, M. M., Fundamentals of the theory of physical adsorption of gases and vapors in micropores, *Adsorption – desorption Phenomena, Proc. Int. Conf.*, **1972**, *2nd*, 3.
26. Dubinin, M. M., Physical adsorption of gases and vapors in micropores, *Progress in Surface and Membrane Science*, **1975**, *9*, 1.
27. Bering, B. P.; Dubinin, M. M.; Serpinsky, V. V., Theory of volume filling for vapor adsorption, *J. Colloid Interface Sci*. **1966**, *21*, 378.
28. Bering, B. P.; Dubinin, M. M.; Serpinsky, V. V., Thermodynamics in micropores, *J. Colloid Interface Sci*. **1972**, *38*, 185.
29. Ruckenstein, E.; Vaidyanathan, A. S.; Youngquist, G. R., Sorption by solids with bidisperse pore structures, *Chem. Eng. Sci*. **1971**, *26*, 1305.

(a)

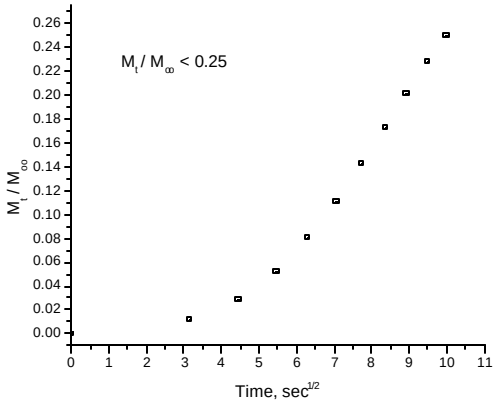

(b)

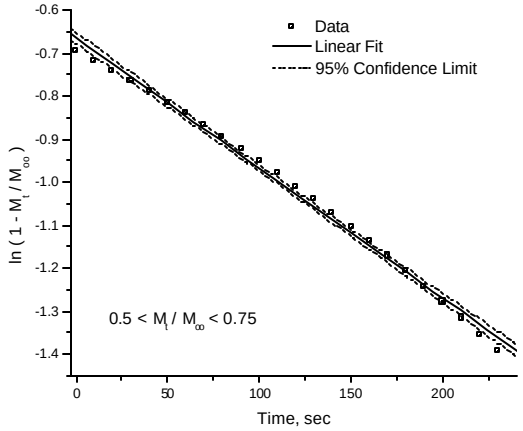

Figure 6.1 A graph of (a) M_t/M_8 against $t^{1/2}$, and (b) ln(1- M_t/M_8) against t for the uptake of carbon dioxide at 200 ^{o}C.

(a)

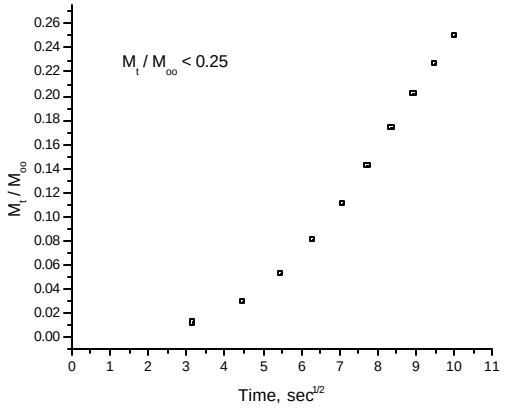

(b)

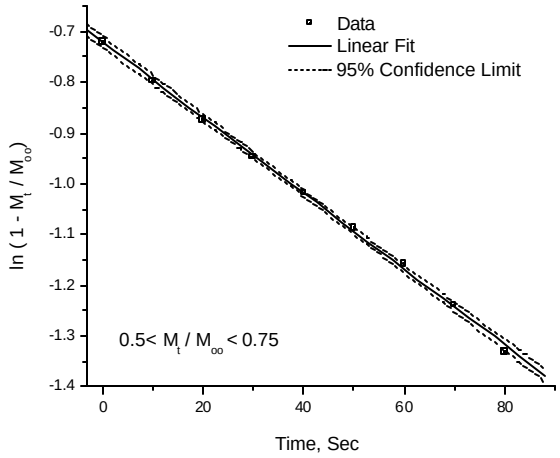

Figure 6.2 A graph of (a) M_t/M_8 against $t^{1/2}$, and (b) ln(1- M_t/M_8) against t for the uptake of carbon dioxide at 225 ^{o}C.

(a)

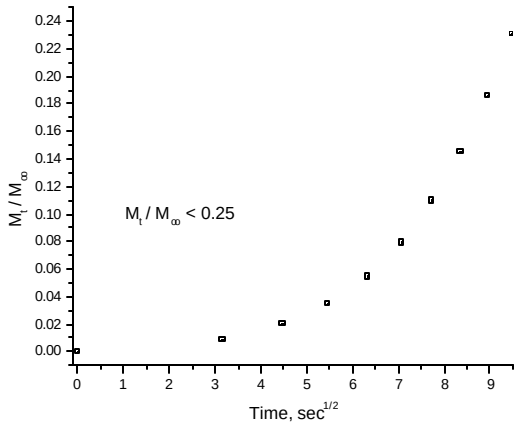

(b)

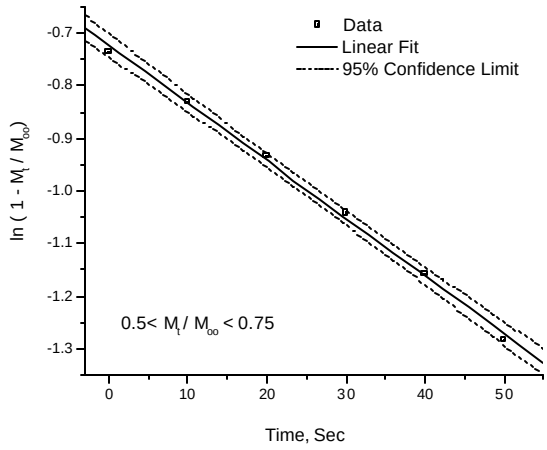

Figure 6.3 A graph of (a) M_t/M_8 against $t^{1/2}$, and (b) ln(1- M_t/M_8) against t for the uptake of carbon dioxide at 250 ^{o}C.

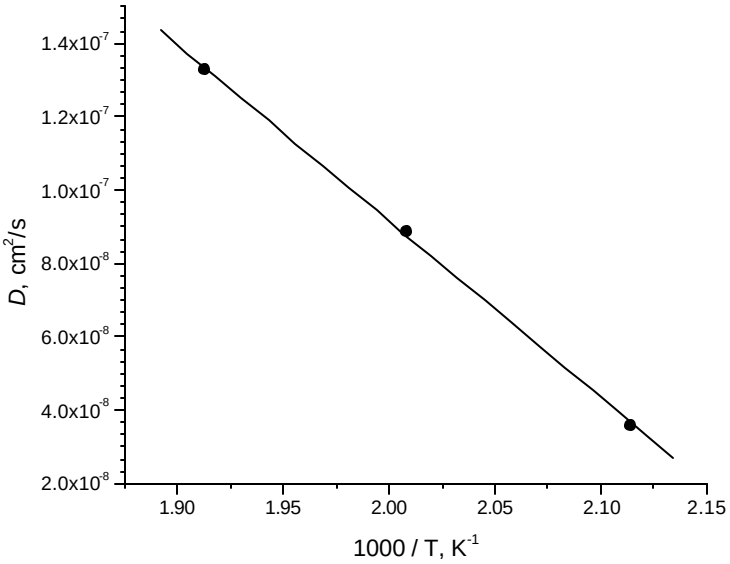

Figure 6.4 Temperature dependence of diffusion coefficient for CO_2 in LDH2.

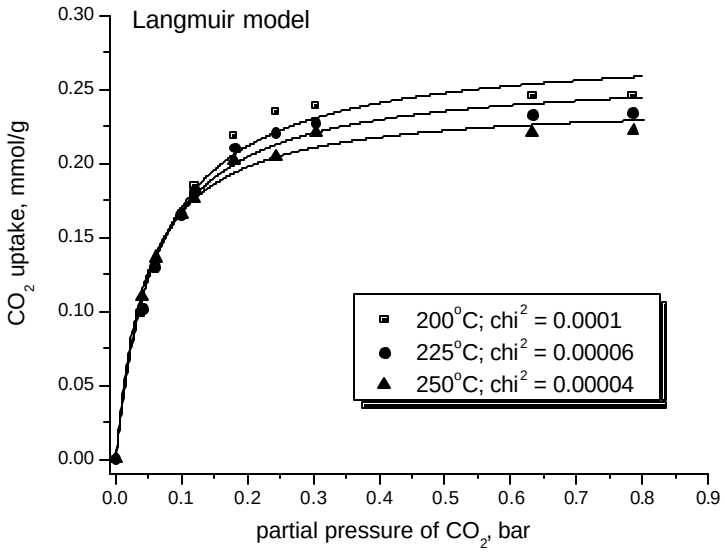

Figure 6.5 The experimental data and nonlinear curve fitting with the Langmuir equation for adsorption isotherm of CO_2 in LDH2.

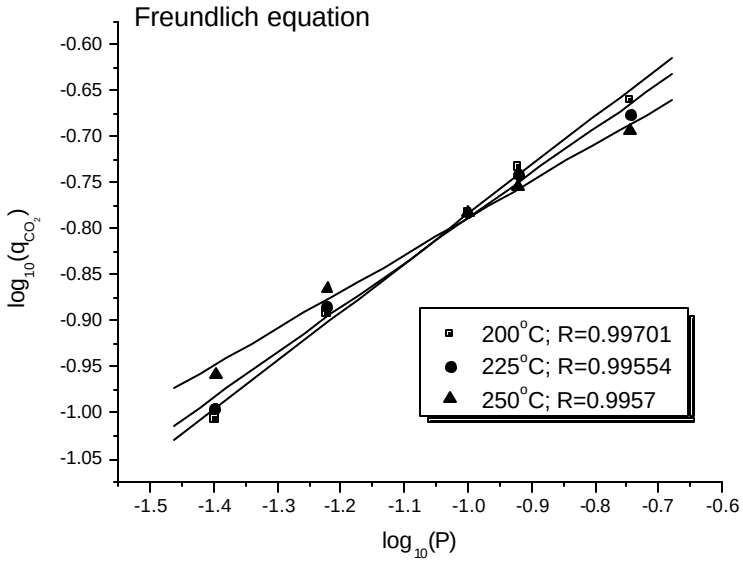

Figure 6.6 The experimental data and the fitting with the linearized Freundlich equation for adsorption isotherm of CO_2 in LDH2.

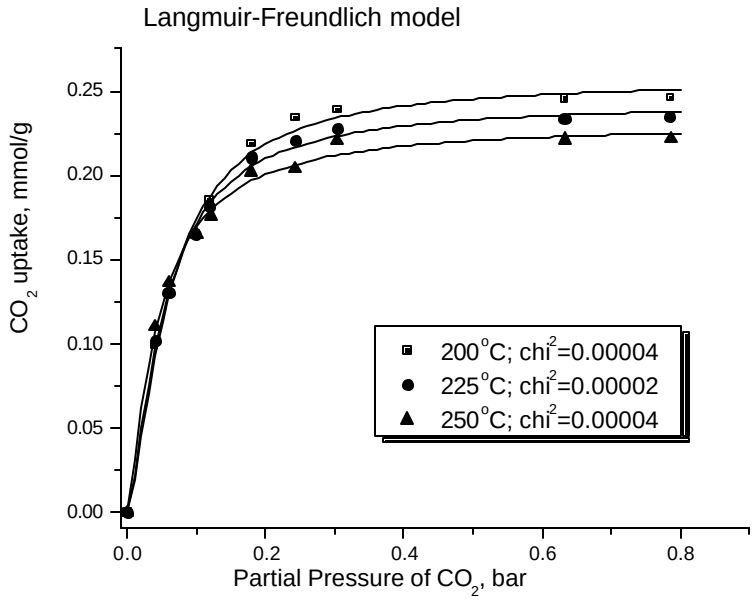

Figure 6.7 The experimental data and nonlinear curve fitting with the Langmuir-Freundlich equation for adsorption isotherm of CO_2 in LDH2.

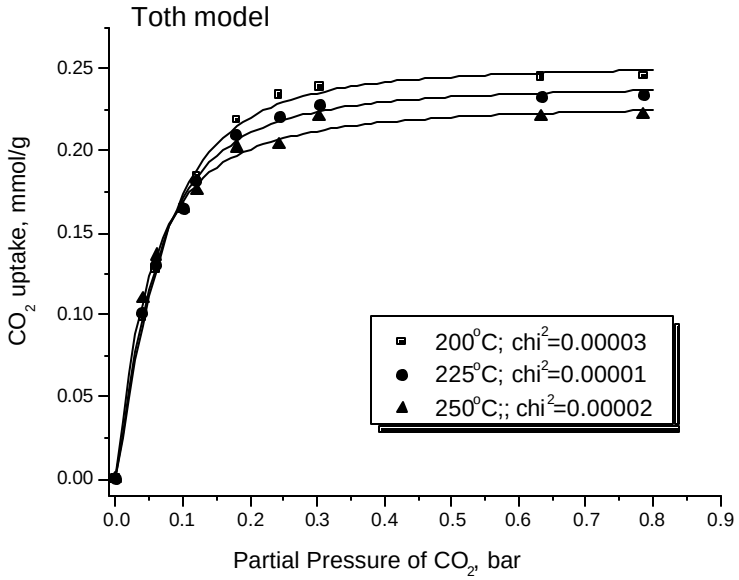

Figure 6.8 The experimental data and nonlinear curve fitting with the Toth equation for adsorption isotherm of CO_2 in LDH2.

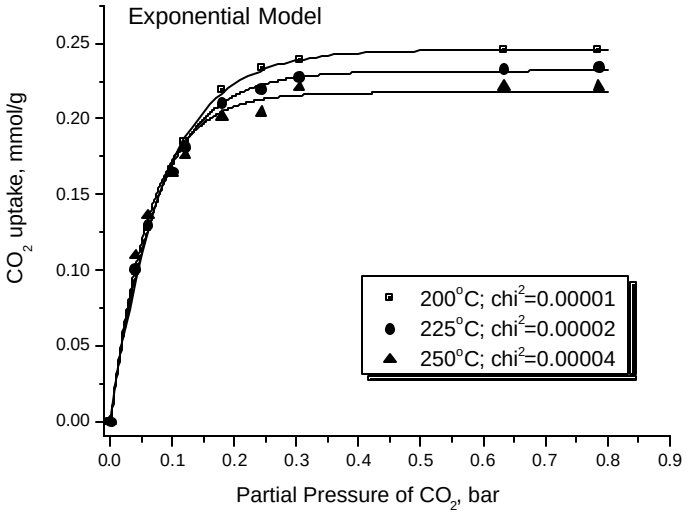

Figure 6.9 The experimental data and nonlinear curve fitting with exponential equation for adsorption isotherm of CO_2 in LDH2.

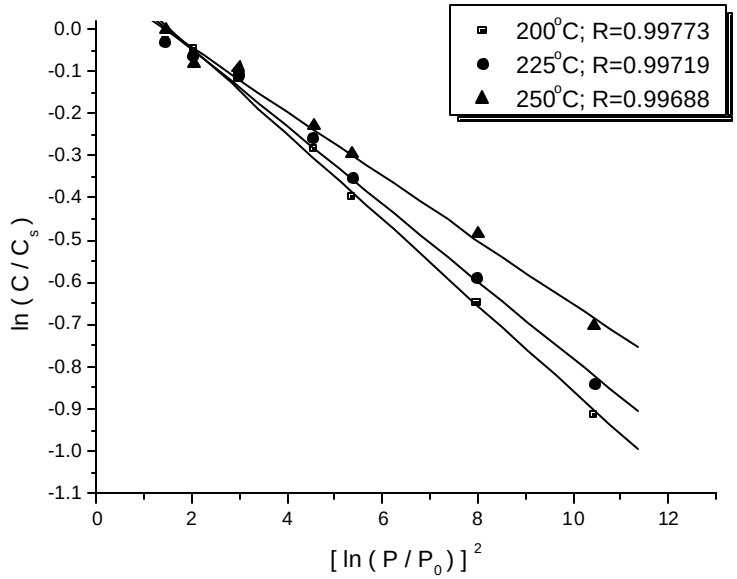

Figure 6.10 The experimental data and linear fitting with linearized DR equation for adsorption isotherm of CO_2 in LDH2.

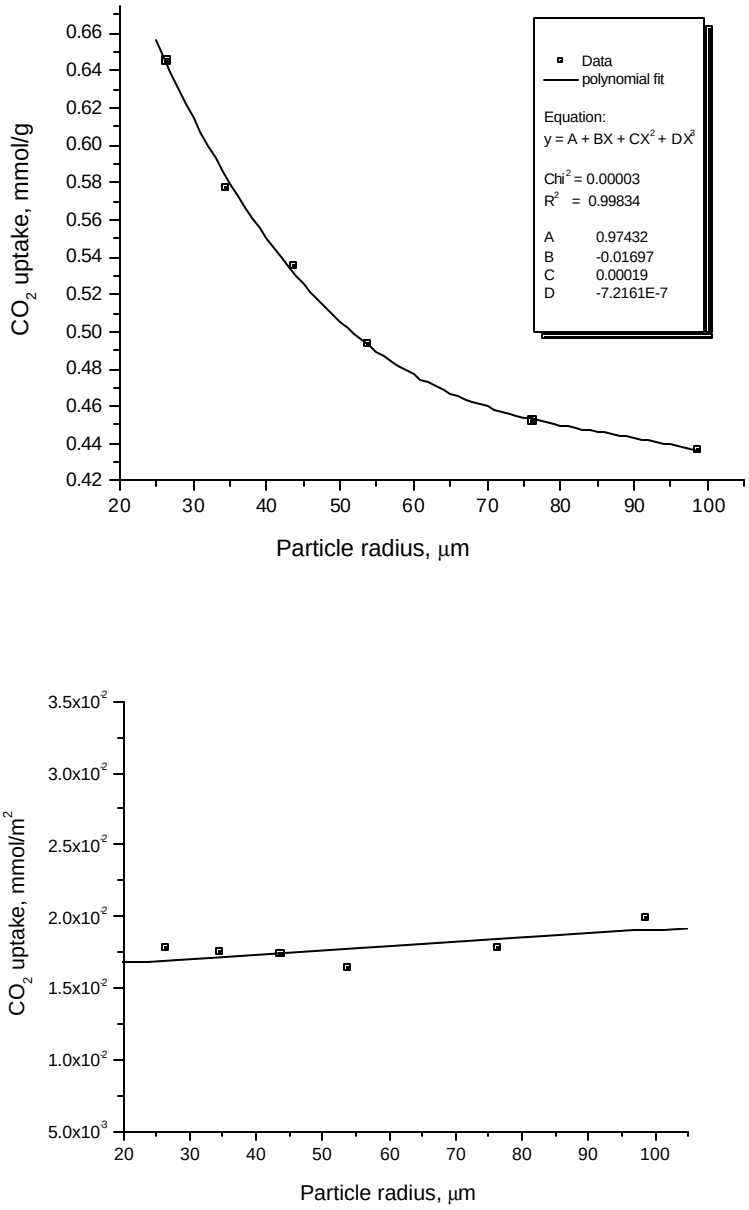

Figure 6.11 The uptake amount of CO_2 with different LDH3 particle sizes at 200^{o}C

(a)

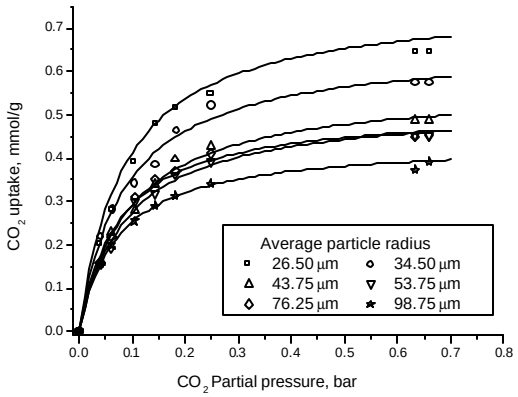

(b)

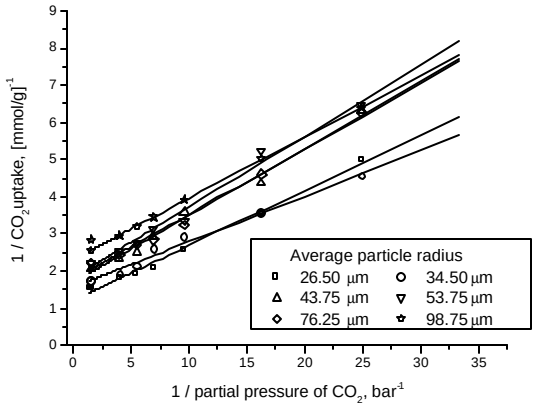

Figure 6.12 (a) The experimental data and nonlinear curve fitting with the Langmuir equation, and (b) the experimental data and linearized Langmuir equation for adsorption isotherm of CO_2 in LDH3.

(a)

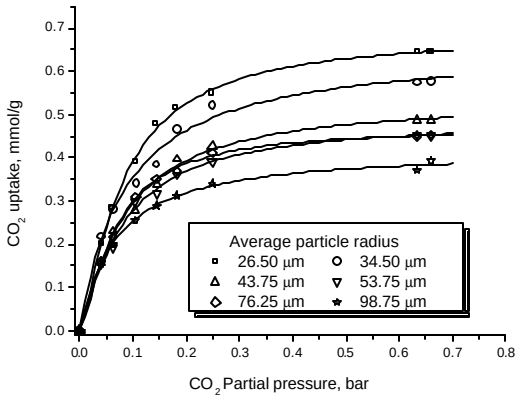

(b)

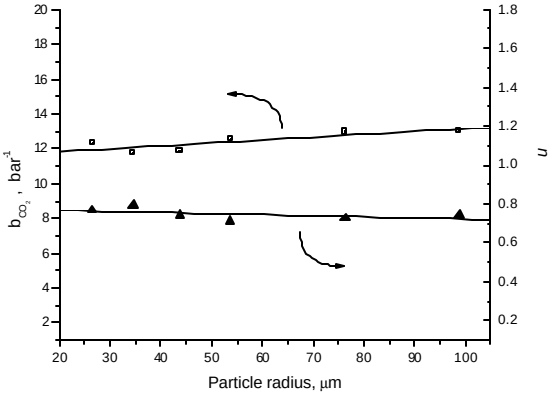

Figure 6.13 (a) The experimental data and nonlinear curve fitting with the Langmuir-Freundlich equation, and (b) the parameter values of Langmuir-Freundlich equation for adsorption isotherm of CO_2 in LDH3.

Chapter 7

Mathematical Simulation and Experimental Verification of Hydrogen Production with Concomitant CO_2 Recovery

7.1 Introduction/Literature Review

Reactive separation processes have been attracting renewed interest for application in catalytic steam reforming and the water gas shift reaction. From the standpoint of hydrogen production with concomitant removal of CO_2, reactive separation could offer a unique opportunity to reduce the hydrogen production cost via the separation of CO_2 from the reactor, making CO_2 ready for sequestration. Commonly discussed reactive separation processes include packed-bed catalytic membrane reactors (MR) [10-15] and, more recently, adsorptive reactor (AR) processes [16-26]. Their potential advantages over the more conventional reactors have been widely discussed. They include (i) increasing the reactant conversion and product yield through shifting the equilibrium towards the products, potentially allowing one to operate under milder operating conditions (e.g., lower temperatures, pressures and/or reduced steam consumption), and (ii) reducing the downstream purification requirements by in situ separating from the reaction mixture the desired product hydrogen (in the case of MR) or the undesired product CO_2 (in the case of AR). MR shows substantial promise in this area and, typically, utilizes nanoporous inorganic or metallic Pd or Pd-alloy membranes[15]. The latter are better suited for pure hydrogen production. However, metallic membranes are very expensive and become brittle during reactor operation [13] or deactivate in the presence of sulfur or coke. Nanoporous membranes are better suited for the steam-reforming environment. They are difficult to manufacture, however, without cracks and pinholes and, as a result, often have inferior product yield. In addition, the hydrogen in the permeate side contains other byproducts, and may require further treatment for use in fuel-cell-powered vehicles.

Adsorptive reactors also show good potential [16-20] for methane-steam-reforming and water gas shift. The challenge here, however, is in matching the adsorbent properties with those of the catalytic system. Two types of adsorbents have been suggested: potassium-promoted layered-double hydroxides (LDHs), which operate stably only at lower temperatures (less than 500°C [25-27]), and CaO or commercial dolomite, which can be utilized at the typical steam-reforming temperatures of 650-700°C [21] but requires temperatures higher than 850°C for regeneration [23,24]. These are very harsh conditions that result in gradual deterioration of the adsorbent properties and potentially sintering of the reforming catalyst [23,24]. The mismatch between the reaction and regeneration conditions is likely to result in significant process complications.

Here, what we propose for use is a novel reactor system, termed the hybrid adsorbent-membrane reactor (HAMR). The HAMR concept [1,2,28] couples the reaction and membrane separation steps with adsorption, which takes place in the reactor and/or membrane permeate side. The HAMR system investigated previously involved a hybrid pervaporation MR system and integrated the reaction and pervaporation steps through a

membrane with water adsorption. Coupling reaction, pervaporation, and adsorption demonstrated significant improvement in performance. Most recently, Elnashaie and co-workers [29-32] mathematically analyzed the behavior of a circulating fluidized-bed HAMR system utilizing Pd membranes. This reactor is assumed to operate at steady state by recirculating the catalyst and adsorbent through a second reactor for regeneration. The ability of Pd membranes to withstand the rigors of the fluidized-bed steam-reforming environment and of the adsorbents to undergo continuous recirculation and regeneration still remains the key challenge.

The HAMR configuration can be potentially used with equilibrium- or selectivity-limited reactions in which one of the products can be adsorbed while another (or the same) product can be simultaneously removed via a membrane. What limits the application of the concept is the availability of stable efficient adsorbents under reaction conditions. Esterification reactions (like the ethanol reaction with acetic acid to produce ethyl acetate previously studied by our group [1,2], through the use of water adsorbents), and the production of hydrogen (through steam reforming or the water gas shift reactions) are two key potential applications. Here, we investigate a HAMR system involving a hybrid packed-bed catalytic MR, coupling the water gas shift reaction through a porous inorganic H_2-selective membrane with a CO_2 adsorption system. This HAMR system exhibits behavior that is more advantageous than either the MR or AR, in terms of the attained yields and selectivities. In addition, the HAMR system potentially allows for significantly greater process flexibility than either the MR or AR system. The membrane, for example, can potentially be used to separate the catalyst from the adsorbent phase, thus allowing for in situ continuous regeneration of the adsorbent. This offers a significant advantage over the ARs, which require the presence of multiple beds (one being in operation while the other is being regenerated) to achieve continuous operation. The HAMR system shows, furthermore, significant potential advantages with respect to the conventional MR system. Beyond the improved yields and selectivities, the HAMR system has the potential for producing a CO-free fuel-cell-grade hydrogen product, which is of significance for the proposed fuel-cell-based mobile applications of such systems.

In this chapter, a mathematical model for the HAMR system is presented and analyzed for a range of temperature and pressure conditions. Through numerical simulation, the behavior of the HAMR system is compared with the conventional packed-bed reactor, as well as a MR and an AR system. In addition, experimental data for the HAMR based on the hydrotalcite type adsorbent and the nanoporous H_2 selective membrane are presented for comparison with the mathematical simulation results.

7.2 Fundamentals

7.2.1 Kinetics for Water Gas Shift Reaction.

For the water gas shift reaction, we utilize an empirical power law-type reaction rate expression. Formation rates for the H_2, and CO_2 products and the disappearance rates for CO and H_2O are given by the following equations:

$$CO + H_2O \Leftrightarrow CO_2 + H_2 \quad (1)$$

$$r = k \frac{P_{CO} * P_{H2O}^{1.4}}{P_{H_2}^{0.9} P_{CO_2}^{0.7}} (1 - b) \frac{1}{Pt^{0.4}} \quad (2)$$

$$b = \frac{P_{CO_2} * P_{H2}}{Ke * P_{H_2O} P_{CO}} \quad (3)$$

$$k = k_0 * \exp(-114218.6/(R + (T + 273))) \quad (4)$$

7.2.2 Mathematical Model of the HAMR System.

A schematic of the HAMR system is shown in Figure 7.1. In this figure, the catalyst and adsorbent are packed in the exterior of the membrane (signified by the superscript F, or the feed side), with additional adsorbent also packed in the interior of the membrane volume (signified by the superscript P, or the permeate side). There are, of course, a number of other potential reactor configurations, as previously noted. For example, the catalyst may be loaded in the feed side, while the adsorbent may also be loaded in the permeate side, or the catalyst and adsorbent may only be loaded in the feed side, with no adsorbent or catalyst being present in the permeate side, which is the configuration that is analyzed here. To simplify matters, in the development of the model, we assume that the reactor operates isothermally, that external mass-transfer resistances are negligible for the transport through the membrane as well as for the catalysts, and that internal diffusion limitations for the catalyst, and internal or external transport limitations for the adsorbent, are accounted for by the overall rate coefficients. Moreover, plug-flow conditions are assumed to prevail for both the interior and exterior membrane volumes, as well as ideal gas law conditions.

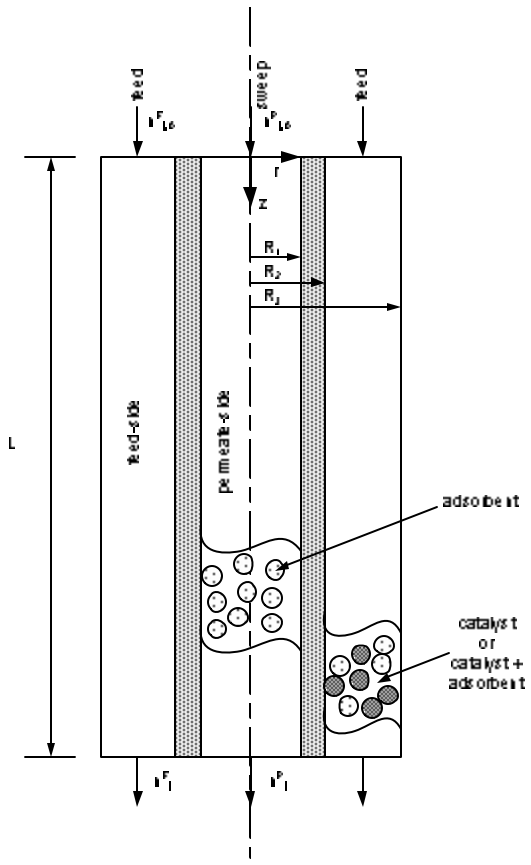

Figure 7.1 Schematic diagram of a HAMR system.

Mass transfer through the porous membrane is described by the following empirical equation:

$$F_j = U_j(P_j^F - P_j^P) \tag{5}$$

where F_j is the molar flux (mol/m^2·s), P_j^F the partial pressure of component j on the membrane feed side (bar), P_j^P the partial pressure of component j on the membrane permeate side (bar), and U_j the membrane permeance for component j (mol/m^2·bar·s). Equation 5 is, of course, a simplified empirical expression for describing flux through a nanoporous membrane for which the size of the pores approaches that of the diffusing molecules. Substantial efforts are currently ongoing by our group and others for a better understanding of the phenomena that occur during molecular transport through such nanoporous systems. Simple analytical expressions for describing transport through such membranes are currently lacking, however, thus the choice of the commonly utilized empirical Equation 5 in this preliminary reactor modeling investigation.

The mass balance on the feed side of the reactor packed with water gas shift reaction catalyst and, potentially, an adsorbent is described by the following equations for CO_2, CO, H_2, H_2O and an inert species (potentially used as a sweep gas or a blanketing agent;

for catalytic water gas shift reaction, a practical sweep gas would be either steam or hydrogen, however):

$$e^F \frac{\partial C_j^F}{\partial t} + \frac{\partial n_j^F}{\partial V} = -a_m U_j (P_j^F - P_j^P) + \left(1 - e_b^F\right) b_c r_c R_j^F - \left(1 - e_b^F\right)(1 - b_c) r_a G_j^F + e_b^F \left(A^F\right)^2 \frac{\partial}{\partial V}\left(D_L^F \frac{\partial C_j^F}{\partial V} \right) \quad (6)$$

In Equation 6, n_j^F is the molar flow rate (mol/s) for species j and C_j^F is the gas-phase concentration (kmol/m^3) equal to n_j^F / Q^F, where Q^F is the volumetric flow rate (m^3/s). V is the feed-side reactor volume variable (m^3), A^F the cross-sectional area for the reactor feed side (m^2), a_m the membrane area per feed-side reactor volume (m^2/m^3), e_b^F the bed porosity on the feed side, e^F the total feed-side bed porosity (it includes the bed porosity and catalyst porosity), b_c the fraction of the solid volume occupied by catalysts (b_c = 1 when no adsorbent is present), ρ_c the catalyst density (kg/m^3), ρ_a the adsorbent density (kg/m^3), and R_j^F the reaction rate expression. Assuming that the adsorbent only adsorbs CO_2, G_j^F is zero for all other components except CO_2. D_L^F (m^2/s) is the axial dispersion coefficient given by the following equation[34] generally applicable for describing dispersion phenomena through packed beds:

$$D_L^F = 0.73\, D_m^F + \frac{0.5\, u^F d_P^F}{1 + 9.49\, (D_m^F / u^F d_P^F)} \quad (7)$$

where D_m^F is molecular diffusivity (m^2/s), u^F is the velocity at the feed side (m/s), and d_P^F is the particle diameter in the feed side (m). One finds a number of approaches in the literature for describing $G_{CO_2}^F$. Ideally, one would like to account explicitly for both external and internal mass transport and finite rates of adsorption. Such an approach goes beyond the scope of this preliminary investigation, however, in addition to the fact that there are currently no experimental high-temperature transport/adsorption CO_2 data to justify this level of mathematical detail. Traditionally, in the modeling of ARs, simpler models have been utilized instead [22,27]. Two such models have received the most attention. They are (i) the model based on the assumption of instantaneous local adsorption equilibrium between the gas and adsorbent phases [2, 22, 27, 28] and (ii) the linear driving force (LDF) models, according to which $G_{CO_2}^F$ is described by the following expression[35]:

$$\frac{dC_s}{dt} = G_{CO_2}^F = k_a (C_{seq} - C_s) \quad (8)$$

where C_{seq} is the adsorption equilibrium CO_2 concentration on the adsorbent (mol/kg) corresponding to the prevailing gas-phase concentration, C_s is the existing adsorbed CO_2 concentration (mol/kg), and k_a (s^{-1}) is a parameter that "lumps" together the effects of external and intraparticle mass transport and the sorption processes and that, as a result, is often a strong function of temperature and pressure[27], although, typically, in modeling it is taken as temperature/pressure-independent. To calculate C_{seq}, we utilize the data reported by Ding and Alpay [22,27] for CO_2 adsorption on potassium-promoted LDH. They showed that the CO_2 adsorption on this adsorbent follows a Langmuir adsorption isotherm under both dry and wet conditions, described by the following equation:

$$C_{seq} = \frac{m_{CO_2} b_{CO_2} P_{CO_2}}{1 + b_{CO_2} P_{CO_2}} \tag{9}$$

where m_{CO2} (mol/kg) is the total adsorbent capacity and b_{CO2} (bar^{-1}) the adsorption equilibrium constant, which is described by the van't Hoff equation:

$$b_{CO_2} = b_{CO_2}(T_0)\exp[-\Delta H_a / R(1/T - 1/T_0)] \tag{10}$$

The heat of adsorption, ΔH_a (kJ/mol), under wet conditions for a region of temperatures from 481 to 753 K was calculated to be -17 kJ/mol, while b_{CO2} at 673 K is equal to 23.6 bar[27]. Equations 6 and 8 must be complemented by initial and boundary conditions. For simplicity, we assume here that the reactor, prior to the initiation of the reaction/adsorption step, has undergone a start-up procedure as described by Ding and Alpay [22] that involves (i) heating the reactor to the desired temperature under atmospheric pressures by feeding H_2 on the reactor feed side and the chosen sweep gas on the permeate side, (ii) supplying water to the system so that the feed H_2O/H_2 ratio is the same as the H_2O/CO ratio to be used during the reaction step, (iii) pressurizing the feed and permeate sides to the desired pressure conditions, and (iv) switching from H_2 to CO to initiate the reaction/adsorption step. In the simulations, the conditions prevailing at the start of step (iv) are those prevailing at steady state during step (iii). In addition, during step (iv) the following conventional boundary conditions prevail [16-20]:

$$\text{at } V = 0; \qquad \frac{dx_j^F}{dV} = -\frac{u_0^F (x_{j_0}^F - x_j^F)}{A^F e_b{}^F D_L^F} \tag{11}$$

$$\text{at } V = V_R; \qquad \frac{dx_j^F}{dV} = 0 \tag{12}$$

where u_0^F is the inlet superficial velocity (m/s), V_R the total reactor volume (m^3), x_j^F the mole fraction, and $x_{j_0}^F$ the inlet mole fraction for species j.

Assuming that the catalyst and adsorbent particles have the same size, the pressure drop in a packed bed can be calculated using the Ergun equation:

$$-\frac{dP^F}{dV} = 10^{-6}\frac{f^F (G_m^F)^2}{A^F g_c d_P^F r_F^F} \tag{13}$$

$$\text{at } V = 0, \quad P^F = P_0^F \tag{14}$$

$$f^F = \left(\frac{1-e_b^F}{(e_b^F)^3}\right)\left(1.75 + \frac{150(1-e_b^F)}{N_{\text{Re}}^F}\right) \tag{15}$$

$$N_{\text{Re}}^F < 500(1-e_b^F) \tag{16}$$

$$N_{\text{Re}}^F = d_P^F G_m^F / m^F \tag{17}$$

where P^F is the feed-side pressure (bar), P_0^F the inlet feed-side pressure, μ^F the viscosity (Pa·s), d_P^F the particle diameter in the feed side (m), $G_m^F = r_F^F m^F$ the superficial mass flow velocity in the feed side (kg/m^2·s), r_F^F the density of the fluid (kg/m^3), and g_c the gravity conversion factor equal to 1 in SI units.

Because the CMS membranes do not show substantial CO_2 permeation [33], we assume that no adsorbent or catalyst is present in the permeate side. For the permeate side, the following equation is, therefore, utilized:

$$\frac{dC_j^P}{dt} + k\frac{dn_j^P}{dV} = a_m k U_j (P_j^F - P_j^P) + (A^F)^2 \frac{d}{dV}\left(D_L^P \frac{dC_j^P}{dV}\right); \quad j=1,2....n \tag{18}$$

where $k = A^F/A^P$, with A^P being the cross-sectional area on the permeate side (m^2), and D_L^P (m^2/s) is the axial Taylor-Aris dispersion coefficient on the permeate side[36] for empty tubes given as:

$$D_L^P = D_m^P + \frac{(u^P)^2 (d_t^P)^2}{192 D_m^P} \tag{19}$$

where D_m^P is the molecular diffusivity (m^2/s), u^P is the velocity at the permeate side (m/s), and d_t^P is the membrane inside diameter (m). In the simulations, the conditions prevailing in the permeate side at the start of step (iv) are those prevailing at steady state during step (iii). In addition, during step (iv) the following conditions prevail in the permeate side:

$$V = 0; \qquad \frac{dx_j^P}{dV} = -\frac{u_0^P (x_{j_0}^P - x_j^P)}{A^F D_L^P} \tag{20}$$

$$V = V_R; \qquad \frac{dx_j^P}{dV} = 0 \tag{21}$$

where x_j^P is the mole fraction, $x_{j_0}^P$ the inlet mole fraction for species j on the permeate side, and u_0^P the superficial flow velocity (m/s) at the inlet. Because no adsorbent or catalyst is present in the permeate side, we ignore any potential pressure drops.

The reactor conversion (based on CO, which is typically the limiting reagent) is defined by the following equation:

$$X_{CO} = \frac{n_{CO_0}^F - (n_{CO_{ex}}^F + n_{CO_{ex}}^P)}{n_{CO_0}^F} \tag{22}$$

where $n_{CO_0}^F$ is the inlet molar flow rate of CO and $n_{CO_{ex}}^F$ and $n_{CO_{ex}}^P$ are the CO molar flow rates at the exit of the reactor feed and permeate sides correspondingly (mol/s). The yield of product hydrogen, defined as the fraction of moles of CO fed into the reactor that have reacted to produce hydrogen, is given by the following equation:

$$Y_{H_2} = \frac{(n_{H_{2,ex}}^F - n_{H_{2,0}}^F) + (n_{H_{2,ex}}^P - n_{H_{2,0}}^P)}{n_{CO_0}^F} \tag{23}$$

where $n_{H_{2,ex}}^F$ and $n_{H_{2,ex}}^P$ are the hydrogen molar flow rates at the exit of respectively the reactor feed and permeate sides and $n_{H_{2,0}}^F$ and $n_{H_{2,0}}^P$ the H_2 molar flow rates potentially present at the inlet of the reactor feed and permeate sides (mol/s). Y_{H2} = 1 when all of the CO has reacted completely to produce CO_2 and H_2.

Equations 6-23 can be written in dimensionless form by defining the following variables and groups:

$$t_a = (k_a)^{-1}; t_F = \frac{e^F V_R}{A^F u_0^F}; g = \frac{t_F}{t_a}; h = \frac{V}{V_R}; u^F = \frac{Q^F}{A^F}; u_0^F = \frac{Q_0^F}{A^F}; x^F = \frac{u^F}{u_0^F}; x^P = \frac{u^P}{u_0^P};$$

$$\Psi^F = \frac{P^F}{P_0^F};\ \Psi^P = \frac{P^P}{P_0^P}; w = \frac{P_0^P}{P_0^F}; a_j = \frac{MW_j}{MW_{H_2}}; x_j^F = \frac{P_j^F}{P^F};\ x_j^P = \frac{P_j^P}{P^P};\ t = k_a t;\ d_j = \frac{U_j}{U_{H_2}};$$

$$K'_{eq1} = \frac{K_{eq1}}{(P_0^F)^2};\ K'_{CO} = K_{CO} P_0^F;\ K'_{H_2} = K_{H_2} P_0^F;$$

$$Da = \frac{b_c\left(1-e_b^F\right) r_c k_1(T_0) V_R RT}{A^F u_0^F (P_0^F)^{1.5}}; b_{CO_2} = b_{CO_2} P_0^F; Pe = \frac{A^F u_0^F}{U_{H_2} V_R a_m RT}$$

$$;\Theta^F = \frac{e_b^F A^F D_L^F}{u_0^F V_R}; \Theta^P = \frac{A^F D_L^P}{u_0^P V_R}$$

$$Ha = \frac{(1-b_c)\left(1-e_b^F\right) V_R r_a k_a RT m_{CO_2}}{A^F u_0^F P_0^F};\qquad \Lambda = \frac{Ha}{Da};\qquad \Omega = (Da)(Pe);$$

$$\Xi = 10^{-6} f^F \frac{(u_0^F)^2 MW_{H_2} V_R}{A^F g_c d_p^F RT};\ l = \frac{A^P u_0^P}{A^F u_0^F};\ q_{seq}^F = \frac{C_{seq}^F}{m_{CO_2}};\ q_s^F = \frac{C_s^F}{m_{CO_2}};\qquad (24)$$

The dimensionless equations equivalent to Equations 6-18 are

$$g\frac{\partial x_j^F}{\partial t} = -\left(x^F \frac{\partial x_j^F}{\partial h} + x_j^F \frac{\partial x^F}{\partial h} + \frac{x_j^F x^F}{\Psi^F}\frac{\partial \Psi^F}{\partial h}\right) - \frac{Da d_j}{\Omega}\left(x_j^F - x_j^P w\frac{\Psi^P}{\Psi^F}\right) + Da\frac{1}{\Psi^F} R'^F_j - Da\Lambda\frac{1}{\Psi^F} G'^F_j +$$

$$+\Theta^F \frac{\partial^2 x_j^F}{\partial h^2} + 2\Theta^F \frac{1}{\Psi^F}\left(\frac{\partial x_j^F}{\partial h}\right)\left(\frac{\partial \Psi^F}{\partial h}\right),\ \text{j=1,2,...,n-1} \qquad (25)$$

$$\frac{\partial x^F}{\partial h} = -\frac{x^F}{\Psi^F}\frac{\partial \Psi^F}{\partial h} - \frac{Da}{\Omega}\sum_j d_j\left(x_j^F - x_j^P w\frac{\Psi^P}{\Psi^F}\right) + Da\frac{1}{\Psi^F}\sum_j R'^F_j - \Lambda Da\frac{1}{\Psi^F} G'^F_{CO_2} \qquad (26)$$

$$\frac{g}{e^F l k}\frac{\partial x_j^P}{\partial t} = -\left(x^P \frac{\partial x_j^P}{\partial h} + x_j^P \frac{\partial x^P}{\partial h} + \frac{x_j^P x^P}{\Psi^P}\frac{\partial \Psi^P}{\partial h} \right) + \frac{Da\, d_j}{l\,\Omega}\left(x_j^F \frac{\Psi^F}{w\Psi^P} - x_j^P \right) +$$

$$\Theta^P \frac{\partial^2 x_j^P}{\partial h^2} + 2\Theta^P \frac{1}{\Psi^P}\left(\frac{\partial x_j^P}{\partial h}\right)\left(\frac{\partial \Psi^P}{\partial h}\right),\ j = 1,2,...,n-1 \tag{27}$$

$$\frac{\partial x^P}{\partial h} = -\frac{x^P}{\Psi^P}\frac{\partial \Psi^P}{\partial h} + \frac{Da}{l\Omega}\sum_j d_j \left(x_j^F \frac{\Psi^F}{w\Psi^P} - x_j^P \right) \tag{28}$$

$$\frac{\partial \Psi^F}{\partial h} = -\Xi (x^F)^2 \Psi^F \sum x_j^F a_j \tag{29}$$

$$\frac{dq_S^F}{dt} = q_{S_{eq}}^F - q_S^F \tag{30}$$

$$X_{CO} = \frac{x_{CO_0}^F - \left(x_{CO}^F \Psi^F x^F \right)_{ex} + \left(x_{CO}^P\, l \Psi^P w x^P \right)_{ex}}{x_{CO_0}^F} \tag{31}$$

$$Y_{H_2} = \frac{(x_{H_2}^F \Psi^F x^F)_{ex} - x_{H_{20}}^F + (x_{H_2}^P\, l \Psi^P w x^P)_{ex} - x_{H_{20}}^P\, l w}{x_{CH_{40}}^F} \tag{32}$$

where in dimensionless form:

$$G'^F_{CO_2} = (q_{seq}^F - q_s^F) \tag{33}$$

$$q_{seq}^F = \frac{b_{CO_2} x_{CO_2}^F \Psi^F}{1 + b_{CO_2} x_{CO_2}^F \Psi^F} \tag{34}$$

and $R_j^{'}$ are dimensionless forms of R_j. Equations 26 and 28 that express the dimensionless velocity distributions are obtained by overall mass balances in the feed and permeate sides. In the absence of substantial pressure drop in the permeate side in Equation 27, $\Psi^P = 1$ and $\frac{\partial \Psi^P}{\partial h} = 0$. The initial conditions at the start of the adsorption/reaction step are those prevailing during step 3 previously described. In addition, the following boundary conditions also apply:

$$t > 0\ ;\ @h = 0;\quad ?^F = 1\ ;\ ?^P = 1 \tag{35}$$

$$x^F = 1\ ;\ \ x^P = 1 \tag{36}$$

$$\frac{\partial x_j^F}{\partial h} = -\frac{1}{\Theta^F}(x_{j0}^F - x_j^F);\ \ i = 1, 2, \ldots, n \tag{37}$$

$$\frac{\partial x_j^P}{\partial h} = -\frac{1}{\Theta^P}(x_{j0}^P - x_j^P);\ \ i = 1, 2, \ldots, n \tag{38}$$

$$t > 0;\ @\ h = 1;\ \ \frac{\partial x_j^F}{\partial h} = 0 \tag{39}$$

$$\frac{\partial x_j^P}{\partial h} = 0 \tag{40}$$

where, $s = \frac{\sum n_{j0}^P}{\sum n_{j0}^F} = l w \frac{\sum x_{j0}^P}{\sum x_{j0}^F}$ is the sweep ratio for the membrane reactor.

The system of coupled nonlinear partial differential Equations 25-34 and accompanying boundary conditions has been solved in MATLAB using the method of lines[37,38]. The system of partial differential equations was converted to a set of ordinary differential equations by discretizing the spatial derivative in the h direction using a five-point-biased upwind finite-difference scheme to approximate the convective term. A fourth-order central-difference scheme has been used to approximate the diffusive term. For finite differences, the reactor volume was divided into n sections with n + 1 nodes. The initial value ordinary differential equations and other explicit algebraic equations at a time t were simultaneously solved using ode45.m, a MATLAB built-in solver for initial value problems for ordinary differential equations.

7.3 Performance Evaluation via Mathematical Simulation

We report here the behavior of the HAMR and AR simulating water gas shift reaction for hydrogen production with concomitant CO_2 removal. Figure 7.2 shows the hydrogen yield attained by both the AR and HAMR as a function of dimensionless time for different values of Wc/F (Wc is the total weight of the catalyst). The reactor temperature is 250°C, and a CO: H_2: H_2O feed ratio of 1:4:1.1 is utilized. Steam is used as the sweep gas. The reaction rate constants are experimentally determined in Sec. 7.3.1 and the membrane permeance are experimentally determined in Sec. 7.3.2. Table 7.5 lists the values of all of the other parameters utilized. Initially, the hydrogen yield for both reactors reaches high values, but it declines as the adsorbent becomes saturated and levels off at the corresponding values for the conventional membrane (in the case of HAMR) or the plug-flow reactor (in the case of AR). The HAMR performs better than the AR. For the conditions in Figure 7.2, the catalyst is sufficiently active that the plug-flow reactor yields (the AR yields level off at these values) approach equilibrium (~84% under the prevailing conditions) for all of the four Wc/F values utilized. On the other hand, the yields for the AR and HAMR systems (prior to the adsorbent saturation) and the MR yields (the HAMR yields level off at these yields) depend on Wc/F, increasing as Wc/F increases, as expected.

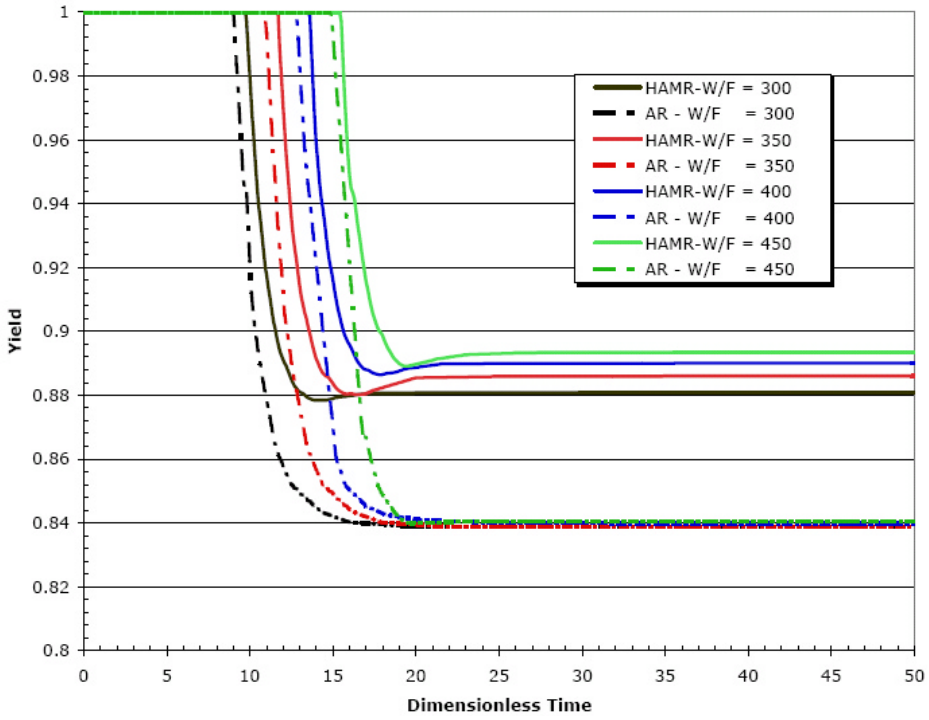

Figure 7.2 Hydrogen yield for the HAMR and AR systems for various Wc/F

Figure 7.3 shows the CO_2 feed-side exit concentration (wet basis) profiles for the HAMR and AR. Low concentrations are observed while the adsorbent remains unsaturated; the concentrations sharply increase, however, after the adsorbent is saturated. The CO_2 concentration for HAMR is higher than that for MR as a result of the hydrogen permeation out of the reactor in the HAMR system.

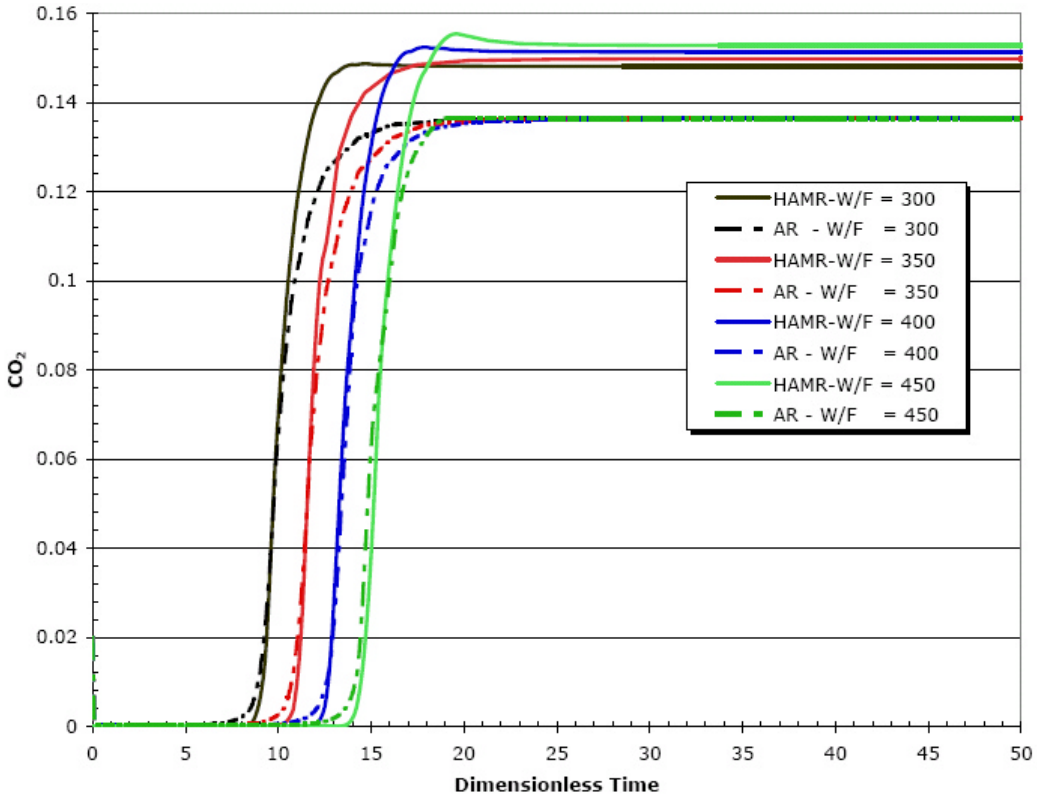

Figure 7.3 CO_2 concentration (wet basis) profiles at the reactor outlet for the AR and HAMR systems at different Wc/F.

Figure 7.4 shows the CO concentration (wet basis) profiles in the permeate-side exit of the HAMR, together with the corresponding exit concentration values for the AR. Clear from Figure 7.4 is the advantage that the HAMR system provides in terms of reduced CO concentrations in the hydrogen product over the AR system, in addition to improved hydrogen yields. The CO concentration in AR jumps to a high value and stays there till the adsorbent gets saturated; after adsorbent saturation there is another big jump and CO concentration levels off to a higher final value as compared to HAMR CO-ppm levels. Thus, unreacted CO is expected to distribute throughout the AR rather quickly. Even though the adsorbent has not been saturated with CO_2; the established equilibrium assures the presence of unreacted CO.

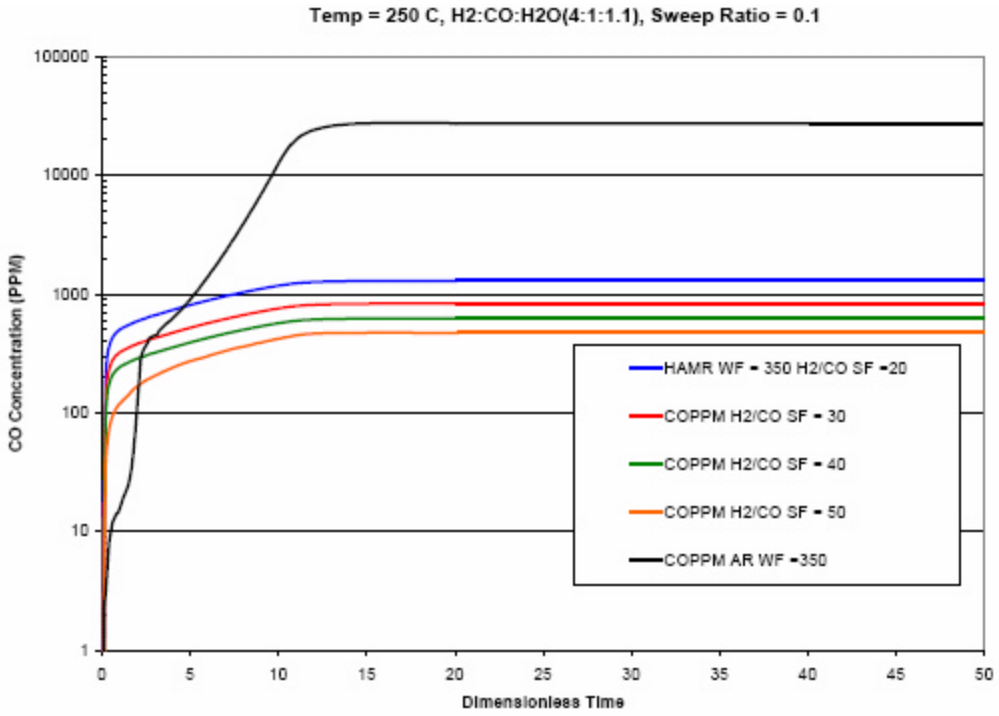

Figure 7.4 CO concentration (wet basis, in ppm) profiles in the HAMR permeate-side exit and AR exit for different Wc/F

A potential disadvantage of the HAMR system, when compared to the AR system, is that only a fraction of the hydrogen product ends up in the permeate stream, while the rest remains mixed with the unreacted CO and CO_2 products in the feed-side stream. The hydrogen recovery is, of course, a strong function of the membrane permeation characteristics and the other operating conditions in the reactor, increasing with increasing membrane permeance and feed-side pressure. Furthermore, one must also take into account, when comparing both reactors that even for the AR system one must eventually separate the hydrogen out of the exit stream and that similar hydrogen losses are likely to occur.

Figure 7.5 shows the effect of ß$_c$ (the fraction of reactor volume occupied by catalyst) on the hydrogen yields, while keeping the total volume occupied by the solids and the Wc/F constant. Decreasing ß$_c$ (i.e., increasing the fraction of sorbent present), while maintaining Wc/F constant, has a significant beneficial effect on the hydrogen yield and also on the product purity for both the HAMR and AR systems (see Figure 7.6 for the CO content of the hydrogen product).

ß$_c$ is the volume of reactor occupied by the catalyst. In these experiments the total reactor volume stays constant. By decreasing ß$_c$ one simultaneously changes both the catalyst volume and the adsorbent volume. Since there is a much larger volume of adsorbent than catalyst changing ß$_c$ mostly affects the level of final conversion.

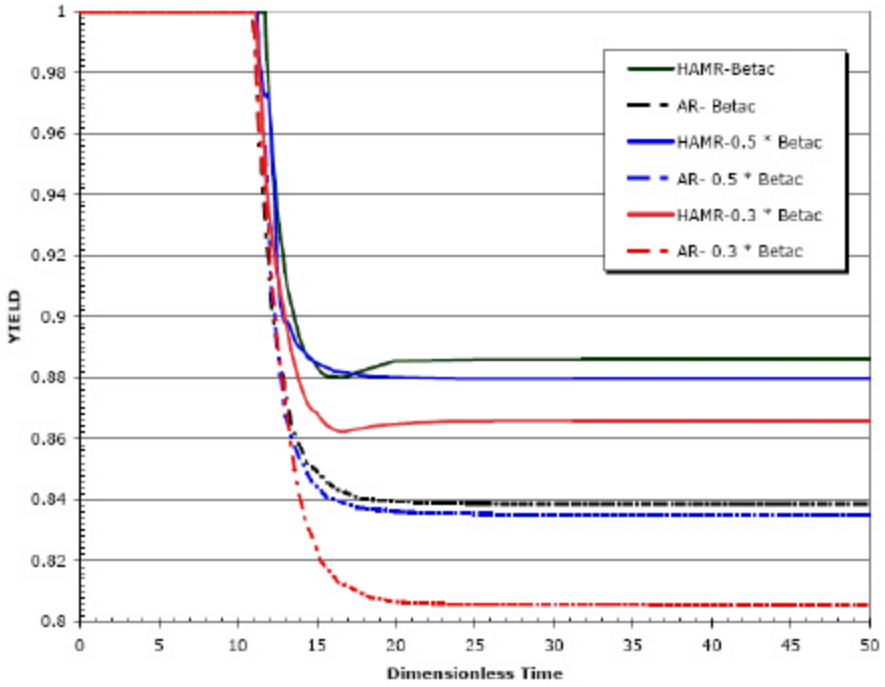

Figure 7.5 Effect of ß$_c$ on the hydrogen yields for both the HAMR and AR systems.

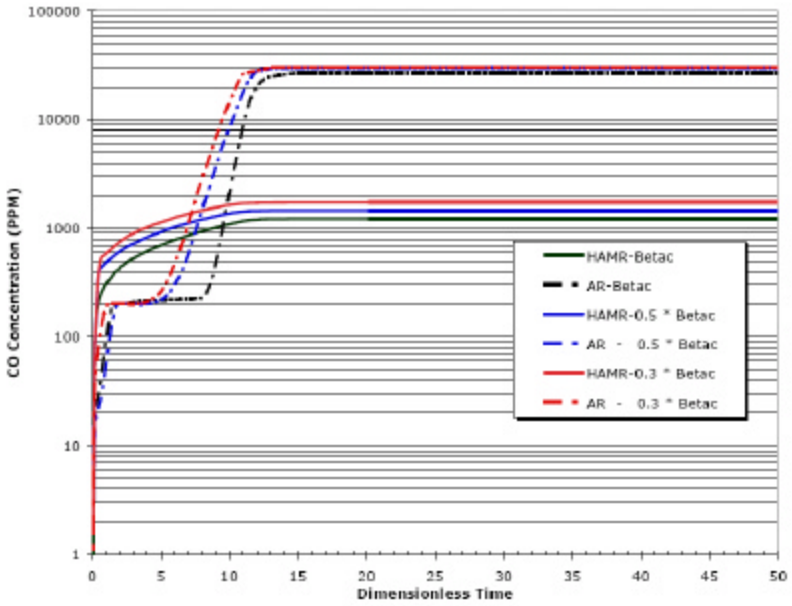

Figure 7.6 Effect of ßc on the CO exit concentration (wet basis, in ppm) for the HAMR (permeate) and AR systems

The effect of using an adsorbent with improved characteristics is shown in Figure 7.7. The hydrogen yields for the HAMR and the AR systems are compared for three values of Ha (Hatta Number)/Da (Damkohler Number), one corresponding to the adsorbent of our experimental result shown in Sec. 7.3.2 and two other cases with corresponding values 3 and 5 times larger. A more effective adsorbent significantly expands the "time window" of operation for both the AR and HAMR systems before regeneration must commence. It also significantly increases the hydrogen yields attained. The degree of run time increase is nearly proportional to the degree of increase in the adsorbent capacity as expected. In addition the effect of Ha/Da appears similar to both HAMR and AR system.

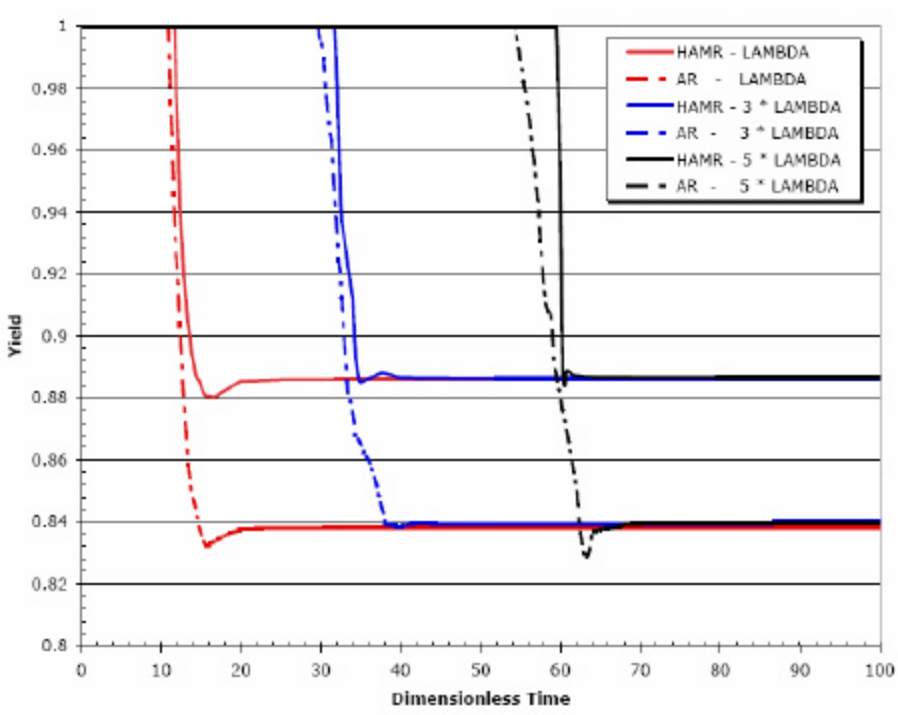

Figure 7.7 Effect of Ha/Da on the hydrogen yield.

The effect of membrane transport characteristics is shown in Figure 7.8, where the reactor yields corresponding to five different membranes (i.e., five different values of (Da)(Pe) ((Damklhler Number)(Peclet Number)) are shown. One corresponding to the CMS membrane and the other four membranes has values that are 0.1, 0.333, 0.5, and 5 times the base value. The HAMR system hydrogen yields do benefit from increased hydrogen permeance. The hydrogen yield increases from ~0.85 to ~0.92 when the permeance increases, i.e. (Da)(Pe) decreases (since (Da)(Pe) is inversely proportional to hydrogen permeance).

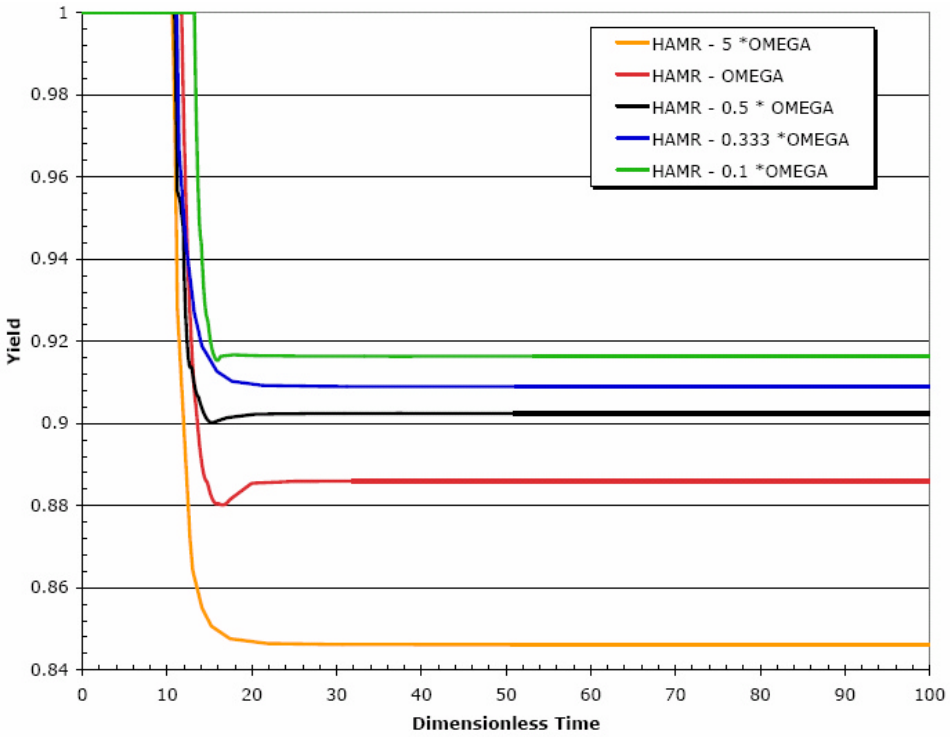

Figure 7.8 Effect of (Da)(Pe) on the hydrogen yield.

Figure 7.9 shows the effect of hydrogen permeance on hydrogen recovery. As expected, increasing the hydrogen permeance has a very beneficial effect on hydrogen recovery, with very high hydrogen recoveries (~87%) attained for 10 times the base case.

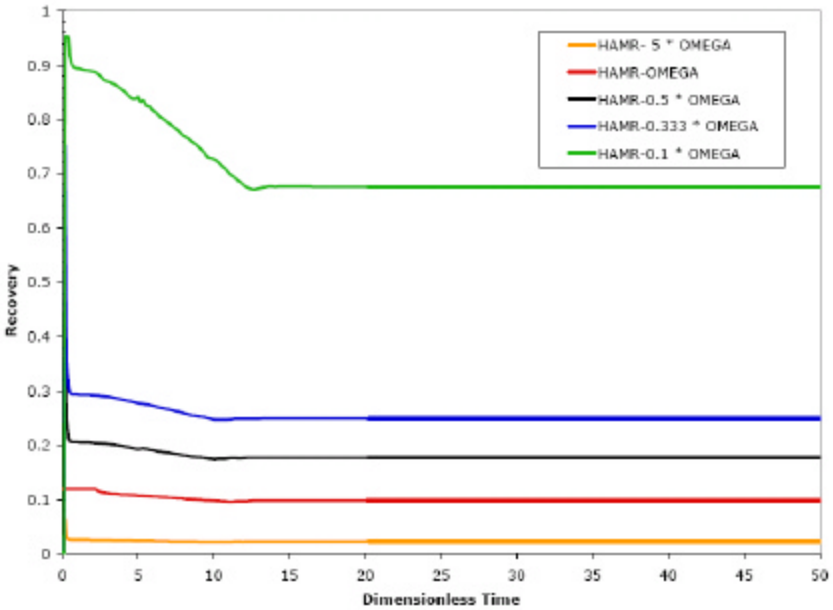

Figure 7.9 Effect of (Da)(Pe) on the hydrogen recovery.

Figure 7.10 shows the effect of the sweep ratio on the hydrogen yield of the HAMR system. Increasing the sweep ratio improves the reactor performance; however, the effect saturates quickly. As shown in Figure 7.10, when the sweep ratio approaches 0.4 time of the base case, the incremental improvement on hydrogen yield becomes insignificant.

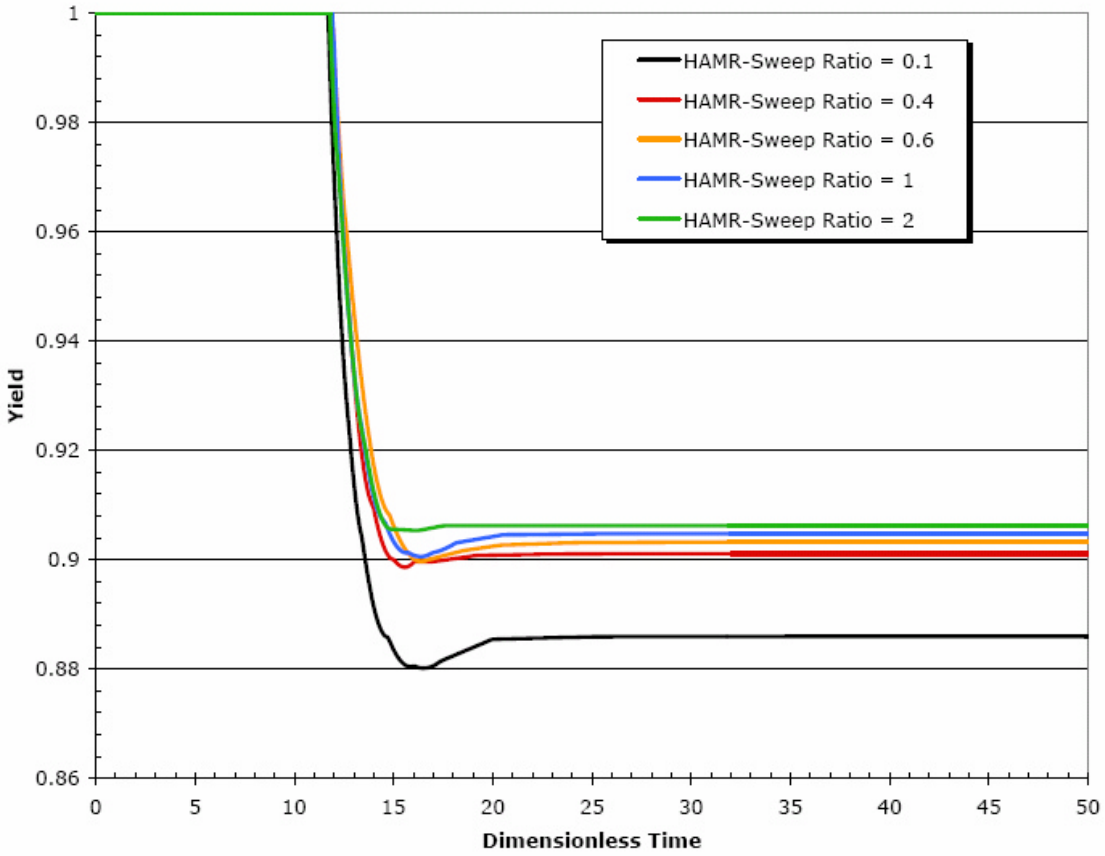

Figure 7.10 Effect of the sweep ratio on the hydrogen yield.

7.4 **Experimental Verification**

7.4.1 Kinetic Study on Catalytic Water Gas Shift Reaction

Kinetic constants for water gas shift reaction are critical input parameters for the performance simulation of our proposed HAMR. A laboratory scale reactor system was established as shown in Figure 7.11 to study the reaction kinetics, which was then employed for the HAMR study. Synthetic feed was prepared from pure gas cylinders with mass flow controllers. The reactor temperature was kept at the target temperature within a constant temperature box. The effluent from the reactor was analyzed with mass spectroscopy after water dropout via condensation.

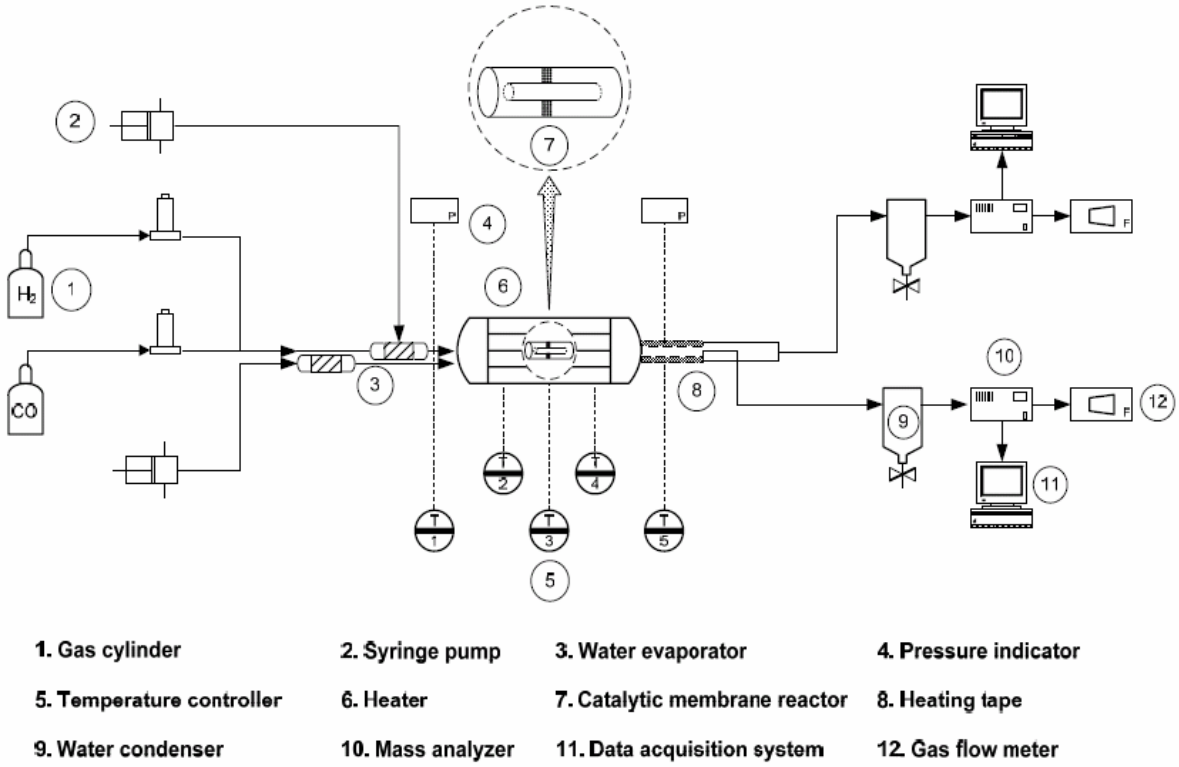

Figure 7.11 Schematic of lab-scale catalytic membrane reactor system

The operating condition selected for determining the reaction kinetics of low temperature shift of the water gas shift reaction is listed in Table 7.2. Three different temperatures were selected, i.e., 205, 225 and 250°C, which covered the temperature range recommended by the catalyst manufacturer for the low temperature shift. Pressure of the reactor was kept at ~50 psig. The feed composition selected for this study was CO: H_2:H_2O = 1.0:4.0:2.5. W/Fo selected ranged from ~30 to as high as ~467, which spanned a wide operating condition for us to obtain representative kinetic parameters.

Table 7.1 Operating conditions for water gas shift reaction kinetic study.

Composition	CO : H2 : H2O = 1.0 : 4.0 : 2.5					
Pressure(psig)	52.5		50		50	
Temperature(C)	205		225		250	
Weight of Catalyst(g)	10		30		30	
Kinetic data	W/Fo CO (g*hr/mol)	CO Conversion(%)	W/Fo CO (g*hr/mol)	CO Conversion(%)	W/Fo CO (g*hr/mol)	CO Conversion(%)
	1.56E+02	77.96	4.67E+02	96.52	4.67E+02	96.63
	7.78E+01	68.47	2.33E+02	95.23	2.33E+02	95.21
	5.19E+01	61.66	1.56E+02	92.22	1.56E+02	92.94
	3.89E+01	50.93	1.17E+02	88.19	1.17E+02	88.43
	3.11E+01	47.96	9.33E+01	79.38	9.33E+01	86.35
	2.59E+01	38.48	7.78E+01	71.78	7.78E+01	77.86
Pre-exponential factor g-mol/(g cat*hr*bar^0.4)	1.52E+08		2.60E+08		2.80E+08	

The reaction rate constants obtained experimentally were then used as shown below to determine the pre-exponential factor and the activation energy.

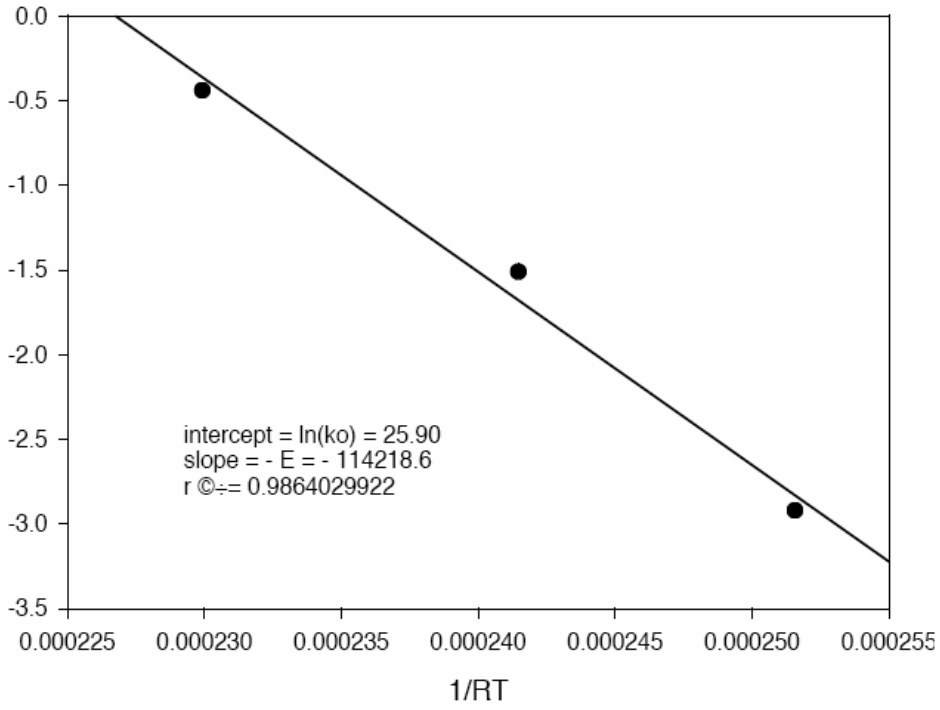

Figure 7.12 Kinetic Parameters Calculations

Table 7.2 Kinetic parameters obtained using experimental data

ko **g-mol/(g cat*hr*bar^0.4)**	**1.77E+11**
E **(J/mol)**	**114218.6**
E **(KJ/mol)**	**114.22**

The pre-exponential factor and the activation energy determined based upon the operating condition listed in Table 7.3 above. These kinetic parameters were used in the mathematical simulation.

7.4.2 Adsorption Isotherm

In addition to the catalytic reaction parameters, the adsorption equilibrium capacity and rate for the CO_2 affinity adsorbent, hydrotalcite, used in this study were experimentally determined. The lab scale adsorption isotherm study was performed in an experimental setup presented in Figure 7.13. The adsorption isotherm for CO_2 on hydrotalcite at 250°C was determined by measuring the difference in the input and output CO_2 molar flow rates. The experimental data were then fitted with the Langmuir adsorption isotherm as presented in Figure 7.14.

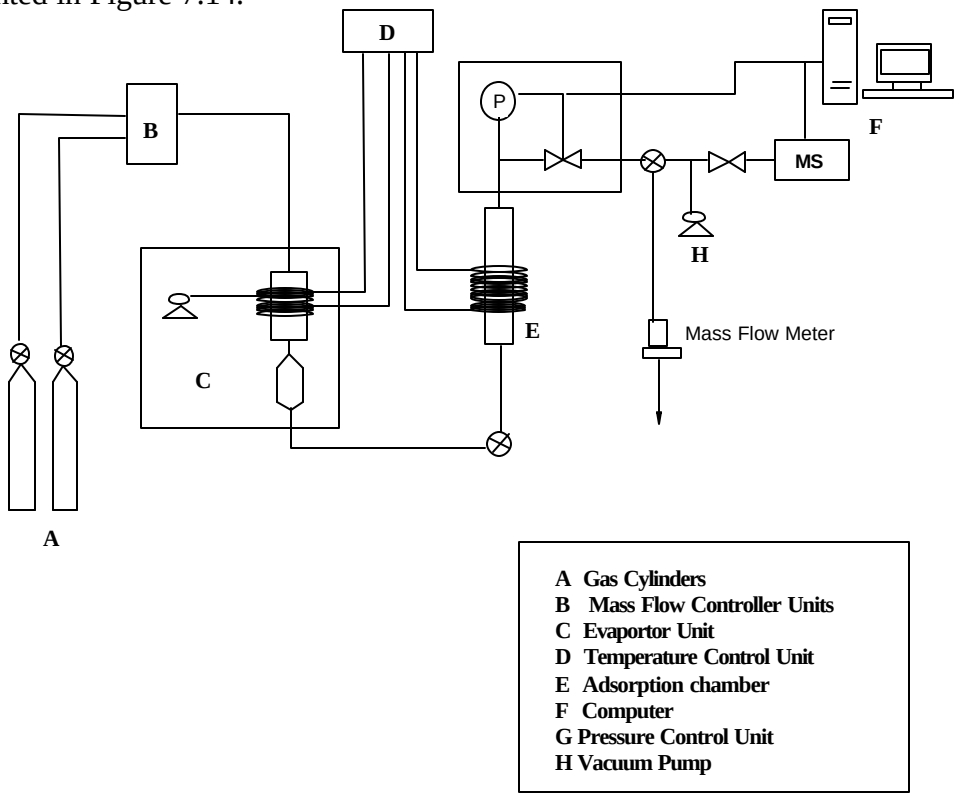

Figure 7.13 Schematic of the lab scale adsorptive system for CO_2 adsorption isotherm study.

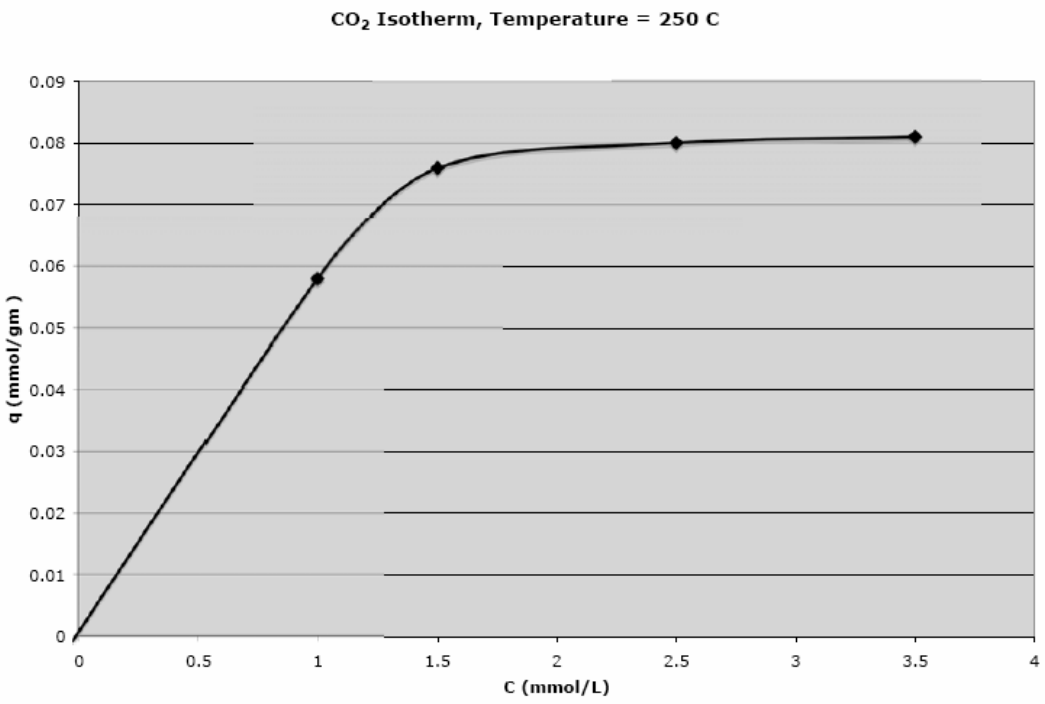

Figure 7.14 Adsorption isotherm of the hydrotalcite adsorbent used for catalytic membrane reactor study.

7.4.3 Characterization of Membranes Selected for HAMR Study

The carbonaceous hydrogen selective membrane was prepared by us and sent to our subcontractor, USC, for performing the catalytic reaction study. Both single component and mixture permeation study were conducted to determine the permeation and separation properties required for the mathematical simulation study. Permeation study of single component, including H_2, CO, CO_2, H_2O, CH_4, N_2 and He, was performed at 15 to 45 psig as shown in Table 7.4. The results from the measurements from both groups are relatively consistent although minor variation exists, which may be resulted from contamination of the membrane and experimental errors. Then the mixture separation study was performed using two different mixture compositions as shown in Table 7.4. The selectivities obtained from the mixtures were about 50% lower than those obtained from the single component. Specifically hydrogen permeance reduced while CO and CO_2 permeances increase significantly. No explanations could be offered for this discrepancy between the single and the mixture separation differences.

Table 7.3 Permeation and Separation Characteristics of CMS Hydrogen Selective Membrane

Surface Area (m2) 0.0027928 Dimention of permeance : [m3/(m2*hr*bar)]

	Single gas						Mixed Gas			
	USC(15psig)		USC(45psig)		MP&T(20psig)		H2/CO/CO2/CH4 5 : 1 : 1 : 1 53 psig		H2/CO/CO2/CH4/H2O 2.5 : 1 : 1 : 1 : 2.5 53 psig	
	Permeance	S.F. on H2	Permeance	S.F. on H2	Permeance	S.F. on H2	Permeance	S.F. on H2	Permeance	S.F. on H2
H2	0.3107	1.00	0.3737	1.00	0.3718	1.00	0.2799	1.00	0.2726	1.00
CO	0.0060	51.78	0.0087	42.80			0.0137	20.46	0.0129	21.16
CO2	0.0156	19.92	0.0244	15.32	0.0144	25.82	0.0297	9.42	0.0333	8.19
H2O	0.4094	0.76							0.4079	0.67
CH4	0.0033	94.16	0.0085	43.90	0.0043	86.85	0.0067	41.62	0.0064	42.79
N2	0.0057	54.95	0.0074	50.18	0.0067	55.41				
He	0.2066	1.50	0.2886	1.29	0.2610	1.42				

7.4.4 Experimental Results from HAMR Study

Some preliminary laboratory study was performed to verify the mathematical simulation presented in Figure 7.2 to 7.11. The M&P hydrogen selective membrane characterized in Sec. 7.4.3 was used as the reactor to selectively remove hydrogen from the water gas shift reaction products, while the CO_2-affinity hydrotalcite adsorbent was packed inside the membrane reactor along with a commercial WGS catalyst. The physical parameters, including catalyst and adsorbent dosages, are listed in Table 7.2. The CO conversion vs time was presented in Figure 7.14. As expected a nearly complete conversion of CO was achieved in the beginning of the reactor run, i.e., up to about 40 minutes. Then, the conversion declined and finally settled at 91.5% when the adsorbent was saturated. In comparison with the simulation presented in Figure 7.5, the overall conversion profiles obtained experimentally here is consistent in general with the predicted profile shown in Figure 7.5. However, the experimental results failed to demonstrate a nearly complete 100% conversion in the beginning of the reactor study. Considering the highly fluctuation of the data in this narrow range (i.e., 2%), it would not be surprised that the reactant by-pass through the bed, unsteady state flow pattern due to significant product loss by adsorption, and others, led to the back-mixing of the reactant and product, which diluted the conversion in the beginning of the reaction run. On the other hand, equilibrium conversion of 91.5% was higher than the predicted 89.5% conversion. Slow adsorption of CO_2 by hydrotalcite may be responsible for this higher-than-predicted conversion level. In spite of these minor discrepancies, the HAMR performance prediction is generally consistent with the experimental results. Comparison between the simulation and the experiment is made below in terms of the conversion level and the breakthrough times:

For W/F =350, simulation time for CO conversion in high levels is ~ 27 minutes, where as experimental data shows ~ 40 minutes.

For W/F =350, simulation time for CO_2 breakthrough is ~ 21 minutes, where as experimental data shows ~ 15-18 minutes.

For W/F =300, simulation time for CO conversion in high levels is ~ 19 minutes, where as experimental data shows ~ 20 minutes.

For W/F =300, simulation time for CO_2 breakthrough is ~ 17 minutes, where as experimental data shows ~ 20 minutes.

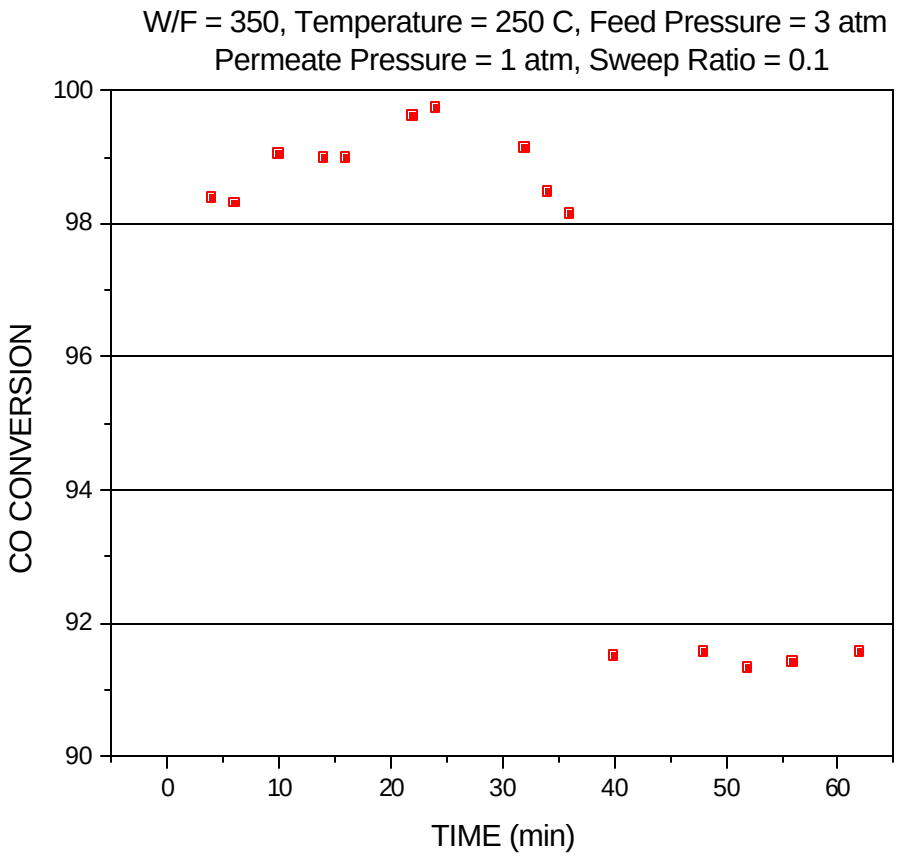

Figure 7.15 CO conversion vs time for HAMR system with W/F=350, T=250C, feed pressure of 3 bar, and permeate pressure =bar, and sweep ratio of 0.1.

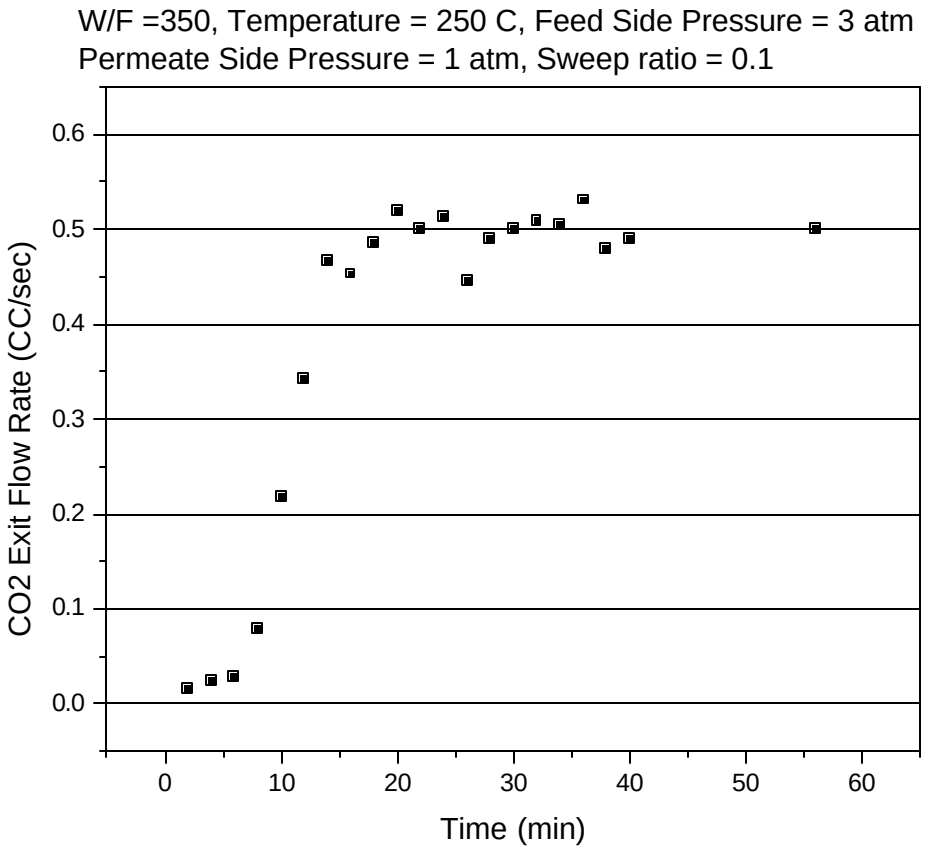

Figure 7.16 CO_2 Concentration at the exit of the reactor

Additional experimental study was performed with W/F=300. The results are presented in Figure 7.16 and 7.18. Since the transition period for CO conversion (i.e., from 100% to the equilibrium % level) in the case of W/F=350 is =~15 minutes, which is much shorter than 20-40 minutes in the case of W/F=300, it is likely that reaction kinetic dominates in this operating condition. Since the transition profile of CO is nearly independent of W/F in this range, it is possible that the reaction kinetics used in this study may require revision.

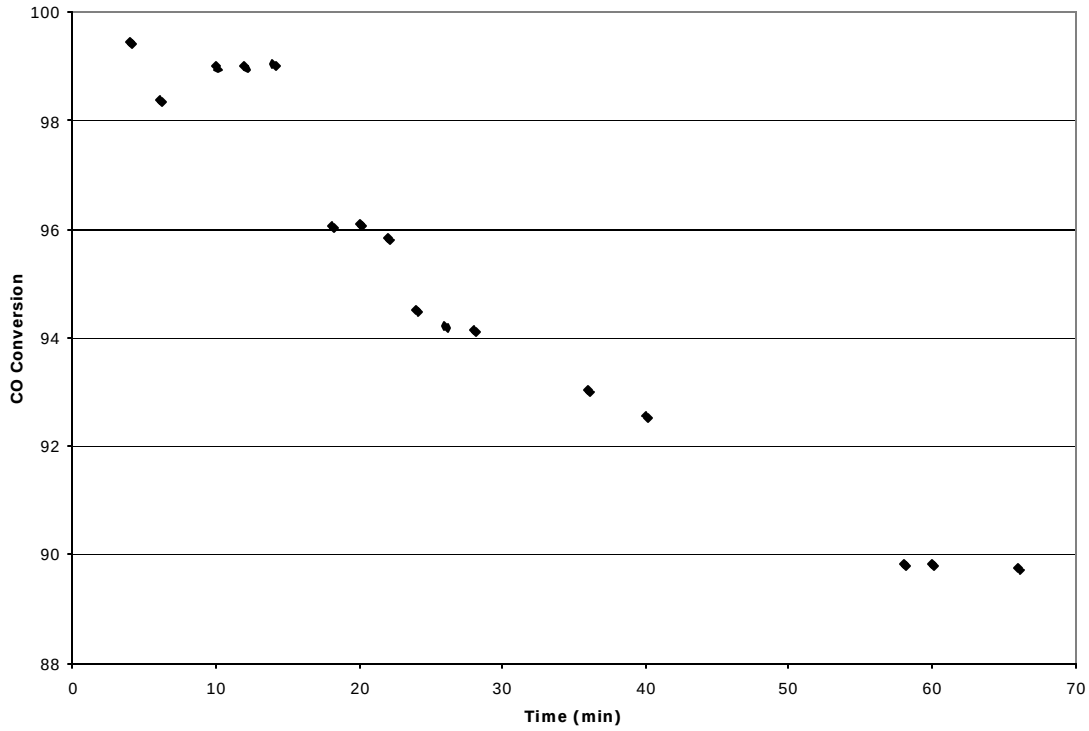

Figure 7.17 CO conversion vs time for HAMR with W/F=300.

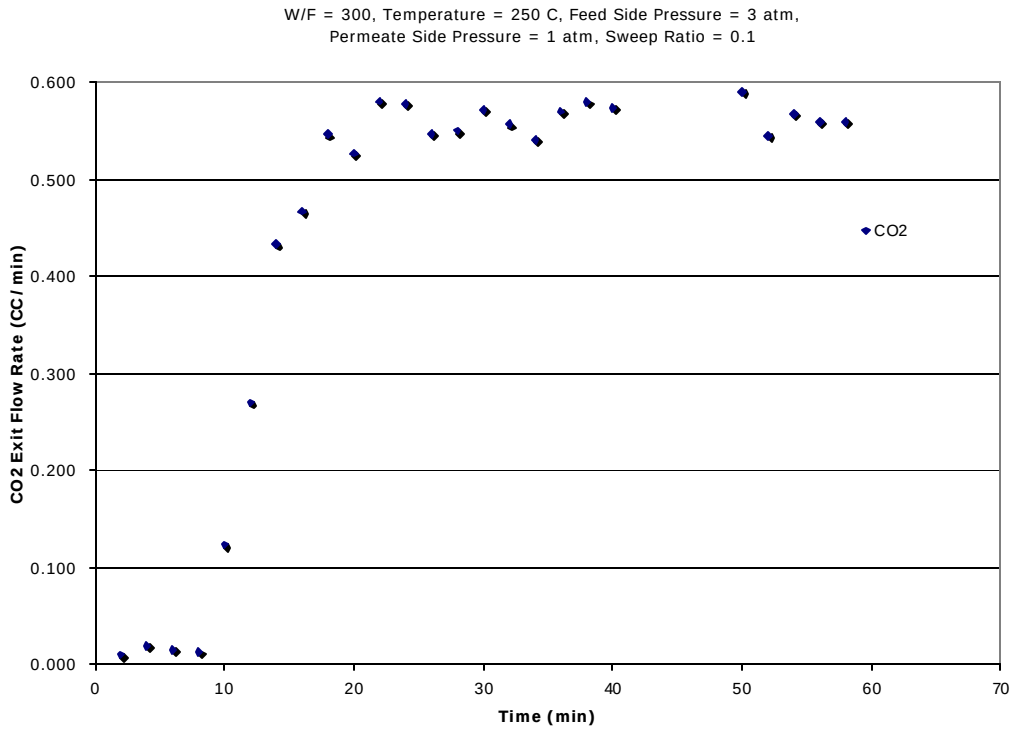

Figure 7.18 CO_2 breakthrough concentrations at the exit of the HAMR reactor. For W/F = 300

The experimental results obtained in this study are generally consistent with the mathematical prediction in terms of CO conversion vs time, CO_2 breakthrough profile and the effect of W/F. However, the nearly complete CO conversion in the beginning of the reaction was not demonstrated by the experimental results, most likely as a result of the non-ideal flow pattern in the small lab-scale reactor. The general trend on the effect of W/F predicted by the simulation was verified by the experimental results although additional improvement in reaction kinetics may be required to use as a quantitative predictive tool.

7.5 Preliminary Economic Analysis

No comprehensive economic analysis was performed due to the time constraint during this project. Instead, a qualitative economic analysis was performed to demonstrate the potential cost advantage of the proposed hybrid reactor. The two outstanding advantages of our proposed reactor are the enhanced conversion and the reduced CO contaminant concentration. According to our simulation selected in this study, CO conversion of 88% can be achieved with our proposed reactor, vs 80% based upon the thermodynamic equilibrium. This would translate into about 10% reduction in the hydrogen production cost. In addition, the CO concentration of 1,000 ppm was achieved with our proposed reactor, as opposed to ~30,000 ppm of the conventional reactor in a side-by-side comparison selected in this study. As a result, the conventional reactor requires additional WGS reaction to further reduce the CO concentration. This reduced and compact WGS reactor of our proposed process would result in significant capital cost savings because WGS is considered one of the least efficient steps in hydrogen production. Once the optimization of the membrane and adsorbent materials is accomplished, we recommend a comprehensive economic evaluation based upon the mathematical model developed here to quantitatively estimate potential capital and operating cost savings of our proposed hybrid reactor.

7.6 Conclusions

We have investigated a novel reactor system, termed the HAMR, for hydrogen production through water gas shift reaction with concomitant CO_2 removal for sequestration. The HAMR combines the reaction and membrane separation steps with adsorption on the membrane feed or permeate sides. The HAMR system is of potential interest to pure hydrogen production for proton exchange membrane (PEM) fuel cells for various mobile and stationary applications. Key conclusions are drawn below:

- The reactor characteristics have been investigated for a range of temperature, pressure, and other experimental conditions relevant to the aforementioned applications and compared with the behavior of the traditional packed-bed reactor, the conventional MR, and an AR. The HAMR outperforms all of the other more conventional reactor systems. It exhibits enhanced CO conversion, hydrogen yield, and product purity for meeting the product purity requirements for PEM operation.

- The performance of the HAMR system depends on the various operating parameters, including the reactor space time, the temperature, and the membrane and adsorbent properties. One of the key advantages of the HAMR system over the corresponding AR system (in addition to improvements in yield) is its ability to deliver a product with a significantly lower CO content through the use of membranes, which preferentially allow the permeation of the hydrogen while excluding CO and other reactants and products. This may be the primary reason for adopting such reactors for fuel-cell application, where a CO-free product is at a premium.

- The disadvantage of the HAMR system is, similar to that for the ARs, in that they require regeneration of the spent adsorbent for continuous operation. The HAMR system may require a dual reactor system, where one of the reactors is in operation while the other reactor is being regenerated.

- Use of effective adsorbent results, for example, in increased yields and longer operational time windows. More highly permeable membranes also increase the reactor yield but, more importantly, also increase the hydrogen recovery ratio.

Our preliminary experimental results are consistent with the prediction with the mathematical model developed here. Additional experimental validation of the HAMR system and extension of the model to incorporate adsorbent regeneration are recommended. Finally, incorption of temperature to simulate the HAMR under the non-isothermal condition is necessary to truly reflect the WGS reaction, an exotherm reaction.

Table 7.4 Parameter Values Used in Simulations

Parameter	Value	Dimension	
b_{CO_2}	22.21	bar^{-1}	
d_p^F	0.001	m	
m_{CO_2}	0.104	mol/kg	
P_0^F	3	bar	
P_0^P	2	bar	
s	0.1	-	(Base case)
T	250	°C	(Base case)

g	0.4536	-
d_1	1	-
d_2	0.0742	-
d_3	0.189	-
d_5	0.375	-
e^F	0.4	-
Λ	0.029	-
l	0.3	-
m^F	0.0004	Pa.s
t_F	10.43	-
t_a	22.98	-
Ω	18.51	-
w	0.33	-

Nomenclature :

A^F	cross sectional area for the reactor feed side (m^2)
A^P	cross sectional area for the reactor permeate side (m^2)
b_{CO_2}	Langmuir model adsorption equilibrium constant for CO_2 (bar^{-1})
C_j^F	gas phase concentration of species j in the feed side ($kmol/m^3$)
C_j^P	gas phase concentration of species j in the permeate side ($kmol/m^3$)
C_s	solid phase concentration of CO_2 (mol/kg)
C_{seq}	equilibrium solid phase concentration of CO_2 (mol/kg)
Da	Damkohler number (dimensionless)
D_L^F	axial dispersion coefficient in the feed side (m^2/s)
D_L^P	axial dispersion coefficient in the permeate side (m^2/s)
D_m^F	molecular diffusivity in feed side(m^2/s)
D_m^P	molecular diffusivity in permeate side (m^2/s)
d_t^p	membrane inside diameter (m)
d_p^F	particle diameter in feed side (m)
f^F	friction factor (dimensionless)
F_j	molar flux ($mol/m^2.s$)
g_c	gravity conversion factor
G_m^F	superficial mass flow velocity in the feed side ($kg/m^2.s$)
$G_j^{'F}$	dimensionless adsorption rate for species j
G_j^F	adsorption rate for species j (mol/kg.s)
Ha	Hatta number (dimensionless)
k	A^F/A^P
k_a	LDF mass transfer coefficient (s^{-1})
K_j	adsorption equilibrium constant for CH_4, CO and H_2 (bar^{-1})
K_{H2O}	dissociative adsorption constant of water
K'_{CO}	dimensionless kinetic parameter (dimensionless)
K_{eq1} , K_{eq3}	equilibrium constant of reaction I and III in Table 1. (bar^2)
K_{eq2}	equilibrium constant of reaction I in Table 1. (dimensionless)
m_{CO2}	Langmuir model total adsorbent capacity constant for CO_2 (mol/kg)
MW_j	molecular weight of species j
N^F_{Re}	Reynolds number for feed side

$n^{F}_{j_0}$	inlet molar flow rate for feed side (mol/s)
$n^{P}_{j_0}$	inlet molar flow rate for permeate side (mol/s)
n_j^F	molar flow rate for component *j* in the feed side (mol/s)
n_j^P	molar flow rate for component *j* in the permeate side (mol/s)
$n^{F}_{i,ex}$	molar flow rates at the exit of the reactor for component *i* in the feed side (mol/s)
$n^{P}_{i,ex}$	molar flow rates at the exit of the reactor for component *i* in the permeate side (mol/s)
P_0^F	inlet feed side pressure(bar)
Pe	Peclet Number
P^F	feed side pressure (bar)
P_j^F	partial pressure of component j in the membrane feed side (bar)
P_j^P	partial pressure of component j in the membrane permeate side (bar)
Q_0^F	volumetric flow rate (m^3/s)
R	ideal gas constant (m^3.bar/mol.K)
r_i	rate of reaction for i^{th} equation (kmol/kg.s)
r_i'	dimensionless rate of reaction for i^{th} equation
R_j	reaction rate expression for species j (kmol/kg.s)
R'_j	dimensionless reaction rate expression for species j
s	sweep ratio
t	time (second)
T	absolute temperature (K)
T_0	reference temperature (K)
u_0^F	superficial flow velocity at the inlet on feed side (m/s)
u_0^P	superficial flow velocity at the inlet on permeate side (m/s)
u^F	superficial flow velocity on feed side (m/s)
u^P	superficial flow velocity on permeate side (m/s)
U_j	membrane permeance for component *j* (mol/m^2.bar.s)
V	reactor volume (m^3)
V_R	total reactor volume (m^3)
W_c	catalyst weight (kg)
X_{CH_4}	methane conversion (dimensionless)

$x_{j_0}^F$	inlet mole fraction for species j in the feed side
$x_{j_0}^P$	inlet mole fraction for species j in the permeate side
x_j^F	mole fraction for species j in the feed side
x_j^P	mole fraction for species j in the permeate side
y_j	mole fraction of component j
Y_{H_2}	hydrogen yield (dimensionless)

Subscripts

0	entrance condition
ads	adsorbent condition
eq.	equilibrium
ex	exit
j	chemical species

Superscripts

F	feed side
P	permeate side

Greek Letters

a_m	membrane area per feed side reactor volume (m^2/m^3)
a_j	MW_j/MW_{H2}
b_c	fraction of the reactor volume occupied by catalysts
b_{CO_2}	$b_{CO_2} P_0^F$ (dimensionless)
g	t_F / t_a (dimensionless)
ΔH_a	heat of adsorption (kJ/mol)
d_j	separation factor (dimensionless)
e^F	total feed side bed porosity

e_b^F	bed porosity in the feed side
x^F	u^F / u_0^F (dimensionless)
x^P	u^P / u_0^P (dimensionless)
h	V/V_R (dimensionless)
Θ^F	$e_b^F A^F D_L^F / u_0^F V_R$ (dimensionless)
Θ^P	$A^F D_L^P / u_0^P V_R$ (dimensionless)
q_s^F	C_s^F / m_{CO_2} ,(dimensionless)
q_{seq}^F	C_{seq}^F / m_{CO_2} ,(dimensionless)
Λ	Ha/Da (dimensionless)
l	$A^P u_0^P / A^F u_0^F$ (dimensionless)
m^F	viscosity (Pa.s)
Ξ	$10^{-6} f^F ((u_0^F)^2 MW_{H_2} V_R / A^F g_c d_p^F RT)$ (dimensionless)
r_a	adsorbent density (kg/m^3)
r_c	catalyst density (kg/m^3)
r_F^F	fluid density (kg/m^3)
t	$k_a t$ (dimensionless)
t_F	$e^F V_R / A^F u_0^F$ (dimensionless)
t_a	$(k_a)^{-1}$ (dimensionless)
Ψ^F	P^F / P_0^F (dimensionless)
Ψ^P	P^P / P_0^P (dimensionless)
Ω	(Da)(Pe) (dimensionless)
w	P_0^P / P_0^F (dimensionless)

Literature Cited

1. Park B. *Models and Experiments with Pervaporation Membrane Reactors Integrated with a Water Removal Adsorbent System*, Ph.D. Thesis, University of Southern California, Los Angeles, California, 2001.
2. Park, B.; Tsotsis, T. T. Models and Experiments with Pervaporation Membrane Reactors Integrated With an Adsorbent System. *Chem. Eng. Proc.* **2004**, 43, 1171.
3. Choi, Y.; Stenger, H.G. Water Gas Shift Reaction Kinetics and Reactor Modeling for Fuel Cell Grade Hydrogen. J. Power Sources **2003,** 124, 432.
4. Darwish, N. A.; Hilal, N.; Versteeg, G.; Heesink, B. Feasibility of the Direct Generation of Hydrogen for Fuel-cell-powered Vehicles by on-board Steam Reforming of Naphtha. *Fuel.* **2003**, 83, 409.
5. Liu, Z.; Roh, H.; Park, S. Hydrogen Production for Fuel Cells Through Methane Reforming at Low Temperatures. J. Power Sources **2002,** 111, 83.
6. Semelsberger, T. A.; Brown, L. F.; Borup, R. L.; Inbody, M. A. Equilibrium Products from Autothermal Processes for Generating Hydrogen-rich Fuel-cell Feeds. *Int. J. Hydrogen Energ.* **2004**, 29, 1047.
7. Elnashaie, S.S.E.H.; Adris, A.; Al-Ubaid, A.S.; Soliman, M.A. On the Non-monotonic Behavior of Methane-steam Reforming Kinetics. *Chem. Eng. Sci.* **1990,** 45, 491.
8. Xu, J.; Froment, G.F. Methane Steam Reforming, Methanation and Water-gas Shift: I. Intrinsic Kinetics. *AIChE J*. **1989,** 35, 88.
9. Han, C.; Harrison, D.P. Simultaneous Shift Reaction and Carbon Dioxide Separation for the Direct Production of Hydrogen. *Chem. Eng. Sci.* **1994,** 49, 5875.
10. Hwang, S. Inorganic Membranes and Membrane Reactors, *Korean J. Chem. Eng*. **2001,** 18, 775.
11. Lim, S.Y.; Park, B.; Hung, F.; Sahimi, M.; Tsotsis, T.T. Design Issues of Pervaporation Membrane Reactors for Esterification. *Chem. Eng. Sci*. **2002,** 57, 4933.
12. Park, B.; Ravi-Kumar, V.S.; Tsotsis, T.T. Models and Simulation of Liquid-phase Membrane Reactors. *Ind. Eng. Chem. Res*. **1998,** 37, 1276.
13. Nam, S.W.; Yoon, S.P.; Ha, H.Y.; Hong, S.; Maganyuk, A.P. Methane Steam Reforming in a Pd-Ru Membrane Reactor. *Korean J. Chem. Eng.* **2000,** 17, 288.
14. Saracco, G.; Specchia, V. Catalytic Inorganic-membrane Reactors: Present Experience and Future Opportunities. *Catal. Rev.-Sci. Eng.* **1994,** 36, 305.
15. Sanchez, J.; Tsotsis, T.T. *Catalytic Membranes and Membrane Reactors*; Wiley-VCH: Weinheim, 2002.
16. Xiu, G. H.; Li, P.; Rodrigues, A. E. Subsection-controlling Strategy for Improving Sorption-enhanced Reaction Process. *Chem. Eng. Res. Des.* **2004**, 82, 192.
17. Xiu, G.; Li, P.; Rodrigues, A. E. Adsorption-enhanced Steam-methane Reforming with Intraparticle-diffusion Limitations**.** *Chem. Eng. J.* (Amsterdam, Netherlands) **2003**, 95, 83.
18. Xiu, G.; Li, P.; Rodrigues, A. E. New Generalized Strategy for Improving Sorption-enhanced Reaction Process. *Chem. Eng. Sci.* **2003**, 58, 3425.
19. Xiu, G.; Soares, J. L.; Li, P.; Rodrigues, A. E. Simulation of Five-step One-bed Sorption-enhanced Reaction Process. *AIChE J.* **2002**, 48, 817.
20. Xiu, G.; Li, P.; Rodrigues, A. E. Sorption-enhanced Reaction Process with Reactive Regeneration. *Chem. Eng. Sci.* **2002**, 57, 3893.

21. Lee, D. K.; Baek, I. H.; Yoon, W. L. Modeling and Simulation for the Methane Steam Reforming Enhanced by in Situ CO_2 Removal Utilizing the CaO Carbonation for H_2 Production. *Chem. Eng. Sci.* **2004**, 59, 931.
22. Ding, Y.; Alpay, E. Adsorption-enhanced Steam-methane Reforming. *Chem. Eng. Sci.* **2000**, 55, 3929.
23. Ortiz, A. L.; Harrison, D. P. Hydrogen Production Using Sorption-Enhanced Reaction. *Ind. Eng. Chem. Res.* **2001**, 40, 5102.
24. Balasubramanian, B.; Ortiz, A. L.; Kaytakoglu, S.; Harrison, D. P. Hydrogen from Methane in a Single-step Process. *Chem. Eng. Sci.* **1999**, 54, 3543.
25. Waldron, W. E.; Hufton, J. R.; Sircar, S. Production of Hydrogen by Cyclic Sorption Enhanced Reaction Process. *AIChE J.* **2001**, 47, 1477.
26. Hufton, J. R.; Mayorga, S.; Sircar, S. Sorption-enhanced Reaction Process for Hydrogen Production. *AIChE J.* **1999**, 45, 248.
27. Ding, Y.; Alpay, E. Equilibria and Kinetics of CO_2 Adsorption on Hydrotalcite Adsorbent. *Chem. Eng. Sci.* **2000**, 55, 3461.
28. Park, B. A Hybrid Adsorbent-membrane Reactor (HAMR) System for Hydrogen Production. *Korean J. Chem. Eng.* **2004**, 21, 782.
29. Chen, Z.; Elnashaie, S. S. E. H. Bifurcation Behavior and Efficient Pure Hydrogen Production for Fuel Cells Using a Novel Autothermic Membrane Circulating Fluidized-Bed (CFB) Reformer: Sequential Debottlenecking and the Contribution of John Grace. *Ind. Eng. Chem. Res.* **2004**, 43, 5449.
30. Prasad, P.; Elnashaie, S. S. E. H. Novel Circulating Fluidized-Bed Membrane Reformer Using Carbon Dioxide Sequestration. *Ind. Eng. Chem. Res.* **2004**, 43, 494.
31. Prasad, P.; Elnashaie, S. S. E. H. Coupled Steam and Oxidative Reforming for Hydrogen Production in a Novel Membrane Circulating Fluidized-Bed Reformer. *Ind. Eng. Chem. Res.* **2003**, 42, 4715.
32. Chen, Z.; Yan, Y.; Elnashaie, S. S. E. H. Novel Circulating Fast Fluidized-bed Membrane Reformer for Efficient Production of Hydrogen from Steam Reforming of Methane. *Chem. Eng. Sci.* **2003**, 58, 4335.
33. Ciora, R. J.; Fayyaz, B.; Liu, P. K. T.; Suwanmethanond, V.; Mallada, R.; Sahimi, M.; Tsotsis, T. T. Preparation and Reactive Applications of Nanoporous Silicon Carbide Membranes. *Chem. Eng. Sci.* **2004**, 59, 4957.
34. Edwards, M. F.; Richardson, J. F. Gas Dispersion in Packed Beds. *Chem. Eng. Sci.* **1968**, 23, 109.
35. Karger, J.; Ruthven, D.M. *Diffusion in Zeolites and Other Microporous Solids*; Wiley Publishers: New York, 1992.
36. Levenspiel, O. *Chemical Reaction Engineering*, 3rd Edition**;** Wiley: New York, 1998**.**.
37. Schiesser, W. E. *The Numerical Method of Lines: Integration of Partial Differential Equations*; Academic Press: San Diego, 1991.
38. Vande Wouwer, A.; Saucez, P.; Schiesser, W. E. Simulation of Distributed Parameter Systems Using a Matlab-Based Method of Lines Toolbox: Chemical Engineering Applications. *Ind. Eng. Chem. Res.* **2004**, 43, 3469.
39. Vasileiadis, S. P. *Catalytic Ceramic Membrane Reactors for the Methane-Steam Reforming Reaction: Experiments and Simulation,* Ph.D. Thesis, University of Southern California, Los Angeles, California 1994

Chapter 8

Overall Conclusions

This chapter summarizes the overall conclusions drawn from this study.

LDH Materials for CO_2-Afinity Membranes and Adsorbents

- *In-situ* DRIFTS, DTA, TG/MS and HTXRD techniques were applied in this study to investigate the thermal evolution behavior of the Mg-Al-CO_3 LDH as a function of temperature and atmosphere. The LDH materials exhibits CO_2 affinity beginning at temperature >190°C. The LDH maintains its double layer structure up to 280°C. Beyond this temperature, the degradation of the LDH structure was observed under the inert atmosphere studied here. However, the LDH structure can be restored when the atmosphere exposed is appropriate.

- The LDHs are shown capable of CO_2 exchanging reversibly for a broad region of conditions. These experimental observations qualify the LDH as base material for the formation of CO_2 permselective membranes and CO_2-affinity adsorbents for high temperature membrane reactor applications as proposed in this project. The ability to reversibly adsorb CO_2 is critical from the standpoint of being able to regenerate the adsorbents. The presence of a relatively mobile CO_2 phase within the LDH structure is important in determining the permeation rate through the membrane.

Synthesis and Characterization of CO_2-Affinity Membranes

- The CO_2 permeation enhancement via the LDH material was demonstrated in several experimental membranes prepared in this project. The two synthesis techniques and one post-treatment technique developed here successfully demonstrated the technical feasibility of the formation of the LDH-based membrane. Additional work with the focus on minimization of defects is recommended to upgrade the CO_2 selectivity and permeance for future commercial use.

- Combining the observations from permeance, pore size distribution, EDAX and SEM, we concluded that the hydrotalcite crystals were deposited within the pore size of the starting Al_2O_3 membranes with the pore sizes of 40Å, 500 Å, and 0.2µm. >90% gas permeance was reduced and the pore size was reduced dramatically, capable of delivering Knudsen selectivity or better. This LDH-based membrane via in-situ crystallization is suitable for post-treatment by the CVD/I technique.

· Post treatment by CVD with the protocol we developed is effective in reducing the residual permeance of the LDH membrane to a minimum. For instance, the CO_2 permeance of 0.26 $m^3/m^2/hr/bar$ at 300°C was observed for one of the membranes after the post treatment by CVD/I technique. Further, our analysis indicates that >50% of the CO_2 permeance is likely attributed to the enhancement by the LDH

materials. The balance is contributed by defects remaining in the membrane.

- The ideal selectivity for CO_2/N_2 of ~1.6 at 100 to 300°C was obtained for the LDH membrane prepared via in-situ crystallization and the CVD/I post treatment. In comparison with the ideal selectivity through Knudsen diffusion of 0.8, the selectivity obtained from the LDH membrane is about double of what delivered by the Knudsen diffusion. Evidently, the enhanced selectivity is not sufficient to be commerically viable. An optimization study is necessary to reduce the defect to a minimum via the membrane synthesis; thus, minimal post treatment is required to achieve the CO_2 enhancement without sacrificing permeance significantly.

- The slip casting technology developed here successfully developed a LDH membrane with the residual pore size of <40Å while keeping most of the original permeance, i.e., 30 to 40 $m^3/m^2/hr/bar$ available, which could be an ideal starting material for the post treatment with CVD/I. Thus, the slip casting technique could be a promising LDH synthesis approach. No post treatment study is performed for this type of the LDH membrane due to the time constraint.

- Another type of membranes, carbonaceous base , demonstrated significant selectivity for CO_2/N_2, i.e., 4 to 10, up to 220°C, which was much beyond the Knudsen selectivity. Surface affinity of the membrane toward CO_2 was identified as the dominating mechanism at this operating temperature range. Selectivity at this level is comparable or higher than the selectivity of CO_2/N_2 reported in the literature at the proposed reaction temperature. Pore size reduction was attempted without any success in boosting the CO_2 affinity. Additional study including characterization of this type of membrane in a mixture environment is recommended for future development.

Characterization of CO_2-Affinity Adsorbents

- Diffusivity constants and adsorption isotherms for carbon dioxide in Mg-Al-CO_3 LDH2 at 200 - 250°C were determined by the gravimetric method. Diffusivity constants determined by experiments and those obtained by molecular dynamic simulations are in good qualitative agreement.

- The experimental results for CO_2 uptake vs pressure have been evaluated with the Langmuir and various empirical adsorption isotherm equations. It was observed that the heterogeneity of the material and the interaction between CO_2 and LDH increased with temperature. Also it was found that the experimental data were nonlinearly fitted best with the Toth equation based on χ^2 values.

- Our study observed that the amount of CO_2 uptake and the BET surface area increased as the particle size decreased. When the uptake amount was normalized with the BET surface area, it was found that the specific uptake amount was fairly constant for all the ranges of particle sizes. The adsorption isotherm obtained from data with different particle sizes of LDH were evaluated with Langmuir isotherm and

Langmuir-Freundlich equation. It was observed that the values of b_{CO_2} and n were relatively constant for the whole range of particle sizes. In summary, the adsorption isotherm can be described with the proposed specific property if the particle size effect is significant.

Hybrid Reactors for Water Gas Shift Reaction

- The HAMR combines the reaction and membrane separation steps with adsorption on the membrane feed or permeate sides. The reactor characteristics have been investigated for a range of temperature, pressure, and other experimental conditions relevant to the aforementioned applications and compared with the behavior of the traditional packed-bed reactor, the conventional MR, and an AR. The HAMR outperforms all of the other more conventional reactor systems. It exhibits enhanced CO conversion, hydrogen yield, and product purity.

- One of the key advantages of the HAMR system over the corresponding AR system (in addition to improvements in yield) is its ability to deliver a product with a significantly lower CO content through the use of membranes, which preferentially allow the permeation of the hydrogen while excluding CO and other reactants and products. This may be the primary reason for adopting such reactors for fuel-cell application, where a CO-free product is at a premium.

- The disadvantage of the HAMR system is, similar to that for the ARs, in that the HAMR requires regeneration of the spent adsorbent. For continuous operation; the HAMR may require a dual reactor system, where one of the reactors is in production while the other reactor is being regenerated.

- Our preliminary experimental results are consistent with the prediction with the mathematical model. Additional experimental validation of the HAMR system and the expansion of the model to incorporate adsorbent regeneration are recommended. Finally, incorporation of temperature as a variable to simulate the HAMR under the non-isothermal condition is necessary to truly reflect the WGS reaction, an exothermic reaction.

Acronyms

A:	Arrhenious constant
AR:	Adsorptive reactor
BET:	Brunauer-Emmett-Teller
CMS:	Carbon molecular sieve
CVD/I:	Chemical Vapor Deposition/Infiltration
D:	Diffusivity
DA:	Double Alkoxide
DCP:	Inductively Coupled Plasma
DSC:	Differential Scanning Calorimetry
DTA:	Differential Thermal Analysis
DRIFTS:	Diffuse Reflectance Infrared Fourier Transform Spectroscopy
E:	Activation energy
HAMR:	Hybrid adsorbption-membrane reactor
HT	Hydrotalcite
HTXRD:	High temperaure x-ray diffraction
ICP:	Inductive Ccoupling plasma
IGCC:	Integrated aas combined cycle
LDF:	Linear driving force
LDH:	Layered double hydroxide
LHV:	Lower Heating Value
LTS:	Low temperature shift
M_∞:	Amount uptaken at complete saturation
MB-MS:	Molecular Beam Mass Spectrometry
MR:	Membrane reactor
MS:	Mass spectroscopy
Mt:	Amount uptaken at time, t
R:	Gas constant
SA:	Single Alkoxide
SEM:	Scanning Electron Microscopy
TEM:	Transmission electron microscopy
TEOS:	Tetraethylotho silicate
TG:	Thermo gravimetric
TGA:	Thermal gravimetric analysis
WGS:	Water gas shift
XRD:	X-ray diffraction

List of Publications

- Kim, N., Kim, Y., Tsotsis, T.T., and Sahimi, M. "Atomistic Simulation of Nanoporous Layered Double Hydroxide Materials and their Properties. I. Structural Properties," *J. Chem. Phys*., 122, 2147, 2005.
- Kim, Y., Yang, W., Liu, P.K.T., Sahimi, M., and Tsotsis, T.T., "The Thermal Evolution of the Structure of a Mg-Al-CO_3 Layered Double Hydroxide (LDH). Sorption Reversibility Aspects," *Ind. Eng. Chem. Res*., 43, 4559, 2004.
- Yang, W., Kim, Y., Liu, P.K.T., Sahimi, M. and T. T. Tsotsis, "A Study by *In-Situ* Techniques of the Thermal Evolution of the Structure of a Mg-Al-CO_3 Layered Double Hydroxide (LDH)," *Chem. Eng. Sci*., 57, 2945, 2002.